UNIVERSITÀ CATTOLICA DEL SACRO CUORE

Sede di Brescia

Dottorato di ricerca in Science

Ciclo XXXVII

S.S.D. PHYS-05/B, BIOS-05/A, STAT-01/B

UNIVERSITÀ
CATTOLICA
del Sacro Cuore

Large scale ozone risk assessment for vegetation, from past years to the end of the century under different climate change scenarios

Coordinatore:

Ch.mo Prof. Luca Gavioli

Tesi di Dottorato di:

Pierluigi R. Guaita

N. Matricola: 5116235

Anno Accademico 2025/2026

LARGE SCALE OZONE RISK ASSESSMENT FOR VEGETATION, FROM PAST YEARS TO THE END OF THE CENTURY UNDER DIFFERENT CLIMATE CHANGE SCENARIOS

A Dissertation

Submitted to the Graduate School
of the University of Notre Dame
in Partial Fulfillment of the Requirements
for the Degree of

Doctor of Philosophy

by

Pierluigi R. Guaita

Giacomo A. Gerosa, Co-Director

Paola Crippa, Co-Director

Riccardo Marzuoli, Co-Director

Graduate Program in Applied and Computational Mathematics and Statistics
Notre Dame, Indiana

May 2026

LARGE SCALE OZONE RISK ASSESSMENT FOR VEGETATION, FROM PAST YEARS TO THE END OF THE CENTURY UNDER DIFFERENT CLIMATE CHANGE SCENARIOS

Abstract

by

Pierluigi R. Guaita

This dissertation presents a global, flux-based assessment of O_3 risks to vegetation across the 21st century, analyzing trends in phytotoxic ozone dose (POD) and the influence of environmental factors on stomatal conductance and thereby O_3 uptake by vegetation. We introduce a dual-sink, big-leaf dry deposition model to estimate POD and the associated effects on crop and forest productivity. First, we demonstrate its capabilities in estimating O_3 risk to wheat at a regional scale for the present time. Subsequently, we perform global assessments throughout the 21st century, under multiple contrasting Shared Socioeconomic Pathways, for both wheat and forests ecosystems. We examine the impacts of temperature, vapor pressure deficit, and soil water availability on plant physiology, and address outstanding challenges in projecting future O_3 risk by quantifying elevated CO_2 effects on stomatal conductance and developing a machine-learning framework for forest ecosystem phenology under warming scenarios.

Results indicate that O_3 damage to vegetation is projected to decline globally for both wheat and forests. While improvements in air quality contribute to this trend, simulations indicate that climatic limitations on stomatal conductance and the protective effect of rising CO_2 concentrations substantially reduce O_3 uptake

even under pessimistic emission scenarios. However, O_3 risk is not expected to decline uniformly. South, South-East, and East Asia emerge as near-term hotspots for both crops and forests, while boreal forests may become increasingly vulnerable. Montane regions surrounding the Tibetan Plateau and parts of Sub-Saharan Africa and South America may also experience persistent or emerging risks depending on future climate and emission trajectories.

Our findings highlight the value of flux-based frameworks for assessing global O_3 risk under climate change, providing a robust basis for prioritizing region-specific mitigation strategies to protect crop productivity and forest ecosystems from O_3 damage under future climate conditions.

Ai miei genitori,

Armando e Maria

CONTENTS

FIGURES

TABLES

ACKNOWLEDGMENTS

There are several people to whom I am deeply indebted for guiding me through this doctoral journey and for their support over the past four years. First and foremost, I would like to thank my three supervisors, who have guided me beautifully as I navigated research. My deepest gratitude goes to Giacomo Gerosa, whose unfaltering presence has been extremely precious during these years. His mentorship and constructive criticism have been fundamental not only in teaching me micrometeorology, but also in shaping my overall approach to science. It has been a privilege to experience firsthand his honesty and integrity, both as a scientist and as a person: I could not have wished for a better guide in this journey. My heartfelt gratitude also goes to Riccardo Marzuoli. His guidance in matters of vegetation biology has been essential during these years and in the development of this project. His gracious presence and constant support deserve my greatest appreciations. My sincerest thanks also go to Paola Crippa for being the perfect mentor and a great teacher during my time at Notre Dame. I would not be the same without her guidance, and I am profoundly grateful for the new, enriching perspectives she has shown me.

I would also like to extend my gratitude to Stefano Castruccio for his inspiring lectures in statistics; to the EnvStat and RBC groups for their stimulating feedbacks and discussions; to Jason McLachlan and the Paleon group for introducing me to new research themes; to Cazimir Kowalski not only for the valuable conversations but, above all, for being a true friend; to Angelo Finco and Davide Plebani for their help in many different forms and for being terrific lab colleagues.

CHAPTER 1

INTRODUCTION

1.1 Tropospheric Ozone

Tropospheric Ozone (O_3) is one of the major greenhouse gases (GHGs) and a secondary photochemical pollutant that negatively affects biological systems through oxidative reactions. It is formed in the troposphere through complex photochemical reactions involving nitrogen oxides (NO_x), volatile organic compounds (VOCs), methane (CH_4), and carbon monoxide (CO) in the presence of sunlight.

Since the mid-20^{th} century, rapid industrialization, fossil fuel combustion, and agricultural expansion have substantially increased emissions of O_3 precursors, leading to elevated O_3 concentrations, in association with densely populated and rapidly developing regions. The first quantitative measurements of O_3 (Paris Municipal Observatory in Parc Montsouris, France, 1876–1910; Pic du Midi, France, 1874–1909) reported annual O_3 concentrations of about 10–14 ppbv. From these 19th-century measurements, reasonably representative of preindustrial conditions, a collection of measurements in high-elevation European O_3 monitoring sites allowed to estimate that tropospheric O_3 increased by a factor of 5 between the late 19th century and the 1990s, and by about a factor of two between the 1950s and 1990s (Marenco et al., 1994; Staehelin et al., 1994). From the 1970s, quantitative O_3 measurements became widespread, first in Europe and then in other parts of the globe. These measurements revealed a consistent global increase in O_3 concentrations up to around year 2000, with locally varying increases between 1 and 5 ppbv $decade^{-1}$ (Cooper et al., 2014;

Gaudel et al., 2018). While Europe and North America experienced conspicuous O_3 increases during the late 20th century, concentrations began to stabilize or even decline after 2000, largely due to stringent air quality regulations such as the U.S. Clean Air Act Amendments and the EU Air Quality Directive (Parrish et al., 2012). In contrast, the most substantial increases in O_3 levels in recent decades have occurred in rapidly industrializing regions. In China, surface O_3 increased markedly during the 2000s and into the 2010s; studies of the 2013–2017 period show worsening urban O_3 in many cities and highlight complex, regionally varying roles of meteorology and emission changes following the 2013 "Action Plan for Air Pollution Prevention and Control" (Liu and Wang, 2020; Li et al., 2025a). For South and Southeast Asia, surface O_3 observations remain limited in spatial and temporal coverage, leading to considerable uncertainty in regional trend assessments. Nonetheless, recent analyses indicate that most monitored sites exhibit positive O_3 trends and high concentrations (Lu et al., 2018; Kunchala et al., 2022; Li et al., 2025a). Historically, O_3 pollution has been mostly a Northern Hemisphere concern, with annual concentrations higher by 10–15 ppbv compared to the Southern Hemisphere (Cooper et al., 2014). However, recent studies observed rising O_3 levels in parts of South America (Seguel et al., 2024) and Southern Africa (Laban et al., 2018; Donnou et al., 2024). In any case, large uncertainties remain for these regions due to the scarcity of long-term surface observations alongside the strong influence of interannual meteorological variability (Gaudel et al., 2018).

Future O_3 concentrations will depend on the interplay between climate change and air quality policy interventions. Model projections indicate that it is unlikely that Europe and North America will experience further increases in O_3 concentrations. In contrast, Asia and sub-Saharan Africa are projected to experience the largest future O_3 increases, with annual mean concentrations rising by approximately 5–10 ppbv by mid-century, particularly under scenarios with weak control of O_3 precursors or

GHG emissions (Turnock et al., 2020).

1.2 O_3 effects on vegetation

By entering the leaves through the stomata, O_3 can cause negative effects on both natural and cultivated vegetation. Once inside the leaf, O_3 causes oxidative stress and disrupts key biological processes at the cellular level, leading to damage to cellular membranes, inhibition of photosynthetic enzymes, and degradation of chlorophyll (Fiscus et al., 2005; Ainsworth et al., 2012; Jolivet et al., 2016). At the individual plant scale, the net effect is a reduced carbon sequestration in forest trees and semi-natural vegetation, and declined yield and protein content in major staple and horticultural crops (Emberson et al., 2018; Grulke and Heath, 2019). Consequently, O_3-induced vegetation damage reduces the capacity of natural ecosystems to mitigate climate change and poses a threat to global food security (Fuhrer et al., 2016; Wright et al., 2018; Ramya et al., 2023; Emberson, 2020).

Over the last decades, numerous collaborative experiments have been conducted to quantify the biological impacts of O_3 by establishing empirical dose–response relationships (DRRs), which express the O_3 effects in terms of growth reductions and yield losses. The most prominent research efforts include the National Crop Loss Assessment Network (NCLAN) in North America (Heck et al., 1982), which provided cornerstone data on O_3-crop interactions, and the ICP-Vegetation Programme under the UNECE Long-Range Transboundary Air Pollution Convention (LRTAP Convention, 2017), which coordinated European monitoring and experimentation on O_3 impacts across vegetation types, and defined common framework for O_3 risk assessments.

As O_3 enters plants primarily through the stomata, its phytotoxic effect depends on the rate of stomatal uptake rather than only on the atmospheric concentration. Therefore, the magnitude of O_3 damage depends strongly on stomatal conductance

(g_s; [m s^{-1}]), which varies among species and is regulated by environmental factors such as humidity, light, soil moisture, temperature, plant's phenological stage, and CO_2 concentration (Emberson et al., 2000a; Mills et al., 2011a). Beyond these environmental and species-specific controls, other stressors can interact with O_3 in complex and often non-linear ways. For instance, drought and heat stress may amplify O_3 injury by increasing oxidative load and impairing antioxidant defenses, but under water limitation stomatal closure can also reduce O_3 uptake and partially mitigate damage (Wilkinson et al., 2012). Particulate matter (PM) can also influence O_3 photochemical production and uptake, by affecting radiation and atmospheric chemistry (Liu et al., 2024). In the context of climate change, elevated CO_2 can partially offset O_3 injury by reducing g_s and enhancing antioxidant capacity (Klingberg et al., 2011). Unlike episodic stresses such as drought or heatwaves, O_3 imposes a chronic oxidative burden on vegetation, progressively reducing photosynthetic capacity and accelerating senescence even at sub-critical concentrations. Because of its distinct physiological mechanism and the complex interactions with other environmental stressors, a direct comparison between O_3 and other factors impacts is challenging.

1.2.1 Assessment of O_3 risk to vegetation: exposure- and flux-based metrics

The experimental frameworks that quantify the O_3 damage to vegetation typically relate the biological responses to metrics based either on O_3 exposure or plant O_3 uptake (i.e. stomatal O_3 flux), which are used as predictors of the biological response of interest (e.g. yield, growth loss, protein content reduction) in the empirical DRRs. Multiple exposure- and flux- based metrics were defined over the years, differing in their correlation with the observed effects (Pleijel et al., 2007). However, they all share some common underlying principles, such as that these metrics consider a detoxification threshold beyond which plants can no longer fully prevent oxidative

damage, or that they are focused on specific stages of the plant growth (Fuhrer et al., 1997; Karlsson et al., 2007).

Exposure-based metrics are derived from atmospheric O_3 concentrations, and they assume that plant injury is proportional to average or cumulative exposure above a threshold concentration, without accounting for any plant physiological process (Fuhrer et al., 1997). These metrics are very simple to compute, as they require knowledge only of O_3 concentrations, and for this reason they are used in policy-oriented frameworks to define air quality standards (e.g., the U.S. NAAQS and the EU Air Quality Directive; U.S. Environmental Protection Agency, 2020; European Parliament and Council of the European Union, 2008). However, it should be noted that DRRs based on such metrics are calibrated using O_3 concentrations at or near canopy height. As a consequence, if O_3 concentrations are provided at a different height, some vertical scaling method should be employed. A commonly used index is the AOT40 (Accumulated exposure Over a Threshold of 40 ppbv, [ppbv h]):

$$\mathrm{AOT40} = \sum_{i=1}^{N} \max\left([\mathrm{O_3}]_i - 40,\, 0\right)\, \Delta t \tag{1.1}$$

where $[O_3]$ is the daylight hourly mean ozone concentration ([ppbv]), and Δt is the time step duration ([h]; typically 1 h). The AOT40 quantifies cumulative exposure above 40 ppbv during $i = 1, \ldots, N$ daylight hours of a defined period of the growing season (usually a fixed 3-month period).

As opposed to exposure-based metrics, flux-based metrics quantify the actual O_3 flux entering the leaf through the stomata, which better represents the physiological dose leading to damage (Emberson et al., 2000a; Mills et al., 2011a). They are based on the g_s to O_3 (g_{s,O_3}, [m s^{-1}]) and the atmospheric O_3 concentrations. The instantaneous stomatal O_3 flux (F_{s,O_3}; [ppbv m s^{-1}], or [nmol m^{-2} s^{-1}]) is generally expressed as:

$$F_{\mathrm{s,O_3}} = g_{\mathrm{s}} \cdot [\mathrm{O_3}] \tag{1.2}$$

where $[\mathrm{O_3}]$ typically refers to the canopy height concentrations.

A widely used flux-based metric is the cumulative phytotoxic $\mathrm{O_3}$ dose above a threshold Y ($\mathrm{POD_Y}$, [mmol $\mathrm{m^{-2}}$ $\mathrm{s^{-1}}$]), given by:

$$\mathrm{POD}_Y = \sum_{t=A_{start}}^{A_{end}} \max(F_{\mathrm{s,O_3}}(t) - Y,\, 0) \cdot \Delta t \cdot 10^{-6} \tag{1.3}$$

Here, $F_{\mathrm{s,O_3}}$ is the instantaneous $\mathrm{O_3}$ stomatal flux averaged over a selected time step (usually one hour), Δt is the time step duration ([s]), Y is the detoxification capacity (often 6 nmol $\mathrm{m^{-2}}$ $\mathrm{s^{-1}}$ for crops and 1 for forests), and the summation covers the experimental accumulation period ($t = A_{start}, \ldots, A_{end}$).

Although exposure metrics are simple to compute and widely adopted, they do not account for species-specific stomatal controls on $\mathrm{O_3}$ uptake. As such, these metrics may not accurately represent the actual $\mathrm{O_3}$ dose received by vegetation and the corresponding biological impacts. On the other hand, flux-based metrics explicitly consider the physiological and environmental controls on g_{s} (e.g., humidity, soil moisture, temperature, light, and $\mathrm{CO_2}$) and allow a more process-oriented assessment of plant $\mathrm{O_3}$ dose (Pleijel et al., 2007). Their improved suitability to predict $\mathrm{O_3}$ effects is also supported by the generally higher correlation that flux-based metrics show with biological responses, comparatively to exposure-metrics (Mills et al., 2011a).

1.2.2 Modeling $\mathrm{O_3}$ risk for vegetation

In the atmospheric surface layer, $\mathrm{O_3}$ concentration vertical profile is influenced by turbulent mixing, surface deposition, and chemical reactions, usually displaying lower concentrations the closer to the ground. Clearly, vegetation interacts the most with $\mathrm{O_3}$ at the canopy height and, as such, experimental studies that aim to estab-

lish DRRs for vegetation (exposure- or flux-based) need to measure and control O_3 concentrations at that level.

Two main experimental frameworks have been developed for this purpose. The first uses Open-Top Chambers (OTC), which consist in semi-enclosed cylindrical or hexagonal enclosures open at the top to allow natural light, rainfall, and some air exchange. Air containing controlled concentrations of O_3 is introduced at the chamber base and vented through the open top, maintaining relatively stable concentrations around the vegetation canopy. The second framework involves Free-Air Concentration Enrichment (FACE) systems. FACE experiments release O_3 from vertical pipes arranged in a circular or polygonal ring around a plot, using continuous feedback control to maintain target concentrations in the air passing through the vegetation canopy, following the varying wind directions. Because FACE systems do not confine the plants, they allow a more realistic assessment of O_3 impacts on mature crops, trees, or grasslands. For both experimental frameworks, the ability to compare treatment and control plots enables the estimation of exposure-based DRRs, relating exposure to growth or yield reduction, and forming the empirical foundation for risk assessment methodology.

For flux-based DRRs, O_3 uptake by vegetation cannot be directly measured at the canopy scale, but it should be estimated from modeled g_s and local O_3 concentration. From a purely experimental standpoint, g_s can be directly measured only at leaf level by using porometers (e.g., AP4 diffusion porometer, LICOR-1600), or portable leaf gas-exchange systems (e.g., PP Systems CIRAS, LICOR-6400). g_s varies in response to environmental drivers (solar radiation, air temperature, vapor pressure deficit, soil water availability, and atmospheric CO_2 concentration), following distinct species-specific functional features. These g_s environmental relationships are commonly described by g_s models (e.g., Jarvis, Ball-Berry-Farquhar), parameterized from experimental data at the leaf scale. Once established, these responses are em-

bedded in flux models to calculate stomatal O_3 fluxes and then flux-based metrics. The experiments that allow to parameterize the g_s-environment relationships are often conducted within OTC and FACE campaigns, thus allowing joint derivation of plant biological features and flux-based DRRs.

To apply these DRRs in large-scale O_3 risk assessments, the relevant meteorological and chemical variables - temperature, humidity, radiation, and O_3 concentration - must be available at or near canopy height. In practice, whether they are provided by weather stations, reanalysis products or earth system models (ESMs) simulations, it is likely that they refer to standard heights (or model level heights), which differ from canopy height. Therefore, a vertical scaling is needed to estimate the mentioned quantities at the canopy. A common approach consists in deploying resistive schemes to describe the transfer of momentum, heat, and trace gases between the atmosphere and the surface. These schemes typically rely on flux–gradient relationships derived from Monin–Obukhov Similarity Theory (MOST). The resulting O_3 concentration at canopy height is then combined with the leaf-level modeled g_s to compute leaf-level O_3 fluxes for leaves located at the top of the canopy. The obtained O_3 dose is then used in the experimental DRRs to estimate the expected biological responses. Within this framework, g_s serves both to vertically scale O_3 concentrations and to compute the stomatal O_3 flux at the leaf level. Throughout the years, several g_s models were developed and employed not only in the field of O_3 deposition to vegetation, but also to estimate carbon and water fluxes. These models vary in complexity, ranging from a simple function of temperature and solar radiation (Wesely, 1989), to a single leaf multiplicative model (Baldocchi et al., 1987; Jarvis, 1976), a sunlit/shade (two-big-leaf) scheme (Emberson et al., 2000b; Zhang et al., 2003a), and a photosynthesis approach (Ball et al., 1987; Charusombat et al., 2010).

At its core, the modeling framework mirrors the experimental design: it seeks to reproduce, through simulation, the canopy-level O_3 concentrations under which

the DRRs were established. Thus, experimental data are prescriptive to model development, providing the physiological and environmental constraints that ensure model realism. However, modeling tends to extend its applicability beyond the prescribed experimental scale, i.e. to plant communities with multiple species, and spatial scales that are well beyond individual plants and field scales. For crops, this scaling is relatively straightforward: agricultural systems are typically monocultures with homogeneous canopy structure, and thus it is possible to directly upscale the leaf-level findings and apply species-specific DRRs. For forests and mixed ecosystems, the coexistence of multiple species forming heterogeneous canopies complicates both the scaling of O_3 concentrations to canopy height and the representation of physiological responses to O_3 uptake. Consequently, when the modeling framework is applied by the book, it implicitly assumes a homogeneous single-species canopy, an assumption that clearly departs from the structural and functional complexity of real-world vegetation. To address this limitation, some approaches have been developed, especially in the attempt to integrate the estimation of O_3 effects into land surface models and ESMs, thereby enabling assessment of O_3-vegetation interactions at regional and global scales. For instance, (Sitch et al., 2007) considered different representative species and DRRs, and Lombardozzi (Lombardozzi et al., 2015) used plant functional types, aggregating physiological responses from different species in the same parameterization. However, it should be noted that, to the author's knowledge, none of the major ESMs currently include O_3 effects on vegetation as a routine component of their coupled simulations.

Until now, only experimental DRRs based solutions were mentioned: all modeling frameworks in this context inevitably include some degree of process-based representation. Since these models must simulate both the O_3 vertical profile and the vegetation's physiological response to environmental drivers and O_3 uptake, there is a varying degree of modeling effort and computational burden, especially when scaling

to regional or global applications. Recently, efforts have emerged to move beyond this "experimental-compliance impasse" by integrating statistical and data-driven approaches with remote-sensing observations. For example, Liu et al. (2024) developed a multi-stage statistical framework linking remote-sensed solar-induced chlorophyll fluorescence, O_3 exposure metrics, and crop yield. This approach offers a data-driven means to infer O_3 impacts without explicitly modeling physiological processes. However, such methods are limited by potential confounding with other stressors, and the lack of explicit O_3–vegetation interaction mechanisms.

1.3 Ozone risk under future climate change scenarios

Future O_3 risk to vegetation under future climate change scenarios is a major concern at the interface of air quality, ecosystem functioning, and climate science. Elevated O_3 concentrations may constitute a threat to food security, while in forest ecosystems O_3 damage not only impairs tree growth and biological functions, but also reduces carbon uptake and storage, potentially weakening the capacity of natural terrestrial ecosystems to mitigate rising atmospheric CO_2 (Ainsworth et al., 2012; Fuhrer et al., 2016; Emberson, 2020). Assessing future O_3 risk for future times has been associated with diverse assumptions and varying degrees of complexity and spatiotemporal extents.

One critical aspect in future O_3-risk assessments is the O_3-climate interaction. Temperature, radiation, water vapour, and large-scale circulation directly affect photochemistry and precursor lifetimes, while O_3 in turn acts as a short-lived climate forcer, influencing radiative forcing and surface climate (Stevenson et al., 2013). Early studies on future O_3 risk to vegetation were mostly based on concentration-based metrics (e.g., Felzer et al., 2004; Van Dingenen et al., 2009; Avnery et al., 2011), largely because of their computational simplicity and modest data requirements. Even in those cases that employed flux-based metrics, some simplifying assumptions were of-

ten made, such as ignoring the effects of O_3 on climate, or using present-day climate variables associated with future emission pathways in chemical transport models (e.g., Klingberg et al., 2014; Simpson et al., 2007; Tang et al., 2014). For the most part, these simplifying assumptions did not originate from a lack of understanding of the underlying processes, but rather from computational resource constraints and limited data availability. Only in recent years novel studies have begun to fill this research gap by employing coupled-chemistry modules, although typically over restricted domains, at coarse spatiotemporal resolutions, or for only a few selected time windows and climate change and emission scenarios (e.g., Zhou et al., 2024; Li et al., 2025b). In this regard, a major step forward is provided by the AerChemMIP (Aerosols and Chemistry Model Intercomparison Project), a coordinated CMIP6 activity specifically designed to investigate interactions between atmospheric composition, climate, and Earth system processes (Collins et al., 2017; Griffiths et al., 2020). AerChemMIP ESMs simulate O_3 using fully coupled chemistry schemes and provide surface O_3 concentrations and meteorological variables at sub-daily temporal resolution across multiple future scenarios. These datasets offer, for the first time, the opportunity to assess future O_3 risk to vegetation in a physically consistent way and under multiple scenarios, by combining ESM outputs with O_3 deposition and stomatal flux models.

Further complexity in estimating future O_3 risk to vegetation is the role of plant physiological responses to rising atmospheric CO_2. Elevated CO_2 generally reduces stomatal conductance, which can lower stomatal O_3 uptake and partially mitigate O_3 damage. In this regard, a substantial body of experimental and observational evidence has accumulated over the past decades. Leaf- and canopy-scale studies consistently show that elevated CO_2 reduces stomatal conductance across a wide range of plant functional types, thereby decreasing transpiration and altering plant–atmosphere gas exchange (Medlyn et al., 2001; Ainsworth and Rogers, 2007). However, the magnitude of this protective effect is uncertain and varies according to species, nutrient

status, and environmental conditions. This response has been incorporated into many land-surface and vegetation models to represent CO_2 fertilization effects on water use efficiency and carbon uptake, but despite its relevance for O_3 uptake, this physiological response has not been applied consistently in assessments of O_3 impacts on vegetation. Past O_3 risk studies often assumed fixed stomatal behavior or present-day conductance when estimating future O_3 dose, thereby neglecting the potential mitigation of O_3 injury under elevated CO_2, and only a limited number of studies explicitly combined elevated CO_2 effects on stomatal conductance with O_3 flux calculations (Klingberg et al., 2011; Zhou et al., 2024).

Finally, a last challenge remains mostly unresolved. Vegetation represents a major sink for tropospheric O_3, and changes in O_3 uptake as a consequence of O_3 damage can alter surface O_3 levels exposure (Ainsworth et al., 2012). Fully resolving this interaction would require the dynamic coupling of O_3 deposition and plant physiological responses within ESMs, allowing vegetation to both respond to and influence atmospheric O_3. To the author's knowledge, such an integrated representation has not yet been systematically implemented in long-term future O_3 risk assessments for vegetation, and thus remains an open research frontier.

1.4 Dissertation Goals and overview

The main objective of this dissertation is to quantify O_3 risk to vegetation during the 21^{st} century, considering both past and future periods and encompassing crop and forest ecosystems, while implementing modeling solutions and simulation frameworks that allow to further the understanding of O_3 risk dynamics in association with climate change and air quality control policies on O_3 precursors.

Four main studies are presented from Chapter 2 to 5. Chapter 2 introduces the O_3 deposition model and applies it to a case-study over Northern Italy for bread wheat, one of the most O_3-sensitive crops, while investigating model sensitivity to different

spatiotemporal scales in the input data. This chapter is accompanied by an appendix which details all equations employed in the model. In Chapter 3, the application of the model is extended to the whole globe, estimating O_3 impacts on wheat across the entire 21st century under multiple climate change scenarios, using state-of-the-art climate simulations from the Climate Model Intercomparison Project 6 (CMIP6; Eyring et al., 2016). This chapter quantifies the resulting global production yield losses and analyzes how O_3 risk mechanisms vary with model assumptions, regions, and climate scenarios, identifying which air quality and emission control strategies may prove most effective in protecting food security. An accompanying appendix covers additional methodology, model evaluation and assessment of the uncertainty associated with input data.

Regarding forests, information on the dates marking the start and end of the growing season (leaf-out and senescence) is required for effective O_3 risk assessment under global warming. Chapter 4 presents a machine learning-based classification algorithm used to estimate these phenological stages from 1850 to 2100 by integrating remote-sensing observations, thereby providing phenological information under a range of climate conditions. Finally, Chapter 5 applies the methodology developed for wheat to forest ecosystems, with minor modifications, to assess O_3 risk across multiple forest species throughout the 21st century under various climate change scenarios.

Chapters 2 to 5 each correspond to individual manuscripts and are followed by a concluding chapter. Chapters 2 and 3 are based on already published papers, with bibliographical references provided within each section. Chapter 4 and 5 correspond to studies currently in preparation. The original studies have been slightly modified to fit the dissertation format, while the main content remains largely unchanged.

CHAPTER 2

A REGIONAL SCALE FLUX-BASED O_3 RISK ASSESSMENT FOR WINTER WHEAT IN NORTHERN ITALY, AND EFFECTS OF DIFFERENT SPATIO-TEMPORAL RESOLUTIONS.

This chapter is a reproduction, with slight modifications, of the journal article *A regional scale flux-based O_3 risk assessment for winter wheat in northern Italy, and effects of different spatio-temporal resolutions* by Pierluigi R. Guaita, Riccardo Marzuoli and Giacomo A. Gerosa, published in Environmental Pollution, 2023, Volume 333, page 121860, DOI: 10.1016/j.envpol.2023.121860. The supplementary material referenced in the text can be found at Guaita et al. (2023).

2.1 Introduction

Tropospheric ozone (O_3) is a harmful atmospheric pollutant that can cause negative effects on vegetation, ranging from oxidative stress at cellular level (Fiscus et al., 2005; Ainsworth et al., 2012; Jolivet et al., 2016) to reduced growth rate and gross primary production of forests and seminatural vegetation (Grulke and Heath, 2019; Proietti et al., 2016) and yield losses on crops and horticultural species (Emberson et al., 2018). Northern Italy and the Lombardy region are strongly subject to high levels of air pollution, and air quality monitoring networks gave evidence that summer O_3 levels in this region often exceeds the critical exposure for vegetation protection (European Environment Agency., 2020; European Parliament and Council of the European Union, 2008). This condition could be a serious threat to crops productivity in this region, which ranks first in Italy for agricultural value output (ISTAT, 2023).

In the last decades many experiments have been carried out to define empirical relationships between O_3 levels and the biological damage to plants (Emberson, 2020). In this context, research activities performed by the scientific communities in North America (under the NCLAN project – National Crop Loss Assessment Network, Heck et al., 1982) and Europe (under the ICP-Vegetation program – Long-Range Transboundary Air Pollution Convention LRTAP Convention, 2017) have been particularly relevant. Their early experiments defined O_3 dose–response relationships using exposure indexes, such as M7 (mean 7-hour daytime) or AOT40 (Accumulated Ozone over a Threshold of 40 ppb), e.g., the AOT40 relationships for spring wheat and beech found by Fuhrer et al. (1997). However, later experiments highlighted that the biological effects of O_3 are more related to the O_3 dose absorbed by plants through stomata (i.e., the cumulated O_3 flux absorbed at leaf level) rather than the simple cumulated O_3 exposure, such as the AOT40 metric (Emberson et al., 2000a; Pleijel et al., 2002; Mills et al., 2011a).

Ozone concentration-based indexes and exposure–response relationships are still in use nowadays, since they allow assessing yield losses and growth reductions for a variety of species in a simple way, as they only require O_3 concentrations, which are available from multiple sources, e.g. monitoring networks, chemical transport models, satellites, etc. (Hůnová et al., 2019; Hu et al., 2020). On the contrary, O_3 flux-based metrics are more challenging to compute compared to exposure-based ones, as they require physiology and air turbulence data (e.g., stomatal conductance and deposition velocity). Examples of O_3 flux-based metrics are CUO_3 (Cumulative Uptake of Ozone per unit projected leaf area from emergence until harvest, Pleijel et al., 2002) and POD_Y (Phytotoxic Ozone Dose above a Y threshold Mills et al., 2011a), being Y the detoxifying threshold for the instantaneous O_3 stomatal flux, with $Y = 1$ nmol, m^{-2}, s^{-1} assumed for forest trees and $Y = 6$ nmol, m^{-2}, s^{-1} for winter wheat (LRTAP Convention, 2017).

Calculating O_3 deposition fluxes on vegetation requires a resistance analogy to describe the deposition pathways, and models for calculating O_3 fluxes often incorporate dry deposition models. The first dry deposition models were developed in the 80s with the aim of estimating the deposition velocities of different chemical compounds, given the major focus on acid rain issues (e.g., Wesely, 1989; Venkatram et al., 1988). These models used the results of prognostic meteorological models as input (Walcek et al., 1986), with coarse spatial resolutions (Sheih et al., 1986; Wesely and Lesht, 1989) from 20 km × 20 km to 120 km × 120 km and temporal resolutions ranging from 1 to 6 hours. Baldocchi et al. (1987) proposed a big-leaf model to assess the dry deposition on vegetation, which has been also used by (Hicks et al., 1987) to estimate the deposition of different compounds on the vegetation of a small network of sites.

Emberson et al. (2000a) set a milestone by producing the first continental map of stomatal O_3 fluxes for wheat and beech O_3 risk assessment in Europe, using a single big-leaf dry deposition scheme. The European Monitoring and Evaluation Program (EMEP) model data was used as input, with a 6-hour temporal resolution and a 150 km × 150 km spatial resolution. Similar models were used by Simpson et al. (2007); Mills et al. (2011a); Tang et al. (2014) to produce maps at higher spatial resolutions (50 km × 50 km and 40 km × 40 km). The increased availability of computational power and meteorological maps at finer resolution for Chemical Transport Models opened up to the possibility of defining regional POD_Y maps at a higher resolution, e.g., 6 km × 6 km (De Marco et al., 2016), 5 km × 5 km (Watanabe et al., 2016; Wang et al., 2022). Other examples of continental POD_Y maps for forests obtained through a similar approach are Anav et al. (2016) at a resolution of 12 km × 12 km and De Marco et al. (2020) at a resolution of 8 km × 8 km, for Europe and Asia respectively. Nussbaum et al. (2003) used ground-measured meteorological and O_3 data to calculate the O_3 stomatal flux for arable crops and pastures, with a 1 km × 1 km spatial resolution and a 3-hour time resolution. The literature on

the use of monitoring networks data to calculate O_3 flux-based maps is very limited and ground-measured O_3 concentrations have been mostly used to produce AOT40 maps, even though at fine resolution, e.g., 0.5 km × 0.5 km (Shimizu et al., 2019) and 0.25 km × 0.25 km (Sicard et al., 2016) and no systematic investigation has been found on the sensitivity of O_3 flux-based maps to different combinations of spatial and temporal resolutions.

Furthermore, ground-measured O_3 concentrations and meteorological variables require spatialization techniques (e.g., Kriging) in order to produce maps at a regional scale, and their relationship with spatial coordinates, especially elevation, should be considered in areas with complex orography where coarse resolutions and/or unidentified altitude trends may produce misleading results. This issue was for example highlighted by the work of (Loibl et al., 1994), who proposed an empirical relationship between O_3 concentration and elevation to predict the hourly O_3 concentration for each 1 km × 1 km grid node over the Austria territorial domain. Coyle et al. (2002) observed that the AOT40 during the central hours of the day is very similar even at different elevations, as the atmosphere during the midday hours is vertically well mixed, and this information was leveraged to map the O_3 exposure in rural areas of UK.

The objectives of this work are: (i) to estimate the O_3 yield loss risk for a reference crop (winter wheat, *Triticum aestivum* L.) in the Lombardy region (Italy) during the 2017 growing season, by spatializing meteorological and O_3 concentration data obtained from regional networks and calculating the POD_6 metrics with a dual-sink big-leaf model; (ii) to evaluate the effect of different altitudinal trend methodologies in the Kriging spatialization to estimate POD_6; (iii) to evaluate how different spatio-temporal resolutions (from 1 km × 1 km to 50 km × 50 km, and 1-hour, 3-hour, 6-hour) affect O_3 risk estimates in a region with a complex orography, and determine the coarsest resolution that allows to identify hotspots for O_3 potential damage; (iv)

to identify the main limiting factors for winter wheat stomatal conductance, among air temperature, water vapour pressure deficit and soil water availability.

In the 2018–2022 period, on average, 16.5% of the Lombardy cropland dedicated to cereals was specifically cultivated with winter wheat, which represents the second most widespread cereal crop after maize (ISTAT, 2023). Nonetheless, this study is focused on the estimation of O_3 damage to this species, since it was selected as the model crop for the O_3 risk assessment at European level and a high number of experiments provided data for defining a specific O_3 dose–response function (Pleijel et al., 2022).

2.2 Materials and methods

2.2.1 Study domain

The chosen domain enclosed the Lombardy region in Italy (boundaries: 8.2°W, 11.55°E, 44.2°S, 47°N; Fig. 2.1a), a complex orography area, with an average elevation of 279 m asl and a maximum of 4020 m asl. Crop fields are mostly in the Po Valley at the center of the study domain and in the valley floors, while forests cover the highlands up to ∼1800 m asl. The main cultivated crops are cereals (maize and wheat) and vegetables. The climate is temperate ranging from continental subhumid to suboceanic axeric (Botti, 2018). The study was focused on the year 2017, which was a relatively dry year (García-Herrera et al., 2019; Baronetti et al., 2020). More specifically, in the cropland area (Fig. 2.1c), during the spring months which are the most representative for the crop growth (March–May), the cumulated rain was 194 mm, 26% less than the 30-year average for the period 1993–2022, 263 mm (i.e., the 17^{th} percentile).

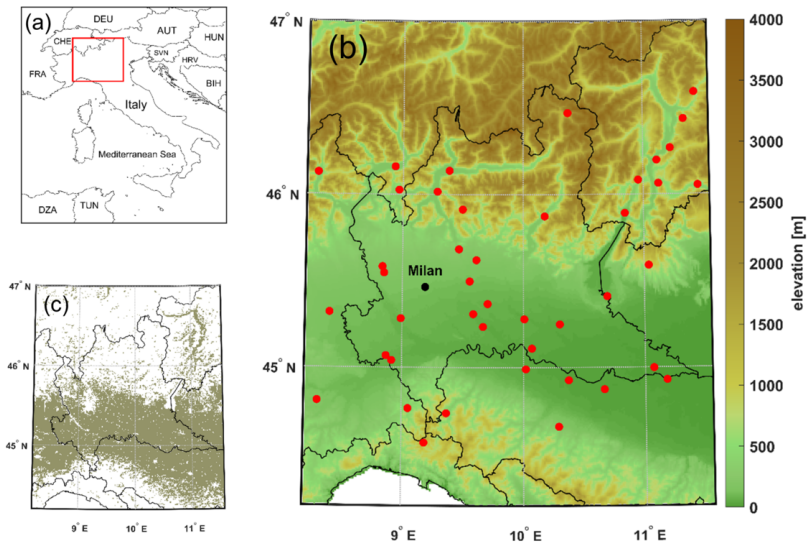

Figure 2.1. Domain: (a) the chosen domain in Italy, (b) digital terrain model and O_3 station positions (red dots) and (c) land use map indicating nodes with a non-zero fraction of cropland within the area

2.2.2 Data sources

Temperature, wind speed, relative humidity, short-wave incoming radiation, and rainfall data were retrieved from the regional meteorological network of Lombardy (meteorologica regionale, 2022). O_3 concentrations were collected from Airbase (EEA - European Environmental Agency), to which regional environmental agencies provide the data collected by their ground monitoring stations. O_3 concentrations and wind speed in these monitoring stations are measured at 3 m agl, while the other variables are measured at 2 m agl. O_3 measurements were collected from background rural stations, or background suburban stations in case rural stations were not available (Fig. 2.1b). For O_3 concentration, all the selected stations had at least 85% of validated data and on average the data capturing was 96.4%. Table 2.1 indicates the number of measuring stations used for each variable, the minimum, the average, and the maximum distance between two adjacent stations.

GTOPO30 by the Earth Resources Observation and Science (Earth Resources Observation and Science (EROS) Center) Center provided the Digital Elevation Model with a horizontal grid spacing of 30 arc-second, which approximately corresponds to 1 km at the latitude of the domain (Fig. 2.1b). Soil field capacity and wilting point data were obtained from EU-SoilHydroGrids ver. 1.0 (Tóth et al., 2017) at 1 km × 1 km resolution (Fig. S1).

Land use data was acquired from the land cover classification map issued by Copernicus (ICDR Copernicus Climate Change Service, 2019) at resolution of 0.3 km × 0.3 km. The data has been rescaled to a resolution of1 km × 1 km for consistency with the maps produced in the data spatialization phase (see section 2.2.3). Each grid node was set to a value between 0 and 1 according to the fraction of cropland within the area, where 1 is scored when all the area within the grid node is occupied by cropland. Fig. 2.1c represents non-zero cropland values within the study domain area.

2.2.3 Mapping variables with a Kriging with Trend Model

Meteorological variables and ozone concentrations have been mapped using a Kriging with Trend Model. Elevation was used as the predictor for the deterministic part (trend), and ordinary Kriging was applied to the residuals for interpolation (see Goovaerts, 1997, for details). Experimental semivariograms were calculated without anisotropy, and the semivariogram models were selected between spherical or exponential based on a best-fit procedure. Lags had multiple spacings, and the lag tolerance was determined so that each semivariogram value was calculated from at least 30 distinct pairs of points.

The algorithm workflow was as follows: (1) reception of input weather variables; (2) search for altitudinal trends; (3) extraction of the trends' residuals; (4) calculation of semivariograms; (5) application of ordinary Kriging on the residuals to obtain

TABLE 2.1

NUMBER OF MEASURING STATIONS USED FOR EACH PARAMETER, AND THE MINIMUM, AVERAGE, AND MAXIMUM DISTANCE BETWEEN ONE STATION AND THE CLOSEST ONE.

Variable	N° of stations*	Min (km)	Mean (km)	Max (km)
Temperature	153	0.9	7.2	37.7
Relative Humidity	113	2.3	8.7	26.0
Shortwave incoming radiation	64	2.4	10.9	33.5
Wind speed	67	1.5	11.2	48.3
Ozone	45	4.2	21.3	63.4
Precipitation	160	1.2	6.8	37.7

*Since data is not available at every hour for each station, the number of stations is the average number of stations available at each hour of the year 2017.
**Minimum distance between stations is important for the data spatialization performed with the Kriging technique.

detrended hourly maps for each variable; (6) reapplying the altitude trends. Elevation trends were identified using two methods: (1) linear regression and (2) empirical trends. Empirical trends were applied to maximize the spatial predictivity of the data, despite a lower interpretability of the equations, and to obtain better maps in terms of RMSE (Root Mean Square Error). Table 2.2 reports the functions used for the empirical trends (method 2). The model parameters were fitted using the least squares method. Two empirical trend examples for temperature and O_3 concentration are shown in Fig. S3.

Hourly maps for each variable were produced from 1st January 2017 to 31st December 2017. Temperature maps were also produced for the period 15th October 2016 – 31st December 2016 to calculate the thermal time (from sowing date; Baruth et al., 2016), which is required to model plant germination and development. Precipitation was spatialized using a simple Inverse Distance Weighting technique (Shepard, 1968), as rainfall spatial patterns are typically patchy, whereas the Kriging method generally reproduces gradual and smooth patterns.

2.2.4 Dry deposition model and calculation of the phytotoxic ozone dose

The hourly maps produced at the previous step – i.e., temperature (°C), water vapour pressure (kPa), incoming shortwave radiation ($W\,m^{-2}$), wind speed ($m\,s^{-1}$) and O_3 concentration (ppb) – were used as input for a dual-sink big leaf dry deposition model. The model calculates the POD_6 (Eq. 2.2), which is the metric used to estimate the O_3 risk for crops (LRTAP Convention, 2017).

The model is briefly outlined in this section and described in detail in the Appendix A. It consists of five modules: a *plant phenology module*, to simulate the crop growth and phenology, a *light module*, to calculate the sunlit and shaded fractions of the canopy, a *stomatal conductance module*, to calculate the stomatal conductance by using the Jarvis algorithm, a *atmosphere module*, to simulate the dry deposition

TABLE 2.2

EMPIRICAL TRENDS IDENTIFIED FOR METEOROLOGICAL VARIABLES AND O_3 CONCENTRATIONS USED IN KRIGING WITH TREND.

Variable	**Function**
T*	$f(x) = \begin{cases} m_1 x + q_1, & x < a \\ m_2 x + q_2, & a \leq x < b \\ m_3 x + q_3, & b \leq x \end{cases}$
VP*	$f(x) = a_{\log} \log(x - x_{0,\log}) + \begin{cases} m_1 x + q_1, & x < a \\ m_2 x + q_2, & a \leq x < b \end{cases}$
SW	$f(x) = \max\left(A_{\min}, \min(A_{\max},\, q + mx + a\log(x - x_{0,\log}) \quad + ax^b \sin(cx - x_{0,\sin}))\right)$
WS	$f(x) = q + mx + a\log(x - x_0)$
O_3*	$f(x) = \begin{cases} m_1 x + q_1, & x < a \\ m_2 x + q_2, & a \leq x < b \\ m_3 x + q_3, & b \leq x \end{cases}$

Notes:
x = elevation [m]; $a, b, m_1, m_2, m_3, q_1, q_2, q_3, a_{\log}, x_{0,\log}, x_{0,\sin}, c, q, m, x_0$ are fitting parameters.
T = Temperature; VP = Water vapour pressure; SW = Shortwave incoming radiation; WS = Wind Speed; O_3 = Ozone concentration.
$A_{\min}$ and $A_{\max}$ are respectively the 5^{th} and the 95^{th} percentiles of the data, respectively.
* Thresholds a and b determined via ordinary least squares.

resistive network used to compute the ozone and water fluxes, and a *soil module*, to dynamically simulate the water content of the soil through a bucket model.

Thermal time drives the *plant phenology module*, which in turn influences the *light module*. The *stomatal conductance*, *atmosphere* and *soil modules* dynamically interact with each other at each hourly timestep, by receiving as input respectively the output of the previous module. The process continues in each grid node of the domain until the reference crop has reached maturity.

The *plant phenology module* uses thermal time calculated from the sowing date (15^{th} Oct Baruth et al., 2016) to predict the daily leaf area index (LAI), the surface area index (SAI), the root depth (R_d), the canopy height (h_c), and the start and end dates of the ozone accumulation period. All these factors will be used to calculate the seasonal POD_6. The *light module* relies on the Weiss and Norman method (Weiss and Norman, 1985) to calculate the photosynthetic active radiation (PAR) reaching sunlit and shaded parts of the canopy (LAI_{sun}, LAI_{shad}), while distinguishing between direct and diffuse radiation. This information is used in the next module to calculate the stomatal conductance of the sunlit and shaded portions of the canopy.

The *stomatal conductance module* uses the Jarvis algorithm (Jarvis, 1976) to describe the stomatal conductance to water of a single leaf of the crop in the upper part of the canopy ($g_{s,w}$, Eq. 2.1) as reported in the Mapping Manual (LRTAP Convention, 2017). To do so, the module considers the maximum stomatal conductance for water ($g_{\text{max},w}$, $\text{nmol}\,\text{m}^{-2}\,\text{PLA}\,\text{s}^{-1}$) and the limiting functions f_{light}, f_{temp}, f_{VPD}, f_{PAW}, f_{O3}, f_{phen}, which describe respectively the dependence of the actual stomatal conductance on light, temperature, water vapour pressure deficit, plant available water, stomatal damage at increasing ozone dose, and natural decline of stomatal conductance during the growing season (phenology):

$$g_{s,w} = g_{\text{max},w} \cdot \min\{f_{\text{phen}}, f_{\text{O3}}\} \cdot f_{\text{light}} \cdot \max\{f_{\text{min}}, f_{\text{temp}} \cdot f_{\text{VPD}} \cdot f_{\text{PAW}}\} \tag{2.1}$$

By using $\mathrm{PAR_{sun}}$ and $\mathrm{PAR_{shad}}$ coming from the *light module* in the f_{light} function, stomatal conductance of sunlit and shaded portions of the canopy are calculated, contributing to the actual stomatal conductance to water $g_{\mathrm{act},w}$. The latter is converted into the actual stomatal conductance to ozone ($g_{\mathrm{act,O3}}$), which is used in the resistive network of the following *atmosphere module*.

The *atmosphere module* is used to scale ozone concentration from the measurement height to the top canopy height ($\mathrm{O_3}(h_c)$). The concentration at this level is then used to calculate the stomatal flux, as done for example by the $\mathrm{DO_3SE}$ model (Emberson et al., 2000a). $\mathrm{O_3}(h_c)$ depends on atmospheric stability, turbulence, and the magnitude of dry ozone deposition in the canopy itself.

The module estimates the friction velocity (u^*), the atmospheric stability with the Monin-Obukhov similarity theory (MOST), the atmospheric resistance for heat, water, and ozone (R_{aH}), the quasi-laminar resistance for heat, water, and ozone transfer (R_{bH}, R_{bW}, R_{bO3}), the in-canopy resistance (R_{inc}), and the water fluxes needed by the *soil module* by means of the Penman-Monteith equation (Monteith, 1965). The dual-sink resistive network that describes the $\mathrm{O_3}$ deposition within the canopy and the water losses through evapotranspiration is shown in Fig. 2.2.

The *soil module* implements a mass balance of water to estimate the soil water availability to the roots of the crop (Mintz and Walker, 1993). This is done by a bucket model that considers rain, intercepted precipitation by the canopy, transpiration of the crop, evaporation from the soil, and evaporation from wet plant surfaces. The maximum amount of extractable water that can be stored in the soil depends on soil field capacity and wilting point. The soil is assumed to be at field capacity on the 1^{st} of January. See Appendix A for details.

Finally, the stomatal flux for a leaf of unitary LAI positioned at top-canopy (F_{sO3}) is computed at each timestep by using $\mathrm{O_3}(h_c)$ obtained from the *atmosphere module*. The $\mathrm{POD_6}$ ($\mathrm{mmol\,m^{-2}\,PLA}$) is then calculated by summing up all the instantaneous

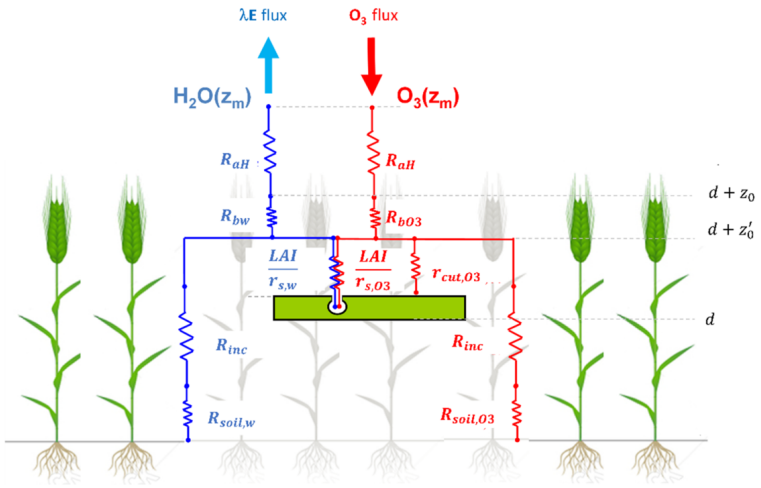

Figure 2.2. Resistive network employed to calculate the ozone concentration at the top of the canopy and to determine the water loss from the crop field

stomatal fluxes $F_{sO3,i}$ (of the i-th hour of the accumulation period, $i = 0, \ldots, t$), above the detoxification threshold of $6\,\mathrm{nmol\,m^{-2}\,s^{-1}}$ determined by the Mapping Manual UN/ECE for winter wheat (LRTAP Convention, 2017):

$$\mathrm{POD}_6 = \sum_{i=0}^{t} \max\left(0, \frac{(F_{sO3,i} - 6) \cdot 3600}{1000000}\right) \tag{2.2}$$

2.2.5 Assessment of the average yield losses

The LRTAP Convention (2017) selected for winter wheat a POD_6 critical level (CL) of $1.3\,\mathrm{mmol\,m^{-2}}$ PLA, which corresponds to a 5% loss in grain yield. A relationship between POD_6 and grain yield is also provided to estimate the relative yield loss (RY, %), expressed as a fraction of winter wheat yield not exposed to ozone:

$$\mathrm{RY} = 1 - 0.038 \cdot \mathrm{POD}_6 \tag{2.3}$$

The dry deposition model allowed the production of a POD_6 map for the generic cropland area represented in Fig. 2.1c. Since there was no information on the exact

wheat coverage within each grid node, the yield losses $(1 - \mathrm{RY}) \cdot 100$ were calculated under the assumption that winter wheat was uniformly distributed in the cropland area.

2.2.6 Assessment of the most limiting functions

To determine the influence of meteorological spatio-temporal features on the stomatal conductance (and hence on the final POD_6 map), we defined the most limiting function (MLF) for stomatal conductance as the function f of the Jarvis model (Eq. 2.1) which has the lowest average value during the daylight hours (radiation $> 50\,\mathrm{W\,m^{-2}}$) of the POD_6 accumulation period. The MLF was identified among temperature, soil water content, and vapour pressure deficit in each individual node of the horizontal grid.

2.2.7 Assessment of mapping performance

To investigate the influence of different spatio-temporal resolutions on $\mathrm{O_3}$ risk estimates, POD_6 maps were calculated for increasingly coarser spatial resolutions from $1\,\mathrm{km} \times 1\,\mathrm{km}$ to $50\,\mathrm{km} \times 50\,\mathrm{km}$ at a 1-hour time resolution, and for 3-hour and 6-hour time resolutions with a grid of $1\,\mathrm{km} \times 1\,\mathrm{km}$. These maps were produced using the variables spatialized with the empirical trends. The assessment metrics used to evaluate the Kriging performance and the POD_6 estimations at different resolutions are RMSE (root mean squared error, Eq. 2.4) and MB (mean bias, Eq. 2.5).

$$\mathrm{RMSE} = \sqrt{\frac{\sum_{i=1}^{n}(\hat{y}_i - y_i)^2}{n}} \tag{2.4}$$

$$\mathrm{MB} = \frac{\sum_{i=1}^{n}(\hat{y}_i - y_i)}{n} \tag{2.5}$$

The sensitivity analysis on different spatial and temporal resolutions was performed by comparing the POD_6 map at the finest resolution of $1\,\mathrm{km} \times 1\,\mathrm{km}$ and

1-hour to POD_6 maps with coarser resolutions (Table 2.3). In this case, $i = 1, \ldots, n$ is the number of grid nodes of the finest resolution, and y_i is the POD_6 value in each of these grid nodes. The maps with a coarser spatial resolution were downscaled for comparison to 1 km × 1 km by dividing each grid cell of the coarse map into 1 km × 1 km cells and assigning to each of them the corresponding POD_6 value of the original coarse cell. $\hat{y}_i$ is the POD_6 value of the map that was being compared. On the other hand, in the spatialization procedure (Table 2.5), $i = 1, \ldots, n$ is the number of stations, $\hat{y}_i$ is the Kriging estimation in the location of the i-th station using the jack-knife method, and y_i is the measured value.

2.3 Results

2.3.1 High resolution O_3 risk assessment

Mean April–June O_3 concentrations for the year 2017 are reported in Fig. 2.3a. While they gradually increase with elevation, particularly in the hilly and mountain areas, in the Po valley plain they could be considered almost uniform around an average of 38.9 ± 1.9 ppb.

The dry deposition model run for the year 2017 at the finest resolution (1 km × 1 km and 1-hour timestep) and with variables obtained using empirical trends in the Kriging model allowed the calculation of the POD_6 map reported in Fig. 2.3b. The map shows only the cropland grid nodes where wheat reached maturity, which were mostly located in the plain and the valley floors. Most of the plain exceeded from 1 to 2.5 times the UNECE CL of 1.3 mmol m^{-2} PLA (CL). Peaks of 4 times the CL were observed in the hills and submontane areas north and south of the Po valley. The only area with POD_6 values below the CL was in the south-eastern part of the domain. Average POD_6 over the whole domain was 2.03 ± 0.81 mmol m^{-2} PLA, corresponding to an average yield loss of $7.5 \pm 3.1\%$, according to Eq. 2.3.

The influence of the soil water availability on the O_3 uptake can be appreciated by simulating the soil water content at field capacity for the whole domain and calculating the POD_6 accordingly (Fig. 2.3c). To distinguish between the POD_6 obtained from this simulation and the one obtained from the water content calculated from the meteorological data, the notations $POD_{6,FC}$ and POD_6 were used, respectively. A higher water availability resulted in increased O_3 uptake by the crop, and $POD_{6,FC}$ was above the CL in the whole domain. However, it is interesting to notice that $POD_{6,FC}$ increased mostly in the plain nodes and less in the hills and piedmont areas. The average $POD_{6,FC}$ was $2.60 \pm 0.82\,\mathrm{mmol\,m^{-2}\,PLA}$, corresponding to an average yield loss of $9.7 \pm 3.1\%$. The higher O_3 uptake at soil field capacity was also evident from the different frequency distribution of the $POD_{6,FC}$ classes compared to POD_6 (Fig. 2.3c). All the $POD_{6,FC}$ values were above the CL, and the mode class shifted from the class $1.30\,\mathrm{mmol\,m^{-2}\,PLA}$ to $1.95\,\mathrm{mmol\,m^{-2}\,PLA}$ to the class $1.95\,\mathrm{mmol\,m^{-2}\,PLA}$ to $2.60\,\mathrm{mmol\,m^{-2}\,PLA}$.

2.3.2 Limiting factors for stomatal conductance

As described in Section 2.4 (Eq. 2.1), stomatal conductance depends on several environmental factors such as light, temperature, water vapour pressure deficit, and plant available water. Fig. 2.4a reports a comparative analysis of the most limiting functions (MLFs, defined in Section 2.6) in the domain, highlighting in different colors the MLF for each grid node. f_{temp} resulted as the MLF for the greater part of the domain (69.7%), while f_{PAW} was the MLF in the south-eastern part (Fig. 2.4a). On the contrary, f_{VPD} was the MLF in just a few areas scattered around the domain.

A subdomain (green borders; Fig. 2.4a) was determined based on similar starting and ending dates of the accumulation period. Within this area, the temporal evolution of f_{temp} and f_{VPD} (Fig. 2.4b and Fig. 2.4c) was similar both in the grid nodes of the plain where f_{temp} was the MLF (Fig. 2.4a, red area within the green border) and

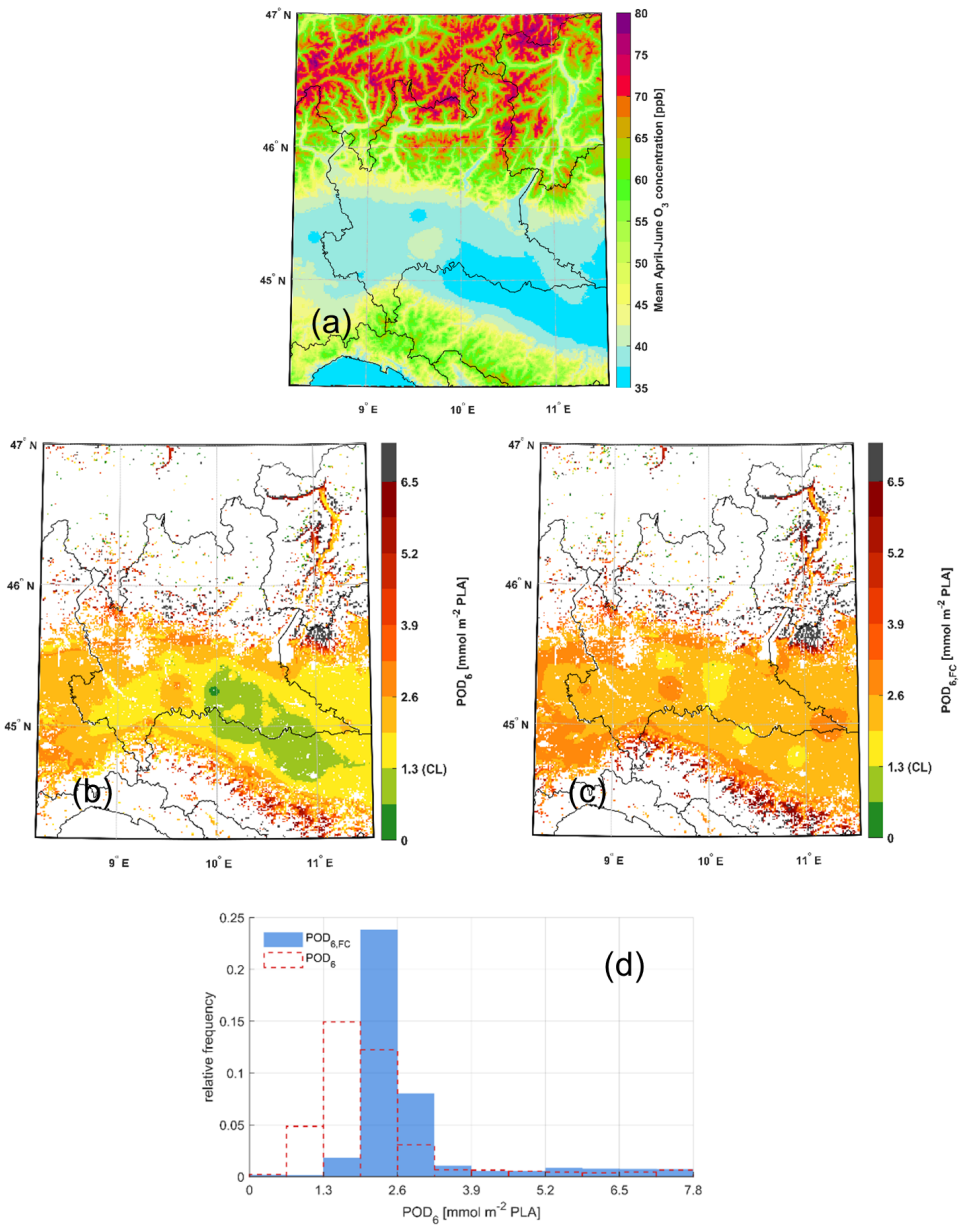

Figure 2.3. (a) Mean April–June O_3 concentrations. (b) POD_6 map for 1 km × 1 km, 1-hour resolution, with modeled soil water content. (c) $POD_{6,FC}$ map with soil water content always at field capacity. (d) Histograms for POD_6 with modeled water content calculated from meteorological data (dashed empty bars) and for $POD_{6,FC}$ obtained from simulating soil water content always at field capacity (blue full bars).

the grid nodes of the plain where f_{PAW} was the MLF (Fig. 2.4a, blue area within the green border).

Instead, f_{PAW} was the only function that was consistently different between the two areas: in the area where f_{temp} was the MLF, f_{PAW} started decreasing around day of year (doy) 140 (Fig. 2.4b), while in the area where f_{PAW} was the MLF, f_{PAW} started decreasing around doy = 130 (Fig. 2.4c). This difference is explained by the different amount of rainfall received by the two areas before the accumulation period. During March and April, a grid node with f_{PAW} as the MLF received 31 mm (-35%) less rainfall on average compared to a grid node with f_{temp} as the MLF.

As a result, f_{temp} limited the stomatal conductance up to about doy = 135 (15th of May), but after that, the stomatal conductance was limited either by PAW or VPD, depending on the area. Although f_{VPD} was just occasionally the MLF, it showed the lowest values between doy = 141 and doy = 153 (i.e., towards the end of the POD_6 accumulation period) in the area where f_{temp} was on average the MLF (Fig. 2.4b).

2.3.3 POD_6 sensitivity on different spatial and temporal resolutions

Each POD_6 map at different spatial and temporal resolutions was compared with the map of the finest resolution available—i.e., 1 km × 1 km with 1-hour time resolution, assumed as the reference map. The mean bias (MB) of the coarser spatial resolution maps versus the reference one (Table 2.3) was almost always negative, i.e., the resulting POD_6 of the coarser maps were lower on average, leading to a general underestimation of the O_3 risk. The lowest MB values were recorded for the maps with resolution 4 km × 4 km and 5 km × 5 km, corresponding to an average POD_6 10% lower than the reference one, and the RMSE rose steadily with increasingly coarser resolutions. At the coarsest resolution (50 km × 50 km), the RMSE reached 1.26 mmol m^{-2} PLA, and at 5 km × 5 km RMSE reached a value corresponding to around half the CL (0.70 mmol m^{-2} PLA).

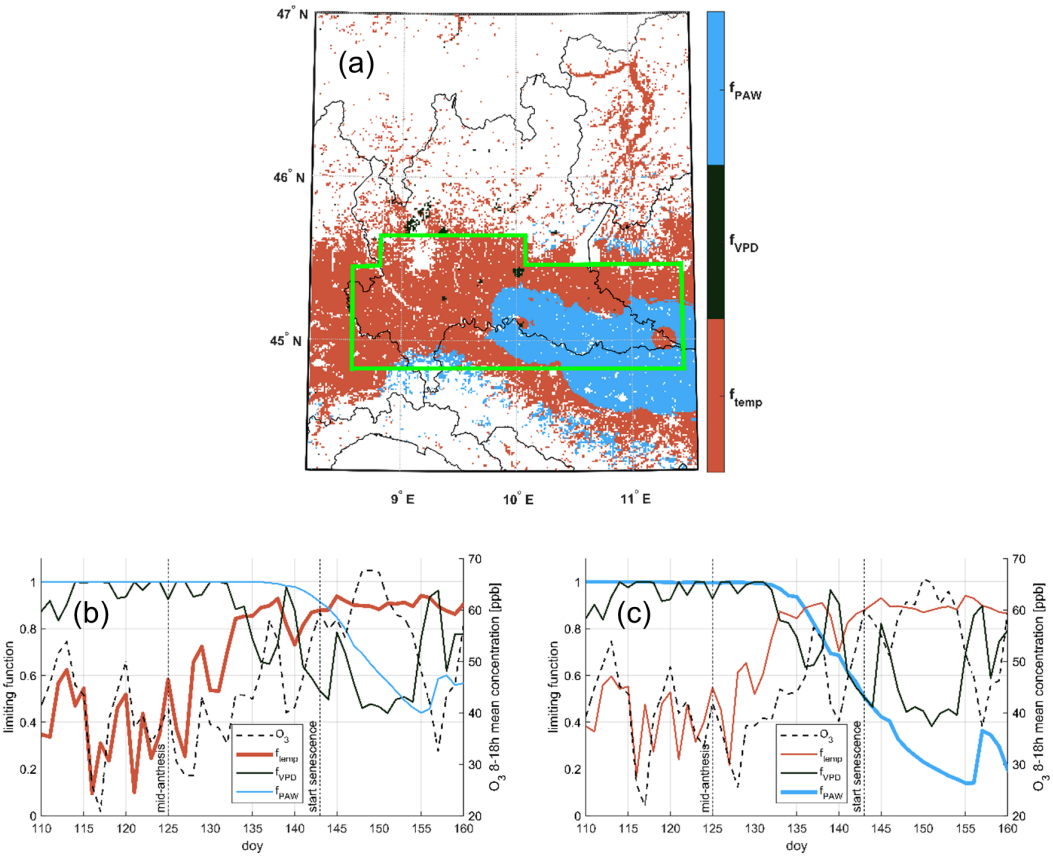

Figure 2.4. Most Limiting Functions (MLFs) for winter wheat stomatal conductance. (a) MLFs over the whole domain. (b) Evolution of f_{temp}, f_{VPD} and f_{PAW} during the accumulation period in the area delimited by green borders, where f_{temp} was the MLF. (c) Evolution of f_{temp}, f_{VPD} and f_{PAW} during the accumulation period in the area delimited by green borders, where f_{PAW} was the MLF.

Apart from a slight reduction of the predicted POD_6, the dose pattern remained essentially identical in the plain region of the domain, while a significant change could be observed in hilly or piedmont areas where the variation of elevation occurs on finer scales (Fig. 2.5a,b). The coarsest resolution runs (Fig. 2.5c–d) were unable to detect O_3 hotspots.

Most of the calculated POD_6 values were in the range $0.65\,\mathrm{mmol\,m^{-2}}$ PLA to $2.60\,\mathrm{mmol\,m^{-2}}$ PLA for each spatial resolution (Fig. 2.6a,d). The finest resolution (dashed red line) had a clear mode in the class $1.30\,\mathrm{mmol\,m^{-2}}$ PLA to $1.95\,\mathrm{mmol\,m^{-2}}$ PLA, followed by the second most frequent class $1.95\,\mathrm{mmol\,m^{-2}}$ PLA to $2.60\,\mathrm{mmol\,m^{-2}}$ PLA. Starting from $4\,\mathrm{km} \times 4\,\mathrm{km}$, the frequency of the three main classes ($0.65\,\mathrm{mmol\,m^{-2}}$ PLA to $2.60\,\mathrm{mmol\,m^{-2}}$ PLA) became more uniform, with the only exception of $50\,\mathrm{km} \times 50\,\mathrm{km}$. Simultaneously, the average POD_6 values (Table 2.4) decreased from $2.03 \pm 0.81\,\mathrm{mmol\,m^{-2}}$ PLA of the reference resolution to the minimum of $1.82 \pm 0.89\,\mathrm{mmol\,m^{-2}}$ PLA of the $4\,\mathrm{km} \times 4\,\mathrm{km}$ resolution and then grew again up to $2.12 \pm 1.03\,\mathrm{mmol\,m^{-2}}$ PLA of the $50\,\mathrm{km} \times 50\,\mathrm{km}$ resolution. The coarsest resolution was the only one that had a slightly higher average POD_6 than the reference resolution, although this is likely due to chance rather than modeling reasons.

Regarding the relaxation of the time resolutions, the spatial patterns of POD_6 maps did not change much from the reference 1-hour resolution. However, the ozone risk for vegetation is underestimated, because as the resolution becomes coarser, the POD_6 lowered up to 16% for the 6-hour resolution, as evident from Table 2.4. The value of MB for the 6-hour resolution ($-0.34\,\mathrm{mmol\,m^{-2}}$ PLA, Table 2.3) confirms this substantial underestimation, which is less evident for the 3-hour resolution ($-0.12\,\mathrm{mmol\,m^{-2}}$ PLA). Compared to the finest resolution, the 3-hour resolution retained a similar frequency distribution of POD_6 (Fig. 2.6e), while the 6-hour resolution was markedly different, with the mode shifted below the CL of $1.3\,\mathrm{mmol\,m^{-2}}$ PLA (Fig. 2.6f).

TABLE 2.3

MEAN BIAS (MB) AND ROOT MEAN SQUARED ERROR (RMSE) OF THE POD_6 ESTIMATION AT DIFFERENT SPATIAL AND TEMPORAL RESOLUTIONS, COMPARED WITH POD_6 OBTAINED AT 1 km × 1 km AND 1-HOUR TIMESTEP.

Map resolution	MB ($\mathrm{mmol\,m^{-2}\,PLA}$)	RMSE ($\mathrm{mmol\,m^{-2}\,PLA}$)
Spatial resolution* ($\mathrm{km^2}$)		
2×2	−0.17	0.38
3×3	−0.14	0.54
4×4	−0.20	0.65
5×5	−0.19	0.70
6×6	−0.18	0.73
7×7	−0.16	0.75
8×8	−0.18	0.79
9×9	−0.17	0.81
10×10	−0.17	0.85
15×15	−0.17	0.95
20×20	−0.15	0.99
25×25	−0.10	1.06
50×50	0.06	1.26
Temporal resolution**		
3-hour	−0.11	0.25
6-hour	−0.33	0.41

*Temporal resolution is always 1-hour. **Spatial resolution is always 1 km × 1 km.

TABLE 2.4

AVERAGE POD_6 AND RELATIVE YIELD LOSS FOR THE DIFFERENT SPATIAL AND TEMPORAL RESOLUTIONS.

Map resolution	Average $POD_6 \pm \sigma$ (mmol m^{-2} PLA)	Average relative yield loss $\pm\sigma$ (%)
Spatial resolution* (km^2)		
1×1	2.03 ± 0.81	7.53 ± 3.09
2×2	1.87 ± 0.82	6.91 ± 3.15
3×3	1.86 ± 0.84	6.87 ± 3.24
4×4	1.82 ± 0.89	6.73 ± 3.42
5×5	1.83 ± 0.90	6.76 ± 3.47
6×6	1.86 ± 0.90	6.85 ± 3.46
7×7	1.87 ± 0.92	6.91 ± 3.53
8×8	1.87 ± 0.92	6.89 ± 3.52
9×9	1.87 ± 0.92	6.91 ± 3.51
10×10	1.88 ± 0.90	6.93 ± 3.47
15×15	1.89 ± 0.92	6.97 ± 3.54
20×20	1.89 ± 0.96	6.97 ± 3.67
25×25	1.95 ± 0.95	7.23 ± 3.66
50×50	2.12 ± 1.03	7.87 ± 3.95
Temporal resolution**		
3-hour	1.93 ± 0.83	7.12 ± 3.18
6-hour	1.71 ± 0.81	6.27 ± 3.11

*Temporal resolution is always 1-hour. **Spatial resolution is always 1 km $\times$ 1 km.

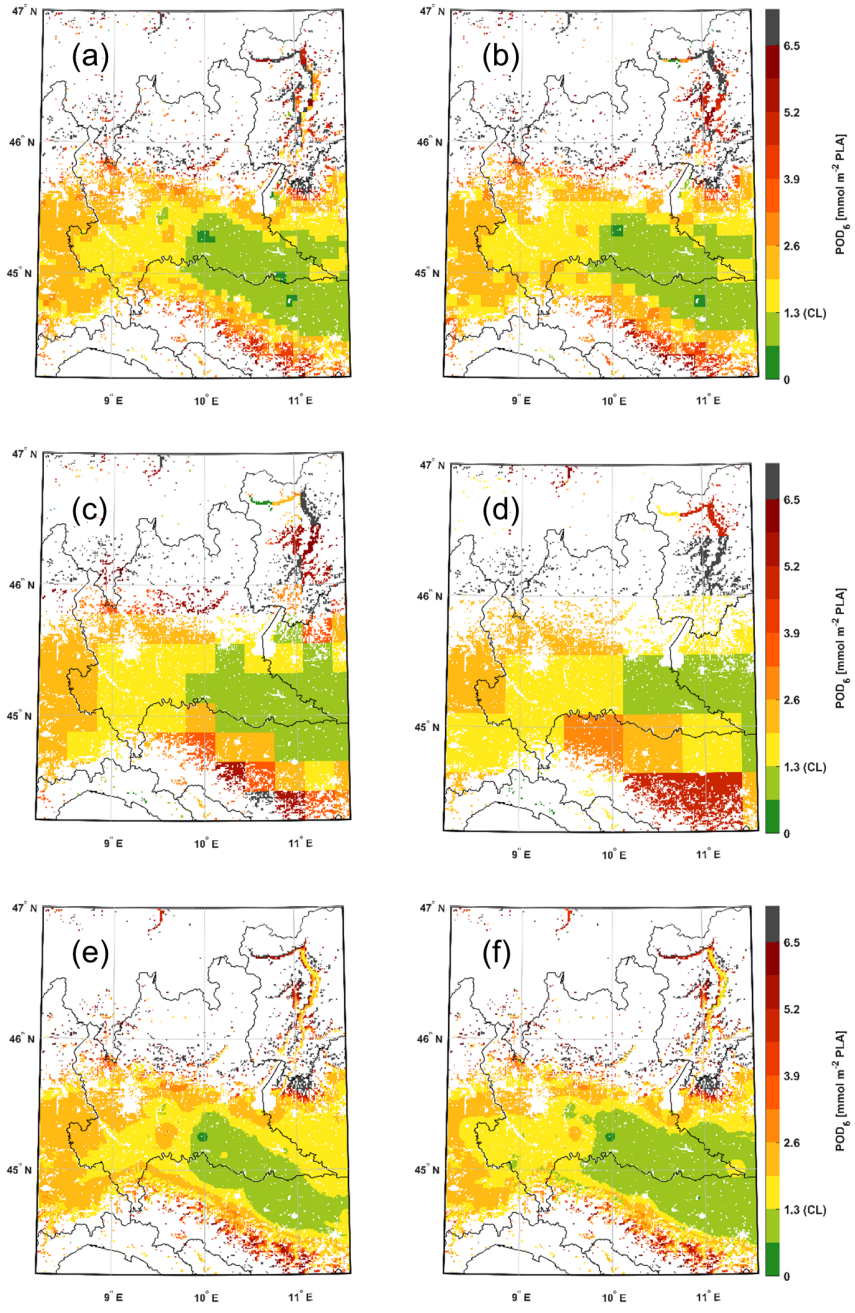

Figure 2.5. POD_6 maps at different spatial and temporal resolutions. Panels (a)–(d) show maps at 5 km × 5 km, 10 km × 10 km, 25 km × 25 km, and 50 km × 50 km, all at 1-hour resolution. Panels (e)–(f) show maps at 3-hour and 6-hour resolutions, respectively, for a 1 km × 1 km grid.

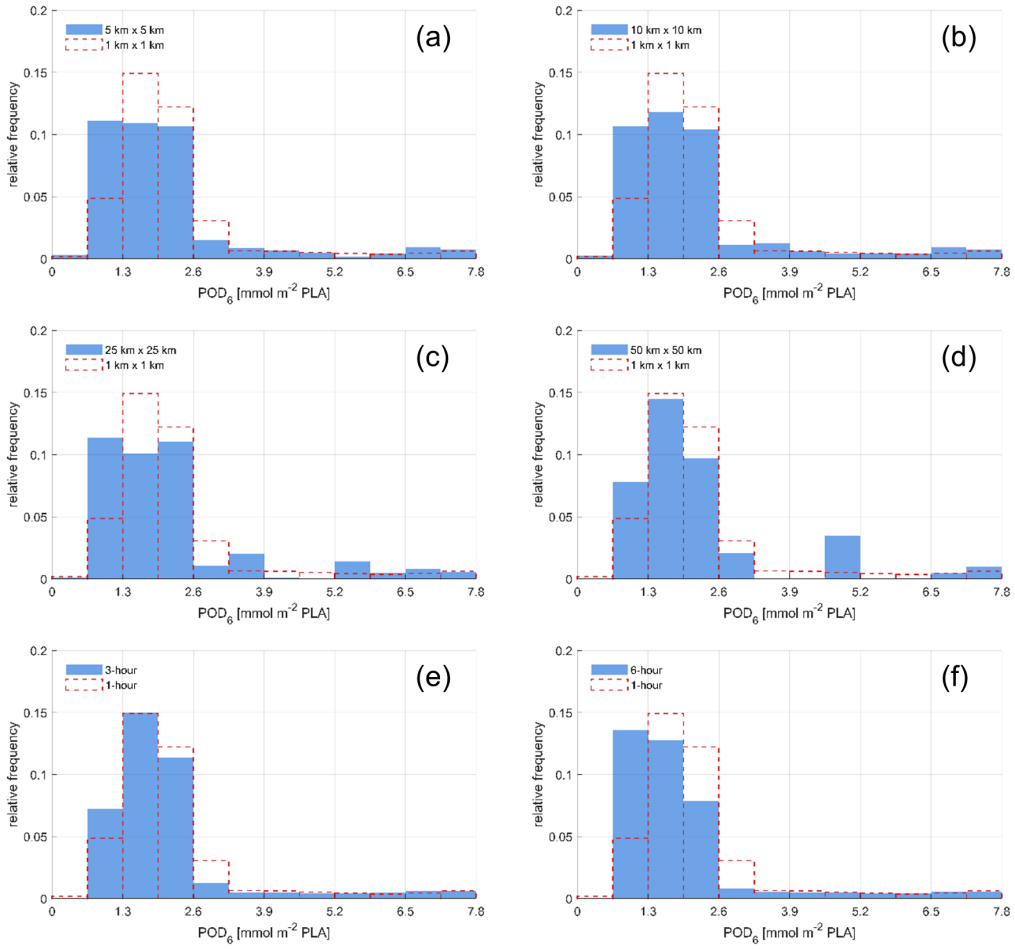

Figure 2.6. Histograms for POD_6 at different resolutions. Panels (a)–(d) show spatial resolutions of 5 km × 5 km, 10 km × 10 km, 25 km × 25 km, and 50 km × 50 km, all at 1-hour resolution. Panels (e)–(f) show 3-hour and 6-hour temporal resolutions, respectively, at 1 km × 1 km. Dashed empty bars indicate the reference resolution (1 km × 1 km, 1-hour).

2.3.4 Impacts of linear regression vs empirical altitudinal trends on POD_6

Before mapping the meteorological variables and O_3 concentrations via Kriging, the presence of a possible altitude dependence of O_3 concentrations was investigated. Only temperature and O_3 displayed a clear altitudinal trend in their hourly data (Fig. S3), while the trends for the other variables were not clear.

The use of linear regressions for elevation trends generally resulted in lower-quality meteorological maps compared to those obtained using empirical trends, as evident from Table 2.5. In fact, mean and median RMSE resulting from the jack-knife test were higher for the meteorological and O_3 concentration maps obtained with linear regressions than for those obtained with empirical trends.

On average, RMSE improved from a minimum of 2% (wind velocity) to a maximum of 10.11% (O_3), with the only exception of vapour pressure. Although the variables with clear trends showed higher improvements in the RMSE, the final POD_6 maps obtained using either linear regression or empirical trend maps as input were very similar. In fact, the mean bias and the RMSE between the two maps were respectively $-0.05\,\mathrm{mmol\,m^{-2}}$ PLA and $0.15\,\mathrm{mmol\,m^{-2}}$ PLA.

2.4 Discussion

2.4.1 Ozone risk assessment for Lombardy in 2017

This work has shown that it is possible to usefully employ hourly data of meteorological variables and O_3 concentrations from regional monitoring networks to obtain flux-based O_3 risk maps for a reference crop over a regional domain. The development of a dual-sink big-leaf model using high-resolution data ($1\,\mathrm{km} \times 1\,\mathrm{km}$, 1-hour) allowed to estimate that 87% of the cropland (Fig. 2.3b) was above the critical level (CL) of $1.3\,\mathrm{mmol\,m^{-2}}$ PLA for winter wheat. However, the magnitude of CL exceedances resulted in relatively moderate yield losses, i.e., $7.5 \pm 3.1\,\%$ on average. It should be

TABLE 2.5

MEAN AND MEDIAN RMSE FOR KRIGING USING LINEAR REGRESSION AND EMPIRICAL ALTITUDINAL TRENDS.

Physical quantity	Statistic	Linear regression	Empirical trend	% Variation
Temperature (°C)	Mean	2.09	1.93	−7.66
	Median	1.22	1.11	−9.02
O_3 (ppb)	Mean	10.11	9.49	−6.13
	Median	5.64	5.07	−10.11
Vapour pressure (kPa)	Mean	0.34	0.34	0
	Median	0.18	0.17	−5.56
Global radiation ($W\,m^{-2}$)	Mean	104.31	97.14	−6.87
	Median	46.54	43.22	−7.13
Wind velocity ($m\,s^{-1}$)	Mean	1.50	1.47	−2.00
	Median	0.68	0.66	−2.94

Note: Mean and median RMSE refer to the jack-knife method employed at every measurement station and each hour. The last column is calculated as % Variation = $(RMSE_{LR} - RMSE_{ET})/RMSE_{LR}$, where LR and ET stand for linear regression and empirical trend, respectively.

noted that this value was calculated using a dose-response relationship based mainly on sensitive cultivars, while moderately tolerant cultivars have also been identified (Bender et al., 1999; Pleijel et al., 2022). For this reason, together with the fact that the actual yield in every node depends on the particular agronomical condition of the site, the present relative yield loss should be considered as a potential one averaged over the whole domain.

Previous studies included this region as a part of larger domains where O_3 risk estimations were performed with coarser resolutions. Simpson et al. (2007), for example, reported POD_6 values between 4 and 6 $\mathrm{mmol\,m^{-2}}$ PLA for the same domain during the year 2000; however, the limiting effect of plant water availability was not considered in the calculation. Schucht et al. (2021), who assessed the O_3 risk for bread wheat in the whole of Europe, estimated a POD_6 between 3 and 4 $\mathrm{mmol\,m^{-2}}$ PLA in our domain for the year 2018, and a POD_6 within the range 1.5–3 $\mathrm{mmol\,m^{-2}}$ PLA for the year 2019, which was recorded as a particularly dry year. This latter value seems to be in line with our estimation for 2017, which was considered a dry year for the Po Valley region as well (García-Herrera et al., 2019; Baronetti et al., 2020). Mills et al. (2018) assessed a relative yield loss of 10–12.5% by using the simplified POD_3 IAM (Integrated Assessment Modelling) index for the period 2010–2012, and Schauberger et al. (2019) calculated a relative yield loss in the class 5–10% for the years 2008–2010 with a Dynamic Global Vegetation Model (DGVM). Considering the coarser resolution of the previous assessment exercises compared to ours, the last estimation is around the same magnitude as ours.

For comparison purposes, the estimated yield loss based on the AOT40 metric was on average 17.0±6.0 %, and the exposure map (Fig. S2a) and the AOT40 distributions (Fig. S2b) are reported in the supplementary materials.

Ozone risk in our domain followed two distinguishable patterns: a pattern related to soil water content in the plain, and a pattern related to elevation in the hilly

and mountain areas. The first pattern divided the plain areas into two distinctive parts: a first part in the south-eastern plain characterized by a POD_6 lower than the CL, because of early water shortage during the accumulation period, and a second part in the rest of the plain above the CL where the water shortage was mild. This feature was captured by Schauberger et al. (2019), despite the coarser resolution applied ($0.5° \times 0.5°$). Such a pattern did not emerge from the other cited studies, not even in (Schucht et al., 2021), who used the finest resolution (i.e., meteorological parameters at $0.1° \times 0.1°$, and O_3 concentrations and land cover at $2\,km \times 2\,km$).

The second POD_6 pattern was related to altitude and was due to the increase of O_3 concentrations with elevation, as also noted by many authors (Vingarzan, 2004; Loibl et al., 2004; Chevalier et al., 2007). This was especially evident in the parts of the domain with complex orography (hills and secondary valley floors), where POD_6 increased following the increasing O_3 concentration.

2.4.2 Key limiting factors to stomatal conductance

Air temperature and soil water availability were found to be the key factors limiting stomatal conductance. The importance of soil water availability to the plant was also highlighted by González-Fernández et al. (2013) and Rydsaa et al. (2016), who showed its crucial role in determining the O_3 stomatal flux and the consequent seasonal POD_Y. However, it should be noted that their conclusions were based on local measurements and were not extended to a regional scale. Attempts to verify the role of soil water content on POD_Y calculation at regional level were made, e.g., by De Marco et al. (2016), who compared O_3 risk maps for forests in northern and central Italy calculated for soil at field capacity versus maps calculated for the actual soil water content. The main conclusion of their study was that the exclusion of soil water content limitation caused a serious overestimation of the POD_Y, confirming the key role of soil water for the O_3 risk assessment. However, our study highlighted

that there was not a single main limiting factor for ozone stomatal conductance valid for the whole region, and that air temperature was the MLF in most of the domain, with soil water content as the second MLF, despite 2017 being a low rainfall year. Nevertheless, soil water content limitation was determinant in defining whether an area fell above or below the CL in relation to small time shifts in the beginning of water-limiting conditions. The latter result confirmed the central role of soil water content in the flux-based O_3 risk assessment, as also highlighted by the aforementioned authors. Nonetheless, the present results should be considered with caution, as the spatialization of soil water content in this study was not tested against field observations. Spatial estimates of soil water content are difficult and strictly dependent on input maps of precipitation, which are also noticeably affected by high levels of uncertainty. Considering the importance of soil water content as a limiting factor for stomatal conductance and for the subsequent O_3 risk assessment, further studies on the spatialization methods for this variable are recommended.

2.4.3 Errors associated with different spatial and temporal resolutions

Sensitivity of the POD_6 estimates to different spatio-temporal resolutions is a literature gap that was investigated thanks to the bottom-up approach based on measured data, providing guidance on resolution requirements for performing O_3 risk assessments.

By comparing the maps at different resolutions (Fig. 2.3b with Fig. 2.5), it was possible to see that the 1 km $\times$ 1 km resolution was the only one able to capture ozone risk hotspots. This is also evident from the frequency distributions, which shifted towards lower values of POD_6 at coarser resolutions (Fig. 2.6). In the maps reported by Watanabe et al. (2016), it is possible to see that higher resolutions can capture important features when the stomatal conductance limiting factors (such as temperature and VPD) vary greatly in space, particularly in relation to elevation.

The same is evident from the work of Schucht et al. (2021) at 2 km × 2 km resolution and Wang et al. (2022) at 5 km × 5 km resolution.

To some extent, our POD_6 maps displayed similar patterns across all resolutions. Nonetheless, since coarse spatial resolutions cannot always capture finer meteorological variability, and large timeframes are not able to capture ozone flux peaks, some distribution shifts and reductions of POD_6 values were found at increasing grid size and time frame.

Average estimated POD_6 was low in this case study, and the relative reduction associated with coarse resolutions (10–16%) would have been non-negligible for higher POD_6 values. However, even relatively small drops of POD_6 may shift large portions of the domain below the critical level. Furthermore, in our case, the RMSE obtained by comparing coarse resolution maps with the finest available increased dramatically with larger grid sizes and timeframes. In general terms, this suggests that coarse resolutions are associated with important uncertainties in O_3 risk assessment, especially in areas with complex orography, and that high RMSE indicates a low ability to detect O_3 risk hotspots.

Within the extent of this study, it can be noted that the 5 km × 5 km resolution could provide a reliable POD_6 estimate at the regional scale, as the associated RMSE is about half the POD_6 critical level, even though it corresponded to a 10% decrease of the average yield loss. However, this result might be affected by the fact that most of the considered cropland area is located in the plain and likely cannot be generalized to croplands in areas with complex orography, where finer resolutions may be required to maintain a low RMSE.

Regarding the time resolution, a 3-hour timeframe would have been acceptable, since it had a low RMSE and implied a reduction of only 5% of the average yield loss, compared to the 1-hour resolution run.

2.4.4 Sensitivity of the model to variable mapping precision

This study assessed the effect of meteorological and O_3 concentration maps' accuracy on the final POD_6 estimate, showing a low sensitivity of the model to data mapping RMSE. The Kriging with Trend model is known to provide maps with low estimate errors compared to other spatialization methods (Ramos et al., 2018; Hůnová et al., 2012), especially when the variables are strongly related to altitude.

In this framework, we explored the use of linear regressions versus the use of empirical trends. The comparison between these two options revealed an improvement in the RMSE in the empirical trend case. This was especially evident for temperature and O_3, which are well known to be strongly related to altitude.

However, improvements in the meteorological and O_3 concentration maps obtained through empirical trends did not translate into significantly different final POD_6 estimates, compared to those calculated with maps spatialized through linear regressions. This is attributable to the fact that the maps obtained with empirical trends were more accurate either before the accumulation period or in correspondence with the hours when the O_3 flux was relatively low or negligible, e.g., in the early morning. Furthermore, since POD_6 is an hourly cumulated index, improvements in input data maps accuracy for specific hours may not be sufficient to influence the seasonal or annual POD_6 estimate.

2.5 Conclusions

The moderate magnitude of the critical level exceedances revealed that O_3 risk for winter wheat in Lombardy was relatively low during the year 2017. This was presumably due to the effect of water shortage during the growing season.

Temperature was the main limiting factor to stomatal conductance in most of the region, and soil water content played a key role in determining spatial patterns

and final values of POD_6, together with the O_3 concentrations and their regional distribution. Moreover, the analysis displayed in this study provides an easily generalizable way to estimate the relative importance of different environmental factors for stomatal conductance at a regional scale.

A model was developed for flux-based O_3 risk assessment, and it is available for applications in other regions and for other plant species, provided that a proper parameterization of stomatal conductance and plant geometry is supplied. Clues toward the low sensitivity of the model to the accuracy of input data were found, which could be a common feature of models based on cumulative indexes.

In the context of modelling O_3 risk assessment, this work provided a methodology to determine data resolution requirements and the uncertainties associated with them. Our study indicates that high spatio-temporal resolutions (e.g., $1\,\text{km} \times 1\,\text{km}$, 1-hour) are the only ones that can identify O_3 risk hotspots to effectively guide spatially based mitigation measures. On the other hand, coarse resolutions could still be used to draw more general assessments, even though they might display lower POD_6 values. Minimum resolution requirements were identified as either $5\,\text{km} \times 5\,\text{km}$ or 3-hour. These results are encouraging, as such resolutions could be obtained from global and regional climate model data through, e.g., downscaling techniques.

CHAPTER 3

GLOBAL FLUX-BASED ASSESSMENT REVEALS DECLINING OZONE RISK FOR WHEAT IN FUTURE CLIMATE CHANGE SCENARIOS

This chapter is a reproduction, with slight modifications, of the journal article *Global flux-based assessment reveals declining ozone risk for wheat in future climate change scenarios* by P. R. Guaita, R. Marzuoli, L. Zhang, S. Turnock, G. Koren, O. Wild, P. Crippa, and G. Gerosa, published in Global Change Biology, 2025, Volume 31(12), page e70643, DOI: 10.1111/gcb.70643. The supplementary material referenced in the text can be found at Guaita et al. (2025).

3.1 Introduction

Tropospheric ozone (O_3) poses a significant threat to global crop production in a changing climate, with potentially serious implications for worldwide food security. With rising greenhouse gas concentrations and shifting emission patterns projected throughout the 21st century, understanding how these environmental changes will affect vital food crops and their response to O_3 becomes increasingly important for agricultural planning and policy decisions.

O_3 damages vegetation by entering the leaf through stomata and altering key biogeochemical and physiological processes, resulting in reduced photosynthesis, accelerated leaf senescence, and causing the expression of detoxification systems. This in turn reduces canopy carbon gain and biodiversity, among other negative effects (Fuhrer et al., 2016; Grulke and Heath, 2019; Ramya et al., 2023; Wright et al., 2018), and have important consequences for food security (Emberson, 2020).

The quantification of O_3 impacts on vegetation can be achieved through two distinct methodologies: an exposure (concentration)-based approach and a dose (flux)-based approach. Several studies have compared the two approaches across a wide range of vegetation types (Anav et al., 2016; Hoshika et al., 2020; Karlsson et al., 2007; Mao et al., 2024; Mills et al., 2018; Paoletti et al., 2019; Pleijel et al., 2022; Simpson et al., 2007; Tai et al., 2021; Tang et al., 2014) highlight that the flux-based approach, which estimates the phytotoxic ozone dose (POD), better represents the biological processes leading to O_3 damage to vegetation, as it accounts for the amount of O_3 entering the plants through the stomata (Paoletti and Manning, 2007).

Existing schemes for estimating O_3 stomatal flux to vegetation vary in complexity, ranging from a simple function of temperature and solar radiation (Wesely, 1989) , to a single-leaf Jarvis model (Baldocchi et al., 1987; Jarvis, 1976), a sunlit/shade (two-big-leaf) scheme (Emberson et al., 2000a; Zhang et al., 2003a), and a photosynthesis approach (**?**Charusombat et al., 2010). Combined models that integrate elements from the above-mentioned schemes have also been developed (Clifton et al., 2023, and references thering).

Regional- to global-scale O_3 risk assessments for various vegetation types have been extensively conducted over the past two decades, using both exposure-based and flux-based approaches to estimate past and present O_3 damage (Anav et al., 2011; Cheesman et al., 2023; Guaita et al., 2023; Mills et al., 2011a; Savi et al., 2020; Sharps et al., 2021; Van Dingenen et al., 2009). Many of these studies concluded that high O_3 concentrations can cause significant crop yield losses and economic damages worldwide (Pleijel et al., 2018; Tai et al., 2021).

However, studies of future O_3 impacts on vegetation have mostly applied exposure-based methods (e.g., Chuwah et al., 2015; Sicard et al., 2017). The few studies that have explicitly adopted flux-based approaches to estimate future O_3 impacts have typically simplifying assumptions, such as applying present-day meteorology with

projected emissions, or present-day emissions with future climate (Klingberg et al., 2014; Simpson et al., 2007; Tang et al., 2014). To our knowledge, a comprehensive, global flux-based analysis of O_3 impacts across the 21st century, considering both future climate and emission scenarios, is still lacking.

A key aspect in O_3 risk assessment over future times is the accurate consideration for the effect of rising atmospheric CO_2 concentrations on plant physiology and O_3 uptake. Elevated CO_2 levels typically induce partial stomatal closure in C_3 crops like wheat, potentially reducing O_3 uptake and subsequent damage. This CO_2-induced effect reflects a complex physiological interaction of plant responses: while increased CO_2 may enhance photosynthesis and water use efficiency, it simultaneously provides a protective effect against O_3 damage by limiting stomatal conductance (Ainsworth et al., 2012; Fiscus et al., 2005). However, this protective effect is complicated by other climate factors, as changes in temperature, vapor pressure deficit, and water stress may counteract stomatal closure. The net effect of these interacting variables will likely differ across geographic regions depending on their specific climatic conditions.

This study addresses these research gaps through a global-scale, flux-based assessment of future O_3 risks for bread wheat (*Triticum aestivum*), which is one of the world's most important staple food crops and a reference for agricultural species with high O_3 sensitivity (Mills et al., 2011b; Sitch et al., 2007). More specifically, the objectives of this research are to: (1) estimate future trends of POD for wheat to the end of the 21st century under different climate change scenarios; (2) identify the regions that are most vulnerable to future food security threats due to the negative O_3 effects on wheat; and (3) evaluate the impact of different adaptation and mitigation strategies in reducing future O_3 risk.

To address these objectives, we employ a dual-sink big-leaf dry deposition model (Guaita et al., 2023), driven by meteorology and O_3 concentration outputs from Earth

System Models (ESMs) participating in the Coupled Model Intercomparison Project 6 (CMIP6; Eyring et al., 2016). To generate a set of future climate simulations, these ESMs use the forcing datasets associated with the shared socioeconomic pathways (SSPs; Riahi et al., 2017), which are future pathways combining different trends in social, economic, and environmental developments with different assumptions about anthropogenic emission mitigation applied on top of these to meet predefined climate targets (radiative forcing; RF).

3.2 Methodology

TABLE 3.1

LIST OF ACRONYMS AND SYMBOLS AND THEIR MEANING.

Acronym/Symbol	**Meaning**
ANOVA	Analysis of variance
CL	Critical Level
EP	Emission Policy
ESM	Earth System Model
FC	Field Capacity
f_{clim}	Jarvis function defined as $f_{\text{temp}} \cdot f_{\text{VPD}} \cdot f_{\text{soil}}$
f_{CO2}	Jarvis function for CO_2
f_{light}	Jarvis function for light
f_{min}	Jarvis function indicating minimum g_s relative to $g_{s,\text{max}}$
f_{O3}	Jarvis function for the O_3-induced senescence
f_{phen}	Jarvis function for phenological growth

Continued on next page

Table 3.1 continued from previous page

Acronym/Symbol	Meaning
F_{sO3}	O_3 stomatal flux
f_{soil}	Jarvis function for soil water availability to the plant
f_{temp}	Jarvis function for temperature
f_{VPD}	Jarvis function for VPD
g_s	Stomatal conductance to O_3
$g_{s,\text{max}}$	Maximum stomatal conductance
I	Interaction factor between EP and RF in the ANOVA
MM	Mapping Manual (LRTAP Convention, 2017)
PLA	Projected leaf area
POD_Y	Phytotoxic Ozone Dose above a threshold of Y nmol m^{-2} PLA
R_a	Atmospheric resistance
R_b	Quasi-laminar sublayer resistance
R_c	Surface resistance
R_{cut}	Cuticular resistance
RF	Radiative Forcing
R_{inc}	Intra-canopy resistance
R_{soil}	Soil resistance
R_{stom}	Stomatal resistance
RYL	Relative Yield Loss
TOAR	Tropospheric Ozone Assessment Report

3.2.1 Selection of CMIP6 models and SSPs

A subset of models from the CMIP6 experiment is selected as input for this work. Specifically, we apply the following criteria to identify the model runs suitable for our study: (i) an online/coupled-chemistry framework (AerChemMIP; Collins et al., 2017) to include the feedback of O_3 on climate and (ii) sub-daily temporal resolution of meteorological variables to enable O_3 flux calculations. According to these criteria, we identify GFDL-ESM4 (Dunne et al., 2020; Horowitz et al., 2020; Krasting et al., 2018) and UKESM1-0-LL (O'Connor, 2020; Sellar et al., 2019; Tang et al., 2019) for this study.

UKESM1-0-LL and GFDL-ESM4 are both fully coupled global ESMs, which include a physical atmosphere–ocean model coupled with additional interactive Earth system components including ocean biogeochemistry, stratosphere–troposphere chemistry and aerosol scheme, and terrestrial carbon cycles coupled to interactive vegetation (Table S1). They both have a horizontal grid resolution of between 100 and 140 km in the mid-latitudes, with vertical levels extending to the upper stratosphere. Comprehensive chemistry schemes are included within both ESMs simulating the reactions and transport of major chemical species involved in O_3 formation. As a result, these ESMs can simulate the interactions between climate and chemistry changes across both historical and future periods. The model variables required for this study are listed in Table S1.

POD calculations require O_3 concentrations to be scaled from the model-level geometric height to the canopy height, which is achieved using the dry deposition model used in this study (Guaita et al., 2023). See Appendix B.1 for details.

Annual O_3 risk for wheat from 2015 to 2100 is quantified relative to a POD baseline value, calculated as the average over the 2000–2014 period. The POD for the baseline years is derived from the historical experiment of CMIP6 (Eyring et al., 2016). Future O_3 risk is estimated based on climate and emission scenarios described

by the SSPs (Riahi et al., 2017). Specifically, we focus on the scenarios SSP1-2.6 (Van Vuuren et al., 2017), SSP3-7.0 (**?**), and SSP5-8.5 (Kriegler et al., 2017), as they represent contrasting characteristics in terms of future radiative forcing (RF) and emission policies (EP) for air quality that impact O_3 concentrations from 2015 to 2100.

Herein we classify SSP1-2.6 as a low-emissions and low-RF scenario, SSP3-7.0 as a high-emissions and high-RF scenario, while SSP5-8.5 as a high-RF and partial emission control scenario, with controls beginning in the second half of the 21st century. Thus, from an O_3 concentration perspective, SSP5-8.5 can be broadly considered as an intermediate scenario, with end-of-century pronounced climate change and O_3 concentrations akin to those observed in the historical baseline (Turnock et al., 2020).

Further, the SSP3-7.0pdSST experiment (present-day sea surface temperature; Zanis et al., 2022) is available from UKESM1-0-LL and is included in this study to assess the effect of changing O_3 concentrations only in a high-emission/present-day climate scenario. ESM outputs show biases in both meteorological variables and O_3 concentrations. An evaluation of the O_3 bias against surface O_3 observations from the Tropospheric Ozone Assessment Report (TOAR) dataset (Schröder et al., 2021) for the baseline years (2000–2014) is presented in Appendix B.2, alongside the effect of meteorological and O_3 biases on the final POD estimate.

3.2.2 Dry deposition model for wheat

The POD calculations follow the approach described in the LRTAP Convention (2017). More specifically, we use a dual-sink big-leaf O_3 dry deposition model that calculates stomatal conductance (g_s) and O_3 uptake by plants, following the DO3SE paradigm originally developed by Emberson et al. (2000b). This model also simulates phenology, soil water available to the plant, and light penetration within the canopy, and accounts for atmospheric stability and instability with the Monin–Obukhov sim-

ilarity theory along with a resistive scheme.

The O_3 stomatal flux model receives as input meteorological and chemical data from the CMIP6 models under the different SSPs. The complete formulation of the O_3 dry deposition model is described in Appendix A. Modifications applied in this study are detailed in Appendix B.3.

O_3 deposition from the lowest model level to the vegetated surface is calculated with a resistive network of three resistances (bulk resistances, uppercase R) in series: an atmospheric resistance R_a, a quasi-laminar sublayer resistance R_b, and a surface resistance R_c. The latter consists of three resistances in parallel: a cuticular resistance R_{cut}, a stomatal resistance R_{stom}, and a ground resistance composed of an intra-canopy resistance R_{inc} and a soil resistance R_{soil}, in series.

Following the DO3SE methodology (Emberson et al., 2000a,b), the canopy-level resistance R_{stom} is obtained by upscaling the leaf-level resistances (lowercase r), while accounting for sunlit and shaded portions of the canopy. Only the stomatal resistance for a sunlit upper canopy leaf is used to calculate the stomatal O_3 uptake.

The leaf-level stomatal resistance is calculated as the inverse of the stomatal conductance g_s, obtained by applying the empirical Jarvis–Stewart approach (Jarvis, 1976; Stewart, 1988):

$$g_s = g_{\max} \cdot \min\{f_{\text{phen}}, f_{\text{O}_3}\} \cdot f_{\text{light}} \cdot \max\{f_{\min}, f_{\text{temp}} \cdot f_{\text{VPD}} \cdot f_{\text{soil}}\} \cdot f_{\text{CO}_2} \tag{3.1}$$

where the f functions (ranging between 0 and 1) are taken directly from the LRTAP Convention (2017), with the only exception of f_{CO_2} (see below). For this study an f_{clim} term is defined as the product $f_{\text{temp}} \cdot f_{\text{VPD}} \cdot f_{\text{soil}}$ to represent the combined effect of the main climatic factors on g_s. The $f_{\min}$ term represents a constant value of 0.01 indicating the minimum g_s expressed relative to $g_{\max}$ during daylight hours.

In addition to the LRTAP Convention (2017) methodology, the $f_{\mathrm{CO_2}}$ function was defined to describe how g_s is affected by CO_2 concentrations, which are projected to further increase in the next decades until the end of the century. Increasing CO_2 concentrations are known to decrease g_s non-linearly (Franks et al., 2017; Haworth et al., 2016; Li et al., 2019). The relationship is represented as:

$$f_{\mathrm{CO_2}}([\mathrm{CO_2}]) = f_{\mathrm{min,CO_2}} + (1 - f_{\mathrm{min,CO_2}}) \exp\left(-a_{\mathrm{CO_2}} \cdot \frac{[\mathrm{CO_2}] - \mathrm{CO_{2,ref}}}{\mathrm{CO_{2,ref}}}\right) \tag{3.2}$$

The inferred parameter values are $a_{\mathrm{CO_2}} = 0.5480$, $f_{\mathrm{min,CO_2}} = 0.2823$, and $\mathrm{CO_{2,ref}} = 384.2$ ppm, consistent with experimental studies (Agrawal and Deepak, 2003; Ainsworth and Rogers, 2007; Del Pozo et al., 2005; Kang et al., 2021; Tuba et al., 1994).

The seasonal phytotoxic ozone dose above a threshold Y (POD_Y) is calculated as:

$$\mathrm{POD}_Y = \sum_{i=0}^{t} \left[\max\left(F_{\mathrm{sO_3},i} - Y, 0\right) \cdot 3600 \cdot 10^{-6}\right] \tag{3.3}$$

with the stomatal O_3 flux defined as:

$$F_{\mathrm{sO_3},i} = O_3(h_c) \cdot \frac{1}{r_s} \cdot \left(1 - \frac{r_b}{r_b + r_c}\right) \tag{3.4}$$

For *Triticum aestivum*, a detoxifying threshold of 6 nmol O_3 m^{-2} s^{-1} (POD_6) is recommended by the LRTAP Convention (2017). The relative yield loss (RYL) is calculated as:

$$\mathrm{RYL} = 3.85 \cdot \mathrm{POD}_6 \tag{3.5}$$

3.2.3 Dry deposition model runs, assumptions, and output analysis

Four runs are presented in this study. The first run estimates POD_6 for the O_3 risk assessment, consistently with a common framework defined by the LRTAP Convention (2017), and is therefore labelled as the *MM run* (Mapping Manual). Soil water available to the plant is assumed at field capacity at the sowing date every year and is dynamically simulated using an online water budget model. In this run, $f_{CO_2} = 1$ at every timestep.

The second run (henceforth *MM+CO_2 run*) simulates soil water availability as in the MM run but calculates f_{CO_2} according to Eq. (2). This allows estimation of the changes in POD_6 due to the reduction of g_{max} at elevated CO_2 concentrations, while accounting for the feedback that the reduced g_s has on transpiration. The MM and the MM+CO_2 runs assume no irrigation and are therefore also labelled as *rainfed runs*.

The third and fourth runs (henceforth *MM_FC run* and *MM+CO_2_FC run*) aim to diagnose the effect of soil water availability on O_3 risk by assuming soil water at field capacity (FC), i.e. $f_{soil} = 1$ at every timestep. These runs are named *FC runs*, as opposed to the rainfed runs.

UKESM1-0-LL simulates O_3 concentrations reasonably accurately, whereas GFDL-ESM4 underestimates upper O_3 concentration percentiles (see Appendix B.2). For this reason, data from UKESM1-0-LL are used for all four runs, while GFDL-ESM4 data from the historical experiment are only used for the MM+CO_2 run.

Each run produces global annual POD_6 maps from 2000 to 2099 for each of the considered SSPs. All maps and tables in this study are masked using the land-use maps from Qiao et al. (2023). Furthermore, for a given year, any grid node where wheat fails to reach maturity before the next prescribed sowing date is excluded.

O_3 concentration and f_{clim} values (Section 3.3.1) are analysed by computing the global mean and the mean interannual variability. First, in each grid node, the mean

yearly value of each variable is calculated over the daylight hours of the accumulation period. Then, for each node, yearly values over a given time window (2000–2014, 2045–2054, or 2090–2099) are considered, and the mean and standard deviation are calculated. The final mean values (Table 3.2) are obtained by averaging the mean values across all grid nodes (global mean). The global interannual variability is calculated as the mean of the standard deviations across all grid nodes (spatial mean of the interannual variability).

The analysis of regional trends in Section 3.3.2 is restricted to the area at O_3 risk, defined as grid nodes exceeding the critical level (CL) for wheat (1.3 mmol m^{-2} PLA) for at least one year of the century under any SSP. This restriction allows us to focus on regions where O_3 risk is non-negligible at any point in time, excluding consistently low-POD_6 areas.

For each region, it is tested whether the mean POD_6 value over a selected future time window significantly differs from the mean POD_6 value during the baseline period using a Welch t-test, with effective sample size accounting for spatial autocorrelation calculated using Moran's Index. The p-values are computed by comparing the 15 annual means of the baseline period with the 10 annual means of each future time window (Table 3.3 and Table S3).

In Section 3.3.3, a grid node is defined as chronically at risk under a given experiment if POD_6 exceeds the CL in at least 75% of the years considered (either 2000–2014 or 2015–2099). This criterion identifies areas where O_3 risk is persistent across the century, even when end-of-century POD_6 declines, allowing assessment of whether a region remains at O_3 risk throughout the century.

Global wheat production losses are estimated for the baseline period, 2050, and 2100. Gridded annual yield output ($Tg\,yr^{-1}$) is obtained from the LPJmL model (Lutz et al., 2019; Von Bloh et al., 2018), as per simulations performed within ISIMIP3b (Jägermeyr et al., 2024) using UKESM1-0-LL as the climate forcing dataset.

This product provides gridded annual yield values (t ha^{-1}) at the global scale for the historical, SSP1-2.6, SSP3-7.0, and SSP5-8.5 experiments.

These yield data are combined with harvested area from the Spatial Production Allocation Model (SPAM2020v2) dataset of the International Food Policy Research Institute (International Food Policy Research Institute (IFPRI), 2024) to calculate total wheat production at each grid node. By combining these products with the estimated relative yield loss (RYL; Eq. 3.5), annual production losses ($Tg\,yr^{-1}$) are derived for both present and future climate scenarios. This approach captures projected yield changes across different SSPs but assumes that the spatial distribution of wheat cultivation remains fixed at present-day levels as defined by SPAM.

3.3 Results

3.3.1 Spatio-temporal patterns of O_3 and impacts of climate variables on stomatal conductance

Figure 3.1a–d shows the mean O_3 concentrations during the baseline years (2000–2014 mean) and their changes (ΔO_3) at 2100 (2090–2099 mean). O_3 concentrations are expressed at wheat canopy height and averaged over the daylight hours of the accumulation period. During the baseline years, UKESM1-0-LL shows global mean O_3 concentrations of 37.1 ± 2.4 ppb (Table 3.2), while GFDL-ESM4 shows slightly lower values (36.0 ± 2.1 ppb). The Northern Hemisphere presents higher O_3 concentrations than the Southern Hemisphere, with the Middle East and Asia the regions with the highest values around the globe (Figure 3.2a). Compared to GFDL-ESM4, UKESM1-0-LL shows stronger latitudinal and elevation gradients (see Figure S2 for GFDL-ESM4 2000–2014 maps) and generally reports higher concentrations at latitudes $< 45°$, except for the Eastern Indian peninsula. Moreover, UKESM1-0-LL simulates the strongest seasonal cycle in Northern Hemisphere surface ozone among

all CMIP6 models, potentially due to excessive NO_x titration of O_3 in this model (Turnock et al., 2020). Under SSP1-2.6, which assumes the implementation of strong air quality policies, UKESM1-0-LL projects a mean O_3 decrease of 8.5 ppb by the end of the century (Figure 3.1b). On the contrary, under SSP3-7.0, which is characterized by weaker air pollution control policies, O_3 concentrations generally increase by 2100, although some exceptions are present (e.g., central U.S.; Figure 3.1c). SSP5-8.5 shows similar spatial patterns as SSP3-7.0, but to a lesser extent, which is consistent with the implementation of strong air quality control policies from 2050 onward (Figure 3.1d).

The f_{clim} function captures the combined effect of key climatic factors (air temperature, VPD and soil water available to the plant) on g_s. Values of $f_{\text{clim}} \approx 1$ indicate minimal limitation, while near zero values denote a strong stomatal closure and reduced O_3 uptake. During the baseline years, the f_{clim} averaged over the accumulation period exceeds 0.5 over large areas of Eastern North America, South America, and East Asia, while strongly limiting conditions ($f_{\text{clim}} < 0.2$) occur mostly in arid regions (Figure 3.1e). Figure 3.1f–h shows the changes in f_{clim} at 2100 compared to the baseline (Δf_{clim}). From an O_3 risk perspective, negative Δf_{clim} values indicate stronger climatic limitation of g_s and thus, potentially, lower POD_6 and O_3 damage. On the contrary, positive Δf_{clim} values correspond to a weaker limitation of g_s and therefore higher POD_6 and increased O_3 damage. SSP3-7.0 and SSP5-8.5 indicate overall similar magnitudes of Δf_{clim} across the globe at the end of the century, while SSP1-2.6 shows smaller changes, as expected from the weaker RF of this scenario. An evident pattern in future changes across all SSPs is the large positive shift at latitudes $> 45°$, which indicates higher g_s (and better growing conditions) for wheat at higher latitude. This is due to increased f_{temp} values, i.e., temperatures closer to the optimum for g_s (Figure S3a–d). The function f_{VPD} (Figure S3e–h) is generally non-limiting ($f_{\text{VPD}} > 0.8$) across most regions of the globe, with the only exception

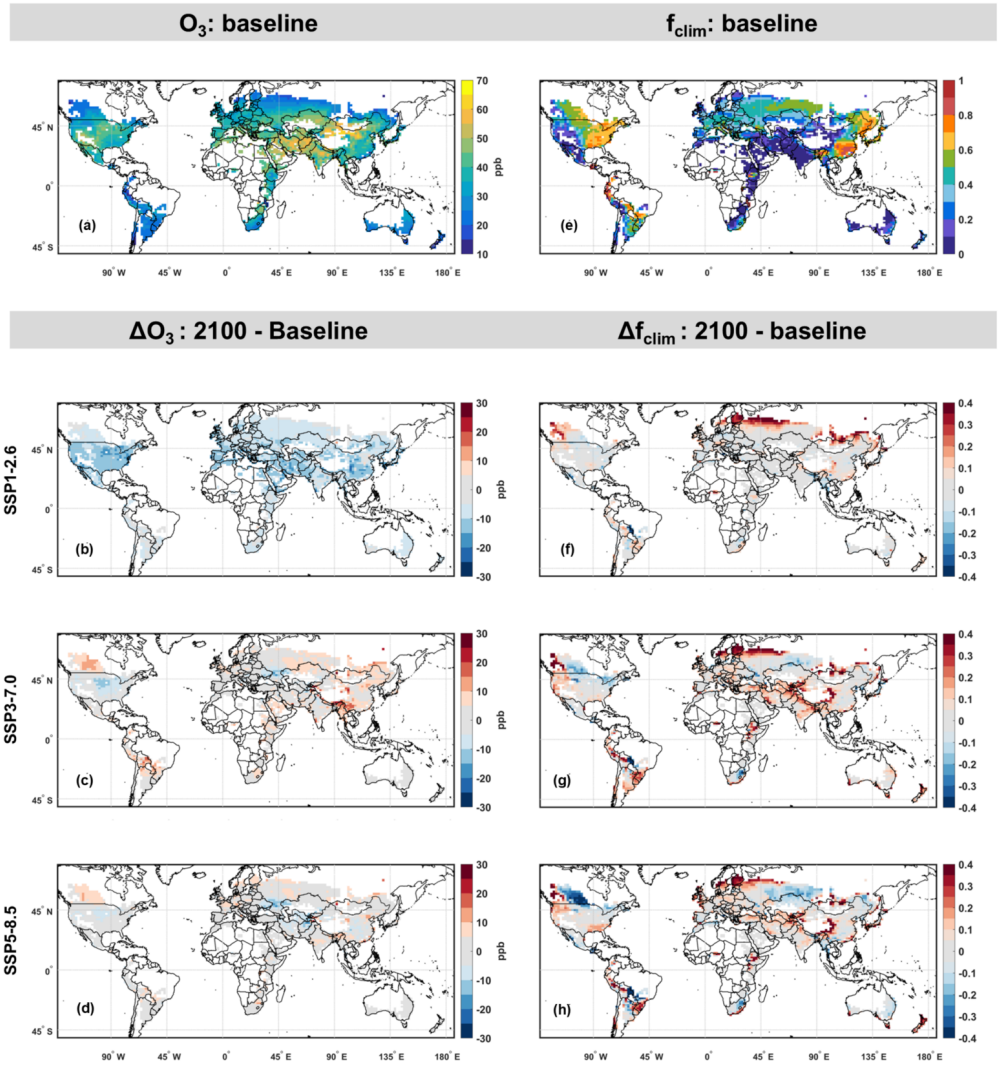

Figure 3.1. Ozone mean concentrations at canopy height and during the daylight hours of the accumulation period for UKESM1-0-LL over the baseline period (a), and ΔO_3 at 2100 with respect to the baseline across the different SSPs (b-d). f_{clim} mean values for the same ESM over the baseline period (e), and Δf_{clim} at 2100 with respect to the baseline across the different SSPs (f-h). $f_{\text{clim}} = f_{\text{temp}} \cdot f_{\text{VPD}} \cdot f_{\text{soil}}$ summarizes the limitations to g_s due to temperature, VPD and soil water available to the plant. Positive or negative Δf_{clim} correspond to higher and lower O_3 risk, respectively (red and blue, in f-h). Baseline indicates the 2000–2014 mean, and 2100 indicates the 2090–2099 mean. White nodes indicate that wheat either is not grown or hasn't reached maturity before the next prescribed sowing date. Map lines delineate study areas and do not necessarily depict accepted national boundaries.

of arid regions, indicating that f_{clim} is only marginally affected by this component. However, f_{VPD} becomes more limiting at the end of the century because of a general decrease in relative humidity, which is a feature frequently observed in future climate simulations (Fang et al., 2022). As expected, f_{soil} is very limiting over arid regions at the present time, but increases considerably at the end of the century under SSP3-7.0 and SSP5-8.5 (Figure S3i–l). Overall, during the baseline, f_{clim} is primarily constrained by f_{soil} (see e.g., Figure 3.1e and Figure S3i). However, the positive changes in f_{clim} at 2100 appear to be driven by the changes in f_{temp} at higher latitudes and in f_{soil} over arid regions, but this effect is counteracted by the negative changes in f_{VPD}, especially under SSP3-7.0 and SSP5-8.5.

Finally, it is important to highlight that the POD_6 accumulation period becomes slightly shorter and noticeably earlier in the future (Table 3.2), especially under SSP3-7.0 and SSP5-8.5, and therefore the O_3 concentrations and the outcomes of the Jarvis functions described in this section are affected by this time shift.

3.3.2 POD_6 trends by region

Figure 3.2 displays the annual POD_6 values averaged over different geographical regions and under different SSPs, for both the MM and MM+CO2 runs. Table 3.3 lists the mean POD_6 at 2050 (2045–2054) and at 2100 (2090–2099) in each region (p-values and 95% confidence intervals are reported in Table S3). POD_6 decreases under SSP1-2.6 in every region for both the MM and the MM+CO2 runs, with values approaching zero well before 2100. These results are associated with very high certainty ($p < 0.001$) in most regions at the end of the century.

For the MM run, POD_6 generally does not decrease under SSP3-7.0, with 7 out of 12 regions displaying increasing POD_6 values at the end of the century ($p < 0.01$). For the same run, under SSP5-8.5, POD_6 changes at 2050 are associated with $p < 0.01$ in 6 regions, and in these cases the timelines rise and then fall, usually reaching

TABLE 3.2

GLOBAL MEANS (± MEAN INTERANNUAL VARIABILITY) OF O_3 CONCENTRATIONS AT CANOPY HEIGHT, JARVIS FUNCTIONS, AND DURATION OF THE ACCUMULATION PERIOD DURING THE BASELINE PERIOD, AT 2050 AND 2100, AND DIFFERENCES IN THE ONSETS OF THE ACCUMULATION PERIODS BETWEEN THE END OF THE CENTURY AND THE BASELINE (ΔONSET), OVER WHEAT-GROWING REGIONS, FOR UKESM1-0-LL UNDER DIFFERENT SSPS.

Variable	Baseline[a]	2050			2100		
		SSP1-2.6	SSP3-7.0	SSP5-8.5	SSP1-2.6	SSP3-7.0	SSP5-8.5
O_3 [ppb]	37.1 ± 2.4	32.6 ± 2.1	38.9 ± 2.3	40.2 ± 2.4	28.6 ± 1.8	39.5 ± 2.4	37.7 ± 2.5
f_{clim} [0,1]	0.34 ± 0.07	0.35 ± 0.07	0.38 ± 0.07	0.36 ± 0.08	0.36 ± 0.07	0.39 ± 0.08	0.36 ± 0.08
f_{temp} [0,1]	0.60 ± 0.06	0.69 ± 0.05	0.68 ± 0.06	0.72 ± 0.05	0.70 ± 0.05	0.69 ± 0.06	0.72 ± 0.05
f_{VPD} [0,1]	0.89 ± 0.04	0.84 ± 0.05	0.86 ± 0.05	0.82 ± 0.05	0.84 ± 0.04	0.83 ± 0.05	0.77 ± 0.06
f_{soil} [0,1]	0.66 ± 0.08	0.61 ± 0.09	0.68 ± 0.08	0.61 ± 0.09	0.61 ± 0.09	0.71 ± 0.08	0.66 ± 0.08
Accumulation period duration [d]	40.6 ± 10.9	41.0 ± 8.8	38.1 ± 9.6	39.6 ± 8.2	40.9 ± 8.8	32.6 ± 9.3	37.1 ± 9.4
Δonset [d]	–	-0.1 ± 5.9	-2.2 ± 5.3	-4.3 ± 5.8	-3.5 ± 5.9	-12.6 ± 4.4	-23.4 ± 5.3

[a]Baseline indicates the mean between 2000 and 2014, 2050 indicates the mean between 2045–2054, and 2100 indicates the mean between 2090–2099.

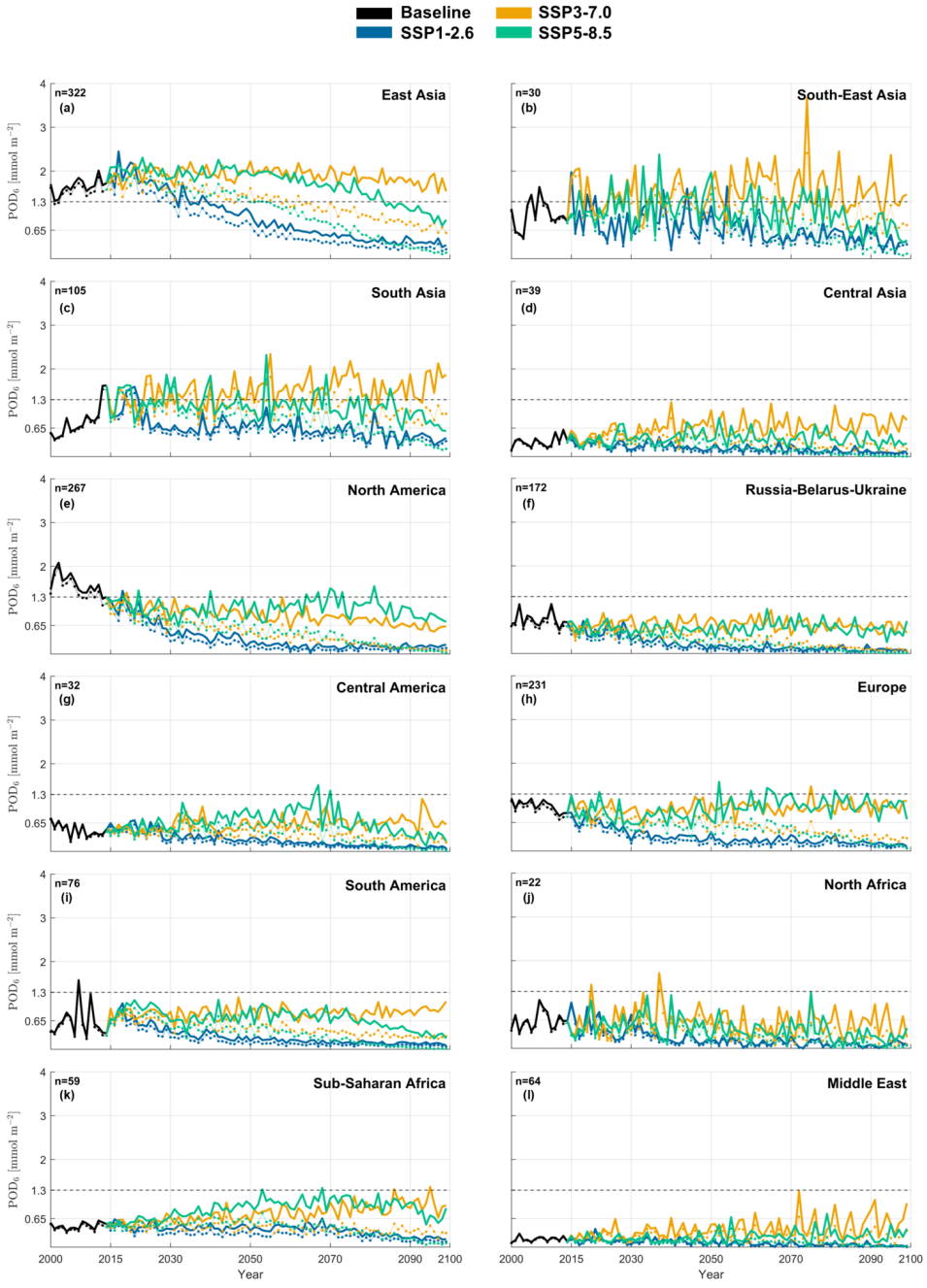

Figure 3.2. POD_6 throughout the century with respect to the baseline average, shown across different SSPs and divided by region, for both the MM run (solid lines) and the MM+CO2 run (dotted lines); only the areas at O_3 risk within each region are considered. The value (n) in the upper-left corner is the number of nodes in the areas at O_3 risk. The dashed horizontal line corresponds to the CL for wheat.

their maxima between 2050 and 2080, and then reverting to values closer to or lower than the baseline at the end of the century. In the MM+CO2 run, POD_6 values decrease in every region, as the limiting effect of increasing CO_2 on g_s dominates the other dynamics (O_3 concentrations and f_{clim} changes). This is especially evident in the differences between MM and MM+CO2 end-century POD_6 values for SSP5-8.5, which are very large precisely due to the high CO_2 concentrations under this scenario. As this feature is consistent across regions and quite straightforward, it will not be commented further, and the rest of this section will refer only to the MM run.

Noticeably, East Asia is the region with the largest area at O_3 risk and with the highest average POD_6 values at both the baseline ($1.65 \pm 0.17\,\text{mmol}\,\text{m}^{-2}$) and across all scenarios, exceeding the CL for the whole century under SSP3-7.0, and for most of it under SSP5-8.5. South Asia has the second greatest POD_6 value across all SSPs ($1.07\,\text{mmol}\,\text{m}^{-2}$) over a fairly large O_3 risk area, experiencing the largest absolute POD_6 increase under SSP3-7.0 at both 2050 and 2100 (+0.71 and +0.88, respectively). In this region, the average POD_6 frequently exceeds the CL under both SSP3-7.0 and SSP5-8.5. South-East Asia has the third highest POD_6 average across all SSPs ($1.01\,\text{mmol}\,\text{m}^{-2}$), although the hotspot region is comparatively small. This region shows the highest variability in POD_6 values, with an interannual standard deviation across SSPs of $0.41\,\text{mmol}\,\text{m}^{-2}$, most likely reflecting the largest interannual variability of O_3 concentrations and f_{clim} among all regions (interannual SD: 4.77 ppb and 0.08, respectively).

Sub-Saharan Africa is another region with a large POD_6 increase across SSPs (+0.19), which corresponds to POD_6 values doubling at mid-century under SSP5-8.5 and at the end of the century under SSP3-7.0. In Europe, the average POD_6 values over areas at O_3 risk are typically just below the CL, and they do not show any detectable change at the end of the century under SSP3-7.0 and SSP5-8.5. Even so, this O_3 risk area covers 79.9% of Europe and, across the century, 28.2% of the

times the CL is exceeded anyway. Furthermore, it should be noted that the close-to-zero changes in POD_6 values are due to the presence of opposing trends between Southern and Northern Europe (see Figure 3.2), rather than due to an actual absence of changes in POD_6 mean values.

North America has the second highest average POD_6 at the baseline over a widespread O_3 risk area, but POD_6 values most certainly decrease across all the scenarios (-0.95, $p < 0.001$), and for future times the mean POD_6 would exceed the CL only under SSP5-8.5 and for just a few years. Russia-Belarus-Ukraine also shows decreasing POD_6 values under any scenario ($p < 0.001$), and while the O_3 risk is quite extended, the CL is seldom exceeded over individual nodes and years.

3.3.3 Global estimates of POD_6 and agronomic losses

Figure 3.3 shows POD_6 global maps for the baseline period and at the end of the century. In this figure, the POD_6 values refer to the two contrasting assumptions on the effect of CO2 concentrations on g_s (MM and MM+CO2 runs). During the baseline years, the mean POD_6 exceeds the CL for wheat over 17.5% and 16.1% of the global wheat area in the MM and MM+CO2 runs, respectively (Figure 3.3a), leading to global production losses of 28.7 and 26.6 $\mathrm{Tg\,yr^{-1}}$, respectively (Table S4). An important indicator to identify hotspots is the percentage of years during which the POD_6 surpasses the CL across the whole century (Figure 3.4). Figure 3.4a shows this indicator at the baseline, during which 11.7% of the nodes can be classified as chronically at risk in the MM run (10.0% in the MM+CO2 run).

Under SSP1-2.6, O_3 risk decreases across the whole globe by the end of the century (Figure 3.3b,c), mostly due to declining O_3 concentrations (Figure 3.1b), with the mean POD_6 above the CL for only 0.8% and 0.5% of the global wheat area in the MM and MM+CO2 runs, respectively (percentage areas chronically at risk: 0.6% and 0.2%; production losses: 5.7 and 3.9$\mathrm{Tg\,yr^{-1}}$). Such decrease is consistent almost

TABLE 3.3

MEAN POD_6 (MMOL M^{-2} PLA) FOR THE MM RUN BY REGION AND SSP FOR AREAS AT RISK AT THE BASELINE (2000–2014), 2050 (2045–2054), AND 2100 (2090–2099). STARRED VALUES INDICATE $p < 0.05$. SEE TABLE S3 FOR ACTUAL P-VALUES AND 95% CONFIDENCE INTERVALS.

Region[a]	Baseline POD_6	2050 POD_6			2100 POD_6		
		SSP1-2.6	SSP3-7.0	SSP5-8.5	SSP1-2.6	SSP3-7.0	SSP5-8.5
East Asia	1.65 ± 1.47	0.95 ± 1.00*	1.97 ± 1.62*	1.98 ± 1.67*	0.37 ± 0.40*	1.71 ± 1.39	1.00 ± 0.93*
South-East Asia	1.01 ± 1.21	0.83 ± 1.06	1.36 ± 1.51*	1.30 ± 1.64*	0.40 ± 0.73*	1.49 ± 1.68*	0.68 ± 1.01*
South Asia	0.81 ± 1.43	0.75 ± 1.45	1.52 ± 2.18*	1.23 ± 2.14*	0.41 ± 0.91*	1.69 ± 2.22*	0.82 ± 1.50
Central Asia	0.34 ± 0.39	0.17 ± 0.29*	0.75 ± 0.73*	0.49 ± 0.62*	0.09 ± 0.15*	0.77 ± 0.66*	0.33 ± 0.33
North America	1.59 ± 1.00	0.30 ± 0.30*	0.90 ± 0.60*	0.99 ± 0.77*	0.18 ± 0.21*	0.61 ± 0.43*	0.84 ± 0.67*
Central America	0.50 ± 0.75	0.26 ± 0.69*	0.58 ± 0.98	0.80 ± 1.23*	0.11 ± 0.36*	0.71 ± 1.04*	0.32 ± 0.61*
South America	0.63 ± 0.85	0.24 ± 0.27*	0.87 ± 0.70*	0.81 ± 0.70*	0.13 ± 0.21*	0.92 ± 0.69*	0.34 ± 0.42*
Russia-Belarus-Ukraine	0.77 ± 0.49	0.18 ± 0.23*	0.66 ± 0.49*	0.55 ± 0.45*	0.09 ± 0.13*	0.59 ± 0.44*	0.53 ± 0.41*
Europe	1.03 ± 0.89	0.27 ± 0.35*	1.04 ± 0.80	0.90 ± 0.86*	0.15 ± 0.21*	1.03 ± 0.73	0.99 ± 0.79
North Africa	0.64 ± 0.67	0.18 ± 0.26*	0.72 ± 0.74	0.46 ± 0.60*	0.10 ± 0.20*	0.54 ± 0.68	0.25 ± 0.49*
Sub-Saharan Africa	0.49 ± 0.60	0.44 ± 0.53	0.71 ± 0.75*	0.99 ± 0.98*	0.21 ± 0.34*	0.98 ± 1.15*	0.76 ± 1.02*
Middle East	0.18 ± 0.42	0.11 ± 0.29*	0.38 ± 0.69*	0.21 ± 0.55	0.03 ± 0.09*	0.64 ± 0.82*	0.26 ± 0.42*

[a]Region definitions are based on those established by the Hemispheric Transport of Air Pollutants (HTAP2 Huang et al., 2017).

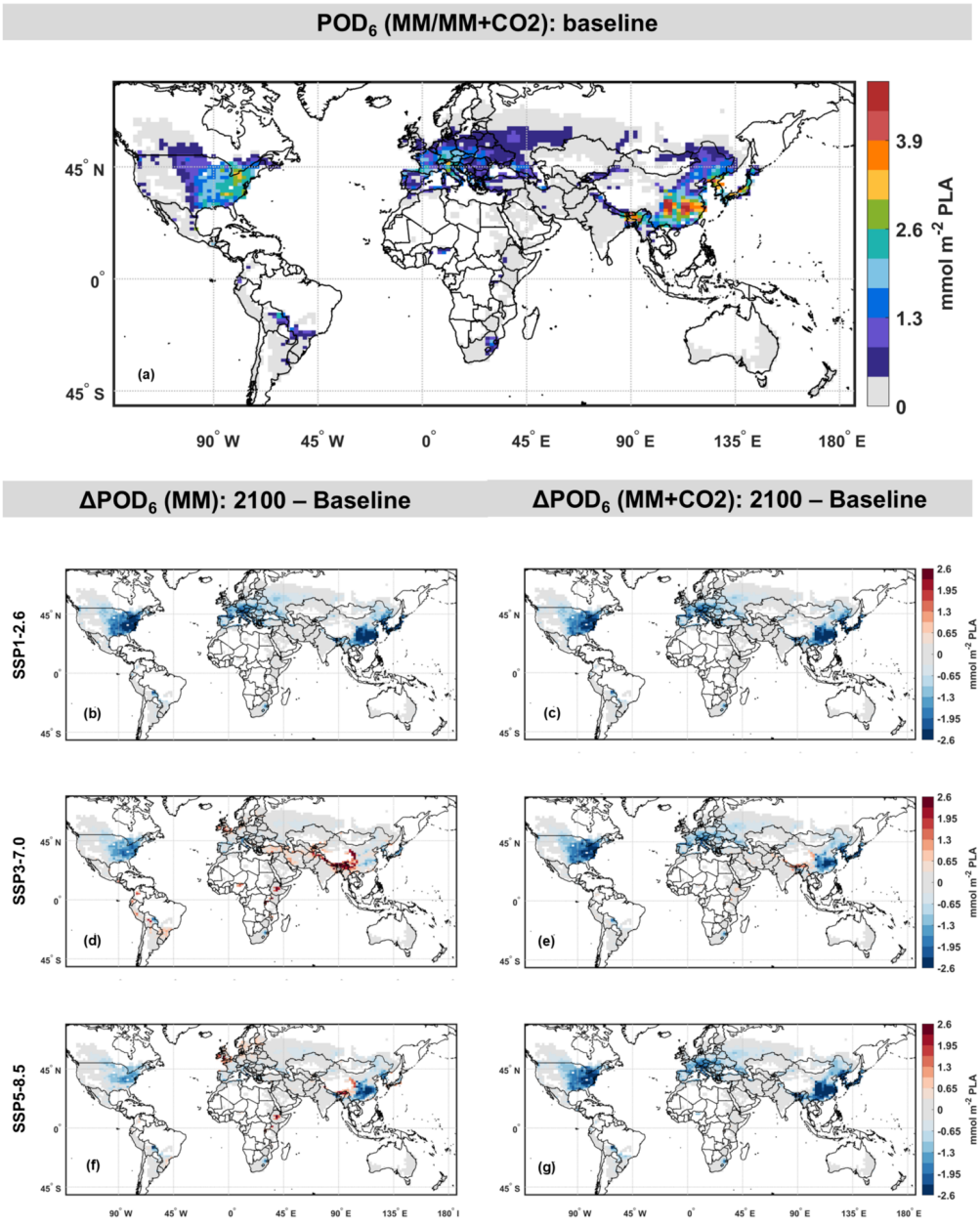

Figure 3.3. Mean POD_6 over the baseline period (a), and ΔPOD_6 at 2100 with respect to the baseline across the different SSPs for the MM run (b,d,f) and the MM+CO_2 run (c,e,g). For the baseline only one map is shown, as the differences between the two runs are barely noticeable. Baseline indicates the mean between 2000 and 2014, and 2100 indicates the mean between 2090–2099. Map lines delineate study areas and do not necessarily depict accepted national boundaries.

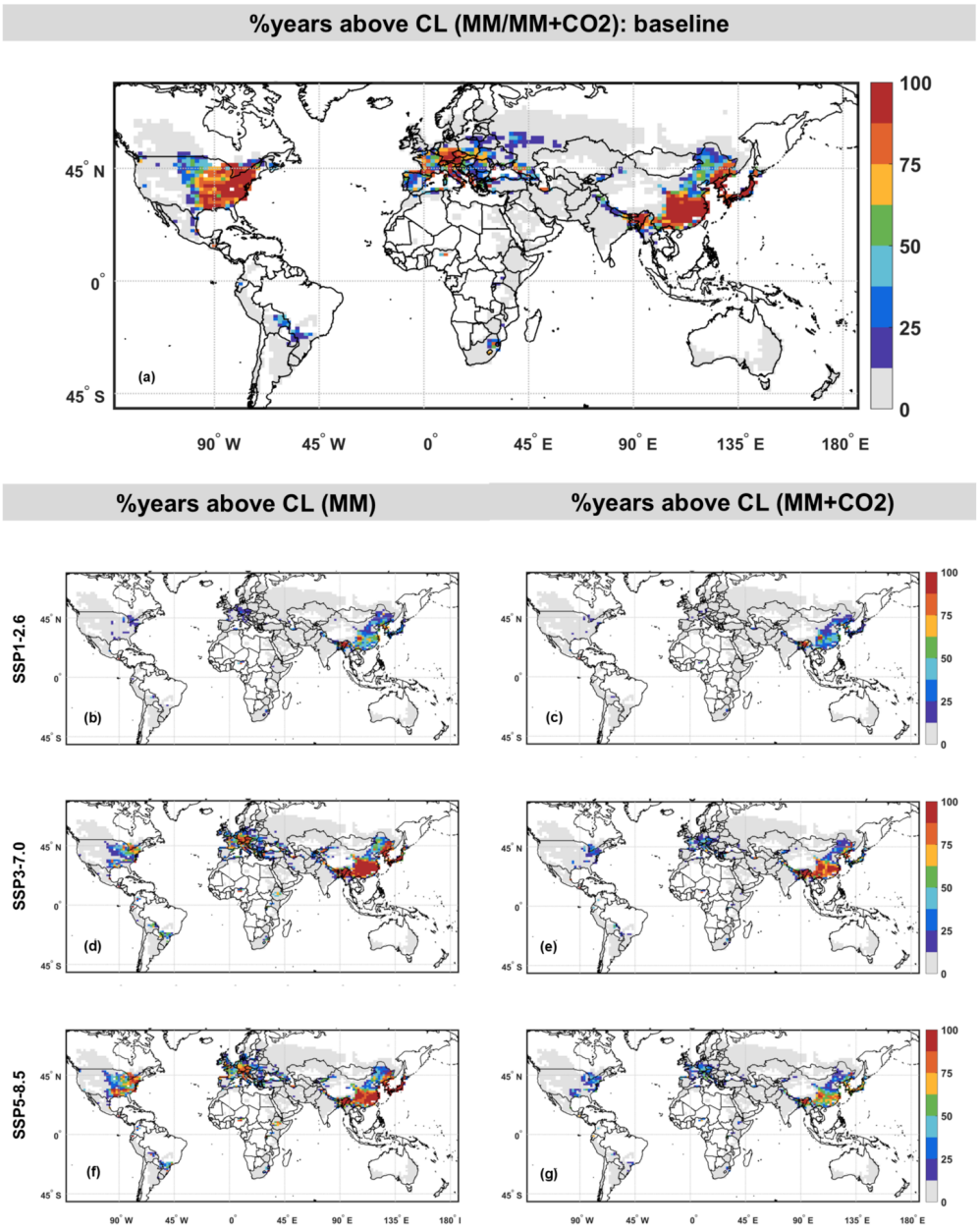

Figure 3.4. Percentage of years exceeding the CL for wheat (1.3 mmol m^{-2}), at the baseline (a) and under different SSPs (b-g), in the MM run (b,d,f) and in the MM+CO_2 run (c,e,g). Reference periods cover the whole experiments: for the baseline 2000–2014, and for the SSPs 2015–2099. Map lines delineate study areas and do not necessarily depict accepted national boundaries.

everywhere also for SSP3-7.0 and SSP5-8.5 in the case of the MM+CO2 run (Figure 3.3e,g), due to the limiting effect on g_s of the increasing CO2 concentrations. On the other hand, changes in the MM run are not as straightforward (Figure 3.3d,f), indicating major spatial discrepancies across regions. In any case, globally, the mean POD_6 at the end of the century exceeds the CL over smaller areas compared to the baseline. In fact, this area amounts to 14.5% (-3.0%) and 10.8% (-5.3%) at the end of the century in the MM run, for SSP3-7.0 and SSP5-8.5, respectively (percentage areas chronically at risk: 9.3% and 5.8%; production losses: 33.3 and 23.4 $\mathrm{Tg\,yr^{-1}}$). For the MM+CO2 run, these areas are even smaller (percentage domain above CL on average: 3.5% and 0.3%; percentage areas chronically at risk: 2.0% and 0.3%; production losses: 12.3 and 3.5 $\mathrm{Tg\,yr^{-1}}$). Since this run predicts a general decrease almost everywhere, no region-by-region investigation is needed.

For the MM run, the three regions with the highest POD_6 values at the baseline (East Asia, North America, Europe) follow different trends and dynamics in the remaining part of the century. In East Asia, POD_6 changes are more complex under SSP3-7.0 and SSP5-8.5, as they appear to be negative or fairly constant in the eastern part of the region (Eastern China, Korea, Japan), but positive closer to the Tibetan plateau (Yunnan, Sichuan and Gansu provinces of China). Regardless of these end-of-century decreases, some areas of chronic risk persist across the century under every SSP. Eastern North America is the only region with an evident decrease in O_3 risk under any scenario, which is due to the decreasing O_3 concentrations (Figure 3.1b) in a fairly constant f_{clim} (Figure 3.1f). This is also reflected in the shrinking of the areas chronically at risk across all scenarios (Figure 3.4d,f). In Europe, O_3 risk hotspots shift from Southern to Northern Europe, following less limiting temperatures for stomatal O_3 uptake at high latitudes (Figure S2c,d), and a slightly more limiting soil water availability to wheat in the southern part of the region (Figure S2k,l). Future chronic risk appears to persist mostly over Central Europe. The MM run identifies

the largest increased risk in the southern and eastern edges of the Tibetan plateau (from Kashmir to the Gansu province) by the end of the century, an area that is included within South, South-East and East Asia, in the present region classification (Huang et al., 2017). Within this region, Nepal, Bhutan, and East India reach the mean POD_6 peak value of $8.6\,\mathrm{mmol\,m^{-2}}$ PLA for SSP3-7.0 and $6.6\,\mathrm{mmol\,m^{-2}}$ PLA for SSP5-8.5 at 2100. This area is chronically at O_3 risk under any scenario, not only for the MM run, but also for the MM+CO2 run. Other areas with increased O_3 risk are also present within Sub-Saharan Africa, Central and South America, especially under scenario SSP3-7.0.

Using Eq. 3.5, the POD_6 in Figure 3.3 can be converted to RYL. In this regard, the highest RYL values achieved across the region can be defined as the 95th percentile over the areas at risk. Based on the POD_6 values calculated in the MM run, the highest RYL values over East Asia are around 17.2% at the present time (mean RYL: 6.4%), with no relevant changes at the end of the century under SSP3-7.0 (95th perc.: 16.7%; mean: 6.6%). Under SSP5-8.5 and SSP1-2.6 these peak values decrease to 10.5% and 4.6% (mean: 3.9% and 1.4%) respectively, by the end of the century. In South Asia, the present-day highest RYL values are above 15.7% (mean: 3.1%), and increase to become the highest worldwide under SSP3-7.0 (95th perc.: 25.3%; mean: 6.5%). Under SSP5-8.5, the increase in RYL is small (95th perc.: 17.1%; mean: 3.2%), while under SSP1-2.6 the highest RYL values considerably decrease to around 9.6%. Nonetheless, this value is the highest across the globe for this scenario and well above the CL for wheat. In Europe, the highest RYL values are estimated to be around 9.4–10.3% (mean: 3.8–4.0%), at the beginning and at the end of the century under SSP3-7.0 and SSP5-8.5. On the other hand, under SSP1-2.6, the 95th percentile of RYL is substantially lower (2.3%). In North America, the highest RYL values at the baseline are 13.1% (mean: 6.1%), and decrease under every scenario, although some areas still experience relevant damage under SSP3-7.0 and SSP5-8.5

(95th perc.: 5.4% and 8.1%; mean: 2.3% and 3.2%). From the present day to the end of the century, the highest RYL values in South-East Asia increase from 12.9% to 18.7% under SSP3-7.0 (mean: from 3.9% to 5.7%), in Sub-Saharan Africa from 6.4% to 12.2% and 11.8% under SSP3-7.0 and SSP5-8.5 (mean: from 1.9% to 3.8% and 2.9%), and in Central America from 7.7% to 12.1% under SSP3-7.0 (mean: from 1.9% to 2.7%).

Figure S3f shows the POD_6 over the baseline calculated with the GFDL-ESM4, for the MM+CO2 run. As expected, given that the O_3 concentrations are largely underestimated in the upper percentiles, the POD_6 values are much lower compared to the UKESM1-0-LL results. For this ESM, only few areas appear to have a relevant O_3 damage, but it should be noted that they correspond to the three regions that were also highlighted in the UKESM1-0-LL case (Eastern North America, Europe, East Asia).

Figure S4 shows the differences between POD_6 calculated with the FC runs and POD_6 calculated with the rainfed runs. Differences in POD_6 are reported for the baseline and for the end of the century and across SSPs. As expected, baseline differences between the FC runs and the rainfed runs vary spatially, mostly in line with soil water availability limitations to wheat (Figure S3i). For future times, when the CO2 effect on g_s is excluded, the spatial pattern of the differences remains similar to the baseline, although with different magnitudes (Figure S4, left column). In this case, the areas at O_3 risk expand by +65.1%, with the average POD_6 increasing by $+0.53\,\mathrm{mmol\,m^{-2}}$. On the other hand, when the CO2 effect is included, the process is largely dominated by the limiting effects of rising CO2, and the differences between FC and rainfed runs become minimal (Figure S4, right column). In the MM_FC run, South-East Asia is the region with the largest increase in POD_6 over O_3 risk areas under all SSPs, relative to the MM run. This is true at both mid- and end-century, with differences reaching up to $2.4\,\mathrm{mmol\,m^{-2}}$ under SSP3-7.0 and SSP5-8.5 at 2050.

Sub-Saharan Africa and Central America O_3 risk areas expand more than twice, with differences as large as $1.15\,\mathrm{mmol\,m^{-2}}$. In Sub-Saharan Africa, the largest differences are located in the region between Kenya and Tanzania, and, unlike the MM run, the average POD_6 value across O_3 risk areas exceeds the CL at the baseline, for all SSPs at 2050, and for SSP3-7.0 at 2100. In South Asia, the most pronounced differences occur mostly in the first half of the century, with a +59% expansion of the O_3 risk areas. In Europe, the largest differences in POD_6 values between the MM_FC and MM runs are located in the southern part of the region, with increases of $+0.50 \pm 0.17\,\mathrm{mmol\,m^{-2}}$ across scenarios.

3.3.4 Drivers of POD_6 changes

Here we perform a two-way ANOVA (see details in Appendix B.6) on the MM run results to assess which factor among EP, RF, and their interaction (I) has the most significant influence on POD_6 changes at the end of the century around the globe. The specific levels of EP and RF associated with each SSP are described in Table B.4. Figure 3.5a shows for each grid node the factor with the most certain effect (i.e., the lowest p-value among the ones smaller than 0.05) as identified by the two-way ANOVA, while Figure 3.5b–d display the total variance explained by each factor (R^2), allowing further quantification of their contributions to POD_6 changes. P-value maps for each factor considered in the ANOVA are shown in Figure S6.

The ANOVA reveals different geographical patterns where the POD_6 changes are mostly driven by the same factor. For example, in East China the decrease of POD_6 under SSP1-2.6 and SSP5-8.5 (Figure 3.2; Figure 3.3; Table 3.3) most certainly depends on EP. Similarly, in South America POD_6 changes are controlled by EP. In the eastern U.S. and in Japan, the large decrease in POD_6 under all SSPs (Figure 3.3) is controlled by the interaction between EP and RF. In Russia-Belarus-Ukraine and in Northern Europe (latitudes $> 45°$), changes in POD_6 are clearly driven by RF,

and this is mostly due to the increasing temperatures lifting the f_{temp} limitations at higher latitudes in future times (Figure S3). These findings suggest that in regions where RF is the dominant driver, POD_6 may increase even under strong EP. In regions where POD_6 decreases, the ANOVA identifies the factors that are mainly responsible for this decrease, such as in East China, Eastern U.S., and Japan. In contrast, where POD_6 increases, the ANOVA indicates which policies could be more effective to mitigate O_3 risk for crops. For instance, in Northern Europe, where RF is responsible for the POD_6 increase, the adoption of stricter reduction policies on greenhouse gas emissions at a global level, rather than only the adoption of local EP, would lead to a reduction of O_3 risk for crops as a climate co-benefit.

At the global scale, we identify the variables most closely associated with relevant POD_6 changes, depending on the considered SSP. Table S5shows the mean 2000–2014 values of several variables (O_3 concentration, f_{clim}, f_{temp}, f_{VPD}, f_{soil}, and duration of the accumulation period) over the areas where a factor was identified by the ANOVA (i.e., the areas marked as EP, RF, or I, but not as U). The table also shows the mean changes ($\pm$SD) in these variables across the nodes and years with large POD_6 changes (i.e., below -0.65 $\text{mmol}\,\text{m}^{-2}$ or above +0.65 $\text{mmol}\,\text{m}^{-2}$) for each SSP.

The larger negative changes in POD_6 are found under SSP1-2.6 and are mainly due to a strong decrease in O_3 concentrations (-10.2 $\pm$ 4.6 ppb). Under SSP3-7.0 and SSP5-8.5, POD_6 reductions are instead mainly associated with a decrease in f_{clim} (-0.08 $\pm$ 0.15 and -0.07 $\pm$ 0.18, respectively). In particular, this decrease is largest in the VPD component under these two scenarios (-0.06 $\pm$ 0.11 and -0.11 $\pm$ 0.14). On the other hand, large increases in POD_6 rarely occur under SSP1-2.6 (0.1% of all the considered nodes) and seem to be driven by a marked increase in f_{clim} (+0.25 $\pm$ 0.13). For SSP3-7.0 and SSP5-8.5, the increases in POD_6 result from a combination of rising O_3 concentrations (7.6 $\pm$ 7.1 ppb and 3.3 $\pm$ 5.4 ppb) and f_{clim} values (0.19 $\pm$ 0.13 and 0.25 $\pm$ 0.14). In these scenarios, the largest contribution to f_{clim} is from

reduced temperature limitations, with f_{temp} increasing by 0.16 ± 0.15 and 0.25 ± 0.18 for SSP3-7.0 and SSP5-8.5, respectively.

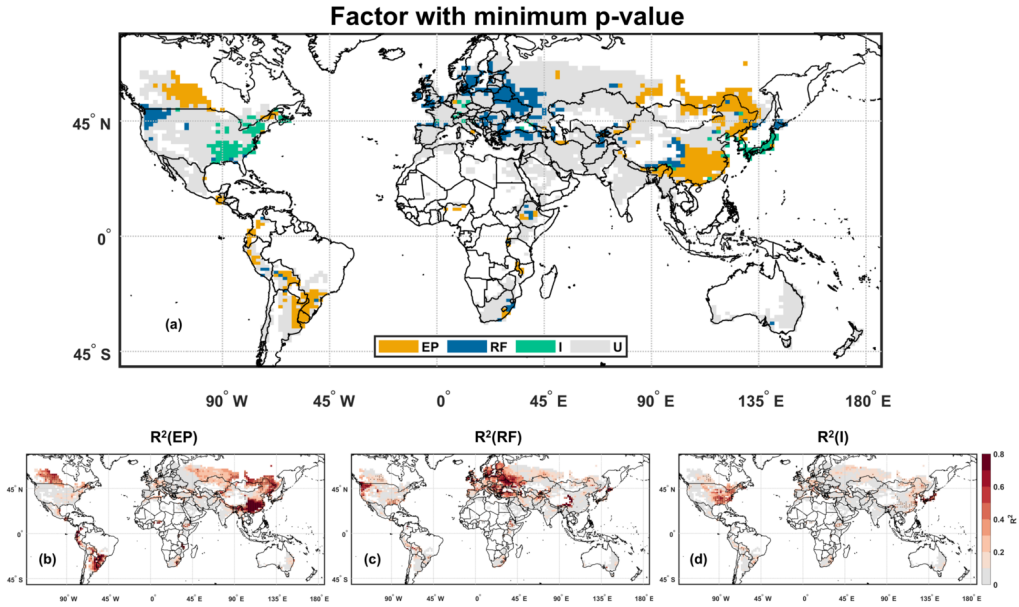

Figure 3.5. Map of the factors with the most certain (minimum p-value, among factors with $p < 0.05$, corrected with Bonferroni) impact on POD_6 changes at the end of the century, identified by the two-way ANOVA (a). Explained variance R^2 associated with each factor in each node, with black dots indicating $p < 0.05$ (b-d). EP = Emission Policy, RF = Radiative Forcing, I = Interaction, U = Uncertain (i.e. $p > 0.05$ for all factors). Map lines delineate study areas and do not necessarily depict accepted national boundaries. See Figure S6 for maps of the p-values for each factor included in the ANOVA.

3.4 Discussion

3.4.1 Future O_3 risk for wheat and implications for food security

This study shows how future O_3 levels and climatic conditions may impact wheat production across different areas of the globe and highlights how varying assumptions can lead to contrasting results in terms of risk estimates. The MM run follows the common approach for O_3 risk assessment and, while being considered suitable for the present time, it does not account for the limiting effect that increasing atmospheric CO_2 may exert on g_s. Conversely, the MM+CO_2 run, which includes CO_2-induced stomatal limitations, projects substantial decreases in future POD_6 values. However, even when considering the CO_2-driven decrease in POD_6 values at the end of the century, there are parts of the globe that remain chronically at risk throughout the century. The FC runs (MM_FC and MM+CO2_FC) provide *stricto sensu* an estimate of the maximum potential damage under no limitation to soil water availability to the plants. These runs could also be interpreted as representing the O_3 risk under optimal irrigation, and could better represent the damage over arid areas, which rely on irrigation for wheat cultivation.

Our results can provide insights into potential consequences for global food security in the broader context of the SSPs. Under SSP1-2.6, a consistent and very certain decline in O_3 risk is observed across all regions and model configurations. This decrease is mostly driven by global reductions in O_3 concentrations, implying minimal impacts on wheat productivity at the end of the century. In fact, the annual global production losses under this scenario range from 3.9–11.5 $\mathrm{Tg\,yr^{-1}}$ (depending on the run considered), which corresponds to 0.5–1.4% of the total wheat production, while during the baseline production losses are in the range of 26.6–40.1 $\mathrm{Tg\,yr^{-1}}$ (3.3–5.0%). Reduced production losses would promote food sovereignty, thus easing climate adaptation challenges.

In contrast, under SSP3-7.0, O_3 risk persists throughout the century, increasing in several world regions such as Asia, South America, and Sub-Saharan Africa, although some of the projected damage may be mitigated by the CO_2 limiting effect on g_s (annual global production losses: 12.3–44.8 $\mathrm{Tg\,yr^{-1}}$, 1.3–4.9%). In this scenario, O_3 risk is driven not only by increased precursor emissions, but also by climate-induced enhancement of O_3 uptake, indicating that precursor controls alone may be insufficient to reduce significantly O_3 damage, especially over regions where POD_6 changes are controlled by RF (Section 3.3.4). Moreover, given SSP3's assumptions of restricted international cooperation and trade, the resulting food security threats would be further exacerbated.

SSP5-8.5 represents an intermediate case: O_3 risk increases until around 2050 in many regions (up to 19.7–44.0 $\mathrm{Tg\,yr^{-1}}$, 2.2–5.0%) and then declines to baseline or lower values by the end of the century (3.5–30.9, 0.5–2.6%). This trend reflects the implementation of mid-century air quality policies explicitly assumed by this scenario (Kriegler et al., 2017). The POD_6 increase is mainly driven by climate forcing, but the extremely high CO_2 levels at the end of the century under this scenario may likely alleviate O_3 damage globally via stomatal limitation. In addition, this scenario envisions strong technological advancement, potentially enabling effective adaptations to emerging food security risks.

O_3 risk hotspots should also be discussed, alongside policies that could potentially reduce the risk in these regions. The Southern and Eastern edges of the Tibetan Plateau (i.e., parts of East and South Asia) show consistent O_3 risk through the century, even when the CO_2 limiting effect on g_s is considered. Here, POD_6 values will remain high even under the MM+CO_2 run, indicating that this region will likely represent a persistent O_3 hotspot throughout the 21st century. This vulnerability may result from the combined effects of stratospheric O_3 transport across this region (Yin et al., 2023) and less limitations to g_s in future climate (Figure 3.1). In this

area, mitigation of O_3 risk would likely require joint reductions in both O_3 precursors and greenhouse gas emissions.

More broadly, South Asia also emerges as a critical region, not only near the Tibetan Plateau, but also across other parts of the region that have a widespread need for irrigation (Brauman et al., 2013; Chiarelli et al., 2020). Over this area, O_3 risk is observed in the FC runs, which might provide a better estimate of POD_6 changes. Given the agricultural importance of the Indian peninsula and the Tibetan Plateau for global wheat production (Monfreda et al., 2008), these regions should be considered at the highest O_3 risk across the 21st century. East Asia is also identified as a high-risk area in the MM run. POD_6 values are projected to decrease under SSP1-2.6 and SSP5-8.5, but not under SSP3-7.0, indicating the effectiveness of O_3 precursor control policies. In fact, under SSP3-7.0, POD_6 values increase substantially, although this projection might be exaggerated, as O_3 precursor emissions in China have already decreased significantly since 2014 (Van Der A et al., 2017).

Beyond these primary risk regions, increases in POD_6, particularly in Central America, South America, and Sub-Saharan Africa, are relatively large compared to the baseline and could grow larger under the FC assumptions (Figure S4). This is particularly concerning for Sub-Saharan Africa, where high population growth and developmental challenges are expected throughout the 21st century (Kc and Lutz, 2017; United Nations Department of Economic and Social Affairs, Population Division, 2022). Nevertheless, our results suggest that strong precursor emission controls could have a key role in reducing O_3 risk in this region. On the other hand, Eastern U.S., which is currently among the most critical regions for wheat O_3 damage, is projected to experience a reduction in POD_6 values under all SSPs, likely due to combined controls on both O_3 precursors and greenhouse gas emissions. In Northern Europe instead, O_3 risk appears to be primarily driven by climate change, suggesting that global efforts in mitigating greenhouse gas emissions may be the viable strategy

to reduce O_3 impacts in the region.

3.4.2 Uncertainty sources in O_3 risk projections

One of the main sources of uncertainty in this study concerns the extent to which rising atmospheric CO_2 concentrations reduce g_s in wheat. Current knowledge on this effect remains limited and uncertain, as experimental data show high variability due to methodological differences (e.g., presence or absence of acclimatization to elevated CO_2 during plant growth), species-specific physiological traits, and diverse environmental conditions during the experiments. Furthermore, unavoidable uncertainties arise from possible future developments in crop breeding, such as, for instance, plant breeding selection for new varieties with higher g_s to enhance photosynthesis, or the emergence of epigenetic responses to prolonged high-CO_2 exposure. These factors make it difficult to accurately predict the magnitude of g_s reductions and their implications for future POD_6 estimates.

A second source of uncertainty relates to the phenological-stage modelling of wheat. Our simulations adopt the accumulated thermal time to determine the beginning and end of the POD accumulation period, following the approach prescribed by the MM (LRTAP Convention, 2017). As shown in Appendix B.5, this method produces globally reasonable estimates of crop maturity dates (Figure B.3). However, regional discrepancies can arise (Figure B.4), introducing additional uncertainty into the POD_6 estimations at the local scale.

Another important source of uncertainty arises from the feedback between O_3 damage and vegetation physiology, which is not accounted for in this study. Specifically, O_3-induced damage may reduce stomatal O_3 uptake by vegetation, thereby increasing atmospheric O_3 concentrations and reinforcing O_3 uptake in other regions, while also influencing local climate conditions (Emberson et al., 2013). The Earth System Models from CMIP6 considered in this study do not include vegetation-O_3

feedbacks, and as a result, may underestimate these dynamics. Capturing this mechanism would require re-running the ESM simulations with an explicit representation of O_3 effects on vegetation. This approach would enable jointly accounting for this specific feedback and for all the other processes that influence O_3 dynamics in the atmosphere (photochemistry), which are already included in CMIP6 models with coupled-chemistry schemes (including GFDL-ESM4 and UKESM1-0-LL).

Our analysis suggests that the uncertainty in the input ESM variables has a modest impact on the results of this study (Appendix B.2). The coarser spatio-temporal resolution from the CMIP6 models can lead to underestimation of O_3 flux peaks (Guaita et al., 2023) and to misrepresentations of local meteorological features influenced by topography and land cover. Furthermore, all CMIP6 models were found to overestimate mean surface O_3 concentrations in the 2005–2014 period when compared to observations, with biases reaching up to 16 ppb in some regions (Turnock et al., 2020). However, O_3 concentrations are known to be lower near the ground surface (Gerosa et al., 2017), while the vertical resolution of CMIP6 models places the first atmospheric layer at 14–20 m above ground. As a consequence, the O_3 concentration absolute bias (Appendix B.2) is much smaller when modelled O_3 concentrations are scaled to measurement height. This evaluation also shows that peak O_3 values are simulated accurately for UKESM1-0-LL after scaling. The effect of the input variables (meteorology and O_3 concentrations) on the final POD_6 estimate is calculated for UKESM1-0-LL (Eq. B.4), and our results show that the uncertainty propagates to the POD_6 estimates mostly through the variability component only, rather than through the bias.

3.4.3 Comparison with previous O_3 risk assessments for wheat

Previous studies, although based on different modelling approaches and typically limited to present-day conditions, generally show good agreement with our findings

in terms of spatial patterns and hotspots of O_3 damage (Lombardozzi et al., 2015; Schauberger et al., 2019; Sitch et al., 2007; Tai et al., 2021). Specifically, these studies identified the eastern U.S., Europe, and East Asia as critical regions for O_3-related crop damage, showing substantial spatial agreement with our results.

Mills et al. (2018) provided a global-scale estimate of O_3 risk for wheat using the POD_3IAM metric for the years 2010–2012, within a modelling framework similar to ours. They also identified the same major hotspots but reported higher relative yield losses and production impacts. Specifically, their study estimated average global production losses of approximately $85.0\,\mathrm{Tg\,yr^{-1}}$, whereas our baseline period estimates are considerably lower (28.7–39.9 $\mathrm{Tg\,yr^{-1}}$). This discrepancy is unlikely to result from differences in model input data or parameterizations, but rather from the different O_3 risk metric employed in their study. In fact, POD_6 has a higher O_3 detoxification threshold, such that null yield losses may occur even when the corresponding POD_3IAM values are greater than zero. Consequently, the RYL calculated via POD_6 could be zero, even when the RYL calculated via POD_3IAM is not, and the production losses calculated with POD_3IAM are expected to be systematically higher, especially in regions where O_3 stomatal fluxes consistently remain lower than 6 but above 3 nmol O_3 m^{-2} s^{-1}.

Some differences emerge when comparing our findings to regional assessments of present-day O_3 impacts on wheat. For example, POD_6 was estimated to reach values up to 8.5 mmol m^{-2} in the Iberian Peninsula (De Andrés et al., 2012), while our results indicate some potential threats without reaching such extreme POD_6 values. On the other hand, our findings are consistent with recent estimates of POD_3IAM in Sub-Saharan Africa under the FC assumption (Sharps et al., 2021), and with studies identifying O_3-affected areas in China (Cao et al., 2024; Wang et al., 2023, 2022).

Li et al. (2025b) calculated O_3-related production losses to wheat over China for both present (2015–2019) and future times (2056–2060, under SSP1-2.6, SSP3-7.0,

and SSP5-8.5), using the Jarvis model to calculate POD12 at a 36 × 36 km resolution. Consistently with other regional-scale studies, they reported much larger present-day O_3 impacts compared to our results (production losses amounting to 26 $Tg\,yr^{-1}$, versus ours 9.9–11.1 $Tg\,yr^{-1}$). As their modelling framework is akin to ours, the different magnitude most likely stems from the much finer spatial resolution used in their study and, possibly, from the different input data, g_s parameterizations, and detoxification threshold for POD (Y=12). Similarly to us, they concluded that, under SSP1-2.6, O_3 damage significantly decreases at future times and identified reductions in O_3 precursor emissions as the main driver of this trend. Furthermore, they found relevant O_3 damage increases under SSP3-7.0. This result is consistent with our MM run, but not with the MM+CO_2 run. As Li et al. (2025b) did not include any CO_2-induced reduction on g_s, this discrepancy is an indication that accounting for CO_2 limitations to g_s constitutes a key feature for estimating O_3 risk at future times.

Few studies have estimated O_3 effects on wheat under future climate change scenarios while explicitly accounting for the CO_2-induced limitation of g_s. One of the most recent examples is provided by Zhou et al. (2024), who used the ModelE2-YIBs model to simulate the effects of O_3 on gross primary productivity (GPP) in 2010 and 2060 under SSP1-2.6 and SSP5-8.5. Despite some minor regional differences, particularly in Western Africa and South America likely due to their broader focus on vegetation rather than wheat, their spatial patterns of O_3 risk closely resemble ours. However, the relatively coarse spatial resolution used in their study (2° × 2.5°) may limit the ability to resolve finer-scale risk patterns captured in our simulations.

Klingberg et al. (2011) also explored future POD changes at 10 European sites, accounting for the effect of rising CO_2 on stomatal O_3 uptake. Their findings, like ours, showed that even under pessimistic greenhouse gas scenarios, future stomatal uptake of O_3 would remain constant or decrease due to CO_2-induced reductions in g_s. Similarly to our approach, they implemented an explicit CO_2-limiting function

(f_{CO_2}) that linearly reduced g_s by 34% between 360 and 560 ppm, with no further decrease beyond this range. While this assumption is biologically reasonable within that interval, a linear extrapolation beyond 560 ppm could yield implausibly low g_s values, potentially approaching zero at very high CO_2 levels. In our case, the f_{CO_2} function is more conservative: we estimate an 18% reduction in g_s between 360 and 560 ppm, with the function extending to higher CO_2 concentrations while avoiding biologically unrealistic values. Under SSP5-8.5, for instance, f_{CO_2} implies a total g_s reduction of 47.2% from 360 ppm to the end-century CO_2 level of 1067 ppm. Zhou et al. (2024) also accounted for the CO_2 effect, though implicitly, through the use of a Ball–Berry-type stomatal conductance model that links g_s to net photosynthesis. While our approach is more explicitly formulated, the parameterization of f_{CO_2} we apply is derived from Ball–Berry–Farquhar simulations, and thus we would not expect major discrepancies in the CO_2-limiting effect between our work and theirs.

3.5 Conclusions

This study quantified the global and regional evolution of O_3 risk to wheat under three SSPs up to 2100 and explored alternative assumptions about the CO_2 limiting effect on g_s and about water availability to the plant. Our results indicate that, at the global scale, O_3 risk is expected to decline by the end of the century, although transient risks may persist in the near future. Even without any assumed CO_2–g_s interaction, the O_3 damage is generally projected to decrease. However, there may be persistent O_3 damage hotspots across several regions, with the extent and intensity of the risk strongly depending on the scenario considered. When the effect of elevated CO_2 on g_s is considered, the O_3 risk is projected to decline to near-zero values across most regions under all SSPs.

Nevertheless, substantial uncertainties remain regarding the limiting effect of elevated CO_2 concentrations on g_s. Moreover, the present modelling framework does

not account for any vegetation feedback to O_3 concentrations and climate. For these reasons, the large projected decrease in POD_6 under CO_2-limiting scenarios may be exaggerated, and a more realistic future O_3 risk probably lies between the outcomes of simulations with and without the CO_2 effect. Consequently, future studies on O_3 risk assessments should aim to reduce these uncertainties. Research efforts should focus on experimental assessments and validation of the physiological interaction between elevated CO_2 and O_3 uptake under field conditions, and their combined effects on stomatal conductance and carbon assimilation.

CHAPTER 4

THE GROWING SEASONS OF GLOBAL FOREST ECOSYSTEMS FROM 1850 TO 2100 ESTIMATED WITH A PROBABILISTIC TEMPERATURE-BASED MODEL

This chapter is a reproduction, with slight modifications, of the journal article *The growing seasons of global forest ecosystems from 1850 to 2100 estimated with a probabilistic temperature-based model* by P. R. Guaita, G. Gerosa, and R. Marzuoli, currently submitted to Biogeosciences.

4.1 Introduction

Vegetation seasonal cycles are a fundamental component of the interactions between ecosystems and environment and are essential in regulating Earth's climate system (Bonan, 2016). At a biogeophysical level, vegetation growing phases and the intensity of its biological activity can affect surface albedo, roughness length and evapotranspiration, altering local water budget and surface energy balance (Miralles et al., 2025). At biogeochemical level, plants are central to the global carbon cycle, influencing planetary radiative balance (Stuart Chapin III et al., 2009), to the cycling of other key nutrients, such as nitrogen and phosphorous (Fowler et al., 2013; Buendía et al., 2010) and to the exchange of reactive trace gases; specifically, vegetation represents a critical sink for tropospheric ozone and modulates atmospheric oxidative capacity (Emberson, 2020). Conversely, environmental variables such as air temperature, radiation, and water availability, interact with plant physiological

controls (e.g. genetics, hormones, metabolism) to constrain vegetation growth at species-specific level (Chapin et al., 2011).

Understanding and accurately predicting the growing season (GS), i.e. the period of plant biological activity, is therefore essential for projecting future ecosystem-climate feedbacks under future global changes. Körner et al. (2023) recently proposed four definitions for GS, each capturing specific biological processes and vegetation-environment interactions: the GS sensu stricto, the phenological season, the productive season, and the meteorological season. Each definition offers unique insights with its own advantages and drawbacks, but their practical applicability largely depends on which aspect are covered when referring to the term GS. The GS sensu stricto refers to actual tissue growth. However, these processes are difficult to measure, as they do not necessarily correspond to more visible developmental stages. On the other hand, the phenological season is defined by visible markers such as leaf flushing (green-up) and senescence (green-down). These markers are more readily monitored via phenological observations and remote sensing, but they do not necessarily reflect actual biomass accumulation and growth. The productive season relies on productivity metrics like net biomass increase, net primary production (NPP) or net ecosystem exchange (NEE). While NEE can be measured via eddy covariance measurements of CO2 fluxes, net biomass increase has no clear-cut seasonal definition, and NPP (canopy photosynthesis minus autotrophic respiration) remains difficult to measure in real-world ecosystems. The meteorological season relies on environmental thresholds (typically air temperature or soil water availability to the plant) to determine the GS, following the notion that long-term climate dynamics induce evolutionary pressure on plants, broadly determining their physiological mechanisms. However, growth and developmental stages could be modified or halted by adverse meteorological events, and the meteorological season, in principle, cannot account for such occurrences. As such, the meteorological season strictly represents

the climatic conditions for potential vegetation activity.

It is apparent that the meteorological and the phenological definitions of GS are more practical than the others, despite their respective caveats. The meteorological season is frequently used to estimate the GS, due to its robustness in describing long-term shifts in developmental stages and biological activity (Mo et al., 2023). The phenological season is particularly effective for calibration and validation of ecosystem and climate models, because it is based on direct observations of phenological markers (e.g., Hufkens et al., 2018; Zheng et al., 2022). Satellite-based remote sensing has become increasingly important in this regard in the last decades, offering global coverage, scalability of the results and broad applicability (e.g., Zhang et al., 2003b; Friedl et al., 2010; Melaas et al., 2013; Claverie et al., 2018). These tools detect phenological events by analyzing reflectance properties of vegetation; in fact, active plants tend to absorb a significant amount of red light (620-670 nm) and reflect near-infrared light (750-900 nm) due to leaf structure and chlorophyll content. These spectral properties are synthesized into indexes such as the Normalized Difference Vegetation Index (NDVI) to determine key phenological dates.

While process-based models can predict phenological stages by simulating plant physiological responses to environmental conditions, they are often more computationally intensive than their statistical counterpart and require detailed parameterization, with uncertainties that are difficult to quantify (Chuine et al., 2013; Meier and Bigler, 2023; Garnot et al., 2025). Alternatively, several studies frequently linked meteorological data to phenological observations to estimate GS using empirical models and often validating model outputs against ground-based phenological records or satellite-derived indices (Mo et al., 2023). However, these models are often limited to specific geographical regions, or to individual vegetation species (e.g., Linderholm et al., 2008; Blümel and Chmielewski, 2012). The primary task of this study is to determine the Start and End of the Growing Season (SGS and EGS) for generic forest

ecosystems at a global scale, using a novel probabilistic, temperature-based model (GS-P) developed within a machine-learning framework. To assess the model's performance and robustness, we conduct a comparative analysis against established deterministic models and a latitudinal benchmark (GS-Lat), using ERA5 reanalysis and MODIS remote-sensing data for calibration and validation. The ultimate outcome is the creation of an open-source dataset that reconstructs, with quantified uncertainty, the trajectories of SGS and EGS from 1850 to 2100 under different climate change scenarios.

Several reasons motivate this effort. First, such product can provide continuous and consistent phenological estimates for forest ecosystems, allowing to infer changes in phenological transitions during the considered two and a half centuries. This product is also essential for reducing uncertainties in terrestrial carbon cycle models and for supporting adaptive forest management strategies in a changing climate. Second, we seek to improve the capability of phenological modelling in predicting the SGS and EGS, and to assess the potential advantages of machine-learning approaches over more traditional methods. Namely, we aim to overcome previous limitation in spatial extent, species specificity, and extrapolation skills under climate change scenarios, by providing a robust, generalizable framework for prediction of phenological stages. Third, using temperature as the sole predictor allows us to clarify its role as a driver of phenological transitions at global scale. In this context, quantification of model uncertainty is not simply a measure of performance quality, but highlights where additional mechanisms (e.g., precipitation seasonality) are likely to dominate, and where future climatic transitions may influence forest phenology and, more broadly, forest ecosystem functioning.

4.2 Data and methods

The study is performed using GS-P, a probabilistic temperature-based model (i.e., a boosted decision tree logistic classifier) specifically developed to predict phenological stages of forest ecosystems at a global scale. Two more traditional temperature-based models (GS-Lin2, GS-BC2; Linderholm et al., 2008; Blümel and Chmielewski, 2012) are employed for comparison, and a latitudinal model (GS-Lat, see e.g. Zhang et al., 2004; Simpson et al., 2012) is used for benchmarking.

4.2.1 Data

Calibration of the considered four GS models is performed by linking ERA5 (Hersbach et al., 2020) reanalysis temperature products with products from the remote-sensing MODIS land data suite (MCD12Q1 and MCD12Q2; Friedl et al., 2010; Zhang et al., 2003b). Simulated temperature fields from UKESM1-0-LL (Sellar et al., 2019) are used to predict the growing season in past and future periods.

4.2.1.1 Temperature Data

ERA5 is the fifth generation of atmospheric reanalysis produced by the European Centre for Medium-Range Weather Forecasts under the Copernicus Climate Change Service. By assimilating data from observations satellites, ground stations, and other sources, it provides hourly estimates of atmospheric, land-surface, and ocean-wave variables at a spatial resolution of approximately 31 km globally, spanning from 1950 to the present. For this study, we use the daily 2-meter surface air temperature. UKESM1 is a fully coupled earth system model (ESM) developed by the UK Met Office, which contributes to the Coupled Model Intercomparison Project Phase 6 (CMIP6; Eyring et al., 2016) and provides global climate simulations for both the historical time and under future climate change scenarios at a $1.25^\circ \times 1.875^\circ$ spatial resolution. This study considers the historical experiment (Eyring et al., 2016), which

is designed to simulate climate from 1850 to 2014 using historical forcings. For future times (2015-2100), we primarly consider SSP1-2.6 (Van Vuuren et al., 2017) and SSP5-8.5 (Kriegler et al., 2017), a low- and high-radiative forcing scenario, respectively. Furthermore, the SSP3-7.0 (Fujimori et al., 2017) is also considered: the results from this scenario are not presented in maps and are not discussed in this study (as they are very similar to the ones from SSP5-8.5). However, values related to this scenario may be found in tables, and the associated GS-P estimations for SGS and EGS may be found in the final published dataset. For all experiments, the run variant r1i1p1f2 is used (Tang et al., 2019; Walton et al., 2022; Good et al., 2019a,b).

4.2.1.2 Phenological data

We used the MCD12Q1 and MCD12Q2 products from the MODIS land data suite to retrieve land cover and phenology data for all available years (from 2001 to 2023, at the time of data preprocessing) at a 500-meter resolution. More specifically, the FAO-Land Cover classification system from MCD12Q1 is used to select all areas with more than 60% forest coverage. Over the nodes selected this way, the MCD12Q2 product provides four fields that describe phenology phases: greenup, mid-greenup, mid-greendown, and dormancy. These fields are identified via the 2-band Enhanced Vegetation Index (EVI-2; Mo et al., 2012), similar to the Normalized Difference Vegetation Index, but designed to improve sensitivity to high-biomass regions, reduce aerosols disturbances, and minimize soil background effects. Each phenological field is filtered on the chosen land use and, after being checked for quality assurance/quality control, upscaled at the ERA5 resolution by averaging all MODIS grid nodes within each ERA5 node. For each year, we identified and removed the outliers, i.e., the values whose deviation from the local spatial mean exceeded twice the standard deviation of the MODIS fields of the year considered.

4.2.2 Description of GS models

This study selected GS models that (1) are based mostly on temperature, and that (2) have simple criteria to determine the SGS and EGS. Two models are based on the ones presented by Linderholm et al. (2008), and Blümel and Chmielewski (2012). These models were originally tailored either to specific species, to limited geographical regions, or to reproduce specific phenological stages. In this study, their scope is expanded to include generic forests ecosystems with a global coverage, and for both SGS and EGS. As an updated version of the original GS models, they are hereby named after their creators (GS-Lin2, GS-BC2). Then, the developed probabilistic temperature-based model (GS-P), based on the estimation of the likelihood of having a GS at a given location and time, is described. Finally, a simple latitude model (GS-Lat) that does not include any explicit relationship with temperature is also included for benchmarking purposes.

4.2.2.1 GS-Lin2

Linderholm et al. (2008) employed simple criteria based on warm spells, cold spells and temperature thresholds to determine the start and the end of the meteorological GS across the Greater Baltic Area. Four parameters determine the SGS and the EGS within the GS-Lin2 model. Namely, the SGS is defined as the last day of the first warm spell, i.e. the last day of a series of n_w days with daily temperatures exceeding a temperature threshold of T_w. Similarly, the EGS is defined as the first day of the first cold spell (n_c subsequent days) with daily temperatures below a temperature threshold of T_c. As these criteria are not very restrictive by themselves and could lead to identifying multiple short GSs in the same year, GS-Lin2 is set to prevent SGS from occurring over the Northern (Southern) Hemisphere in Oct-Dec (Apr-Jun), and the EGS occurring in Apr-Jun (Oct-Dec). Furthermore, during a certain year, the SGS is required to start before the EGS in the Northern Hemisphere (NH), while

in the Southern Hemisphere (SH) this requirement is the other way around.

4.2.2.2 GS-BC2

The Blümel and Chmielewski (2012) model was originally formulated to calculate the beginning of apple blossom in Germany, building on the notion that heat accumulation releases ecodormancy in plants, thus acting as forcing. Compared to other models, an additional feature is that the heat accumulation is adjusted for the photoperiod; in this sense, this model is not purely temperature based. This model was selected because it was reported to perform well compared to others, for both deciduous needleleaf forest and mixed forests (Mo et al., 2023).

For GS-BC2, the forcing at a given timestep t ($F_{\mathrm{SGS}}(t)$; °C d) for the SGS is defined as:

$$F_{\mathrm{SGS}}(t) = \sum_{i=t_{1,\mathrm{SGS}}}^{t} \max(0,\, T_i - T_{\mathrm{BF,SGS}})\ \Delta t \left(\frac{L_i}{10}\right)^{a_{\mathrm{SGS}}} \tag{4.1}$$

where $t_{1,\mathrm{SGS}}$ is the start of the accumulation (d), either from 1 January for the Northern Hemisphere (NH) or from 1 July for the Southern Hemisphere (SH); T_i is the daily mean temperature (°C); $T_{\mathrm{BF,SGS}}$ is the base temperature for heat accumulation (°C); Δt is the timestep considered for the summation (here, $\Delta t = 1$ d); L_i is the photoperiod (h), normalized to 10 h; and a_{SGS} is a parameter modulating the effect of the photoperiod. The exceedance of a critical threshold $F_{\mathrm{crit,SGS}}$ by the forcing $F(t)$ determines the timing of the SGS (t_{SGS}). Therefore, this model requires four parameters: $t_{1,\mathrm{SGS}}$, $F_{\mathrm{crit,SGS}}$, $T_{\mathrm{BF,SGS}}$, and a_{SGS}.

The same formulation is applied to the EGS by replacing the maximum in Eq. (1) with a minimum (i.e. cold accumulation) and by introducing EGS-specific parameters ($t_{1,\mathrm{EGS}}$, $F_{\mathrm{crit,EGS}}$, $T_{\mathrm{BF,EGS}}$, and a_{EGS}). In this case, $t_{1,\mathrm{EGS}}$ is counted from 1 July for the NH and from 1 January for the SH. Using a minimum instead of a maximum allows the accumulation of negative values; consequently, $F_{\mathrm{crit,EGS}}$ is negative. As

cold accumulation should have a stronger effect under shorter photoperiods, a_{EGS} is also set to be negative.

4.2.2.3 GS-P

The probabilistic model GS-P estimates the SGS and EGS from temperature dynamics. It relies on the following temperature-based predictors: the 14-day moving average of daily temperature ($T_{14\mathrm{d}}$), the associated regression slope ($\nabla T_{14\mathrm{d}}$) and moving standard deviation ($\sigma_{14\mathrm{d}}$), and the 60-day moving average ($T_{60\mathrm{d}}$). This allows the model to capture not only the influence of current short- and long-term temperature averages on GS timing, but also how stability and warming or cooling trends can signal transitions into and out of the GS.

More formally, the GS-P model is a two-step model. First, a binary classification model uses $T_{14\mathrm{d}}$, $\nabla T_{14\mathrm{d}}$, $\sigma_{14\mathrm{d}}$, and $T_{60\mathrm{d}}$ as inputs to determine the daily likelihood of being in the GS or not (0 = non-GS, 1 = GS). Then, the SGS and the EGS are identified by defining probability thresholds p_{SGS} and p_{EGS} that mark transitions between GS and non-GS. However, transitions defined in this way may in principle occur multiple times within a year and may also happen within a short time frame. For this reason, the GS-P model identifies the SGS and the EGS as the first and the last of the respective transition days. Further details on the GS-P model are provided in Appendix C.1.

4.2.3 Parameters calibration

The MODIS product is used for calibration and validation of the models, thus linking the SGS and EGS inferred from EVI-2 (phenological season) with temperatures (meteorological season) from ERA5. Of the years available for training the GS models (2001–2023), a randomly selected 75% of the observations, together with the complete years 2005, 2010, 2015, and 2020, are used for calibration. The remaining

25%, together with the complete years 2006, 2011, 2016, and 2021, are retained for validation.

GS-Lin2, GS-BC2, and GS-P all rely on temperature-related parameterizations. However, reasonable parameterizations are expected to depend on the climate type of each region of the globe, which broadly determines phenological transition behaviour. For this reason, we define regions based on the Köppen–Geiger (KG) climate classification (Peel et al., 2007) and calibrate a separate set of parameters for each region. The KG classification identifies each climate through three letters: the first indicating the main group, the second precipitation seasonality, and the third temperature seasonality. In this study, the main groups B (dry climate) and E (polar climate) are excluded due to the absence of forests, while group A (tropical climate) is not considered because the meteorological GS for humid tropical forests extends throughout the year. We calibrate the three temperature-based models for each subgroup of the temperate climate (C) and the continental climate (D), accounting only for temperature seasonality. Consequently, the second letter of the KG classification is omitted from the notation (e.g. "C*a" indicates a temperate climate with hot summers regardless of seasonal precipitation). Furthermore, because C*c has very few occurrences globally, it is aggregated with C*b. The criteria used to define each region are listed in Table D.1. Figure D.1 and Fig. D.2 show global maps of KG classes obtained from ERA5 and UKESM1-0-LL temperatures, respectively.

For GS-Lin2 and GS-BC2, the modelled SGS and EGS are evaluated against satellite observations, and parameters are estimated by selecting the parameter combination that yields the lowest error (i.e. that minimizes the loss function). The loss function is based on the root mean squared error (RMSE) of SGS and EGS. However, for some grid nodes and years, temperature-based models fail to predict transitions when temperatures never satisfy the criteria required to identify GS onset or termination. To address this limitation and favour parameterizations that effectively predict

SGS and EGS, the loss function includes a penalty proportional to the fraction of missing predictions. For each KG class, the parameters of GS-Lin2 and GS-BC2 are calibrated using simulated annealing (a probabilistic optimization algorithm for the search of local minima; Delahaye et al., 2019), with 3000 iterations and frequent reannealing (every 50 iterations).

The GS-Lat model, being a linear regression based solely on geographical coordinates, is calibrated globally using ordinary least squares, without stratification by KG class.

In GS-P, the binary classification model consists of an ensemble of decision trees calibrated using the XGBoost algorithm (Chen and Guestrin, 2016). For this component of GS-P, there are no parameters in the usual statistical sense; instead, the classifier behaviour can be interpreted through probability profiles with respect to the input variables $\mathbf{x} = [T_{14\mathrm{d}}, \nabla T_{14\mathrm{d}}, \sigma_{14\mathrm{d}}, T_{60\mathrm{d}}]$ (Fig. D.3). At each grid node, probability thresholds determining GS transitions are inferred by first associating observed SGS and EGS dates from MODIS with the corresponding GS probabilities. Then, for each KG class, node-specific threshold inference is performed using empirical Bayesian estimation under a hierarchical Normal–Normal model with shrinkage (Gelman et al., 2025). This hierarchical model assumes that each node-specific probability threshold is drawn from a population distribution whose parameters (mean μ, between-node variance τ^2, and within-node variance σ^2) are empirically estimated from observations. The node-specific thresholds p_{SGS} and p_{EGS} (posterior means) are estimated as weighted averages of the node-specific sample mean and the global mean, with weights reflecting the relative uncertainty of each node's observations. Further details on parameter calibration are provided in Appendix C.2.

For the GS-Lat model, parameter confidence intervals (CIs) are provided directly by the regression model. For GS-Lin2 and GS-BC2, conventional CIs cannot be derived because the parameters enter the model nonlinearly and inference is per-

formed using a global optimization heuristic (simulated annealing). In such cases, CI estimation would typically require non-parametric methods (e.g. bootstrapping), but these are computationally prohibitive. For the Bayesian estimator hyperparameters and the probability thresholds of GS-P, CIs are estimated using non-parametric bootstrapping over years (resampling entire maps).

4.2.4 Performance evaluation and prediction uncertainty

The evaluation of the models is performed in terms of mean bias (MB), mean absolute error (MAE), and Pearson's correlation (ρ) using the validation dataset, and separately for SGS and EGS. The MB is defined as:

$$\mathrm{MB} = \frac{\sum_{i \in I} \left(\hat{Y}_i - Y_i \right)}{n} \tag{4}$$

where Y_i are the MODIS observations, $\hat{Y}_i$ are the values predicted by the model, and $I = \{1, \ldots, n\}$ is the set of values for which the model predicts SGS and EGS dates. The MAE is defined as:

$$\mathrm{MAE} = \frac{\sum_{i \in I} \left| \hat{Y}_i - Y_i \right|}{n} \tag{5}$$

Pearson's correlation coefficient is defined as:

$$\rho = \frac{\mathrm{Cov}(Y, \hat{Y})}{\sigma_Y \, \sigma_{\hat{Y}}} \tag{6}$$

However, these measures do not account for the number of times $\tilde{n}$ in which the models fail to provide valid predictions. Therefore, MB and MAE are corrected analogously to the loss function λ by multiplying their values by the same penalization factor based on the fraction of failed predictions (Eq. C.2). The correlation coefficient ρ is also corrected in a similar way, but in this case the metric is divided by the

penalization factor. Performance measures are computed both within individual KG classes and globally.

To compare the performance of different GS models, skill scores are computed for MAE and ρ following Murphy (1988), using the GS-Lat model as a benchmark. The skill score (SS) for a given metric A expresses the improvement achieved by a model GS-X over the benchmark GS-Lat as a fraction (in percent) of the difference between a hypothetical perfect model (GS-PM) and GS-Lat. Positive values indicate improvement over GS-Lat, whereas negative values indicate degradation:

$$\mathrm{SS(GS\text{-}X)} = 100 \cdot \frac{A(\mathrm{GS\text{-}X}) - A(\mathrm{GS\text{-}Lat})}{A(\mathrm{GS\text{-}PM}) - A(\mathrm{GS\text{-}Lat})} \tag{8}$$

In this case, MAE(GS-PM) = 0 and ρ(GS-PM) = 1.

Uncertainty in the predictions is quantified using spread functions based on bootstrapped absolute errors. For each observation, the GS model prediction is paired with its absolute error, forming the sample set $\left\{\left(\hat{Y}_i, \left|\hat{Y}_i - Y_i\right|\right)\right\}_{i \in I}$. This set is resampled 5,000 times (bootstrapping), and for each bootstrap sample a second-degree polynomial (spread function) is fitted. To estimate the uncertainty associated with a given prediction value $\hat{Y}$, the 5,000 spread functions are evaluated at $\hat{Y}$. The 95$^{\mathrm{th}}$ percentile of the resulting distribution of error estimates (p_{95}) provides the upper bound of the uncertainty range, yielding a prediction interval of the form $\hat{Y} \pm p_{95}$.

Uncertainty in the yearly hemispherical SGS and EGS averages (Fig. 4.3) is quantified using a Monte Carlo framework that propagates model error. Spatially and temporally correlated perturbations, scaled by the bootstrapped error spread functions, are added to the predictions, and hemispherical means are recomputed for each realization. The final hemispherical estimate is given by the ensemble median, while the 2.5$^{\mathrm{th}}$ and 97.5$^{\mathrm{th}}$ percentiles define the uncertainty bounds, representing the expected range of hemispherical SGS and EGS values under model uncertainty.

4.3 Results

4.3.1 Parameters spaces

Table 4.1 lists all inferred parameters for each GS model, separated by KG class, with the respective search ranges in the last column.

TABLE 4.1

PARAMETER VALUES FOR THE GS-LIN2, GS-BC2, AND GS-P MODELS FOR EACH KG CLASSIFICATION, AND REGRESSION COEFFICIENTS FOR GS-LAT FOR EACH HEMISPHERE.

Parameter	KG class						Search Range
	C*a	C*b ∨ C*c	D*a	D*b	D*c	D*d	
GS-Lin2							
T_w [°C]	22.0	13.9	5.9	7.7	6.5	3.5	[0, 30]
n_w [days]	3	3	11	5	7	14	[3, 15]
T_c [°C]	18.8	12.0	4.9	6.5	7.2	9.5	[0, 30]
n_c [days]	9	7	4	13	7	11	[3, 15]
GS-BC2							
$t_{1,\mathrm{SGS}}$	88	64	63	1	11	33	[1, 100]
$F_{\mathrm{crit,SGS}}$ [°C d]	110.3	100.0	437.7	437.3	218.3	1014.5	[100, 5000]
$T_{\mathrm{BF,SGS}}$ [°C]	0.0	0.1	0.4	0.0	0.1	0.5	[0, 30]
a_{SGS}	4.9	2.6	3.8	4.2	0.2	2.8	[0, 5]
$t_{1,\mathrm{EGS}}$	17	88	77	49	59	49	[1, 100]
$F_{\mathrm{crit,EGS}}$ [°C d]	-558.8	-694.1	-568.5	-461.6	-100.6	-198.8	[-5000, -100]
$T_{\mathrm{BF,EGS}}$ [°C]	24.6	28.6	25.7	18.3	17.1	22.9	[0, 30]

Continued on next page

TABLE 4.1 (CONTINUED)

Parameter	KG class						Search Range
	C*a	C*b ∨ C*c	D*a	D*b	D*c	D*d	
a_{EGS}	-0.1	-0.2	-1.2	0.0	0.0	0.0	[-5, 0]
GS-P							
μ_{SGS}	0.555	0.537	0.608	0.585	0.583	0.606	-
τ^2_{SGS}	0.503	0.554	0.373	0.406	0.488	0.458	-
σ^2_{SGS}	0.056	0.054	0.049	0.052	0.058	0.045	-
μ_{EGS}	0.039	0.038	0.031	0.028	0.038	0.025	-
τ^2_{EGS}	0.013	0.017	0.033	0.032	0.034	0.040	-
σ^2_{EGS}	0.018	0.022	0.051	0.050	0.045	0.051	-
GS-Lat Regression Coefficients							
	NH			SH			
Parameter	Estimate	SE	t-stat	Estimate	SE	t-stat	-
$\beta_{0,\mathrm{SGS}}$	19.41	0.11	172.48	297.89	0.62	479.31	-
$\beta_{1,\mathrm{SGS}}$	1.93	0.00	975.56	-1.38	0.02	-78.47	-
$\beta_{2,\mathrm{SGS}}$	10.07	0.04	272.84	-8.45	0.26	-31.93	-
$\beta_{0,\mathrm{EGS}}$	342.14	0.17	2054.64	197.27	0.52	377.98	-
$\beta_{1,\mathrm{EGS}}$	-1.14	0.00	-389.01	-1.28	0.01	-86.78	-
$\beta_{2,\mathrm{EGS}}$	-9.94	0.05	-182.34	-5.85	0.22	-26.31	-

For GS-Lin2, temperature thresholds (T_w, T_c) are higher for the temperate (C) class (12.0 °C to 22.0 °C) compared to the continental (D) class (3.5 °C to 9.5 °C), reflecting that leaf flushing is controlled by higher temperatures in warmer climates and by lower temperatures in colder ones. In C climates, only short warm spells of 3

days are sufficient to trigger GS onset, while longer cold spells of 7–9 days are required to trigger EGS. In D climates, spell durations show more variability. In particular, for D*a (hot summer) and D*d (severe winter subarctic) climates, sustained warm and cold spells of 11 and 14 days, respectively, are required to trigger GS transitions, whereas other continental climates exhibit more variable spell durations.

For GS-BC2, heat and cold accumulation parameters ($t_{1,\mathrm{SGS}}$, $t_{1,\mathrm{EGS}}$) generally trigger late, with $t_1 < 30$ only for SGS in D*b and D*c, and for EGS in C*a. This is accompanied by relatively low critical thresholds (F_{crit}), suggesting that heat and cold accumulation may last only a few days in warmer and colder climates, respectively. The only exception is D*d, which requires a conspicuous SGS threshold of 1014.5 °C d, cumulated from DOY 33. The base temperature for SGS ($T_{\mathrm{BF,SGS}}$) is near zero in all KG classes; although including negative values could lower the parameters in some cases, the inference was restricted to biologically relevant values. The base temperature for EGS ($T_{\mathrm{BF,EGS}}$) shows no clear pattern, with cold accumulation potentially starting at relatively high temperatures (up to 17.1 °C to 28.6 °C, depending on the KG class). Photoperiod strongly influences heat accumulation for SGS in most classes, except D*c, where $a_{\mathrm{SGS}} \approx 0$ (i.e., heat accumulation is largely temperature-driven). For EGS, low temperatures dominate control, with photoperiod relevant only in hot summer continental climates (D*a).

For GS-P, the binary classifier predicts clear GS probability profiles as a function of $T_{14\mathrm{d}}$ and $T_{60\mathrm{d}}$ (Fig. D.3, first and last columns), indicating that absolute temperatures are the main determinants of GS likelihood. Temperature gradients ($\nabla T_{14\mathrm{d}}$, Fig. D.3, second column) and short-term variability ($\sigma_{14\mathrm{d}}$, Fig. D.3, third column) show weaker relationships but still contribute to transition identification, as non-GS states are associated with large slopes or unstable temperatures. Continental (D) climates exhibit sharper GS probability profiles than temperate (C) climates, allowing clear identification of transitions, whereas temperate classes display noisier

relationships. GS-P probability thresholds were inferred separately for each KG class (Table 4.1). The mean probability threshold μ is generally higher for SGS (0.537 to 0.606) than for EGS (0.373 to 0.554), indicating approximately symmetric behavior for entering and exiting GS. The 95% confidence intervals of μ (Table S2) show that SGS conditions are more tightly constrained by temperature (CI range: 0.013–0.088) than EGS (0.025–0.117). Between-node variances τ^2 are larger for SGS (0.049 to 0.058) than for EGS (0.025 to 0.039), indicating greater spatial heterogeneity in SGS behavior. Within-node variances σ^2 are smaller in temperate climates (0.013–0.022) than in continental climates (0.032–0.051), reflecting sharper probability-temperature profiles in D classes. These patterns are consistent with the width of the 95% CIs and are also evident in the node-level probability thresholds p_{SGS} and p_{EGS} (Fig. D.4).

GS-Lat regression parameters behave as expected in the Northern Hemisphere (NH). SGS delays by 1.93 d per degree north, and EGS anticipates by 1.14 d; per km of altitude, SGS delays by 10.07 d and EGS anticipates by 9.94 d. In the Southern Hemisphere (SH), the expected patterns hold for EGS (-1.28 d/°S, -5.85 d/km), but SGS shows counterintuitive signs. This is likely due to topography in South America, where the Andes span a wide latitudinal range, concentrating high-elevation forests closer to the equator. Wider 95% CIs in the SH, especially for the elevation coefficient (Table D.2; SGS: [-8.97, -7.94] d; EGS: [-6.29, -5.42] d), further highlight this disrupted latitudinal-altitudinal relationship.

4.3.2 GS models performance

Table 4.2 shows the skill scores (SS) for MAE and Pearson's correlation (ρ) of the three temperature-based models, indicating the percentage of improvement relative to the benchmarking model GS-Lat. SS are computed over different KG classes and globally, using performance metrics penalized by the number of failed instances (Table D.3).

TABLE 4.2

MAE AND ρ SKILL SCORES (SS, %) OVER EACH KG CLASS FOR THE THREE MODELS GS-LIN2, GS-BC2, AND GS-P, COMPUTED FROM MAE AND ρ PENALIZED BY THE NUMBER OF FAILED INSTANCES.

Metric	Model	C*a	C*b $\vee$ C*c	D*a	D*b	D*c	D*d	Global
SS(MAE) SGS	GS-Lin2	-90.1	-71.0	-38.6	-0.8	24.9	-9.8	-15.0
	GS-BC2	38.1	55.5	36.2	53.2	33.3	45.9	44.2
	GS-P	20.3	26.3	48.1	68.1	62.5	49.5	45.8
SS(MAE) EGS	GS-Lin2	-13.9	14.3	30.2	35.0	24.9	60.1	17.5
	GS-BC2	23.3	53.8	63.7	57.5	57.2	83.4	52.0
	GS-P	27.0	25.5	58.5	59.3	62.2	77.5	45.3
SS(ρ) SGS	GS-Lin2	-349.3	-297.6	45.2	35.0	-66.6	22.7	-106.1
	GS-BC2	16.7	26.9	58.3	56.9	-8.2	31.8	44.4
	GS-P	-33.2	-131.5	78.6	79.9	63.0	56.8	8.5
SS(ρ) EGS	GS-Lin2	-25.5	-83.9	-1.6	28.4	18.3	-45.3	-4.8
	GS-BC2	-5.1	57.8	23.0	49.2	36.5	-4.7	49.3
	GS-P	17.4	-5.1	32.8	59.2	66.4	-6.3	29.8

At the global scale, GS-Lat shows MAE values of 20.6 d for SGS and 25.2 d for EGS. GS-P leads to substantial improvements globally (SGS: 45.8%, EGS: 45.3%), corresponding to MAE of 11.2 d for SGS and 13.8 d for EGS. GS-Lin2 shows smaller improvements only during EGS (17.5%), whereas GS-BC2 performs similarly to GS-P in both transitions (SGS: 44.2%, EGS: 52.0%).

In terms of linear correlation, GS-Lat shows relatively high values for SGS (0.84) and lower values for EGS (0.65). GS-P shows modest improvements globally for SGS (8.5%) and larger improvements for EGS (29.8%). Conversely, GS-Lin2 displays considerable degradation in SGS, while GS-BC2 yields large improvements (SGS: 44.4%, EGS: 49.3%).

Model performance is clearly better over continental (D) than temperate (C) climates. For MAE, GS-P shows improvements between 48.1% and 77.5% over D classes, and between 20.3% and 27.0% over C classes. In continental climates, MAE values are negligible for most applications (3.0–7.6 d), whereas values are higher in temperate climates (22.3–39.2 d). GS-P maintains high correlation across all KG classes, with the only notable exception being EGS in D*d (0.32), and generally shows improved or comparable performance relative to GS-Lat.

GS-Lin2 performs similarly to GS-Lat overall, with some improvements in D climates for MAE, but noticeable degradations in SGS over C climates for both MAE and ρ. GS-BC2 performs similarly to GS-P across KG classes, outperforming it in temperate climates, while GS-P remains superior in continental regions.

Regarding systematic biases, GS-P exhibits essentially no bias over continental climates, with MB between -1.4 and 1.4 d. Over C climates, however, there is a consistent early bias of 15.4–18.2 d for SGS and a late bias of 17.3–21.7 d for EGS. GS-Lin2 shows a late bias in SGS across all KG classes (minimum 0.5 d over D*d, maximum 78.7 d over C*b and C*c), while the MB range is smaller for EGS (-7.1 to 6.3 d). GS-BC2 shows virtually no bias across all KG classes and transitions, with

the only exception being C*a (13.9 d).

As explained in Section C.2, temperature-based models may fail to produce valid predictions under certain conditions. GS-P provides robust predictions across all KG classes, whereas GS-Lin2 fails to produce valid estimates for 31.78% and 31.73% of cases for SGS and EGS, respectively, over C*b and C*c. GS-BC2 also has limitations, failing in 16.95% of predictions over C*a.

The evaluation described above is reflected in the average MB maps (Fig. 4.1), with GS-Lin2 showing the largest magnitudes, together with GS-Lat, followed by GS-P and GS-BC2. All GS models show similar critical areas: larger biases, either early or late, are generally observed over parts of Central America, Southeastern China, and South and Southeast Asia. Beyond these areas, GS-Lin2 and GS-Lat generally show larger biases than GS-BC2 and GS-P, especially across the SH and over parts of the US and Europe.

Figure D.5 shows the mean across the years of the error spread p_{95} for each of the GS models. This figure further confirms the spatial features of the MB. For GS-P (Fig. D.5e,f) the uncertainty in the prediction is small for a large part of the NH, while the largest error spread is observed over India and South America, especially in the equatorial Andes. GS-BC2 performs similarly to GS-P, although the uncertainty appears to be generally greater for SGS, and smaller across the SH. The remaining two models show similar spatial patterns, although with varying magnitudes.

A final component of model evaluation considers the predictive capabilities of GS models outside their ERA5 calibration range. Figure D.6 shows the percentage of failed predictions over C and D climates using UKESM1-0-LL historical (1850–2014) and SSP5-8.5 (2015–2100) temperatures. UKESM1-0-LL is known to have a substantial cold bias over the historical period (Sellar et al., 2019), and to project one of the strongest warming trends among CMIP6 ESMs (Zelinka et al., 2020). As such, this ESM constitutes a suitable testing ground for the robustness of the GS models.

Across all models, failed predictions are more frequent during the historical period than under SSP5-8.5, likely because temperatures colder than the training range impair model performance. Under global warming, UKESM1-0-LL temperatures become closer to or larger than ERA5 temperatures, reducing the number of failed predictions. Among GS models, GS-BC2 has the highest failure rate across all 250 years, with about 15–25% failed instances in the historical period, and 5–15% under SSP5-8.5, whereas GS-P and GS-Lin2 failure ratios are much lower (5–10% over the historical period, <2.5% under SSP5-8.5).

4.3.3 Forest GS from 1850 to 2100 using GS-P model

Figure 4.2 shows the SGS and EGS calculated by GS-P using UKESM1-0-LL near-surface air temperatures, for the preindustrial period (1850–1879), and as end-of-century mean differences relative to the preindustrial conditions under SSP1-2.6 and SSP5-8.5. The SGS and EGS are computed only over grid cells with at least 10% forest cover in at least one year of any experiment.

During the preindustrial period (historical experiment, 1850–1879; Fig. 4.2a,b), the SGS and EGS show the expected large-scale behaviour across most of the globe: for a given year, SGS precedes EGS in the Northern Hemisphere (NH), while the opposite ordering is observed in the Southern Hemisphere (SH), and transition timings broadly follow the latitude–elevation gradient. Only limited regions, such as north-western Australia and the tropical Andes, exhibit an inversion of the typical SGS–EGS order.

Under SSP1-2.6 and SSP5-8.5, global warming leads to earlier SGS and later EGS (Fig. 4.2c–f). In this regard, Table D.5 shows the SGS and EGS values over different KG classes, as identified in the preindustrial period (1850–1879), and relative changes over present-day (1985–2014) and end-of-century periods (2071–2100). In the NH, from the preindustrial to the present-day period, on average, the SGS is estimated

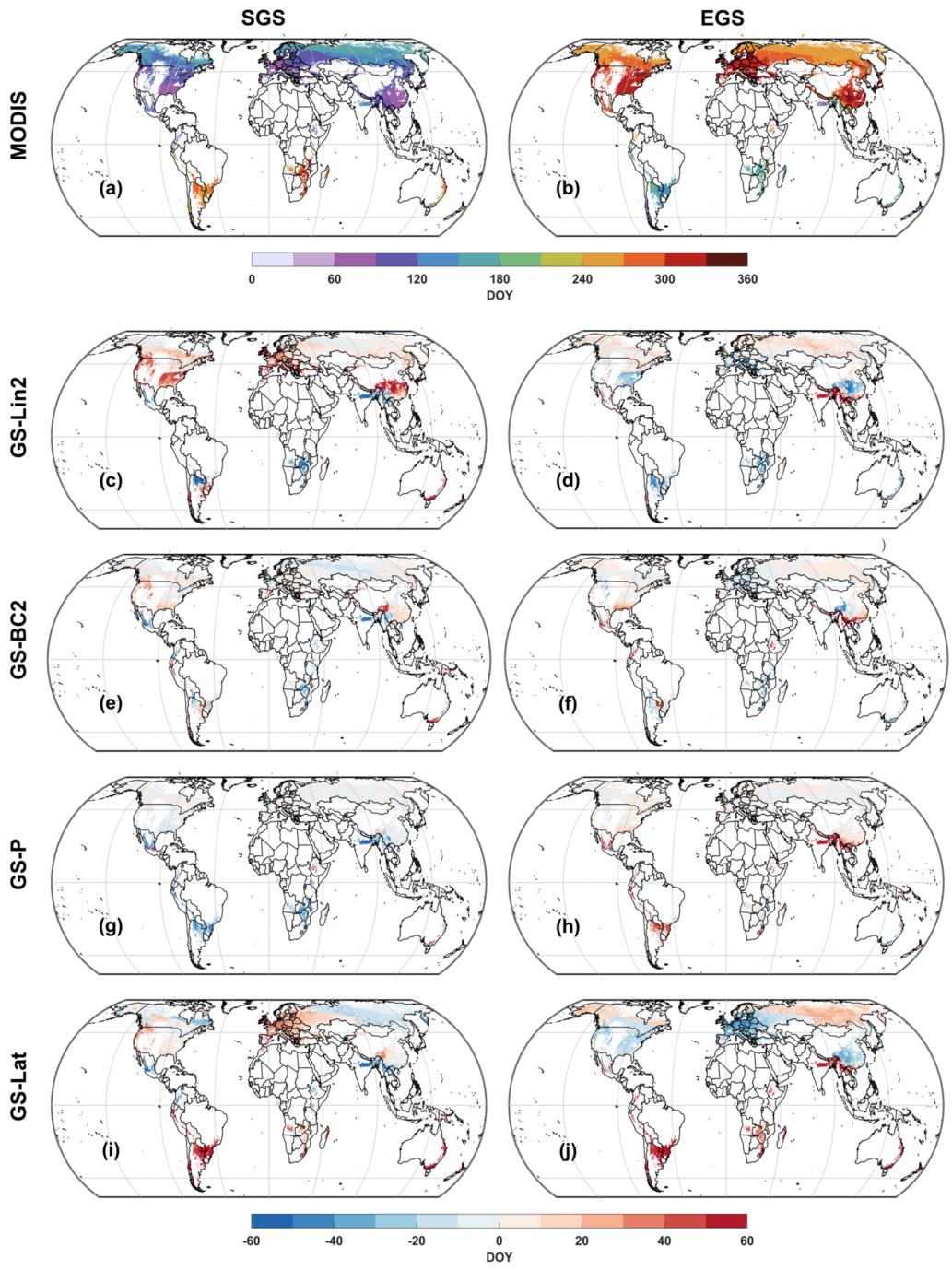

Figure 4.1. MODIS-derived average SGS and EGS maps over the 2001–2023 period (a,b) and mean bias (MB) maps (Model − MODIS) for SGS (first column) and EGS (second column) as estimated by GS-Lin2 (c,d), GS-BC2 (e,f), GS-P (g,h), and GS-Lat (i,j). The MB maps illustrate spatial patterns of early or late biases in phenological transition predictions.

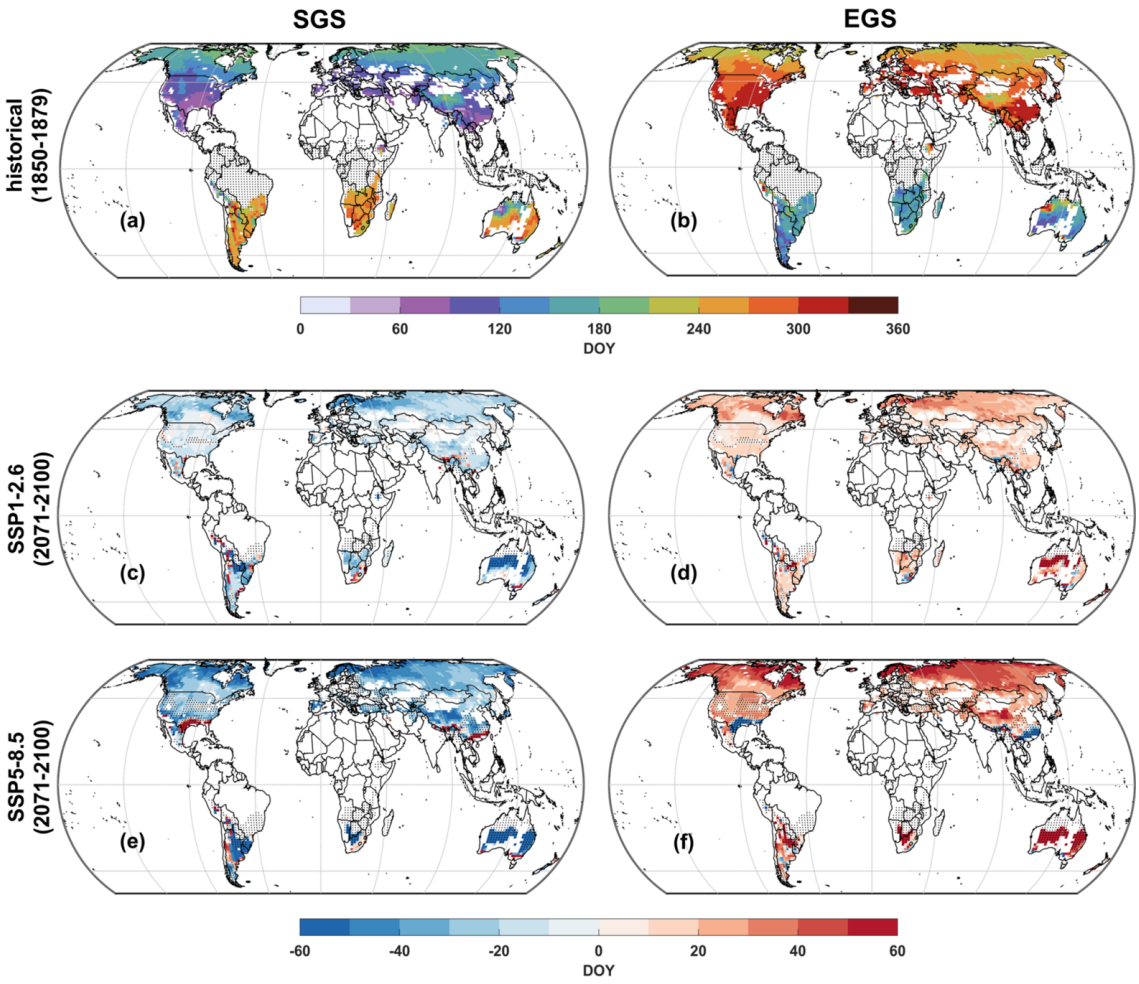

Figure 4.2. Mean SGS (first column) and EGS (second column) calculated by GS-P for the preindustrial period 1850-1879 (a,b), and differences between the preindustrial period mean and the 2071-2100 mean, under SSP1-2.6 (c,d) and under SSP5-8.5 (e,f). In (a,b) the dots indicate nodes with at least one year of the KG class A. In (c-f) dots indicate nodes that transitioned between main classes (i.e. from C and D to A, B, or C) or that present GS-flipping behaviour, i.e. those locations where the order of SGS and EGS switches, comparatively to the preindustrial period. SGS and EGS are calculated only over the nodes with at least 10% primary or secondary forest cover in at least one year of any experiment.

to advance by 0.5–3.1 days and the EGS to delay by 0.5–3.4 days, depending on the KG class considered (Table D.5). Consequently, the GS duration is estimated to increase by 1.4–5.4 days on average, with the preindustrial C-class areas experiencing the largest effect. For future periods, these shifts become consistently more evident across most classes and scenarios, with the largest differences over preindustrial D-class areas: between 2071 and 2100, the GS is projected to last up to 48.5 days longer on average (compared to the preindustrial period) under SSP1-2.6, and up to 85.4 days longer under SSP5-8.5.

In the SH, similar trends occur over preindustrial C*a and D*c climates, with the GS becoming on average 10.2–13.2 days longer at present day, and 34.8–53.9 days longer at the end of the century under SSP5-8.5. However, for C*b and C*c climates, a slight shortening of the GS is projected for all future scenarios.

Beyond SGS and EGS shifts, two additional features emerge. First, regions near the boundaries of KG classes undergo climatic shifts, leading to changes in the model parameterization (e.g., a transition from a D to a C GS regime) that mitigate the end-of-century differences in SGS and EGS relative to preindustrial conditions. Second, GS-P identifies GS-flipping regions, where the SGS–EGS ordering is inverted compared to the preindustrial period, causing observed large differences. This exclusively occurs at the interface between temperate (C) and warmer (A or B) climates. For instance, in the southeastern United States under SSP5-8.5 (Fig. 4.2e), the SGS shifts abruptly from February–March during the preindustrial period to July–August at the end of the 21st century, while EGS shifts from November–December to May–June, following a regime that is typically observed in the SH or in monsoon-controlled regions, such as South and Southeast Asia (Fig. 4.1a,b).

At the preindustrial period, prediction uncertainty is remarkably low (< 10 days) for most of the NH, but increases in several SH regions (Fig. D.5). In addition, for the end-of-century period, the largest error spread occurs in areas associated with the GS-

flipping behaviour, reflecting predictions that strongly deviate from the calibration range of SGS and EGS.

Figure 4.3 shows the yearly averages of SGS and EGS calculated in the two hemispheres by GS-P, from 1850 to 2100, under SSP1-2.6 and SSP5-8.5. GS-flipping nodes were excluded from the calculation in order to produce consistent averages for the whole 1850–2100 period. Stable average SGS and EGS dates are observed for both hemispheres from 1850 to around 1970. During the long and stable historical period (1850–1969), SGS and EGS average at around DOY 134.8 (15 May) and 272.5 (29 September) in the NH, and around DOY 244.6 (2 September) and 156.8 (6 June) in the SH, respectively. Changes in phenological transition timing appear to emerge from the 1970s.

Table 4.3 shows shift ratios in yearly mean SGS and EGS timing calculated over the late-historical period (1970–2014) and over the end of the 21$^{\text{st}}$ century (2071–2100), across different areas as identified by preindustrial KG classes. During the 1970–2014 period, SGS is estimated to advance at a statistically significant rate between 0.7 and 3.5 $\mathrm{d\,dec^{-1}}$, and EGS to delay between 1.4 and 3.6 $\mathrm{d\,dec^{-1}}$ over preindustrial C, D*c, and D*d areas. Projections for 2071–2100 under SSP1-2.6 show that these rates may be dampened, enhanced, or no longer significant depending on the region. In contrast, these effects are usually greatly enhanced under SSP5-8.5 for the same period, with rates reaching values of -9.1 $\mathrm{d\,dec^{-1}}$ for SGS and $+9.2$ $\mathrm{d\,dec^{-1}}$ for EGS over the preindustrial D*d area.

Beyond these regions, preindustrial D*a areas typically display the opposite behaviour, with delayed SGS and anticipated EGS, while rates over preindustrial D*b areas are either not significant or comparatively small. Figures D.8 and Fig. D.9 show the yearly averages calculated via GS-Lin2 and GS-BC2. For the NH, they both show behaviour similar to GS-P, although they differ in absolute timing of transitions and magnitude of transition shifts. For the SH, it should be noted that GS-Lin2 produces

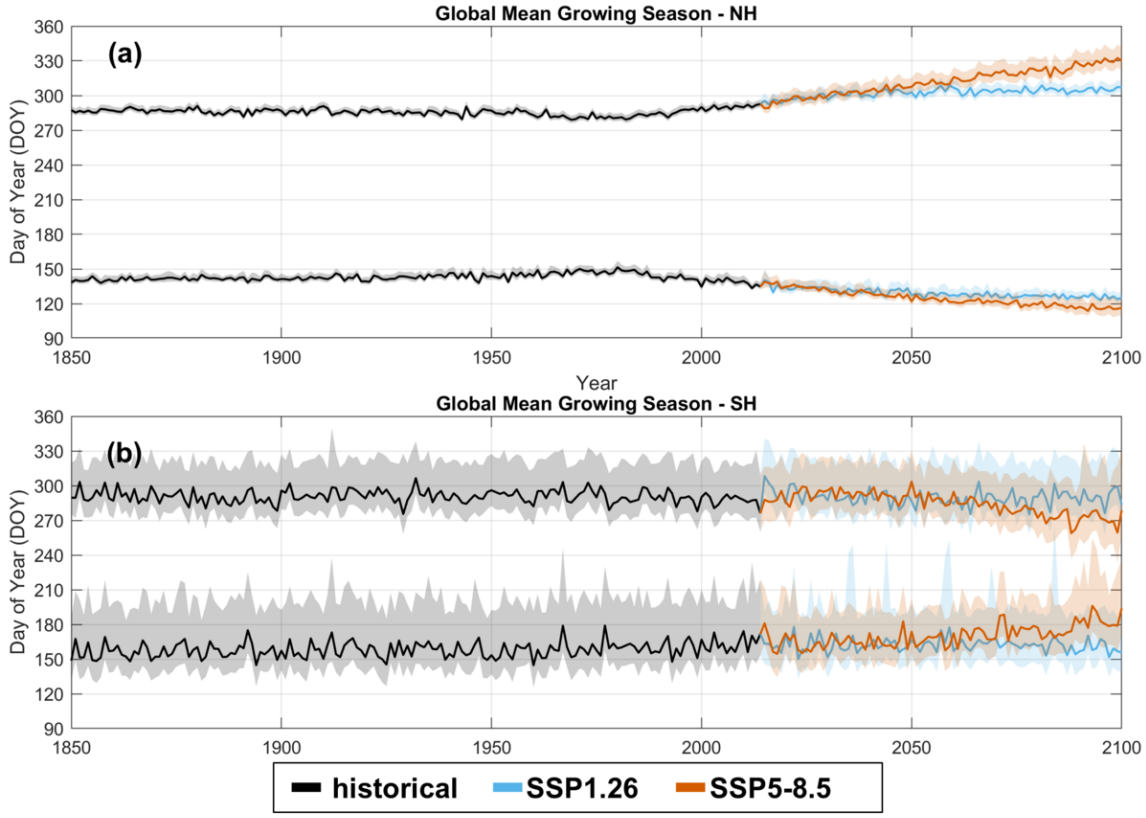

Figure 4.3. Area-weighed yearly averages of SGS and EGS from 1850 to 2100, for the Northern (a) and the Southern Hemisphere (c), as simulated by GS-P over UKESM1-0-LL temperatures, only considering non-KG transition, non-flipping nodes. In the NH, the bottom lines refer to the SGS, while the top lines refer to the EGS. In the SH, the order is reversed. Shaded areas indicate the 95% confidence interval.

ill-defined results, with an extremely large prediction interval for both SGS and EGS.

TABLE 4.3

RATIOS OF CHANGES ($\mathrm{d\,dec^{-1}}$) IN YEARLY MEAN SGS AND EGS OVER DIFFERENT KG CLASSES DURING THE HISTORICAL YEARS WHEN SHIFTS IN PHENOLOGICAL TRANSITIONS STARTED TO EMERGE (1970–2014), AND DURING THE END OF THE 21$^{\mathrm{ST}}$ CENTURY (2071–2100) UNDER DIFFERENT SCENARIOS. KG CLASSES IDENTIFY NODES PREDOMINANTLY WITHIN THAT CLASS DURING THE PREINDUSTRIAL PERIOD (1850–1879). STARRED NUMBERS INDICATE $p < 0.05$ FOR TESTING NON-NULL RATIOS.

Metric	Period	Experiment	C*a	C*b ∨ C*c	D*a	D*b	D*c	D*d	C	D	Global
SGS	1970–2014	historical	−3.2*	−3.3*	1.0*	0.0	2.8*	10.4*	−3.2*	−1.5*	−2.1*
	2071–2100	SSP1-2.6	−2.2*	−0.1	0.8*	0.1	−0.7*	−1.6*	−1.8*	−1.1*	−1.2*
	2071–2100	SSP3-7.0	−5.4*	−2.4*	0.6*	−0.2	−2.3*	−2.2	−5.4*	−2.6*	−3.1*
	2071–2100	SSP5-8.5	−6.1*	−5.4*	0.3*	−0.1	−3.5*	−3.5	−6.9*	−3.2*	−3.9*
EGS	1970–2014	historical	3.6*	2.3*	−0.7*	0.6	1.3*	2.5*	3.4*	2.0*	2.4*
	2071–2100	SSP1-2.6	1.7*	−1.1*	−0.5*	0.1	1.0*	3.1*	1.4*	1.2*	1.1*
	2071–2100	SSP3-7.0	4.5*	−1.0*	0.0	0.5*	2.8*	6.5*	5.1*	3.1*	3.2*
	2071–2100	SSP5-8.5	4.7*	1.3*	0.4*	0.2	3.8*	8.3*	6.4*	3.8*	3.9*

4.4 Discussion

4.4.1 Historical trends and future projections of GS transitions

The GS-P model estimates of this study indicate that the SGS and EGS remained stable from 1850 until the 1970s. Following this period, systematic phenological shifts emerged: over 1970–2014, the average global rate of change was approximately $-2.1\,\mathrm{d\,dec^{-1}}$ for the SGS and $2.4\,\mathrm{d\,dec^{-1}}$ for the EGS, with stronger shifts at higher latitudes compared to lower ones. Richardson et al. (2013) reviewed shifts of a similar order, although more extreme rates have been observed in specific biomes and time periods (e.g., up to $+14\,\mathrm{d\,dec^{-1}}$ for boreal forests in recent decades).

Consistent satellite-based estimates were also reported by Park et al. (2016) and Barichivich et al. (2013) who found a GS duration increase of +2.6 and $+2.2\,\mathrm{d\,dec^{-1}}$, respectively, in the last four decades. Most phenological trend studies focus on the NH, with far fewer addressing vegetation phenological phases in the SH. Moreover, studies in the SH typically focus on flowering dates rather than on the timing of SGS and EGS. From the few long-term studies performed for the SH, evidence of responses to global warming seems weaker and uncertain. For instance, while the review by Chambers et al. (2013) reported an average advance in flowering time of -5.6 $\mathrm{d\,dec^{-1}}$, it should be noted that 72% of the considered datasets lacked statistically significant trends. Similarly, Everingham et al. (2023) investigated species-specific responses in the shifts of flowering dates of 37 herbaceous taxa and found significant shifts in only 12 species.

For future periods, GS duration is projected to increase substantially across the NH, comparatively to the present-day climatological mean (1985–2014). By the end of the 21$^{\mathrm{st}}$ century, GS duration is expected to increase by approximately 24.0–48.8 d over regions with preindustrial temperate climates and by 32.4–67.0 d over regions with preindustrial continental climates, depending on the scenario. In the SH, the

response is generally weaker: GS duration increases by approximately 14.8–18.2 d in temperate climates and 26.7 d in continental climates under SSP5-8.5, while a shortening of 13.1 d is projected under SSP1-2.6 for the same continental regions.

Although the shifts simulated by the GS-P model may seem large, they are consistent with the physiological response to temperature reported in the literature. For instance, Liu et al. (2021) derived a GS length sensitivity to temperature of 8.22 d $°C^{-1}$ (95% CI: [2.04, 14.40]) from controlled experiment data. Since CMIP6 projections indicate a global mean temperature increase of 1.18 °C and 7.20 °C $century^{-1}$ under SSP1-2.6 and SSP5-8.5, respectively (Fan et al., 2020), this yields a GS lengthening of approximately 2.4–17.0 d $century^{-1}$ for the low emissions scenario and 14.7–103.7 d $century^{-1}$ for the high-emissions scenario.

Few studies have explicitly modelled future changes in SGS and EGS. Sun et al. (2025), using a boosted random forest (XGBoost) with 18 temperature-related predictors, estimated SGS timing up to 2100 for boreal vegetation in the NH (which broadly corresponds to D*c and D*d climate class in our study). They found much smaller shifts than those obtained in this study; they estimated an advance, at the end of the century, of only 0.5–1.2 and 6.8–8.3 days under SSP1-2.6 and SSP5-8.5, respectively, depending on forest ecosystem type. In contrast, our estimates indicate earlier SGS shifts of 19.3–23.8 days under SSP1-2.6 and 37.3–41.7 days under SSP5-8.5.

This discrepancy likely reflects differences in modelling assumptions. Sun et al. (2025) trained their model on present-day boreal ecosystems and extrapolated the resulting eco-climatic relationships into the future, implicitly assuming the persistency of the ecosystem type. Consequently, their approach may underestimate future phenological shifts by applying boreal forest features in regions likely to experience transitions in vegetation types. In contrast, our approach constrains the ecosystem-climate relationship within KG climate classes, effectively assuming equilibrium be-

tween climate and ecosystem compositions, and allowing ecosystem behaviour to track projected climate change.

4.4.2 Performance comparison between GS-P and other temperature-based models

Benchmarking the three temperature-based models against GS-Lat for the 2001–2023 period allows for a broad ranking of their performance. The GS-Lin2 model, arguably the simplest among the three considered, performs on-par with GS-Lat in terms of prediction errors. GS-P and GS-BC2 show similar overall performance, although their skill varies across regions and KG climate classes.

The most extensive spatial difference occurs in the SH, where GS-P shows more systematic bias than GS-BC2. However, a critical limitation of GS-BC2 is its substantially higher number of failed predictions compared to GS-P, indicating poorer extrapolation capabilities and, overall, greater robustness of GS-P.

All temperature-based models show limited skills in reproducing GS transitions over the SH, suggesting the presence of non-temperature drivers that determine timing of SGS and EGS. However, GS-P better represents climate-associated shifts in phenological transitions compared to other models. Since earlier SGS and later EGS are generally expected in a warmer climate, GS-P reasonably reproduces this behaviour in both hemispheres, while GS-Lin2 and GS-BC2 show some shortcomings.

A further advantage of GS-P is that computing confidence intervals on the parameters is straightforward, whereas this task is not trivial for GS-Lin2 and GS-BC2 and requires computationally expensive workarounds. This allows for a more grounded interpretation of GS-P results, whereas interpretation of the parameters for GS-BC2 and GS-Lin2 is mostly speculative.

GS-P can also be compared with the similar model proposed by Sun et al. (2025): their boosted random forest model was evaluated to have an MAE smaller than 6 days in 41% of the nodes (across all vegetation types), whereas for GS-P this

threshold is met by 88% of the nodes over the forested boreal region. GS-P can also be compared with other traditional phenological models. Mo et al. (2023) compared the predictive ability of 17 different phenological models in predicting SGS in a variety of vegetation types along a north-south transect of Northeast Asia. In their study, model performance over mixed and deciduous needleleaf forests yielded RMSE values between 4.9 and 8.2 d and correlation coefficients between 0.54 and 0.76. Over the same sub-domain, and evaluated over the 2001–2023 period, GS-P achieves an RMSE of 5.4 d and a correlation coefficient of 0.97, suggesting that our model performs among the top tier of traditional phenological models.

4.4.3 Ecological interpretation of GS-P parameters

GS-P parameters can be interpreted ecologically to understand the physiological features captured by the model. First, GS-P requires approximately symmetric temperature evidence to signal transitions into and out of the GS, as shown by the mean probability thresholds (μ) associated with each KG class, which represent the average level of temperature-based evidence required to trigger a phenological transition. However, the lower uncertainty associated with SGS thresholds indicates a stronger temperature-phenology signal in spring than in autumn. This finding aligns with previous literature reporting well-defined responses in spring phenology to temperatures, while autumn phenology often showed more variable and less predictable responses (Menzel et al., 2006; Richardson et al., 2013; Chmielewski and Rötzer, 2001).

Second, GS-P reveals that conditions for the SGS are more spatially heterogeneous than EGS conditions (between-node variance, τ^2). This suggests that spring phenology timing is a more critical period, potentially more sensitive to microclimatic conditions, species compositions, and local adverse events such as late frosts.

Third, GS-P shows that phenological transitions are more easily detected in continental (D) than in temperate (C) climates using only temperature-based criteria.

This is suggested by the sharper temperature-probability profiles in the D climates than in the C climates and, consequently, by the larger values of the within-node variance (σ^2) of the probability thresholds: over continental regions, relatively small temperature changes lead to large changes in the probability of GS presence, consistent with stronger seasonality and less interference by other environmental factors. In temperate climates, noisy probability curves and lower predictive skill indicate that temperature provides a weaker signal for GS transitions in these regions, with σ^2 lower than in D climates.

Finally, the GS-flipping feature identified at the interface between temperate and warmer climates requires careful interpretation. Rather than an actual phenomenon, it should be interpreted as a signal of large-scale climate-ecosystem instability. This instability reflects a transitional state anticipating a full shift to tropical or arid ecosystems, depending on the region's precipitation regime. GS-flipping zones are also associated with areas of large prediction uncertainty (Fig. D.7). These values do not represent actual uncertainty but rather climate-ecosystem instability emerging from climate transitions. These areas should be considered of particular interest for ecosystem conservation strategies, as rapid climate changes might outpace ecological adjustments, increasing the risk of biome reorganization or loss of ecosystem function (Seidl and Turner, 2022; Wu et al., 2025).

4.5 Conclusions

In this study, we developed and calibrated GS-P, a probabilistic, temperature-based model designed to estimate the start (SGS) and end (EGS) of the growing season for generic forest ecosystems at a global scale from 1850 to 2100. Our results indicate a general prolongation of the growing season under climate warming, with an increase of approximately one month under SSP1-2.6 and two months under SSP5-8.5 by the end of the 21st century, comparatively to the preindustrial period.

GS-P successfully identified key biological features of forest ecosystems, highlighting meaningful differences in phenological strategies. Specifically, SGS transitions are characterized by a more certain and spatially heterogeneous temperature signal, whereas autumn transitions are more homogeneous and exhibit greater uncertainty in their temperature dependence. Furthermore, GS-P enabled the detection of temperature-driven climate transitions and associated climate-ecosystem instability, identifying regions where ecosystems may be exposed to rapidly changing climatic conditions. These areas represent priority zones for ecosystem research, monitoring, and conservation strategies.

The model was directly compared with two other temperature-based models reformulated and recalibrated for this study. GS-Lin2 provided reasonable large-scale estimates in the Northern Hemisphere but exhibited high uncertainty in the Southern Hemisphere, performing similarly to coordinate-based models. GS-BC2 achieved comparable or slightly better accuracy than GS-P but showed very limited extrapolation capabilities, likely due to overparameterization, which restricts its utility mainly to geographically and climatically constrained regions under present-day conditions. In contrast, GS-P proved suitable for large-scale and climate-change applications, though its assumption of synchronous climate-GS regime transitions may overestimate future phenological shifts. Moreover, GS-P allowed for the calculation of confidence intervals for model parameters, providing rigorous insight into phenological processes, whereas GS-BC2 and GS-Lin2 offer limited interpretability in this regard.

Finally, a comparison with existing models from previous research indicates that, in terms of predictive accuracy, ecological realism, and general applicability, GS-P ranks among the top-performing phenological models for simulating forest growing seasons.

CHAPTER 5

GLOBAL FLUX-BASED ASSESSMENT OF OZONE RISK TO FOREST ECOSYSTEMS UNDER FUTURE CLIMATE CHANGE SCENARIOS

5.1 Introduction

Tropospheric ozone (O_3) is a secondary air pollutant that poses a chronic risk to forest ecosystems, as it has been shown to impair photosynthesis, increase dark respiration for metabolic defenses, and ultimately reduce carbon assimilation and biomass growth rate (Wittig et al., 2009; Grulke and Heath, 2019). Forests represent a fundamental component of the global carbon cycle, and the long-term success of any climate mitigation strategy depends on their future role as carbon sinks (Pan et al., 2011). However, forests' capacity to sequester atmospheric carbon is increasingly challenged by the combined effects of air pollution and climate change (Bonan, 2008; Ren et al., 2011). Assessing how these interacting stressors will affect forest productivity, and the related ecosystem services, over the 21st century remains a major scientific challenge.

Ozone damage to vegetation is primarily governed by the stomatal uptake of the phytotoxic pollutant (i.e. the absorbed dose) and the subsequent oxidative stress produced at the cellular level in leaf tissues (Cho et al., 2011). Therefore, forest tree responses to O_3 depend not only on ambient concentrations but also on species-specific physiological traits and environmental drivers controlling stomatal conductance (g_s). Experimental and observational studies have repeatedly documented significant reductions in growth rates and biomass production in a wide range of forest species

exposed to elevated O_3 (Franz et al., 2018). However, these responses can frequently vary in magnitude across different functional types, climatic regions, and environmental conditions (Wittig et al., 2009; Matyssek et al., 2010; Grulke and Heath, 2019).

Over the past two decades, modeling approaches have increasingly adopted flux-based metrics, such as the phytotoxic ozone dose accumulated over a detoxifying threshold Y (POD_Y), to better quantify O_3 damage and characterize O_3 risk assessment at large scales. Recent studies using this approach have demonstrated that climate variables, particularly temperature, vapor pressure deficit, and soil moisture, can strongly modulate O_3 uptake and its impact on forest productivity (Sitch et al., 2007; Lombardozzi et al., 2015; Karlsson et al., 2025). These studies concluded that the flux-based methodology is central for robust ozone risk assessment under future climatic scenarios, as it can explicitly account for interactions and feedbacks between air pollution and plant physiological behavior (De Marco et al., 2022).

Despite this methodological improvement, assessments of future O_3 impacts on forest productivity remain limited, especially at the global scale. Many studies focus on recent or present-day conditions, while long-term simulations of future conditions have traditionally relied on simplified damage functions or static representations of plant sensitivity to O_3 (e.g., Ashmore, 2005; Felzer et al., 2005; Fuhrer et al., 2016; Sicard et al., 2017). Sitch et al. (2007) addressed this limitation by introducing a mechanistic flux-based approach to account for CO_2–O_3 interactions in plant stomatal conductance, providing the conceptual basis for modeling O_3–climate–vegetation interactions under future climate change scenarios. Nonetheless, most global analyses have focused on croplands and food security (Van Dingenen et al., 2009; Mills et al., 2018; Guaita et al., 2025), leaving forest ecosystems relatively underexplored despite their longer lifespans and cumulative exposure to multiple stressors.

Climate change is expected to alter O_3 risks to forest ecosystems in potentially

contrasting ways. On one hand, rising atmospheric CO_2 may reduce g_s (and photorespiration) and increase water-use efficiency (Adams et al., 2020; Mathias and Thomas, 2021), potentially limiting O_3 uptake. On the other hand, increasing temperatures, enhanced atmospheric vapor pressure deficit, and altered precipitation regimes may counteract this effect by extending or shifting the growing season or increasing plant physiological stress. A recent modeling study, for example, indicated that O_3 damage in European forests strongly depends on the balance between atmospheric chemistry, climate-driven stomatal responses, and species-specific traits (Karlsson et al., 2025). This highlights the need to capture and model the spatial and functional heterogeneity of O_3 risk, explicitly accounting for forest vulnerability in different contexts rather than assuming uniform responses (De Marco et al., 2022).

In this regard, a critical knowledge gap remains concerning the differential sensitivity of forests across major climatic zones. Boreal, temperate, and tropical forests differ substantially in phenology, stomatal regulation, growth strategies, and exposure patterns, leading to potentially divergent O_3–climate interactions and damage responses. Tropical forests, despite their dominant contribution to global gross primary productivity, remain particularly understudied in O_3 impact assessments. Meanwhile, boreal and temperate forests are expected to experience pronounced climate-driven shifts in growing season length, with uncertain implications for accumulated stomatal O_3 uptake.

In this study, we present a global, flux-based assessment of future O_3 impacts on forest biomass growth from the present day to 2100, explicitly addressing interactions between air pollution and climate change. Four representative tree species characterizing major climatic zones are considered: *Picea abies* (boreal), *Quercus robur/petraea* (temperate), *Fagus sylvatica* (temperate), and *Inga edulis* (tropical). By integrating climate and air quality projections consistent with contrasting Shared Socioeconomic Pathways (SSPs; Riahi et al., 2017) and accounting for species-specific

physiological responses, our analysis aims to clarify how future O_3 pollution may differentially affect forest productivity across the world's major forest biomes.

5.2 Methodology

5.2.1 UKESM1-0-LL meteorological and O_3 concentration data

Meteorological variables and O_3 concentrations produced by the UKESM1-0-LL model (Sellar et al., 2019) were used as input for calculations of stomatal O_3 fluxes. UKESM1-0-LL is a fully coupled global Earth System Model (ESM) participating in the Aerosol and Chemistry Model Intercomparison Project (AerChemMIP; Collins et al., 2017). It includes a physical atmosphere–ocean model coupled with additional interactive Earth system components including ocean biogeochemistry, stratosphere–troposphere chemistry and aerosol schemes, and terrestrial carbon cycles coupled to interactive vegetation. Its horizontal atmospheric resolution is approximately 140 km at mid-latitudes, with vertical levels extending to the upper stratosphere. A comprehensive chemistry scheme is included within the ESM, simulating transport and reactions of major chemical species involved in O_3 formation. As a result, UKESM1-0-LL is able to simulate interactions between climate and atmospheric chemistry across both historical and future periods. The model variables required for this study are listed in Table F.1.

In this study we perform stomatal O_3 flux calculations over the period 2000–2014 using data from the historical experiment (Eyring et al., 2016). Future O_3 risk is estimated based on climate and emission scenarios described by the SSPs. Specifically, we focus on the scenarios SSP1-2.6 (Van Vuuren et al., 2017) and SSP3-7.0 (Fujimori et al., 2017), which represent contrasting trajectories of future radiative forcing and air-quality emission policies affecting O_3 concentrations from 2015 to 2100.

UKESM1-0-LL outputs exhibit biases in both meteorological variables and O_3 concentrations. An evaluation of the O_3 bias against surface O_3 observations from the Tropospheric Ozone Assessment Report (TOAR) dataset (Schröder et al., 2021) for the baseline period (2000–2014) is provided in Appendix B.2.

5.2.2 Dry deposition model for forests

The POD calculations are first performed at a species-specific level, following the approach described in LRTAP Convention (2017). More specifically, we use a dual-sink big-leaf O_3 dry deposition model that calculates stomatal conductance (g_s) and O_3 uptake by plants, following the DO_3SE paradigm originally developed by Emberson et al. (2000b).

This model also simulates phenology and light penetration within the canopy, while accounting for soil water limitations to g_s. Furthermore, it considers atmospheric stability and instability using Monin–Obukhov similarity theory together with a resistive scheme. The stomatal O_3 flux model receives as input meteorological and chemical data from CMIP6 models under the different experiments. The complete formulation of the O_3 dry deposition model is described in Appendix A; however, for this study a key modification to the deposition scheme is applied to the O_3 concentration scaling in order to allow application to forests. In the original formulation, O_3 concentrations are scaled directly from the model input height (20 m for UKESM1-0-LL) to the canopy height below. In this study we instead employ the approach described by Gerosa et al. (2017).

First, the input O_3 concentration at each grid node is scaled from the model level height to a reference height of 50 m, representing a level where O_3 concentrations are assumed to be largely decoupled from surface influences. The roughness length of this surface is calculated based on the land-cover composition within each grid node (Eq. E.2), while the surface g_s is assumed to correspond to that of a grassland

surface (see Gerosa et al., 2017, for more details). Then, O_3 concentrations are scaled from this reference height to the target surface, assumed to be a homogeneous canopy composed of the species under consideration. This surface is characterized by its own roughness length, derived from the parameterized canopy height, and its species-specific g_s parameterization. The treatment of soil water availablity to the plant is described in Appendix E.1.1.

Following the DO_3SE methodology, canopy-level resistances are used to scale O_3 concentration to canopy height, whereas leaf-level resistances of a sunlit upper-canopy leaf are used to calculate stomatal O_3 uptake. In particular, the leaf-level stomatal resistance is calculated as the inverse of g_s, obtained by applying the empirical Jarvis–Stewart approach (Jarvis, 1976). Within this framework, we also account for the effect of elevated CO_2 concentrations on g_s, following an approach similar to that described by Guaita et al. (2025). The specific formulation of the CO_2 effect is described in Section 5.2.3.

Once g_s is obtained, the seasonal stomatal O_3 dose received by each forest species is calculated as the phytotoxic O_3 dose above the $1\,\mathrm{nmol\,m^{-2}\,s^{-1}}$ threshold (POD_1), which accounts for plant detoxification capacity. This is computed by integrating the hourly stomatal O_3 flux ($F_{sO_3,i}$) over the flux accumulation period ($i = 0, \ldots, t$, where i is the i-th hour of the accumulation period):

$$POD_1 = \sum_{i=0}^{t} \max\{F_{sO_3,i} - 1,\, 0\} \cdot 3600 \cdot 10^{-6} \tag{5.1}$$

The species-specific POD_1 values are used to estimate losses in relative gross annual stem volume increment (rGAI) through species-specific dose–response relationships (DRRs).

5.2.3 Species selection, DRRs, g_s parameterizations, growing season, CO_2 effects on g_s

This study considers four tree species selected to broadly represent the major global forest biomes. Only species for which a DRR is available were included and, whenever possible, species were chosen based on the availability of well-established and robust g_s parameterizations. Among all available species, four were identified as the minimum number required to adequately represent the main biome types, while additional species were not included due to computational constraints. The selected species are: *Picea abies* (boreal biome), *Quercus robur/petraea* (temperate biome), *Fagus sylvatica* (dry temperate biome), and *Inga edulis* (tropical). To assess the O_3 effects on plants, we use the DRRs based on rGAI provided by Karlsson et al. (2025) for *Fagus sylvatica*, *Picea abies*, and *Quercus robur/petraea*. For *Inga edulis*, we derived the GAI-based DRR using the biomass growth reduction assessed by Cheesman et al. (2024) in their O_3 fumigation experiment involving different tropical species. Table F.2 reports the four rGAI-based DRRs used in this study. Stomatal conductance parameterizations (Table F.3) for the first three species were taken from LRTAP Convention (2017), while the parameterization for *Inga edulis* was taken from Cheesman et al. (2024).

Each parameterization is associated with a Köppen–Geiger (KG) class as indicated in Table F.3, and the attribution of species may overlap among classes. The KG classifications are based on 30-year climatological monthly means (Peel et al., 2007). Because climate conditions change under the different SSP scenarios simulated by UKESM1-0-LL, KG classes may shift over time, and consequently the spatial attribution of parameterizations changes. Figure F.1 shows the global distribution of the parameterizations for the year 2000, and for 2100 under SSP1-2.6 and SSP3-7.0. For each species, the calculated POD_1 is converted to rGAI losses, and then averaged across species to obtain a single annual rGAI loss map.

The growing season (GS) is used to define the POD_1 accumulation period. The start and end of the GS are determined as described in Chapter 4 using a temperature-based probabilistic model (GS-P) developed to estimate forest phenology globally for generic forest ecosystems. The model consists of a boosted random forest algorithm calibrated with MODIS remote-sensing data and produces daily probability profiles indicating whether forests at a given location are within or outside the GS. Transitions into and out of the GS are identified using probability thresholds, explicitly accounting for different phenological regimes across Köppen–Geiger climate classes.

Rising levels of CO_2 in the atmosphere are expected to substantially modify stomatal functioning in forests over the course of the twenty-first century. From a physiological perspective, g_s is generally reduced under elevated CO_2, as partial stomatal closure occurs in response to increased intercellular CO_2 concentration, leading to lower transpiration rates, higher water-use efficiency, and potentially reduced O_3 uptake per unit leaf area. However, experimental evidence also indicates that this response is not consistent among forest species and time-scales: depending on environmental and structural conditions (e.g., changes in leaf area, hydraulic status, long-term acclimation), g_s may remain unchanged or even increase under elevated CO_2 (Purcell et al., 2018). Since neglecting the CO_2–g_s relationship would likely bias estimates of future stomatal O_3 flux in forests, we implement a stomatal response to increasing atmospheric CO_2 within the Jarvis-type algorithm following Guaita et al. (2025), using the following function:

$$f_{\mathrm{CO2}} = 1 - (1 - f_{\mathrm{min,CO2}}) \cdot \tanh\left(a_{\mathrm{CO2}} \cdot \frac{[CO_2] - CO_{2,\mathrm{ref}}}{CO_{2,\mathrm{ref}}} \right) \tag{5.2}$$

where $f_{\mathrm{min,CO2}}$ (adim; $[0, 1]$) represents the asymptotic fractional value of $g_{\max}$ attained for very high CO_2 concentrations, a_{CO2} (adim) controls the sensitivity to CO_2 concentrations, and $CO_{2,\mathrm{ref}}$ ([ppm]) is the reference CO_2 concentration for which $f_{\mathrm{CO2}} = 1$ (i.e., no effect on g_s).

The parameters of this function are calibrated using a hybrid process- and data-driven approach. First, synthetic g_s values at extremely high CO_2 concentrations are obtained from the output of a FvCB model for photosynthesis (Farquhar–von Caemmerer–Berry; Farquhar et al., 1980) coupled with a Ball–Berry scheme for g_s (Ball et al., 1987). Calculations are performed for a deciduous forest under non-limiting soil moisture and optimal light, humidity, and air temperature, accounting for diurnal g_s maxima at increasing ambient CO_2 concentrations from 380 to 4000 ppm. These synthetic values are used for an initial fit of Eq. 5.2, determining a theoretical asymptotic response of g_s to elevated CO_2 concentrations of $f_{\mathrm{min,CO2}} = 0.16$.

Then, experimental data describing g_s responses to elevated CO_2 concentrations are collected from published experimental studies. For *Picea abies*, *Fagus sylvatica*, and *Quercus robur/petraea*, data are collected on a species-specific basis (Bunce, 1992; Egli et al., 1998; Epron et al., 1996; Hagan Brown et al., 2025; Heath, 1998; Heath and Kerstiens, 1997; Keel et al., 2007; Klein et al., 2016; Körner, 2004; Košvancová et al., 2009; Leuzinger and Bader, 2012; Sigurdsson et al., 2002; Uddling and Wallin, 2012; Urban et al., 2019, 2014); for *Inga edulis*, data from other tropical species were used (Berryman et al., 1994; Fauset et al., 2019; Goodfellow et al., 1997; Hasper et al., 2017; Khurana and Singh, 2004; Reekie and Bazzaz, 1989).

Eq. 5.2 is then fitted again on a species-specific basis to estimate a_{CO2} and $CO_{2,\mathrm{ref}}$, while $f_{\mathrm{min,CO2}}$ is held fixed at 0.16. To account for uncertainty in g_s responses emerging from experimental work, the 95% prediction interval (PI) of f_{CO2} is quantified via non-parametric bootstrapping (i.e., by repeatedly resampling the experimental dataset with replacement and recalculating the fitted response to obtain a distribution of predictions). The resulting lower and upper bounds of the 95% PI are finally refitted using Eq. 5.2, producing parameter sets that allow an analytical representation of the lower and upper uncertainty limits of the g_s response to elevated CO_2 (Table F.4).

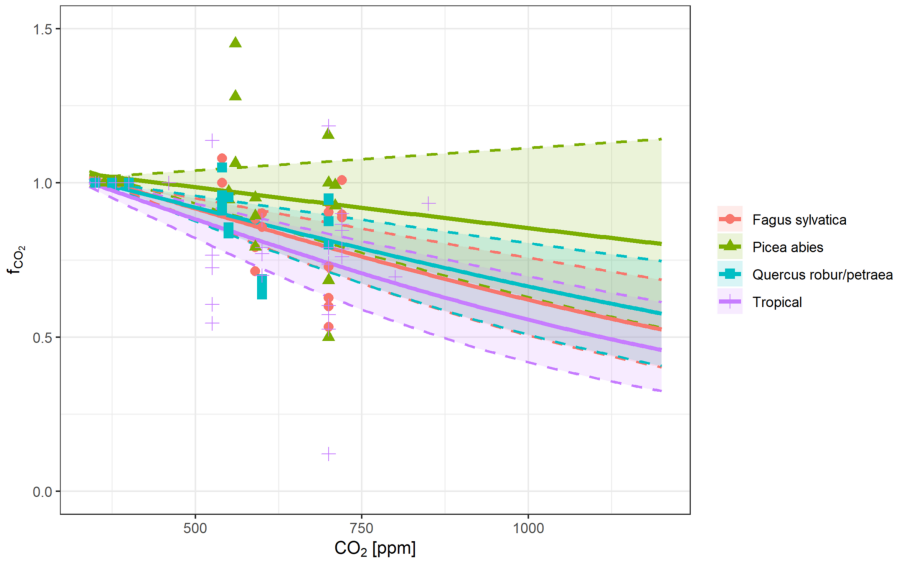

Figure 5.1. f_{CO2} curve describing relative g_{max} responses to increasing CO_2 concentrations. Dashed lines and shaded areas indicate the 95% PI.

5.2.4 Dry Deposition Model Runs, Assumptions, and Output Analysis

Four dry deposition model runs are performed to quantify the CO_2 effect on the final rGAI estimates. The first run estimates POD_1 for the O_3 risk assessment, consistently with the standardized framework of LRTAP Convention (2017), and is therefore labelled as MM run (Mapping Manual). In this run, f_{CO2} is set to 1 at all timesteps, i.e., implying no CO_2 effect on g_s. The second run accounts for the mean CO_2 effects by calculating f_{CO2} according to Eq. 5.2, and is subsequently labeled MM+CO2 run. The third and fourth runs also calculate f_{CO2} with the same method, but with parameter values corresponding to the lower and upper bounds of the 95% PI of f_{CO2}. These two latter runs are used to assess the uncertainty related to g_s responses to elevated CO_2 concentrations and are named MM+CO2low and MM+CO2up.

Over the baseline period (2000-2014), only the MM run is performed, as CO_2 effects are negligible. For future times, the MM+CO2 run is performed for both SSP1-

2.6 and SSP3-7.0 (2015-2099). Only for SSP3-7.0 the MM+CO2low and MM+CO2up runs are performed, as that scenario simulates the largest CO_2 effect on g_s.

Runs produce global annual POD_1 maps, which are masked to include only grid cells with at least 60% primary or secondary forest cover for at least one year of the 21st century, as provided by UKESM1-0-LL. Mean maps may refer to the baseline period (2000-2014), mid-century or 2050 (2045-2054), or end-century or 2100 (2090-2099). O_3 concentration and f_{clim} values (Section 5.3.1) are surveyed by computing, across nodes, the global mean and the mean of the interannual variability. The end-century uncertainty range due to the CO_2 effect on g_s (Figure F.3) is calculated by computing the difference between the mean rGAI values obtained from the MM+CO2up and the MM+CO2low runs. The same two runs are used to compute the bands shown in Figure 5.4, Figure 5.5 and Figure F.4.

5.3 Results

5.3.1 Spatio-Temporal Patterns of O_3 and Impacts of Climate Variables on Stomatal Conductance

Figure 5.2a–c shows the mean O_3 concentrations during the baseline period and their projected changes (ΔO_3) at end-century. O_3 concentrations are expressed at tree canopy height and averaged over the daylight hours of the accumulation period. During the baseline years, UKESM1-0-LL shows global mean O_3 concentrations of 32.1 ± 2.4 ppb (Table 5.1), and adequately reproduces the expected large-scale patterns: the Northern Hemisphere presents higher O_3 concentrations than the Southern Hemisphere, and latitudinal and elevation gradients are apparent. Under SSP1-2.6, which assumes the implementation of strict air quality policies, UKESM1-0-LL projects a mean O_3 decrease of 4.2 ppb by the end of the century (Figure 5.2b). On the contrary, under SSP3-7.0, which is characterized by weaker air pollution control

policies, O_3 concentrations generally increase by 2100, although regional exceptions are also present (e.g. U.S., Southeastern China; Figure 5.2c).

The f_{clim} function captures the combined effect of key climatic factors (air temperature, VPD and soil water available to the plant) on g_s. Values of $f_{\text{clim}} \approx 1$ indicate minimal limitation, whereas near-zero values denote a strong stomatal closure and reduced O_3 uptake. During the baseline period, f_{clim} averaged over the accumulation period exceeds 0.75 over most areas of the globe, while stronger limiting conditions occur mainly at the border of the forest mask, indicating progressively more unfavourable conditions towards forest ecotones (Figure 5.2d). Figure 5.2e–f shows the changes in f_{clim} at 2100 relative to the baseline (Δf_{clim}). From an O_3 risk perspective, negative Δf_{clim} values indicate stronger climatic limitation of g_s and thus, potentially, lower POD_1 and O_3 damage. On the contrary, positive Δf_{clim} values correspond to a weaker limitation of g_s and therefore higher POD_6 and increased O_3 damage. Both future climate change scenarios show similar spatial features, with generally greater stomatal conductance limitations relative to the baseline, and larger changes under SSP3-7.0 than SSP1-2.6, coherently with the stronger climate signal. The lower f_{clim} values appear to be mostly driven by the more limiting f_{VPD} (Figure F.2e,f), which appears to dominate even over the f_{temp} increases that happen at upper latitudes.

5.3.2 Global relative rGAI losses, trends by species and by region

Figure 5.3 shows the mean rGAI losses over the baseline period and their changes under SSP3-7.0 at the end of the century, while accounting for the effects of CO_2 on stomatal conductance (MM+CO2 run). Over the baseline period, rGAI exhibit a clear latitudinal gradient, with the largest values occurring at low latitudes and values approaching zero at higher latitudes.

The highest rGAI losses (around 24%) are found across the Congo Basin tropical rainforests, Jiang Nan subtropical forests, Guizhou Plateau broadleaf and mixed

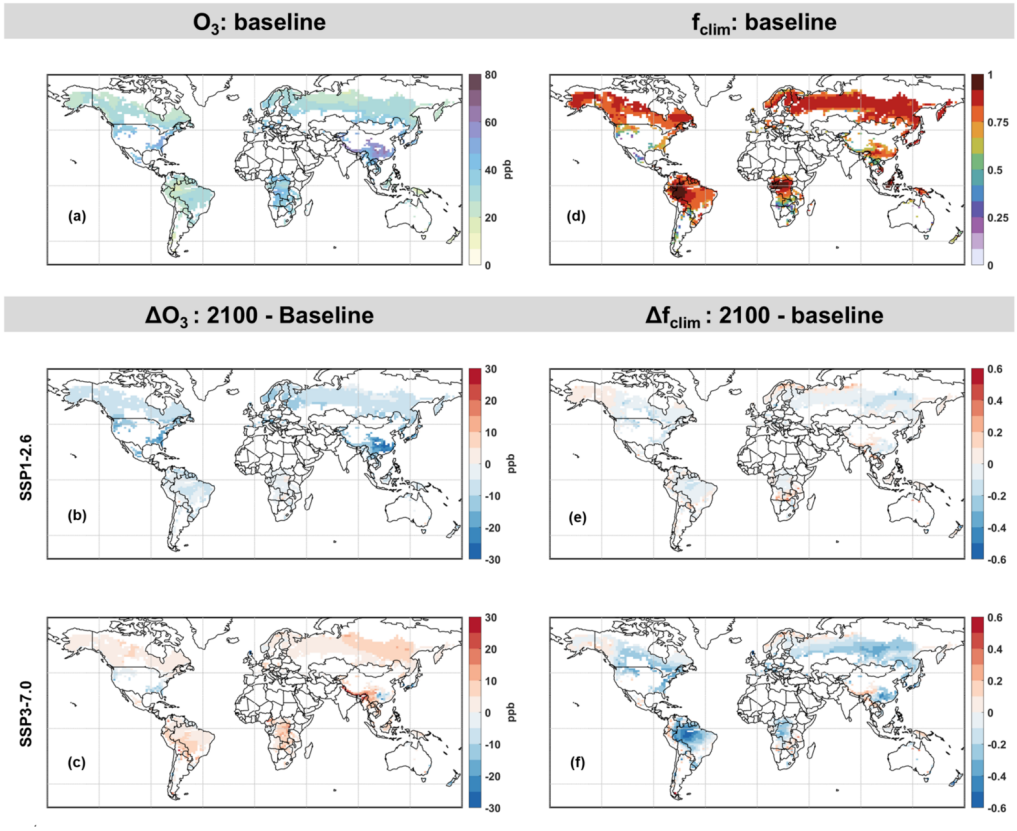

Figure 5.2. Mean O_3 concentrations at canopy height and mean f_{clim} values during the baseline period (a,d), and their changes (Δ) at 2100 with respect to the baseline for SSP1-2.6 (b,e) and SSP3-7.0 (c,f). Only values corresponding to light hours of the growing season were considered for averaging. For all figures hereafter, baseline indicates the 2000–2014 mean, and 2100 indicates the 2090–2099 mean; only nodes whose area is occupied by at least 60% primary or secondary forest are considered; map lines delineate study areas and do not necessarily depict accepted national boundaries.

TABLE 5.1

GLOBAL MEAN VALUES (MEAN INTERANNUAL SD) OF O_3 CONCENTRATIONS AT CANOPY HEIGHT AND JARVIS FUNCTIONS DURING THE BASELINE PERIOD, AT 2050 AND 2100 UNDER SSP1-2.6 AND SSP3-7.0, AND OVER REGIONS WITH AT LEAST 60% PRIMARY OR SECONDARY FOREST COVER.

		2050		2100	
Variable	Baseline	SSP1-2.6	SSP3-7.0	SSP1-2.6	SSP3-7.0
O_3 [ppb]	32.1 (2.2)	27.9 (1.2)	34.8 (1.4)	24.3 (0.9)	35.7 (1.6)
f_{clim} [0,1]	0.79 (0.05)	0.77 (0.04)	0.76 (0.05)	0.77 (0.04)	0.65 (0.06)
f_{temp} [0,1]	0.86 (0.03)	0.87 (0.02)	0.87 (0.02)	0.87 (0.02)	0.81 (0.04)
f_{VPD} [0,1]	0.92 (0.03)	0.89 (0.03)	0.88 (0.04)	0.89 (0.03)	0.79 (0.05)
f_{soil} [0,1]	0.97 (0.03)	0.98 (0.02)	0.98 (0.02)	0.97 (0.02)	0.97 (0.02)

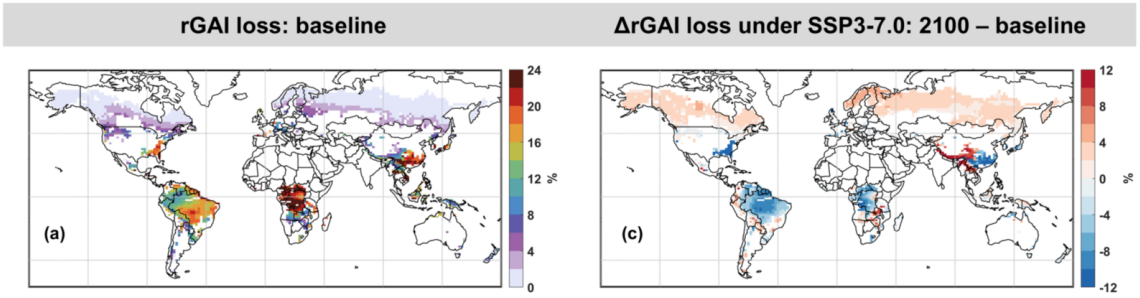

Figure 5.3. Relative rGAI losses over the baseline period (a; MM run), and corresponding changes (ΔrGAI) at 2100 under SSP3-7.0 (MM+CO2 run) with respect to the baseline (b).

forests, and Yunnan Plateau subtropical evergreen forests. Other tropical and subtropical forest regions – including Borneo lowland rainforests, the Amazon Basin rainforests, Northern Indochina subtropical forests, and the Southeastern U.S. mixed forests – also show substantial mean losses in the 2000–2014 period, ranging from approximately 12% to 20%. The Western and Eastern Himalayan forests (including Hengduan Mountains and Qionglai-Minshan conifer forests) exhibit intermediate losses, generally between 4% and 14%. In contrast, boreal forests across both North America and Eurasia show relatively low losses, typically ranging from 0% to 4%.

At the end of the century under SSP3-7.0 (MM+CO2 run), rGAI losses across most tropical and subtropical ecoregions decrease, with reductions reaching up to ∼12% and resulting in absolute losses generally between 6% and 16%. In contrast, the Himalayan forests show the largest increases among all regions, with losses reaching absolute values between 14% and 24%. Boreal forests also experience moderate increases in losses of up to ∼4%, resulting in rGAI losses in the range of approximately 2%–6%.

Figure F.3 shows the reductions in rGAI losses due to CO_2 effects on g_s. We estimate that neglecting CO_2 effects on g_s results, on average, in additional 2.1–5.5%

rGAI losses by the end of the century under SSP3-7.0. As such effects scale with g_s values, which in turn determine the final rGAI, both the magnitude of the CO_2 effect and its associated uncertainty are largest in regions with high rGAI values, such as equatorial forests and Himalayan forests. In such regions, the uncertainty range in rGAI loss reductions due to elevated CO_2 reaches values up to 9.5%.

Figure 5.4 shows the annual mean global rGAI losses across the 21st century, under both SSP1-2.6 (blue line) and SSP3-7.0 (orange), as calculated by the MM+CO_2 (solid) or by the MM run (dotted). Table 5.2 reports the corresponding globally averaged values for the baseline period, mid-century and end-century, under both SSPs and for both model configurations. At the baseline, rGAI losses amount to 10.0%. When the CO_2 effect on g_s is considered, rGAI losses follow a consistently decreasing trend under SSP1-2.6, reaching a global mean of 7.1% at the end of the century. Under SSP3-7.0, rGAI losses increase slightly during the early part of the century, stabilizing around 10.4% between 2020 and 2040, and then decrease after about 2055, reaching an end-century value of 7.6%. This late-century decrease is largely driven by the rising CO_2 concentrations: in fact, neglecting this feature delivers conflicting results, with rGAI losses increasing up to 11.5% at mid-century, and then persisting at a similar level up to the end of the century.

Figure 5.5 shows the global annual mean of rGAI losses for each of the four considered species, during the baseline and under SSP3-7.0. Three out of four species exhibit a decrease in the rGAI losses starting early in the century around 2030. This trend is most evident for *Q. robur/petraea*, with a mean rGAI loss of 13.6% at the baseline decreasing to 5.5% at the end of the century (and with CO_2 effect uncertainty estimated from the runs leading to the interval [4.0,6.7]). This species is followed then by *I. edulis*, shifting from 17.3% to 10.8% ([8.4,12.8]), and then by *F. sylvatica*, from 15.0% to 12.9% ([10.9,14.7]). In contrast, *P. abies* is the only species with increasing rGAI losses, rising from 2.9% at the baseline to 4.6% ([3.3,6.1]) at the end of the

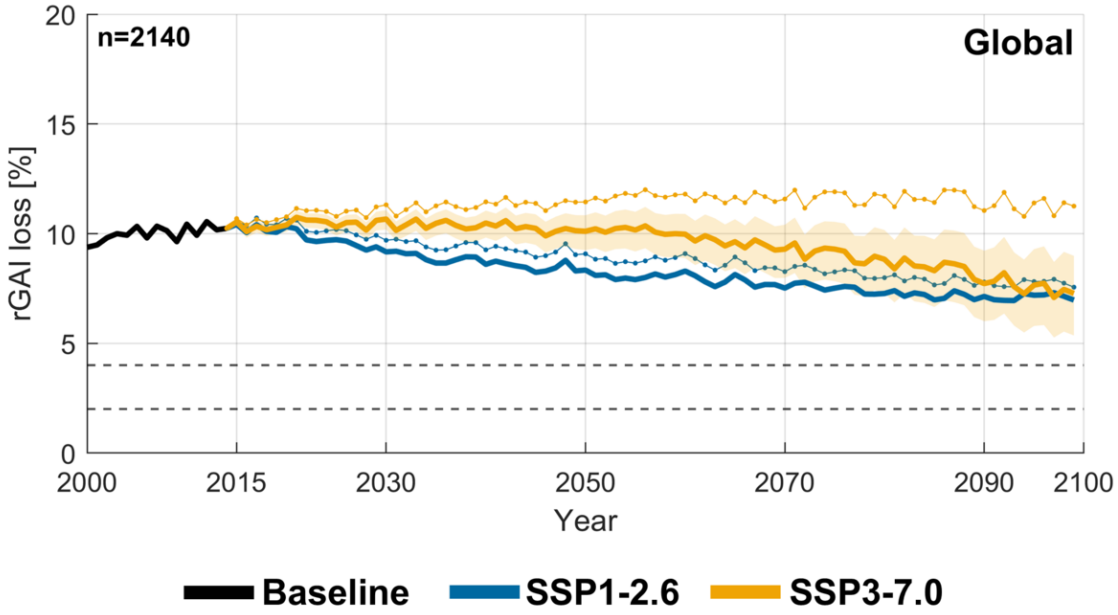

Figure 5.4. Global annual mean relative rGAI losses throughout the 21st century. Solid lines refer to the MM+CO2 run and the dotted lines to the MM run. Bands cover the MM+CO2up and MM+CO2low range (only for SSP3-7.0).

TABLE 5.2

GLOBAL ANNUAL MEAN OF RELATIVE GROSS ANNUAL INCREMENT LOSSES [%] AT THE BASELINE, AT 2050 AND AT 2100 UNDER SSP1-2.6, AND UNDER SSP3-7.0.

	Historical	SSP1-2.6		SSP3-7.0	
	MM	MM	MM+CO_2	MM	MM+CO_2 [low,up]
Baseline	10.0	-	-	-	-
2050	-	9.0	8.2	11.5	10.2 [9.3,10.9]
2100	-	7.7	7.1	11.3	7.6 [5.8,9.2]

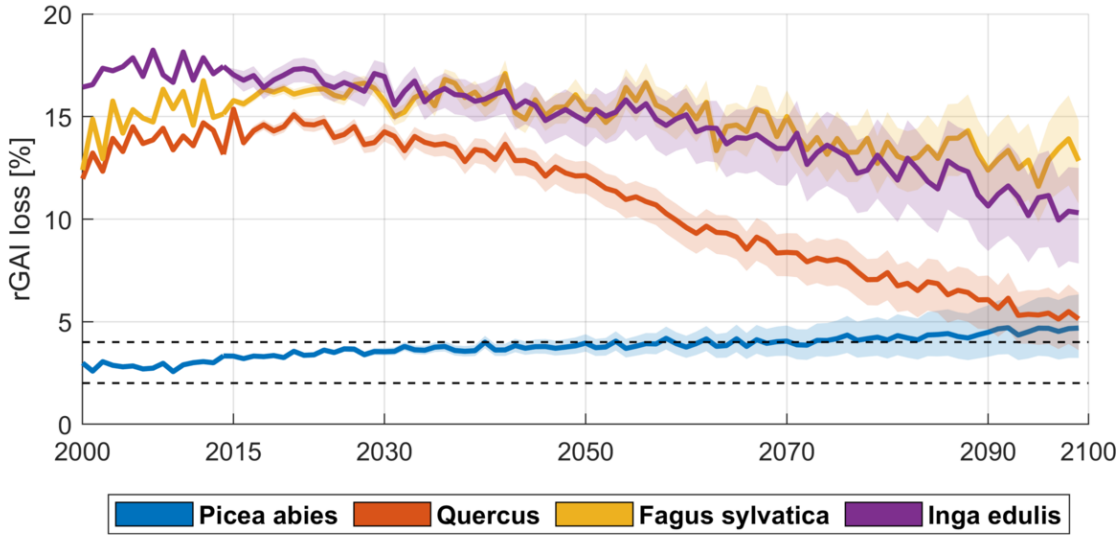

Figure 5.5. Global annual mean of rGAI losses [%] by species for the SSP3-7.0. Bands correspond to the MM+CO2up and MM+CO2low runs.

century.

Some of these species-level features are reflected on the regional scale (Figure F.4, Table F.5). In fact, regions dominated by tropical ecosystems (South America, Central America, Sub-Saharan Africa) show markedly decreasing trends. On the contrary, Russia-Belarus-Ukraine shows an increasing rGAI trend, as *P. abies* is attributed to most forests over this region. North America and Europe display low rGAI losses at the baseline and maintain relatively constant values through the century. On the other hand, East and South-East Asia display bell-like trajectories, with rGAI losses increasing until mid-century and subsequently declining toward values close to or lower than the baseline by 2100.

5.4 Discussion

5.4.1 Future O_3 risk for forest ecosystems

This study demonstrates how future O_3 concentrations and climatic conditions might affect global forest ecosystems and influence forest productivity differentially by species and region.

Overall, O_3 risk shows a decreasing trend over future times. Under SSP1-2.6, this trend is consistent across the whole century, whereas rGAI changes under SSP3-7.0 are more complex. In this latter scenario, rGAI losses increase slightly during the early part of the century, remain approximately constant until around 2055, and then decline to levels below present-day O_3 impacts. This behaviour does not emerge from a spatially uniform response at a global scale, but rather from contrasting species-specific and regional responses. The equatorial regions (South America, Central America, Sub-Saharan Africa), which contain the largest forested areas globally, show consistently decreasing rGAI losses throughout the century. At the same time, other forested regions (North America and Europe) exhibit relatively low and stable O_3 risks. On the other hand, the Asian region would appear to play a dominant role in sustaining global rGAI losses until mid-century. In fact, East and South-East Asia show higher rGAI losses up to around mid-century. Only when O_3 risk begins to decline in these regions does the global mean trend also decrease.

At the biome level, forest ecosystems seem to experience progressively lower O_3 damage throughout the century, largely as a consequence of the increasing limitation to g_s by the rising CO_2 concentrations. However, an exception may be found in the boreal forests, represented here by *P. abies*, which are the only biome with consistently increasing rGAI losses. This response reflects not only increasing O_3 at higher latitudes under SSP3-7.0, but also the comparatively weak stomatal sensitivity of *P. abies* to elevated CO_2. This result suggests that boreal forests may become

more vulnerable to O_3 damage at future times, especially considering their exposure to concurrent climate-driven stressors and increasing disturbance regimes (Girona et al., 2023; Price et al., 2013; Venäläinen et al., 2020). Such vulnerability is evident not only at high latitudes, but also in mountainous ecosystems surrounding the Tibetan plateau (e.g., Eastern and Western Himalayan forests, Hengduan Mountains and Qionglai-Minshan conifer forests).

Our results indicate that a critical aspect in assessing O_3 damage to forest ecosystems is the effect of CO_2 on g_s. In fact, while under SSP1-2.6 the decrease in rGAI losses is globally robust regardless of the inclusion of the CO_2 effect, under SSP3-7.0 neglecting this mechanism leads to the emergence of very different signal in the rGAI trend, i.e., in a slight increase in rGAI losses instead of an overall decrease.

Among climatic variables, vapor pressure deficit emerges as the key factor controlling future O_3 risk. In fact, a common feature of climate projections is that rising temperature are associated with declining relative humidity (Fang et al., 2022). While rising temperatures alone tend to promote slightly favourable stomatal responses, the associated increase in vapour pressure deficit leads to enhanced stomatal limitations, which results in a net reduction of O_3 stomatal uptake. This mechanism is especially evident in the equatorial region, where O_3 concentrations appear to rise under SSP3-7.0, but correspond to a decreasing rGAI losses due to stronger climatic limitation of g_s.

Most previous studies assessing O_3 risk to vegetation over future periods has relied on exposure-based indices. For instance, Sicard et al. (2017) projected, with the AOT40 metric, considerably higher O_3 risks to vegetation by the end of the century under pessimistic emission scenario (approximately 70% higher than present-day levels). This result largely derives from the choice of an exposure-based metric, which neglects both the relationship between meteorological conditions and stomatal O_3 uptake, as well as the generally protective effect of elevated CO_2 on stomatal

conductance. Similarly, Fuhrer et al. (2016) reached broadly similar conclusions using the M12 exposure metric. In contrast, Otu-Larbi et al. (2020) developed an approach to estimate the combined effects of drought and O_3 effects on GPP at both present and future conditions across three European forest sites, while explicitly accounting for stomatal O_3 fluxes and the influence of CO_2 on stomatal conductance. In their simulation, GPP was projected to increase overall due to CO_2 fertilization, with the negative impacts of O_3 becoming increasingly less important in the future.

5.4.2 Uncertainties in O_3 risk projections

Regardless of the key importance of CO_2 effects on g_s, there are several sources of uncertainty associated with this feature. The magnitude of the CO_2 response can vary substantially among species and becomes particularly relevant in biomes characterized by high stomatal conductance. For instance, this is quite evident across the tropical biomes, where mean rGAI losses are estimated at 10.8% by the end of the century under SSP3-7.0, while the uncertainty range associated the CO_2 effect amounts to 4.5%. Importantly, uncertainties are present not only in the magnitude of the effect, but also in its direction. Experimental studies have shown that, in some cases or for certain species, g_s may increase rather than decrease under elevated CO_2 concentrations (e.g. Purcell et al., 2018). Our modelling framework partially accounts for this possibility, as illustrated by *P. abies* in the MM+CO2up run, where g_s is simulated to increase rather than decrease. Furthermore, some experimental works (Dumont et al., 2013; Garosi et al., 2025) suggested that O_3 damage may dampen stomatal sensitivity to rising CO_2 concentrations, which might indicate smaller protective CO_2 effects than those represented in our modelling framework.

Another source of uncertainty in this study is related to the duration of the growing season. A longer growing season implies a longer POD accumulation period and therefore a greater predicted O_3 risk to forests. Although the start and the end

of the growing season may contribute marginally to cumulated O_3 uptake, because physiological activity is lower and climatic constraints on g_s are stronger during these periods, an overestimation of GS length may nonetheless lead to a slight overestimation of rGAI losses.

One final source of uncertainty arises from the assignment of parameterizations based on the KG climate classes. In this framework, species parameterizations are assumed to shift synchronously with changes in climate class, following the emergence of a new 30-year climatological regime. For example, in our simulations, *P. abies* is replaced by *Q. robur/petraea* in large portions of the high latitudes once a change in climate class is detected. In reality, such transitions are likely to occur with a temporal lag. However, the timing of ecosystem shifts is highly uncertain and depends not only on climate change but also on disturbance regimes such as fires (Brice et al., 2019). Given the existing uncertainties on the rates of biome transitions (Stemkovski et al., 2026; Brice et al., 2020; Feeley et al., 2011), we preferred the adoption of a clearer and internally consistent assumption for species reassignment.

5.5 Conclusions

This study provides a global, flux-based assessment of future O_3 risks on forest productivity by explicitly accounting for interactions between air pollution, climate change, and plant physiological responses. Overall, our results indicate a general decline in O_3-related damage to forests (expressed as rGAI) over the 21st century, even under the scenario with weak air-quality and climate mitigation policies (SSP3-7.0). However, such decline is not spatially uniform, but emerges from contrasting regional and biome-specific responses. In particular, boreal forests and mountainous regions surrounding the Tibetan Plateau are projected to become more vulnerable to future O_3 risk than at present times. More broadly, mountain ecosystems may face similar risks because of their functional affinities with boreal forests; however, they could not

be explicitly resolved in this study due to the coarse spatial resolution of the climate and chemistry simulations. Improving the representation of complex topography and associated microclimates, together with fine-scale O_3 fields over mountainous areas, therefore represents an important challenge for future research on O_3 risks to natural ecosystems.

Rising atmospheric CO_2 concentrations emerge as a key factor in the projected decline of O_3 risk. Nonetheless, this mechanism is affected by substantial uncertainty. Experimental evidence on stomatal responses to elevated CO_2 remains limited, species dependent, and costly to obtain, highlighting the need for additional long-term experiments across forest types and climatic conditions. Moreover, uncertainties in CO_2 effects are not confined to O_3 damage estimates but also propagate to broader projections of stomatal conductance, evapotranspiration, and land–atmosphere feedback, with implications for both carbon and water cycles. Climatic controls on stomata further modulate future O_3 risk. Increasing vapor pressure deficit (VPD) acts as an additional constraint on stomatal conductance, globally enhancing forest protection from O_3 uptake. This mechanism, jointly with rising CO_2 concentrations, offsets the increases in O_3 concentrations especially in the tropics, and contributes to the overall decline in projected O_3 damage.

Finally, our results suggest that although O_3 risk to vegetation is likely to decline in the future, its impacts on natural ecosystems are likely to persist for some time before becoming negligible. Continued O_3 exposure may therefore hinder conservation and reforestation efforts and influence key ecosystem processes, including carbon uptake and storage as well as the surface energy balance. Because these processes constitute the core of land-atmosphere biogeochemical interactions, neglecting O_3 damage to vegetation may lead to incomplete process representations of future ecosystem-climate relationships. In this perspective, explicitly integrating O_3 impacts on vegetation into ESMs is essential for the quantification of O_3 not only as an

air pollutant, but also as a contributor to climate-biosphere feedback.

CHAPTER 6

CONCLUSIONS AND FUTURE WORK

This dissertation presented a global, flux-based assessment of O_3 risk to vegetation during the 21st century. By integrating developments in dry deposition modelling, methodological advances, large-scale simulations and plant physiological responses, this work further the understanding of how air-quality policies, climate change, and plant physiology may jointly determine O_3 impacts on ecosystems at future times.

We developed a dual-sink, big-leaf dry deposition model to estimate the phytotoxic ozone dose (POD). The modelling framework was validated and applied to produce spatially resolved maps of O_3 risk to wheat over northern Italy. This regional analysis indicated a moderate risk over the study area. We showed that temperature emerged as the most limiting factor for stomatal conductance across large portions of the study domain, while soil water availability played a key role in constraining the magnitude of POD over specific areas. In addition, higher-altitude areas tended to experience greater O_3 risk, as a consequence of higher atmospheric O_3 concentrations. Together, these results illustrate how environmental constraints can mitigate O_3 risk, even in regions with relatively high O_3 concentrations.

This model was then extended to the global scale and across the 21st century and under different climate change scenarios. Our assessment indicates that O_3 damage to vegetation is projected to decline globally during the 21st century in both wheat and forests. This is only partially due to air-quality improvements; in fact, it is rather evident from the more pessimistic scenarios that, despite rising O_3 concentrations, climatic limitations and elevated CO_2 concentrations can substantially reduce stom-

atal opening and therefore limit O_3 uptake. Nonetheless, O_3 risk is not expected to disappear uniformly across the globe. For instance, South, South-East, and East Asia emerge as regions of increased O_3 risk in the near future for both wheat and forests. Boreal forests may become increasingly vulnerable to O_3 damages in the future, as climate warming sustains stomatal activity and stomatal conductance of boreal species is relatively insensitive to elevated CO_2 concentrations. Montane and submontane regions surrounding the Tibetan Plateau appear particularly vulnerable to future O_3 damages, due to the combined influence of favourable climatic conditions for stomatal uptake and elevated O_3 concentrations. Other regions, including Sub-Saharan Africa and South America, may also emerge as O_3 risk hotspots, depending on regional air-quality policies, climate trajectories, and agricultural practices.

As such, results in this dissertation suggest that O_3 risk to vegetation are likely to persist for several decades and remain significant in specific regions and ecosystems. By comparing simulations based on Earth System Model outputs from experiments with contrasting assumptions about emissions pathways and climatic forcing, our analysis provided a systematic way to understand the relative roles of air-quality policies and climate-driven environmental controls in shaping future O_3 risk. Consequently, our approach allowed identification of regions where reductions in O_3 precursor emissions are likely to be most effective in mitigating crop damage, as well as regions where climatic factors may dominate the future evolution of O_3 uptake. In areas where air-quality policies exert the strongest influence, targeted reductions of precursor emissions could substantially decrease O_3 risk for crops. Conversely, in regions where climatic drivers exert greater control over stomatal activity, the effectiveness of emission reductions alone may be limited, and broader climate mitigation efforts may play a more important role in determining future O_3 impacts on agricultural productivity.

While the main goal of this dissertation was to estimate O_3 risk at future times,

it also provided methodological advances.

As experimental evidence indicates that elevated CO_2 can substantially reduce stomatal conductance and thereby O_3 uptake, quantifying the protective effect of rising future CO_2 concentrations was a key aspect of assessing future O_3 risk in this work. In this context, experimental evidence on the magnitude of this effect remains limited and uncertain, largely due to the high economical cost of experiments under elevated CO_2 conditions. Consequently, a flexible framework was developed to explore alternative assumptions about the CO_2–g_s relationship. By combining theoretical formulations with data-driven constraints, our modelling approach allows the quantification of O_3 risk under different physiological response assumptions, thereby explicitly accounting for a major source of uncertainty in future projections. In particular, this work led to the development of a novel non-linear formulation of the CO_2–stomatal conductance relationship that can be integrated into the Jarvis–Stewart empirical model for stomatal conductance.

Accurate representations of changing agricultural practices (particularly sowing date timing) and vegetation phenology under climate change are critical for reliable O_3 risk assessments throughout the 21st century. While sowing dates were obtained from a previous study, several shortcomings were identified in existing products and models describing the timing of leaf-out and senescence in forest ecosystems. To address this limitation, this dissertation introduced a probabilistic, temperature-based modelling framework capable of estimating the start and end of the forest growing season globally. Our analysis indicates that this model ranks among the top-performing phenological models for forest simulations, reproduces observed changes in growing season duration successfully, and is suitable for applications across diverse forest ecosystems and climatic conditions. Results indicate a substantial extension of the growing season under climate warming, with an increase of approximately one month under low-emission scenarios and up to two months under high-emission sce-

narios by the end of the century relative to preindustrial conditions. Importantly, this methodology is flexible and can be readily extended or adapted to target different phenological phases not only of forests but also of agricultural species.

Based on the findings of this dissertation, new research directions and scientific challenges can be identified.

The most prominent issue concerns the integration of flux-based O_3 damage into broader modelling frameworks, particularly Earth System Models. Because continued O_3 impacts on vegetation in the upcoming decades may influence key processes such as carbon uptake, water fluxes, and surface energy exchanges, coupling O_3 uptake with models that represent plant carbon and water cycles would allow a more consistent representation of biogeochemical feedbacks between land and atmosphere. Particularly, a key scientific challenge is to represent the net effect of multiple, often counteracting, physiological drivers on vegetation productivity. Elevated CO_2 concentrations not only reduce stomatal conductance (and thus O_3 uptake) but also directly stimulate photosynthesis and water-use efficiency, leading to increased net primary productivity (NPP). However, the CO_2 fertilization effect could be partially or fully offset by heat stress, drought, and persistent O_3 damage. Therefore, coupling O_3 uptake schemes with dynamic vegetation models that explicitly simulate carbon assimilation, allocation, and phenology under changing climate and CO_2 would allow ESMs to resolve the competition between CO_2-driven gains and O_3- and climate-driven losses.

A second research direction emerging from this work is the assessment of O_3 risk in mountainous regions. Our analyses consistently indicate elevated O_3 risk at higher elevations, both in the regional application and in the global simulations. Higher background O_3 concentrations at altitude, combined with climatic conditions that can sustain stomatal activity, may increase the vulnerability of mountain ecosystems to O_3 exposure. Since mountains host many relatively undisturbed ecosystems and

biodiversity hotspots, understanding their vulnerability to O_3 pollution may be particularly relevant for conservation strategies. Capturing O_3 risk hotspots in these areas requires high-resolution modelling, which entails multiple scientific challenges, such as obtaining accurate high-resolution meteorological and O_3 fields and improving the representation of transport and deposition processes in complex terrain, where the basic assumptions of surface-layer similarity theory are violated.

Finally, a longstanding scientific and experimental challenge concerns the scalability of O_3 risk assessments across different spatial and biological scales. Experimental studies often quantify plant physiological responses to O_3 exposure at the leaf or chamber scale, whereas field measurements typically assess ecosystem-level fluxes, and large-scale models operate at regional or global scales. Bridging these scales remains difficult because plant responses observed under controlled experimental conditions may not fully capture the complexity of environmental interactions occurring in natural ecosystems. Improving the scalability of O_3 risk assessments will therefore require coordinated efforts combining experimental studies, long-term field and remote-sensing observations, and modelling approaches capable of linking leaf-level physiological processes with ecosystem-scale and global-scale dynamics.

APPENDIX A

FORMULATION OF THE OZONE DRY DEPOSITION MODEL

The following appendix describes the model explicitly. For the meaning of the symbols, please refer to the Table A.5 at the end of this appendix.

A.1 Plant phenology module

Thermal time controls phenological phases and plant development (Campbell & Norman, 1998). Thermal time ([°C d]) at a certain day of the year (DOY) is defined by Eq. A.1 as the cumulated difference between the average daily temperature (T_i; °C) and a plant dependent base temperature (T_0; °C) specific of the considered crop, day by day, from the sowing day ($\mathrm{DOY_{sow}}$) up to the desired DOY. For wheat $T_0 = 0\,°\mathrm{C}$.

$$\mathrm{TT_{sow}}(\mathrm{DOY}) = \sum_{i=\mathrm{DOY_{sow}}}^{\mathrm{DOY}} \max(T_i - T_0,\, 0) \tag{A.1}$$

Each plant development stage is expected to occur when the thermal time reaches some threshold values listed in the literature. The Mapping Manual UN/ECE (LRTAP Convention, 2017) listed those thresholds for wheat but expressed them from the 1st January of the year ($\mathrm{TT_{1J}}$) and not from the sowing day, which is usually 2–3 months before for winter wheat. In our case, sowing date was fixed at the 15th of October 2016 (Baruth et al., 2016). Hence, the threshold values of the Mapping Manual were converted to the respective ones expressed from the sowing day ($\mathrm{TT_{sow}}$), with Eq. A.2.

$$\mathrm{TT_{sow}} = \mathrm{TT_{1J}} + 561 \tag{A.2}$$

where 561 is the average thermal time (°C d) experienced by wheat from sowing to the 1st of January, in every cell determined with the land use map. Table A.1 reports the thermal time thresholds of the phenological phases of wheat expressed form the sowing date. It is also indicated the value of the leaf area index (LAI; $\mathrm{m^2}$ leaf $\mathrm{m^{-2}}$ soil) of the green leaves in each stage. The thermal time progressions for the LAI have been taken from González-Fernández et al. (2013) and Zhang et al. (2018). Phenological observations in the area confirmed the present harvesting parametrization (Vignudelli and Gizzi, 2017, ; Ventura F. personal comm.).

The functions predicting the green LAI and surface area index (SAI; [$\mathrm{m^2}$ plant surface $\mathrm{m^{-2}}$ soil]) value at each thermal time, LAI(TT) and SAI(TT) were obtained by interpolating the TT values with LAI and SAI values listed in Table A.1 with a first order spline.

Values for SAI were obtained considering a ratio between LAI and SAI, set to the constant value 1.42, following the DO3SE model (Emberson et al., 2000). When SAI begins to decline (after TT_{A_2}), SAI does not follow this ratio anymore. Instead, it declines linearly until the harvest, reaching 75% of its maximum value.

The root depth R_d (Williams et al., 1989; m) is given by Eq. A.3.

$$R_d(\mathrm{HUI}) = \min(R_{d,\max}, 2.5 \cdot R_{d,\max} \cdot \mathrm{HUI}) \tag{A.3}$$

where $R_{d,\max} = 1\,\mathrm{m}$ (Fan et al., 2016) is the maximum root depth and Heat Unit Index (HUI) is defined as:

$$\mathrm{HUI} = \frac{\mathrm{TT}}{\mathrm{TT}_{A_{\mathrm{end}}}}$$

The height growth of the wheat was assumed to proportionally follow the SAI. Hence, the height of the canopy h_c was scaled to the maximum plant height $h_{c,\max}$ (set to 1 m for wheat), which is reached when the SAI assumes its maximum value

TABLE A.1

THERMAL TIME THRESHOLDS OF WHEAT PHENOLOGICAL PHASES EXPRESSED FROM THE SOWING DATE. LAI VALUE AT EACH STAGE IS ALSO INDICATED.

Phenological phase	Thermal time (°C d)	LAI	SAI
Emergence	370	0.1	0.14
Tillering	530	0.3	0.43
Stem elongation	900	4.5	6.39
Flag leaf emergence, i.e. start of O_3 accumulation period	1425	6.0	8.52
Phenological phase f_2	1725	6.0	8.52
Phenological phase f_3	2150	4.2	7.01
Harvest, i.e. end of O_3 accumulation period	2325	0.0	6.39

Note: the ozone accumulation will be calculated during the grain filling period, i.e. from anthesis ($\mathrm{TT}_{A_{\mathrm{start}}}$) to harvest ($\mathrm{TT}_{A_{\mathrm{end}}}$).

($\mathrm{SAI}_{\mathrm{max}}$):

$$h_c(\mathrm{SAI}) = \frac{\mathrm{SAI}}{\mathrm{SAI}_{\mathrm{max}}} \cdot h_{c,\mathrm{max}} \qquad [\mathrm{m}] \tag{A.4}$$

A.2 Light module

The quantity of solar radiation intercepted by the canopy influences both the stomatal aperture of sunlit and shaded leaves, and water evaporation from the below canopy soil.

The measured global radiation in the visible waveband Q_{sw} ($\mathrm{W\,m^{-2}}$) is first con-

verted into actual total photosynthetically active radiation $PAR_{\text{tot,act}}$ (W m^{-2}) by multiplying Q_{sw} by 0.45 (Jacovides et al., 2003).

Then $PAR_{\text{tot,act}}$ is partitioned into direct and diffuse radiation to assess the amount of PAR absorbed by sunlit and shaded portions of the canopy. Instead, the near-infrared radiation is not considered since leaves absorb very little radiation in this waveband (Bonan, 2019) compared to the PAR.

Weiss and Norman (Weiss and Norman, 1985) devised a method to estimate direct and diffuse PAR from the measured total radiation. First of all, the potential direct and diffuse PAR ($PAR_{\text{dir,pot}}$, $PAR_{\text{diff,pot}}$; both W m^{-2}) are estimated, i.e. the photosynthetically active radiation which can reach the earth surface at our latitude as direct beam or diffuse radiation:

$$PAR_{\text{dir,pot}} = 600 \cdot \exp\left(-0.185 \left(\frac{P}{P_0}\right) m_{oa}\right) \cdot \sin B \tag{A.5}$$

$$PAR_{\text{diff,pot}} = 0.4 \cdot (600 - PAR_{\text{dir,pot}}) \cdot \sin B \tag{A.6}$$

where $m_{oa} = 1/\sin B$ is the adimensional optical mass of the atmosphere, B is the solar elevation (° over the horizon), and P and P_0 are the measured air pressure and the sea-level pressure, respectively (Pa).

The value 600 is the average amount of visible PAR (W m^{-2}) available at the top of the atmosphere (solar constant = 1320 W m^{-2}); the value 0.185 is the extinction coefficient of the light in the clear atmosphere and 0.4 is the fraction of the intercepted direct PAR that is transformed into diffuse radiation by the surface.

The sum of the potential direct and diffuse PAR gives the total potential PAR ($PAR_{\text{tot,pot}}$). This latter is needed to estimate the measured-to-potential PAR ratio (PAR_{ratio}) from the actual (i.e. measured) total PAR ($PAR_{\text{tot,act}}$). This is achieved through Eq. A.7.

$$PAR_{\text{ratio}} = \min\left\{0.9, \frac{PAR_{\text{tot,act}}}{\max\left\{PAR_{\text{tot,pot}}, PAR_{\text{tot,act}}\right\}}\right\} \tag{A.7}$$

where PAR_{ratio} is capped at 0.9 for domain reasons in Eq. A.8.

The PAR_{ratio} is used to estimate the fractions of direct ($f_{\text{PAR,dir}}$) and diffuse ($f_{\text{PAR,diff}}$) PAR on the total actual PAR by Eq. A.8 and Eq. A.9.

$$f_{\text{PAR,dir}} = \left(\frac{PAR_{\text{dir,pot}}}{PAR_{\text{tot,pot}}}\right) \cdot \left[1 - \left(\frac{0.9 - PAR_{\text{ratio}}}{0.7}\right)^{2/3}\right] \tag{A.8}$$

$$f_{\text{PAR,diff}} = 1 - f_{\text{PAR,dir}} \tag{A.9}$$

By means of Eq. A.8 and Eq. A.9, the actual values of direct PAR ($PAR_{\text{dir,act}}$; $\mathrm{W\,m^{-2}}$) and diffuse PAR ($PAR_{\text{diff,act}}$; $\mathrm{W\,m^{-2}}$) can be estimated, using Eq. A.10 and Eq. A.11.

$$PAR_{\text{dir,act}} = f_{\text{PAR,dir}} \cdot PAR_{\text{tot,act}} \tag{A.10}$$

$$PAR_{\text{diff,act}} = f_{\text{PAR,diff}} \cdot PAR_{\text{tot,act}} \tag{A.11}$$

Direct and diffuse PAR reach sunlit (PAR_{sun}; $\mathrm{W\,m^{-2}}$) and shaded (PAR_{shad}; $\mathrm{W\,m^{-2}}$) green leaves. These quantities are estimated with Eq. A.12 and Eq. A.13, following Norman (1982), who assumed a spherical distribution of leaf angle within the canopy. γ_l in the formula is the leaf angle and is assumed to be 60°.

$$\begin{aligned} PAR_{\text{shad}} = {} & PAR_{\text{diff,act}} \exp\left(-0.5\, LAI^{0.7}\right) \\ & + 0.07\, PAR_{\text{dir,act}}(1.1 - 0.1\, LAI)\exp(-\sin B) \end{aligned} \tag{A.12}$$

$$PAR_{\text{sun}} = PAR_{\text{dir,act}} \cdot 0.8 \cdot \cos(\gamma_l) \cdot \frac{1}{\sin B} + PAR_{\text{shad}} \tag{A.13}$$

The sunlit and shaded LAI ($\mathrm{m^2\,leaf\,m^{-2}\,soil}$) of the canopy are estimated by Eq. A.14 and Eq. A.15 (Norman, 1982).

$$LAI_{\mathrm{sun}} = \left(1 - \exp\left(-0.5 \cdot \frac{LAI}{\sin B}\right)\right) \cdot 2 \sin B \tag{A.14}$$

$$LAI_{\mathrm{shad}} = LAI - LAI_{\mathrm{sun}} \tag{A.15}$$

Finally, the stomatal conductance module requires the photosynthetic photon flux density (PPFD; $\mu\mathrm{mol\,m^{-2}\,s^{-1}}$) instead of PAR ($\mathrm{W\,m^{-2}}$) to calculate the actual value of the stomatal conductance.

PAR is converted into PPFD by multiplying it by a factor 4.57 ($PPFD = 4.57 \cdot PAR$; Sager et al., 1997).

A.3 Stomatal conductance module

Stomatal conductance $g_{s,w}$ ($\mathrm{mmol\,m^{-1}\,PLA^2\,s^{-1}}$) is regulated by environmental factors and it controls both ozone uptake and evapotranspiration. For this application the empirical Jarvis approach (Jarvis, 1976) was adopted and the hourly value of $g_{s,w}$ is obtained by the multiplicative expression Eq. A.16.

$$g_{s,w} = g_{\mathrm{max},w} \cdot \min\left\{f_{\mathrm{phen}}, f_{\mathrm{O_3}}\right\} \cdot f_{\mathrm{light}} \cdot \max\left\{f_{\mathrm{min}}, f_{\mathrm{temp}} \cdot f_{\mathrm{VPD}} \cdot f_{\mathrm{PAW}}\right\} \tag{A.16}$$

where $g_{\mathrm{max},w}$ ($\mathrm{mmol\,m^{-1}\,PLA^2\,s^{-1}}$) is the leaf maximum stomatal conductance to water flux which is determined by plant genetics, and the remaining symbols f_{light}, f_{min}, f_{temp}, f_{VPD}, f_{SW}, f_{phen}, $f_{\mathrm{O_3}}$ are dimensionless functions that describe the $g_{s,w}$ dependence on different environmental variables for a given plant species.

All dimensionless functions have values between 0 and 1 so that the resulting $g_{s,w}$

is a fraction of the maximum stomatal conductance $g_{\max,w}$. Each function is defined on a set of plant-species-specific parameters. Table A.2 shows the parameters adopted for wheat as suggested by the Mapping Manual UN/ECE (LRTAP Convention, 2017). The meaning of each dimensionless function is discussed below.

A.3.1 f_{phen}

The phenological function f_{phen} is a piecewise linear function which describes the evolution of the stomatal conductance across the different growth phases of the crop. Its expression is based on the formula provided by the Mapping Manual UN/ECE (LRTAP Convention, 2017), but its validity has been extended before A_{start} to take into account early evapotranspiration. f_{phen} is a function of the thermal time TT_{1J} (with respect to 1st of January). Fig. A.1 shows the plot of the phenological function f_{phen}, while Eq. A.17 describes each of its six segments.

$$f_{\text{phen}}(TT) = \begin{cases} \dfrac{p_a}{A_{\text{start}}} \cdot TT, & TT < A_{\text{start}} \\ p_a + \dfrac{1 - p_a}{p_1 - A_{\text{start}}} \cdot (TT - A_{\text{start}}), & A_{\text{start}} \leq TT < p_1 \\ 1, & p_1 \leq TT < p_2 \\ 1 + \dfrac{p_e - 1}{p_3 - p_2} \cdot (TT - p_2), & p_2 \leq TT < p_3 \\ p_e + \dfrac{-p_e}{A_{\text{end}} - p_3} \cdot (TT - p_3), & p_3 \leq TT < A_{\text{end}} \\ 0, & TT \geq A_{\text{end}} \end{cases} \tag{A.17}$$

The TT values indicated in Table A.2, following the approach of González-Fernández et al. (2013), are simply expressed from the 1st of January, whereas the Mapping Manual (LRTAP Convention, 2017) refers to mid-anthesis.

TABLE A.2

PARAMETERS FOR WINTER WHEAT (*TRITICUM AESTIVUM*) EMPLOYED IN THE JARVIS' ALGORITHM. THERMAL TIMES ARE WITH RESPECT TO 1ST JANUARY.

Parameter	**Value**	**Description**
$g_{\max,w}$	825 mmol H_2O m^{-2} s^{-1}	Leaf maximum stomatal conductance for water
$light_a$	0.0105	Increasing rapidity of the f_{light} function
T_{opt}	26 °C	Optimal temperature for stomatal opening ($f_{\text{temp}} = 1$)
$T_{\min}$	12 °C	Minimum temperature below which f_{temp} assumes $f_{\min}$ value
$T_{\max}$	40 °C	Maximum temperature above which f_{temp} assumes $f_{\min}$ value
$VPD_{\max}$	1200 Pa	VPD below which f_{VPD} assumes maximum value (=1)
$VPD_{\min}$	3200 Pa	VPD above which f_{VPD} assumes minimum value $f_{\min}$
ΣVPD_{crit}	8000 Pa	Diurnal threshold above which stomata cannot open if humidity rises
PAW_t	50 %	Threshold below which f_{PAW} starts to decrease
a_{O_3}	14	Parameter for f_{O_3}
b_{O_3}	8	Parameter (exponent) for f_{O_3}
A_{start}	875 °day	Start of accumulation period
A_{mid}	1075 °day	Mid-anthesis
A_{end}	1775 °day	End of the accumulation period
p_a	0.3	Fraction of $g_{\max}$ at A_{start}
p_e	0.7	Fraction of $g_{\max}$ at p_3
p_1	875 °day	TT when f_{phen} reaches maximum
p_2	1175 °day	TT when f_{phen} stops being maximum
p_3	1600 °day	TT when f_{phen} is p_e

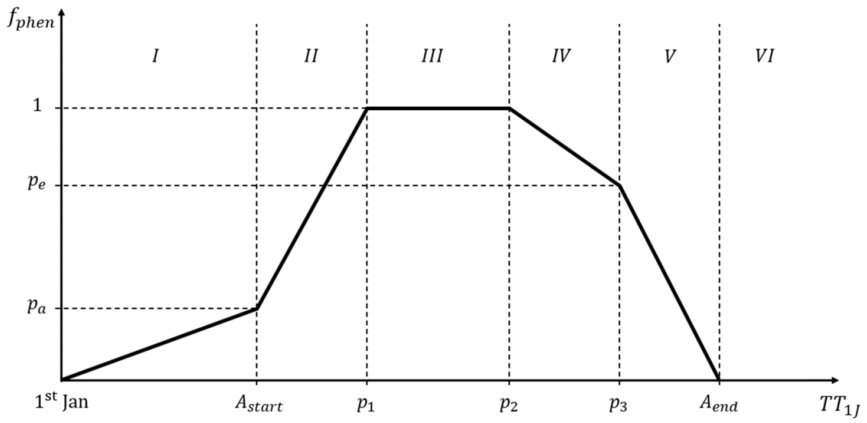

Figure A.1. The phenological function f_{phen}. The constants are constrained such that $A_{\text{start}} \leq p_1 \leq p_2 \leq p_3 \leq A_{\text{end}}$. If necessary, two or more constants may collapse to the nearest one, as long as continuity of f_{phen} is preserved.

A.3.2 3.2 $f_{\text{light}}, f_{\text{temp}}, f_{\text{VPD}}, f_{\text{PAW}}, f_{\text{O}_3}$

The functions f_{light}, f_{temp}, f_{VPD}, f_{PAW}, f_{O_3} are reported respectively in Eq. A.18, Eq. A.19, Eq. A.20, Eq. A.21 and Eq. A.22 and are taken from the Mapping Manual (LRTAP Convention, 2017).

The light function f_{light} describes the dependence of g_w on solar irradiance, expressed as photosynthetic photon flux density PPFD ($\mu\text{mol}\,\text{m}^{-2}\,\text{s}^{-1}$). It is a saturation-like curve where the maximum is reached asymptotically at high irradiances. The rapidity of the initial increase is regulated by the parameter $light_a$ (adim).

The temperature function f_{temp} describes the g_w dependence on air temperature T (°C). The maximum is reached when the air temperature is optimal for the plant species (T_{opt}), while the function is set to its minimum f_{min} when air temperature drops below T_{min} or rises above T_{max}.

The VPD function f_{VPD} describes the g_w dependence on air humidity expressed as vapour pressure deficit VPD (Pa). f_{VPD} assumes its maximum value when VPD is below VPD_{max}, its minimum value f_{min} when VPD is above VPD_{min}, and declines

linearly between $VPD_{\max}$ and $VPD_{\min}$. Following Uddling et al. (2004), when the cumulative VPD from dawn (ΣVPD) exceeds the critical threshold ΣVPD_{crit}, f_{VPD} is capped at 92% of the previous hour's value.

The plant available water function f_{PAW} describes the g_w dependence on soil humidity, expressed as Plant Available Water (PAW, %). PAW is the soil available water content relative to the maximum water holding capacity. $f_{\text{PAW}} = 1$ as long as $PAW \geq PAW_t$ and declines linearly to zero below that threshold. See Eq. 62 for a more detailed definition of PAW.

The ozone function f_{O_3} describes the decline of g_w following early leaf senescence due to ozone uptake. It requires the phytotoxic ozone dose POD_0 (nmol m^{-2} PLA) assumed by leaves up to the previous hour. See Eq. 53 for the definition of POD_0.

$$f_{\text{light}} = 1 - \exp(-light_a \cdot PPFD) \tag{A.18}$$

$$f_{\text{temp}} = \max\left\{f_{\min}, \frac{T - T_{\min}}{T_{\text{opt}} - T_{\min}} \cdot \left(\frac{T_{\max} - T}{T_{\max} - T_{\text{opt}}}\right)^b\right\}, \quad b = \frac{T_{\max} - T_{\text{opt}}}{T_{\text{opt}} - T_{\min}} \tag{A.19}$$

$$f_{\text{VPD}} = \min\left\{1, \max\left[f_{\min}, f_{\min} + (1 - f_{\min}) \cdot \frac{VPD_{\min} - VPD}{VPD_{\min} - VPD_{\max}}\right]\right\} \tag{A.20}$$

$$f_{\text{PAW}} = \begin{cases} \text{I)}\ 1 + \dfrac{PAW - PAW_t}{PAW_t}, & PAW < PAW_t \\ \text{II)}\ 1, & PAW \geq PAW_t \end{cases} \tag{A.21}$$

$$f_{\text{O}_3} = \frac{1}{1 + \left(\dfrac{POD_0}{a_{O_3}}\right)^{b_{O_3}}} \tag{A.22}$$

A.3.3 Stomatal conductance

Since the canopy is partly shaded and partly sunlit, Eq. A.16 is computed twice. The first time using PAR_{sun} (Eq. A.13) to obtain the PPFD; the second time using PAR_{shad} (Eq. A.12). The stomatal conductance for the sunlit canopy, $g_{sw,\text{sun}}$, and the shaded part of the canopy, $g_{sw,\text{shad}}$, are obtained respectively. The actual stomatal conductance for water, $g_{\text{act},w}$, is then obtained by weighting $g_{sw,\text{sun}}$ and $g_{sw,\text{shad}}$ according to the respective portions of LAI, LAI_{sun} and LAI_{shad}.

$$g_{\text{act},w} = \frac{g_{sw,\text{sun}} \cdot LAI_{\text{sun}} + g_{sw,\text{shad}} \cdot LAI_{\text{shad}}}{LAI} \tag{A.23}$$

Finally, the actual stomatal conductance for ozone, $g_{\text{act},\text{O}_3}$, is obtained by multiplying the actual stomatal conductance for water $g_{\text{act},w}$ by 0.66, which is the ratio between the diffusivities of ozone and water in air (Massman, 1998):

$$g_{\text{act},\text{O}_3} = 0.66 \cdot g_{\text{act},w} \tag{A.24}$$

A.4 Atmosphere module

This module describes the calculation of thermodynamic variables, the resistive network, and the atmosphere stability indicators. Moreover, it scales ozone concentrations to the canopy height and computes ozone fluxes and evapotranspiration. Table A.3 reports the constants used in this module.

A.4.1 Calculations of thermodynamic variables

A range of thermodynamic variables are calculated. The saturated vapor pressure at air temperature T, $e_{\text{sat}}(T)$, is obtained with the Tetens-Murray formula (Murray, 1967), Eq. A.25. Then the actual vapor pressure $e(T)$, the slope of the Clausius-Clapeyron curve Δ, the specific humidity q, the air density ρ, and the specific heat of

TABLE A.3

CONSTANTS USED IN THE ATMOSPHERE MODULE.

Constant	**Value**	**Description**
κ	0.41	von Kármán constant
Pr	0.70673	Prandtl number
g	9.8067 $\mathrm{m\,s^{-2}}$	Gravity
M_{dry}	29 g $\mathrm{mol^{-1}}$	Molar mass of dry air
M_w	18 g $\mathrm{mol^{-1}}$	Molar mass of water
R	8.314472 J $\mathrm{mol^{-1}\ K^{-1}}$	Universal gas constant
$D_{w,\mathrm{STP}}$	0.2178 $\mathrm{cm^2\ s^{-1}}$	Diffusion coefficient of water in air at $T = 0°\mathrm{C}$, $P = 1$ atm
$D_{O_3,\mathrm{STP}}$	0.1444 $\mathrm{cm^2\ s^{-1}}$	Diffusion coefficient of ozone in air at $T = 0°\mathrm{C}$, $P = 1$ atm
$D_{H,\mathrm{STP}}$	0.18055 $\mathrm{cm^2\ s^{-1}}$	Diffusion coefficient of heat in air at $T = 0°\mathrm{C}$, $P = 1$ atm
$c_{p,\mathrm{std}}$	1004.8 J $\mathrm{kg^{-1}\ K^{-1}}$	Specific heat of dry air
γ	67 Pa $\mathrm{K^{-1}}$	Psychrometric constant

air at constant pressure c_p are calculated using Eq. A.26 to Eq. A.29. The latent heat of vaporization λ is derived from regression of Table A.3 of Monteith and Unsworth (2013), Eq. A.31. The psychrometric constant γ is given by Eq. A.32. The diffusivities of water D_W and ozone D_{O_3} in air are calculated using Massman (1998), Eq. A.33 and Eq. A.34. The Schmidt numbers for water (Sc_W) and ozone (Sc_{O_3}) are calculated using Eq. A.35 and Eq. A.36 (Hicks et al., 1987). All temperatures are absolute (K), and $\nu(T)$, the kinematic viscosity of air, is determined by linear interpolation from Monteith and Unsworth (2013).

$$e_{\text{sat}}(T) = \begin{cases} 611 \cdot \exp\left[17.269 \cdot \frac{T-273}{T-36}\right], & T > 273.15 \text{ K} \\ 611 \cdot \exp\left[21.875 \cdot \frac{T-273}{T-8.15}\right], & T \leq 273.15 \text{ K} \end{cases} \qquad [\text{Pa}] \tag{A.25}$$

$$e(T) = e_{\text{sat}}(T) \cdot \frac{RH}{100} \qquad [\text{Pa}] \tag{A.26}$$

$$\Delta = \begin{cases} e_{\text{sat}}(T) \cdot \frac{17.269 \cdot 237.3}{(T-36)^2}, & T > 273.15 \text{ K} \\ e_{\text{sat}}(T) \cdot \frac{21.875 \cdot 265.5}{(T-8.15)^2}, & T \leq 273.15 \text{ K} \end{cases} \qquad [\text{Pa K}^{-1}] \tag{A.27}$$

$$q = \frac{0.622 \cdot e}{P - e + 0.622 \cdot e} \qquad [\text{kg}_{\text{H}_2\text{O}}\,\text{kg}_{\text{air}}^{-1}] \tag{A.28}$$

$$\rho = \frac{P \cdot M_{\text{dry}}}{R \cdot T \cdot (1 + 0.61 \cdot q)} \cdot \frac{1}{1000} \qquad [\text{kg m}^{-3}] \tag{A.29}$$

$$c_p = c_{p,\text{std}} \cdot (1 + 0.84 \cdot q) \qquad [\text{J kg}^{-1}\,\text{K}^{-1}] \tag{A.30}$$

$$\lambda = -2733.33333 \cdot (T - 273.15) + 2501333.33333 \qquad [\text{J kg}^{-1}] \tag{A.31}$$

$$\gamma = \frac{c_p \cdot P}{0.622 \cdot \lambda} \qquad [\text{Pa K}^{-1}] \tag{A.32}$$

$$D_W = D_{W,\text{STP}} \cdot \frac{101325}{P} \cdot \left(\frac{T}{273.15}\right)^{1.81} \qquad [\text{cm}^2\ \text{s}^{-1}] \tag{A.33}$$

$$D_{O_3} = D_{O_3,\text{STP}} \cdot \frac{101325}{P} \cdot \left(\frac{T}{273.15}\right)^{1.81} \qquad [\text{cm}^2\ \text{s}^{-1}] \tag{A.34}$$

$$Sc_W = \nu / D_W \cdot 10^4 \qquad [\text{adim}] \tag{A.35}$$

$$Sc_{O_3} = \nu / D_{O_3} \cdot 10^4 \qquad [\text{adim}] \tag{A.36}$$

A.5 Geometries

Measurement height, surface type, and canopy height affect a variety of atmospheric parameters, particularly the resistance network. Table A.4 reports the measurement heights assumed for ozone, temperature, relative humidity, and wind speed.

The roughness length and displacement height are related to the canopy height h_c. The roughness length for momentum is set to (Brutsaert, 1982)

$$z_{0m} = 0.13 \cdot h_c$$

and the displacement height to (Campbell and Norman, 1998)

$$d = 0.65 \cdot h_c$$

TABLE A.4

MEASUREMENT HEIGHTS USED FOR ATMOSPHERIC PARAMETERS.

Parameter	**Value**	**Description**
z_{mO_3}	2 m	Measurement height for ozone
z_{mT}	2 m	Measurement height for temperature and relative humidity
z_{mw}	3 m	Measurement height for wind speed

A.6 Estimation of energy fluxes and atmospheric stability

Net radiation (R_n) and sensible heat flux (H) are needed to calculate atmospheric stability and evapotranspiration. They are calculated using a cloud cover index N (Holtslag and Van Ulden, 1983; Gerosa et al., 2017).

$$N = \min\left\{1, \sqrt{3.4 \cdot \max\left[0, \frac{1}{0.74}\left(1 - \frac{Q_{sw}}{990 \cdot \sin(B) - 30}\right)\right]}\right\} \qquad \text{[adim]} \qquad \text{(A.37)}$$

Net radiation and sensible heat flux are then obtained as:

$$R_n = \frac{(1 - A) \cdot Q_{sw} + c_1 \cdot T^6 - \sigma \cdot T^4 + c_2 \cdot N}{1 + c_3} \qquad [\mathrm{W\,m^{-2}}] \qquad \text{(A.38)}$$

$$H = \begin{cases} -\alpha\beta, & Q_{sw} < 50 \\ \dfrac{1 - \alpha + S}{1 + S} \cdot (R_n - G) - \alpha\beta, & Q_{sw} \geq 50 \end{cases} \qquad [\mathrm{W\,m^{-2}}] \qquad \text{(A.39)}$$

Here, $A = 0.2$ is the wheat albedo (Yeşilköy et al., 2015), $G = 0.1 \cdot R_n$ is the ground heat flux fraction, $S = 1.5 \cdot \exp(-0.060208041 \cdot T)$, $c_1 = 5.31 \cdot 10^{-13}$ $\mathrm{W\,m^{-2}\,K^{-6}}$,

$c_2 = 60\ \mathrm{W\,m^{-2}}$, $c_3 = 0.38 \cdot ((1-\alpha) \cdot S + 1)/(S+1)$, and $\sigma = 5.67\ \mathrm{W\,m^{-2}\,K^{-4}}$ is the Stefan-Boltzmann constant.

A.6.1 Friction velocity and Obukhov length

The friction velocity u_* is calculated depending on atmospheric stability (Hanna and Chang, 1993). If $H < -1$ (stable):

$$u_* = f_1 \cdot \Big(1 + \sqrt{f_2}\Big), \tag{A.40}$$

with $f_1 = \frac{0.5 \cdot \kappa \cdot u(z_{mw})}{\log \frac{z_{mw}-d}{z_{0m}}}$, $f_2 = 1 - \frac{4 \cdot (4.7 \cdot g \cdot z_{mw} \cdot \theta_* \cdot \log((z_{mw}-d)/z_{0m}))}{\kappa \cdot T \cdot u(z_{mw})^2}$,
and $\theta_* = \min\Big\{0.09 \cdot (1 - 0.5 \cdot N^2), \frac{\kappa \cdot T \cdot u(z_{mw})^2}{18.8 \cdot g \cdot z_{mw} \cdot \log((z_{mw}-d)/z_{0m})}\Big\}$.

If $-1 \leq H < 1$ (neutral):

$$u_* = \frac{\kappa \cdot u(z_{mw})}{\log((z_{mw}-d)/z_0)} \tag{A.41}$$

If $H \geq 1$ (unstable):

$$u_* = \frac{\kappa \cdot u(z_{mw})}{\log((z_{mw}-d)/z_{0m})} \cdot \big(1 + d_1 \cdot \log(1 + d_2 \cdot d_3)\big), \tag{A.42}$$

with $d_1 = \begin{cases} 0.128 + 0.005/\log((z_{mw}-d)/z_{0m}), & z_0/(z_{mw}-d) \leq 0.01 \\ 0.107, & z_0/(z_{mw}-d) > 0.01 \end{cases}$,
$d_2 = 1.95 + 32.6 \cdot (z_{0m}/(z_{mw}-d))^{0.45}$, and $d_3 = \frac{H}{c_p \rho} \frac{\kappa g (z_{mw}-d)}{T} \left(\frac{\log((z_{mw}-d)/z_{0m})}{\kappa u(z_{mw})}\right)^3$.

The Obukhov length L (m) is calculated as:

$$L = -\frac{u_*^3}{\kappa \cdot g/T \cdot H/(\rho \cdot c_p)} \tag{A.43}$$

The wind speed at the top of the canopy $u(h_c)$ ($\mathrm{m\,s^{-1}}$) is:

$$u(h_c) = \frac{u_*}{\kappa}\Big[\ln\frac{h_c-d}{z_{0m}} - \Psi_m\Big(\frac{h_c-d}{L}\Big) + \Psi_m\Big(\frac{z_{0m}}{L}\Big)\Big] \tag{A.44}$$

The stability functions for momentum $\Psi_m(\zeta)$ and scalars $\Psi_H(\zeta)$ are (Bonan, 2019):

$$\Psi_m(\zeta) = \begin{cases} \ln\Big[\frac{1+x^2}{2}\Big(\frac{1+x}{2}\Big)^2\Big] - 2\arctan(x) + \pi/2, & \zeta < 0 \\ -5\zeta, & \zeta \geq 0 \end{cases} \tag{A.45}$$

with $x = (1-16\zeta)^{1/4}$.

$$\Psi_H(\zeta) = \begin{cases} 2\ln\Big[\frac{1+y^2}{2}\Big], & \zeta < 0 \\ -5\zeta, & \zeta \geq 0 \end{cases} \tag{A.46}$$

with $y = (1-16\zeta)^{1/4}$.

A.7 Resistive network

The resistive network describing ozone deposition pathways and water evaporation is derived from Wesely (1989) (Fig. 2 in main paper).

The atmospheric resistance $R_{aH}(z_1, z_2)$ ($\mathrm{s\,m^{-1}}$) for the transfer of a scalar (heat, water, ozone) between two heights z_1 and z_2 ($z_1 < z_2$) is (Bonan, 2019):

$$R_{aH}(z_1, z_2) = \frac{1}{\kappa\, u_*}\Big[\ln\frac{z_2-d}{z_1-d} - \Psi_H\Big(\frac{z_2-d}{L}\Big) + \Psi_H\Big(\frac{z_1-d}{L}\Big)\Big] \tag{A.47}$$

In our context, R_{aH} is calculated between the height $d + z_{0m}$ (where wind speed is expected to be zero) and the measuring heights z_{mO_3}, z_{mT}.

The quasi-laminar resistance for heat in the whole canopy, R_{bH}, is (Hicks et al., 1987):

$$R_{bH} = \frac{2}{\kappa u_*} \tag{A.48}$$

Resistances for ozone (R_{bO_3}) and water (R_{bw}) transfer are obtained by multiplying R_{bH} by $(Sc/Pr)^{2/3}$, where Sc is the Schmidt number for ozone (Eq. A.36) or water (Eq. A.35).

The cuticular resistance for ozone deposition on one leaf is $r_{\mathrm{cut,O_3}} = 2500$ s m^{-1} (LRTAP Convention, 2017). The stomatal resistances are reciprocals of the corresponding stomatal conductances:

$$r_{s,O_3} = \frac{1}{g_{\mathrm{act,O_3}}}, \quad r_{s,w} = \frac{1}{g_{\mathrm{act,w}}}$$

Lowercase indicates "one-leaf level resistances", uppercase indicates "bulk canopy resistances".

The in-canopy resistance for scalar transfer is:

$$R_{\mathrm{inc}} = \frac{14 \cdot \mathrm{LAI} \cdot h_c}{u_*} \qquad [\mathrm{s\ m^{-1}}] \tag{A.49}$$

The soil resistance is $R_{\mathrm{soil,w}} = R_{\mathrm{soil,O_3}} = 200$ s m^{-1}.

The overall surface resistance to ozone deposition, $R_{\mathrm{surf,O_3}}$, is:

$$R_{\mathrm{surf,O_3}} = \left[\frac{\mathrm{LAI}}{r_{s,O_3}} + \frac{\mathrm{SAI}}{r_{\mathrm{cut,O_3}}} + \frac{1}{R_{\mathrm{inc}} + R_{\mathrm{soil,O_3}}} \right]^{-1} \qquad [\mathrm{s\ m^{-1}}] \tag{A.50}$$

The leaf-level boundary-layer resistance for heat is:

$$r_{bH} = 150 \cdot \sqrt{\frac{L_d}{u(h_c)}} \qquad [\mathrm{s\ m^{-1}}] \tag{A.51}$$

Leaf-level ozone resistance $r_{bO_3} = 1.3 \cdot r_{bH}$, and leaf-level water resistance $r_{bW} = 0.828 \cdot r_{bH}$.

A.8 Ozone concentrations and fluxes to one uppermost leaf

Ozone concentration at canopy height $O_3(h_c)$ is:

$$O_3(h_c) = O_3(z_{mO_3}) \cdot \left[1 - \frac{R_{aH}(h_c, z_{mO_3})}{R_{aH}(d + z_{0m}, z_{mO_3}) + R_{bO_3} + R_{\mathrm{surf,O_3}}}\right] \qquad \text{[ppb]} \quad \text{(A.52)}$$

The ozone stomatal flux for an uppermost leaf of unit LAI (LAI = 1) is:

$$F_{sO_3} = O_3(h_c) \cdot \frac{1}{r_{s,O_3}} \cdot \left(1 - \frac{r_{bO_3}}{r_{bO_3} + r_c}\right), \qquad \text{(A.53)}$$

with

$$r_c = \left[\frac{1}{r_{s,O_3}} + \frac{1}{r_{\mathrm{cut,O_3}}}\right]^{-1} \qquad \text{[ppb m s}^{-1}\text{ PLA]}$$

To convert F_{sO_3} into nmol m^{-2} s^{-1} PLA, multiply by $P/(\mathcal{R}\,T)$, where P is air pressure, T is air temperature, and $\mathcal{R}$ is the universal gas constant (LRTAP Convention, 2017).

The phytotoxic ozone dose for wheat, $\mathrm{POD_6}$, is the cumulative stomatal flux above a threshold of 6 nmol m^{-2} s^{-1}:

$$\mathrm{POD_6} = \sum_{i=0}^{t} \max\left(0, \frac{(F_{sO_3,i} - 6) \cdot 3600}{10^6}\right) \qquad \text{[mmol m}^{-2}\text{ PLA]} \qquad \text{(A.54)}$$

Here, $F_{sO_3,i}$ are hourly stomatal fluxes and $3600/10^6$ converts from nmol s^{-1} to mmol h^{-1}.

A.9 Water fluxes

Water losses by evapotranspiration are required to estimate the soil water content in the Soil Module. Transpiration of the canopy, evaporation from wet surfaces, and

from the soil below the canopy are calculated following Penman-Monteith (Monteith, 1965), which assumes closure of the surface energy balance.

The transpiration of the whole canopy, E_{can} (W m^{-2}), is:

$$E_{\text{can}} = \frac{\rho\, c_p\, \frac{e_{\text{sat}}(T_{z_{mT}}) - e}{R_{aH}(d+z_{0m}, z_{mT}) + R_{bH}} + \Delta\,(R_n - G)}{\Delta + n\,\gamma\, \frac{R_{aH}(d+z_{0m}, z_{mT}) + R_{bw} + r_{sw}/\text{LAI}}{R_{aH}(d+z_{0m}, z_{mT}) + R_{bH}}} \tag{A.55}$$

where e and $e_{\text{sat}}(T_{z_{mT}})$ are the actual and saturated vapor pressures at measurement height z_{mT}, R_n is net radiation (Eq. A.38), G is ground heat flux ($0.1\,R_n$), R_{aH} is the atmospheric resistance for scalars, R_{bH} and R_{bw} are quasi-laminar resistances, $r_{sw} = g_{\text{act,w}}^{-1}$, ρ, c_p, Δ, γ are defined in Eqs. A.29, A.30, A.27, A.32, LAI is leaf area index, and n is 2 for hypostomatous plants such as wheat.

During rain episodes, intercepted rain evaporates from wet surfaces. Maximum interception is $0.1 \cdot \text{LAI}$ (Sellers et al., 1996), and evaporation from wet surfaces, E_{wet} (W m^{-2}), occurs only during rain or within one hour after, with $n = 2$:

$$E_{\text{wet}} = \frac{\rho\, c_p\, \frac{e_{\text{sat}}(T_{z_{mT}}) - e}{R_{aH}(d+z_{0m}, z_{mT}) + R_{bH}} + \Delta\,(R_n - G)}{\Delta + n\,\gamma\, \frac{R_{aH}(d+z_{0m}, z_{mT}) + R_{bw}}{R_{aH}(d+z_{0m}, z_{mT}) + R_{bH}}} \tag{A.56}$$

Evaporation from soil below the canopy, E_{soil} (W m^{-2}), occurs only when plant available water (PAW) exceeds 50%, with $n = 2$:

$$E_{\text{soil}} = \frac{\rho\, c_p\, \frac{e_{\text{sat}}(T_{z_{mT}}) - e}{R_{aH}(d+z_{0m}, z_{mT}) + R_{bH} + R_{\text{inc}}} + \Delta\,(R_{n,\text{soil}} - G)}{\Delta + n\,\gamma\, \frac{R_{aH}(d+z_{0m}, z_{mT}) + R_{bw} + R_{\text{inc}} + R_{\text{soil,w}}}{R_{aH}(d+z_{0m}, z_{mT}) + R_{bH} + R_{\text{inc}}}} \tag{A.57}$$

Here, $R_{n,\text{soil}} = R_n\, e^{-\kappa\,\text{LAI}}$ (with $\kappa = 0.65$, Williams et al., 1989) is the net radiation at the soil, R_{inc} is the in-canopy resistance, and $R_{\text{soil,w}}$ is the soil resistance to water evaporation.

Evaporation fluxes are converted to hourly mm by dividing by λ (latent heat of vaporization) and multiplying by 3600.

A.10 Soil Module

The soil is represented by a simple bucket model (Mintz and Walker, 1993).

The maximum water holding content (MWHC, mm) is:

$$\mathrm{MWHC} = 1000\, R_d\, (\theta_{\mathrm{FC}} - \theta_{\mathrm{WP}}) \qquad [\mathrm{mm}] \tag{A.58}$$

where θ_{FC} and θ_{WP} are volumetric water contents at field capacity and wilting point, respectively.

The maximum canopy storage is:

$$S_{c,\max} = 0.1 \cdot \mathrm{LAI} \qquad [\mathrm{mm}] \tag{A.59}$$

The current stored water on the canopy is:

$$S_{c,i} = \min\Big(S_{c,\max}, \max(p + S_{c,i-1} - E_{\mathrm{wet}}, 0)\Big) \qquad [\mathrm{mm}] \tag{A.60}$$

Water reaching the soil is:

$$W_{\mathrm{in}} = \max(p + S_{c,i-1} - E_{\mathrm{wet}} - S_{c,\max}, 0) \qquad [\mathrm{mm}] \tag{A.61}$$

The current available water content for plants, AWC_i, is:

$$AWC_i = W_{\mathrm{in}} - E_{\mathrm{can}} - E_{\mathrm{soil}} + AWC_{i-1} \qquad [\mathrm{mm}] \tag{A.62}$$

AWC is initialized at MWHC on 1st January.

The plant available water (PAW, %) is:

$$PAW_i = \frac{AWC_i}{\mathrm{MWHC}} \cdot 100 \qquad [\%] \tag{A.63}$$

A.11 Unit Conversions

From time to time, unit conversions are necessary. Eq. (A.64) converts ozone fluxes from $\mathrm{ppb\,m\,s^{-1}}$ to $\mathrm{nmol\,m^{-2}\,s^{-1}}$, with T air temperature (K) and R universal gas constant ($\mathrm{J\,mol^{-1}\,K^{-1}}$). Eq. (A.65) converts conductance from $\mathrm{m\,s^{-1}}$ to $\mathrm{mmol\,m^{-2}\,s^{-1}}$. Evapotranspiration fluxes are converted from $\mathrm{W\,m^{-2}}$ to mass units $\mathrm{kg_{H2O}\,m^{-2}\,s^{-1}}$ using λ latent heat of vaporization (Eq. A.31). To convert from $\mathrm{kg\,m^{-2}\,s^{-1}}$ to hourly $\mathrm{mm\,h^{-1}}$, multiply by 3600.

$$F_{[\mathrm{nmol\ m^{-2}\ s^{-1}}]} = F_{[\mathrm{ppb\ m\ s^{-1}}]} \cdot \frac{P}{RT} \tag{A.64}$$

$$g_{\mathrm{stom}}\ [\mathrm{mmol\,m^{-2}\,s^{-1}}] = g_{\mathrm{stom}}\ [\mathrm{m\,s^{-1}}] \cdot 10^3 \cdot \frac{P}{RT} \tag{A.65}$$

$$E_{[\mathrm{kg_{H2O}\,m^{-2}\,s^{-1}}]} = \frac{E_{[\mathrm{W\,m^{-2}}]}}{\lambda} \tag{A.66}$$

TABLE A.5

LIST OF SYMBOLS OF VARIABLES

Symbol	**Name**	**Units**
A	Albedo	adim
B	Solar elevation	$^\circ$
c_p	Specific heat of air at constant pressure	$\mathrm{J\,kg^{-1}\,K^{-1}}$
DOY	Day of the year	day
d	Displacement height	m
D_w, D_{O_3}	Diffusivities of water and ozone	$\mathrm{cm^2\,s^{-1}}$
Δ	Slope of Clausius-Clapeyron curve	$\mathrm{Pa\,K^{-1}}$
E	Evaporation or transpiration	$\mathrm{W\,m^{-2}}$

TABLE A.5 (CONTINUED)

Symbol	**Name**	**Units**
e, e_{sat}	Actual and saturated vapor pressure	Pa
f_{phen}	Phenological function	adim
F_{sO_3}	Ozone stomatal flux per unit leaf area	$\text{nmol}\,\text{m}^{-2}\,\text{LAI}\,\text{s}^{-1}$
G	Ground heat flux	$\text{W}\,\text{m}^{-2}$
$g_{s,w}, g_{s,O_3}$	Stomatal conductance for water and ozone	$\text{mmol}\,\text{H2O}\,\text{m}^{-2}\,\text{PLA}\,\text{s}^{-1}$
$g_{\text{act,w}}, g_{\text{act,O}_3}$	Actual stomatal conductance weighted for sunlit and shaded canopy fractions	$\text{mmol}\,\text{H2O}\,\text{m}^{-2}\,\text{PLA}\,\text{s}^{-1}$
γ	Psychrometric constant	$\text{Pa}\,\text{K}^{-1}$
H	Sensible heat flux	$\text{W}\,\text{m}^{-2}$
h_c	Canopy height	m
LAI	Leaf Area Index (Plant Area Index, PLA)	$\text{m}^2\,\text{leaf}\,\text{m}^{-2}\,\text{soil}$
LAI_{sun}, LAI_{shad}	Sunlit and shaded LAI	$\text{m}^2\,\text{leaf}\,\text{m}^{-2}\,\text{soil}$
λ	Latent heat of vaporization	$\text{J}\,\text{kg}^{-1}$
N	Cloud cover index	adim
$O(z)$	Ozone concentration at height z	ppb
P	Pressure	Pa
PAR	Photosynthetically Active Radiation	$\text{W}\,\text{m}^{-2}$
PAW	Plant available water	%
POD_Y	Phytotoxic Ozone Dose above threshold Y	$\text{mmol}\,\text{O3}\,\text{m}^{-2}\,\text{PLA}$
Ψ_m, Ψ_H	Stability functions for momentum and scalars	adim
q	Specific humidity	$\text{kg}_{\text{H}}\text{2O}\,\text{kg}_{\text{a}}\text{ir}^{-1}$
Q_{sw}	Global short-wave radiation	$\text{W}\,\text{m}^{-2}$
R_{aH}	Aerodynamic resistance	$\text{s}\,\text{m}^{-1}$
R_b	Quasi-laminar resistance	$\text{s}\,\text{m}^{-1}$
R_d	Root depth	m
R_{inc}	In-canopy scalar resistance	$\text{s}\,\text{m}^{-1}$
R_{soil}	Soil resistance	$\text{s}\,\text{m}^{-1}$

TABLE A.5 (CONTINUED)

Symbol	**Name**	**Units**
R_{surf}	Bulk surface resistance to deposition	$\text{s}\,\text{m}^{-1}$
r_b	Leaf boundary-layer resistance	$\text{s}\,\text{m}^{-1}$
r_{cut}	Cuticular resistance to ozone deposition	$\text{s}\,\text{m}^{-1}$
$r_{s,w}, r_{s,O_3}$	One-leaf stomatal resistance	$\text{s}\,\text{m}^{-1}$
RH	Relative humidity	%
R_n	Net radiation	$\text{W}\,\text{m}^{-2}$
ρ	Air density	$\text{kg}\,\text{m}^{-3}$
SAI	Surface Area Index	$\text{m}^2\,\text{plant}\,\text{m}^{-2}\,\text{soil}$
Sc	Schmidt number	adim
S_c	Canopy water storage	mm
T	Air temperature	K
TT_{sow}, TT_{1J}	Thermal time from sowing and from 1st January	$^\circ\text{C}\,\text{day}$
$u(z)$	Wind speed at height z	$\text{m}\,\text{s}^{-1}$
u^*	Friction velocity	$\text{m}\,\text{s}^{-1}$
VPD	Vapor pressure deficit	Pa
z_{0m}	Roughness length for momentum	m
z_{0H}	Roughness length for heat, water, ozone	m
z_{mO_3}, z_{mT}, z_{mw}	Measurement heights for ozone, temperature/humidity, wind	m

APPENDIX B

APPENDIX OF GLOBAL FLUX-BASED ASSESSMENT REVEALS DECLINING OZONE RISK FOR WHEAT IN FUTURE CLIMATE CHANGE SCENARIOS

B.1 Conversion from model levels to geometric height above the ground

The conversion from model levels to geometric height above the ground is achieved using the hydrostatic assumption and integrating the following equation from the surface pressure to the actual pressure at the model level:

$$dz = \frac{R_d T_v(p)}{gp}\, dp \tag{B.1}$$

Here, p denotes pressure, $R_d = 287\,\mathrm{J\,kg^{-1}\,K^{-1}}$ is the specific gas constant of dry air, $g = 9.81\,\mathrm{m\,s^{-2}}$ is the acceleration due to gravity and it is assumed constant since calculations are performed for the model levels closest to the ground, and thus there is no need to incorporate geopotential height. $T_v(p)$ [K] denotes the virtual temperature profile, obtained by interpolating between model levels after converting the values from air temperature T [K] through

$$T_v = T\,(1 + 0.609133q)\,, \tag{B.2}$$

with q being the specific humidity [$\mathrm{kg_{H_2O}\,kg_{air}^{-1}}$].

This method is necessary for GFDL-ESM4. On the other hand, UKESM1-0-LL explicitly indicates that the near-surface model level for O_3 concentration is at 20 m above the ground (mid-point of the lowest vertical level), and therefore no calculation for geometric height is required.

B.2 ESM meteorology bias, evaluation of O_3 concentration bias in input, and effect on POD_6 estimates

ESM simulations show biases in both meteorological variables and O_3 concentrations, which may affect the final POD estimates. Specifically, Sellar et al. (2019) reported that UKESM1 displays a

cold bias in both DJF (December–January–February) and JJA (June–July–August) seasons, ranging between $-2\,^{\circ}\mathrm{C}$ and $2\,^{\circ}\mathrm{C}$ for both hemispheres during summer. For this model, precipitation mean bias over land during summer typically ranges between -2 and 2 $\mathrm{mm\,d^{-1}}$ but is larger in specific areas (e.g. up to $-8\,\mathrm{mm\,d^{-1}}$ in South Asia during JJA, and between $-8\,\mathrm{mm\,d^{-1}}$ and $8\,\mathrm{mm\,d^{-1}}$ in South America during DJF). Dunne et al. (2020) showed that GFDL-ESM4 is also globally biased towards colder temperatures ($-0.526\,^{\circ}\mathrm{C}$), with a range between -3 and 2 $^{\circ}\mathrm{C}$ for most of the globe. The precipitation bias is quite small for this model (mostly between -1 and 1 $\mathrm{mm\,d^{-1}}$), with features that are similar to UKESM1 (e.g. larger dry bias over South Asia). Dunne et al. (2020) also evaluated relative humidity and found biases that are generally between $-10\,\%$ and $10\,\%$, with larger biases over Siberia and North America (up to $25\,\%$).

The bias of the O_3 concentrations from the ESMs models is evaluated against the surface O_3 observations from the Tropospheric Ozone Assessment Report (TOAR) dataset (Schröder et al., 2021) for the baseline years (2000–2014). For each measurement station, the mean bias (MB) is defined as:

$$\mathrm{MB}(x) = \frac{\sum_{t=1}^{n} [M(x,t) - O(x,t)]}{n} \tag{B.3}$$

where x indicates the station location, and $t = 1, \ldots, n$ are the considered timesteps (daylight hours, over the POD accumulation period for that location). $O(x,t)$ is the TOAR surface O_3 concentration, and $M(x,t)$ is the O_3 output from the considered CMIP6 models, but scaled from the lowest model level to the same measurement height as the corresponding TOAR station by means of the dry deposition scheme used in this study (Guaita et al., 2023). The ground stations are selected to be representative of the agricultural context, and therefore only rural, background or crop locations are included. Since the dry deposition model of this study scales O_3 from the height of the lowest model level of the CMIP6 models to the crop canopy height ($\sim$1 m), only ground stations with measurement heights equal or below 3 m are considered. Furthermore, only stations with more than a 10-year long timeseries are included. In this regard, an exception is made for China, as the stations that could represent wheat fields have data reported only for the years 2013–2014. The MB is evaluated over Europe, North America and East Asia, as only these regions have enough stations to produce a robust estimate of the MB. Furthermore, as the peak concentrations are more important in determining the POD_6 rather than just the mean bias, the differences in the 75^{th} and the 95^{th} percentiles between the modelled and observed O_3 distributions are also evaluated over the same regions.

The UKESM1-0-LL input O_3 concentrations are compared to the O_3 measurements from the

TOAR database (Schröder et al., REF Schröder et al. 2021) over the baseline years (2000–2014). First, the O_3 concentrations from the ESM are scaled to measurement height by means of the dry deposition model and then compared with observations. O_3 concentrations from UKESM1-0-LL, that are used to calculate the POD_6, display a small negative mean bias when averaged across the globe (MB: -2.82 ± 5.90 ppb, Table B.1, Figure B.1), and this underestimation is generally smaller for the upper percentiles. When analyzing spatial variability in MB, O_3 values show good agreement with observations across Europe and North America. In contrast, a positive bias is evident in East Asia, with a notably larger overestimation of the 75th percentile (4.29 ± 14.27 ppb). However, it should be noted that this evaluation was performed over a short time frame for measurement stations over China (years 2013 and 2014), and this contributes to the large SD observed across East Asia. The GFDL-ESM4 shows a similar mean bias to the one observed in UKESM1-0-LL, but greatly underestimates the upper percentiles, with differences in the 95th percentile up to -13.68 ± 6.89 ppb over Europe. These evaluation results suggest that UKESM1-0-LL provides more accurate O_3 estimates. Therefore, for this ESM, all POD_6 calculations in this study are performed using all the four runs and all relevant CMIP6 experiments. In contrast, POD_6 calculations using GFDL-ESM4 data are limited to the MM+CO_2 run and the baseline years (historical experiment) with the aim of assessing whether different models identify different regions at risk of O_3-induced damage to wheat.

The sensitivity of the input variables on the final POD_6 estimate is evaluated by regressing (with interaction) the yearly POD_6 differences with the baseline 2000–2014 average (ΔPOD_6) in every node against the mean temperature, the mean VPD, and the 75th percentile of O_3 concentrations differences with the baseline over the accumulation period:

$$\Delta \mathrm{POD}_6 = f\left(\Delta \overline{T}, \Delta \overline{\mathrm{VPD}}, \Delta \overline{\mathrm{pr}}, \Delta [O_3]_{75}\right) + \varepsilon \tag{B.4}$$

where f indicates the formula of the regression with interactions, $\overline{T}$, $\overline{\mathrm{VPD}}$ and $\overline{\mathrm{pr}}$ are the mean temperature, VPD, and precipitation over the accumulation period (with Δ indicating the difference between the yearly average with the baseline average), $[O_3]_{75}$ is the 75^{th} percentile of the O_3 concentrations over the accumulation period, and $\varepsilon \in \mathcal{N}(0, \sigma^2)$ is the error. This regression is calibrated over all the experiments (historical and SSPs) of the MM run to consider all the possible ranges of the input variables and ensure the robustness of the relationship. Once calibrated, the regression allows to estimate the effect of the bias in the input variables on the final estimate of the POD_6, i.e. to propagate the uncertainty. This is achieved by assuming normal distributions for the

biases ($\Delta\overline{T}$, $\Delta\overline{\mathrm{VPD}}$, $\Delta\overline{\mathrm{pr}}$ and $\Delta[O_3]_{75}$), whose means and variances are inferred from the literature for the first three variables and estimated from the bias calculations carried out in this study for O_3. Table B.2 reports summary results of the regression analysis.

The results show that globally the uncertainty in the input variables propagates to the POD_6 estimates mostly through the variability component only, rather than on the propagated bias. In fact, globally, the POD_6 is essentially unperturbed on average ($-0.02 \pm 0.79\,\mathrm{mmol\,m^{-2}}$). Europe and North America have small uncertainties due to input variables ($-0.01 \pm 0.75\,\mathrm{mmol\,m^{-2}}$ and $-0.10 \pm 0.75\,\mathrm{mmol\,m^{-2}}$). As expected, East Asia has the largest uncertainty, both in terms of propagated bias and variability, as the POD_6 appears to be overestimated by $0.23 \pm 1.00\,\mathrm{mmol\,m^{-2}}$ in this region, largely due to the uncertainties in the O_3 input variables (4.29 ± 14.27 ppb in the 75^{th} percentile difference). In any case, such overestimation is not sufficient to broadly classify this region as not at risk, and it should be also noted that the O_3 bias evaluation in this region could be the result of the lack of long-term observations in the evaluation period (for China, only years 2013 and 2014 are available) rather than the result of a systematic overestimate.

B.3 Differences with the original dry deposition model

Compared to the original model described in Guaita et al. (2023), in this exercise (i) pressure and sensible heat flux are provided as CMIP6 input, (ii) vapor pressure is calculated from specific humidity by

$$e\ [\mathrm{kPa}] = \frac{p \cdot q}{0.622}, \tag{B.5}$$

with p air pressure [kPa], and q the specific humidity [$\mathrm{kg_{H_2O}\,kg_{air}^{-1}}$], (iii) net radiation is calculated by summing the radiation components provided by the CMIP6 models, and (iv) Soil Water Content (SWC, [% volume]) to compute f_{soil} for the Mediterranean parameterization is calculated as the difference between the actual SWC and the SWC at wilting point.

B.4 Performance of the dry deposition model

The dry deposition model (Guaita et al., 2023) is compared to eddy covariance measurements on a wheat field in Comun Nuovo (Italy) (Gerosa et al., 2003). The model is tested for its ability to reproduce (i) the total O_3 flux (F_{O_3}) over a wheat field, which reflects the performance of the entire resistance network, (ii) the latent heat flux (LE, $\mathrm{W\,m^{-2}}$), a proxy for stomatal conductance and thus indicative of the stomatal component of the resistance network, and (iii) the friction velocity

TABLE B.1

O_3 MEAN BIAS AND PERCENTILE DIFFERENCES FOR UKESM1-0-LL AND GFDL-ESM4 O_3 CONCENTRATIONS AGAINST O_3 MEASUREMENTS IN THE TOAR DATABASE. UKESM1-0-LL O_3 CONCENTRATIONS ARE SCALED TO THE TOAR MEASUREMENT HEIGHTS FOR THESE COMPARISONS. BOLD VALUES INDICATE $p < 0.05$.

Region	O_3 MB ± SD (95% CI)	O_3 p75 ± SD (95% CI)	O_3 p95 ± SD (95% CI)
UKESM1-0-LL			
Global	-2.82 ± 5.90 $(-3.14, -2.51)$	-0.71 ± 6.72 $(-1.07, -0.35)$	-1.04 ± 8.14 $(-1.48, -0.61)$
North America	-3.70 ± 4.74 $(-4.10, -3.29)$	-2.28 ± 5.06 $(-2.71, -1.84)$	-0.57 ± 7.13 $(-1.19, 0.04)$
Europe	-3.09 ± 5.28 $(-3.49, -2.70)$	-0.51 ± 4.86 $(-0.88, -0.15)$	-1.96 ± 5.64 $(-2.38, -1.53)$
East Asia	1.91 ± 9.65 $(0.21, 3.60)$	4.29 ± 14.27 $(1.78, 6.79)$	1.46 ± 17.34 $(-1.59, 4.50)$
GFDL-ESM4			
Global	-2.89 ± 6.11 $(-3.22, -2.56)$	-4.83 ± 6.49 $(-5.18, -4.48)$	-11.99 ± 8.44 $(-12.44, -11.53)$
North America	-2.73 ± 4.07 $(-3.08, -2.37)$	-4.96 ± 4.49 $(-5.35, -4.58)$	-10.47 ± 6.17 $(-11.01, -9.94)$
Europe	-3.88 ± 5.92 $(-4.32, -3.43)$	-5.91 ± 5.44 $(-6.32, -5.50)$	-13.68 ± 6.89 $(-14.20, -13.16)$
East Asia	1.31 ± 10.32 $(-0.45, 3.07)$	1.01 ± 12.31 $(-1.08, 3.11)$	-9.47 ± 17.06 $(-12.38, -6.57)$

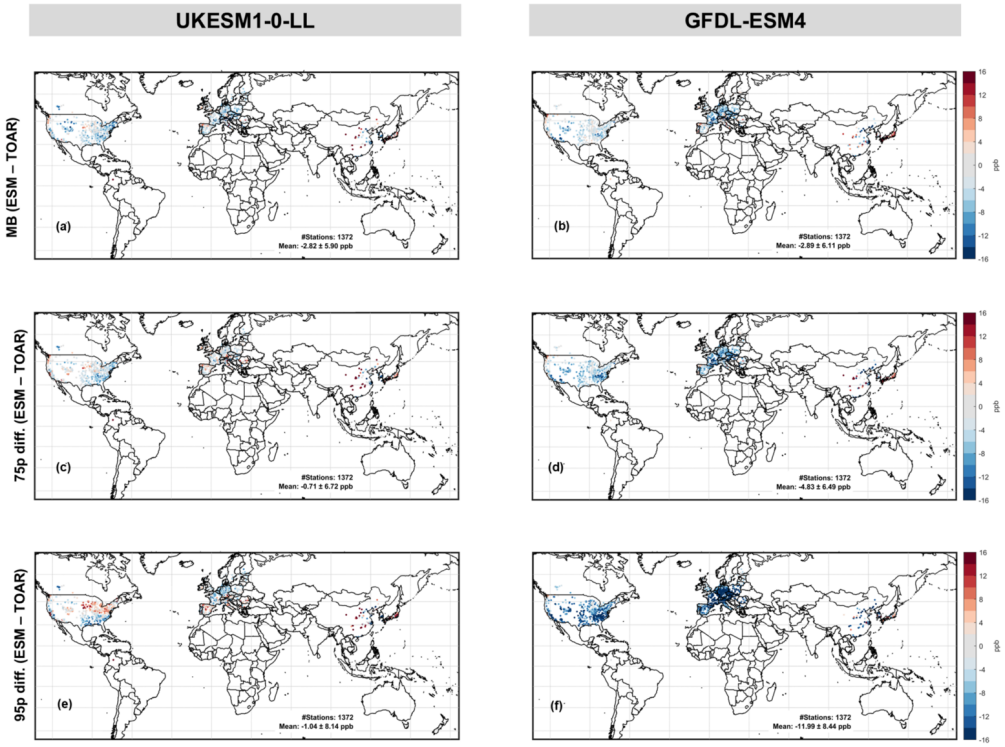

Figure B.1. Evaluation against the TOAR database of the input O_3 concentrations (UKESM1-0-LL, first column; GFDL-ESM4, second column) scaled at the measurement height by means of the resistive network of the dry deposition model. Mean Bias (first row) and percentile differences (second and third row) are calculated over the years 2000–2014 only for the light hours of the accumulation period. Map lines delineate study areas and do not necessarily depict accepted national boundaries.

TABLE B.2

SUMMARY OF THE REGRESSION (EQ. A2), REPORTING COEFFICIENTS' ESTIMATES, STANDARD ERRORS (SE), T-STATISTICS, AND P-VALUES. FOR THIS REGRESSION, THE ADJUSTED R^2 IS 0.422, AND THE RMSE IS 0.485 MMOL M^{-2}. T IS IN °C, VPD IS IN KPA, pr IS IN MM D^{-1}, AND $[O_3]$ IS IN PPB.

Predictor	Coefficient estimate	SE	tStat	pValue
Intercept	0.026166	0.912×10^{-3}	28.69642	$< 10^{-5}$
$\overline{\Delta T}$	0.030914	0.424×10^{-3}	72.96777	$< 10^{-5}$
$\overline{\Delta(\mathrm{VPD})}$	−1.024078	3.630×10^{-3}	−282.12474	$< 10^{-5}$
$\overline{\Delta(pr)}$	0.025327	0.573×10^{-3}	44.16919	$< 10^{-5}$
$\Delta[\mathrm{O_3}]_{75}$	0.048617	0.091×10^{-3}	536.33975	$< 10^{-5}$
$\overline{\Delta T} \cdot \overline{\Delta(\mathrm{VPD})}$	0.063822	0.616×10^{-3}	103.64335	$< 10^{-5}$
$\overline{\Delta T} \cdot \overline{\Delta(pr)}$	−0.002243	0.223×10^{-3}	−10.05959	$< 10^{-5}$
$\overline{\Delta T} \cdot \Delta[\mathrm{O_3}]_{75}$	−0.003052	0.040×10^{-3}	−76.38022	$< 10^{-5}$
$\overline{\Delta(\mathrm{VPD})} \cdot \overline{\Delta(pr)}$	0.030780	1.486×10^{-3}	20.71094	$< 10^{-5}$
$\overline{\Delta(\mathrm{VPD})} \cdot \Delta[\mathrm{O_3}]_{75}$	−0.012797	0.285×10^{-3}	−44.90730	$< 10^{-5}$
$\overline{\Delta(pr)} \cdot \Delta[\mathrm{O_3}]_{75}$	0.000448	0.035×10^{-3}	12.62871	$< 10^{-5}$

u_* ($\mathrm{m\,s^{-1}}$), a proxy for stomatal conductance, representing the aerodynamic component of the resistance network. Namely, the total O_3 flux is calculated as follows:

$$F_{\mathrm{O_3}} = \frac{O_3(z_{m\mathrm{O_3}})}{R_{aH}(d + z_{0m}) + R_{b\mathrm{O_3}} + R_{\mathrm{surf,O_3}}} \tag{B.6}$$

where $z_{m\mathrm{O_3}}$ is the measurement height, d is the displacement height, z_{0m} is the roughness length for momentum, $O_3(z_{m\mathrm{O_3}})$ is the O_3 concentration at measured height, $R_{aH}(d + z_{0m}, z_{m\mathrm{O_3}})$ is the aerodynamic resistance between $d+z_{0m}$ and $z_{m\mathrm{O_3}}$, $R_{b\mathrm{O_3}}$ is the quasi-laminar resistance, and $R_{\mathrm{surf,O_3}}$ is the bulk overall surface resistance to deposition. For details on the calculation for each of these variables, see the Appendix A. All the input variables required by the dry deposition model are available in the Comun Nuovo dataset. Furthermore, it includes exhaustive auxiliary information to determine the relevant parameters required by the model (e.g., leaf area index, measurement heights, canopy height, start of anthesis, maturity date), which replaced the standardized parameterization used for the simulations of this study.

The latent heat flux output from the dry deposition model is also compared to eddy covariance measurements from the FLUXNET2015 dataset (Pastorello et al., 2020) for three selected sites (in Belgium, Finland and US) that carried out measurements on wheat fields during multiple years and that provided enough input variables and information to run the dry deposition model (site IDs: BE-Lon, FI-Jok, US-ARM). In these cases, not all the necessary information is available, and parameterizations are either inferred from the papers that described the site characterizations (Fischer et al., 2007; Lohila et al., 2004; Moureaux et al., 2006; Raz-Yaseef et al., 2015) or kept the same as in the model runs of this study. All diagnostic runs were performed at half-hourly resolutions, and the performance statistics are also referred to this timestep and to the data filtered according to the reported quality control flags.

The dry deposition model performance is evaluated against measured eddy covariance fluxes. The O_3 total flux is evaluated for the Comun Nuovo dataset (Gerosa et al., 2003) and shows good performance on a half-hourly basis (Table B.3), with a mean bias (MB) of $2.91\,\mathrm{ppb\,m^{-2}\,s^{-1}}$ (the maximum observed value is $26.06\,\mathrm{ppb\,m^{-2}\,s^{-1}}$). The time series also appears to be reproduced correctly, although overestimated on some individual days. In contrast, the latent heat flux, evaluated on both the Comun Nuovo dataset and on three FLUXNET2015 sites, is slightly underestimated at three of the four sites (Comun Nuovo, BE-Lon, US-ARM), with the MB ranging between $-22.30\,\mathrm{W\,m^{-2}}$ and $-8.23\,\mathrm{W\,m^{-2}}$, while FI-Jok is positively biased with $53.43\,\mathrm{W\,m^{-2}}$ (maximum observed value across sites: $468.59\,\mathrm{W\,m^{-2}}$). BE-Lon R^2 has the lowest correlation among the four sites (0.45),

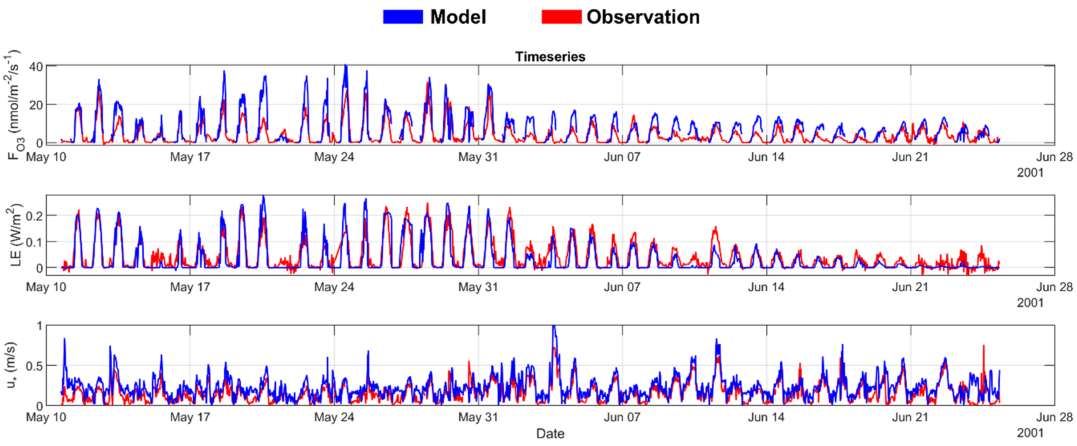

Figure B.2. Timeseries for modelled and observed F_{O_3}, LE and u_* for the Comun Nuovo dataset. The timeseries include all timesteps, regardless of the quality control flags.

while in the other cases it ranges between 0.51 and 0.77. Friction velocity (u_*) is overall estimated correctly across the four sites, with a MB between 0.02 m s^{-1} and 0.14 m s^{-1} (maximum observed value across sites: 1.04 m s^{-1}) and an R^2 between 0.65 and 0.86.

B.5 Evaluation of the prediction of phenological stages

The MM (LRTAP Convention, 2017) prescribes the use of Thermal Time to determine the accumulation period for PODY, whose start is defined for wheat at "the flag leaf fully unrolled, with ligule just visible" and the end at maturity. To ensure reasonable estimates at a global scale, we compared the estimated maturity dates as determined by thermal time with those provided by the Global Gridded Model Intercomparison Project (GGCMI) Crop Calendar (Jägermeyr et al., 2021) product (Figure B.3). We also compared the heading and maturity dates provided across China by Luo et al. (2020) with the predicted start and end of the accumulation period for both CMIP6 models (Figure B.4).

The comparison with the GGCMI product showed reasonably good performance, especially for UKESM1-0-LL (Figure B.3a), where mean biases across the globe are centred around 5.2 days (median) and 69.1% of the nodes have an absolute bias smaller than 30 days. It should be noted

TABLE B.3

MEAN BIAS, RMSE AND R^2 OF THE DRY DEPOSITION MODEL IN REPRODUCING LATENT HEAT FLUX (LE), FRICTION VELOCITY (u_*), AND TOTAL OZONE FLUX (F_{O_3}). THE COMUN NUOVO DATASET HAD MEASUREMENTS FOR THE TOTAL O_3 FLUXES AND FAIRLY COMPLETE AUXILIARY INFORMATION ON REQUIRED PARAMETERIZATIONS. THE MEASUREMENT SITES FROM THE FLUXNET DATASET DID NOT INCLUDE ALL AUXILIARY INFORMATION AND DID NOT MEASURE O_3 FLUXES.

	Comun Nuovo	BE-Lon	FI-Jok	US-ARM
Dataset citation	-	De Ligne et al. (2016)	Lohila et al. (2016)	Biraud et al. (2016)
Reference paper	Gerosa et al. (2003)	Moureaux et al. (2006)	Lohila et al. (2004)	Fischer et al. (2007)
LE ($\mathrm{W\,m^{-2}}$)				
MB	-22.30	-12.95	53.43	-8.23
RMSE	50.24	89.22	72.41	83.22
R^2	0.77	0.45	0.75	0.51
u_* ($\mathrm{m\,s^{-1}}$)				
MB	0.02	0.11	0.09	0.14
RMSE	0.08	0.15	0.12	0.17
R^2	0.65	0.86	0.73	0.86
F_{O_3} ($\mathrm{ppb\,m^{-2}\,s^{-1}}$)				
MB	2.91	-	-	-
RMSE	5.57	-	-	-
R^2	0.57	-	-	-

that the error spread around the median may be exaggerated due to the aggregation of data at the national level in the GGCMI product. As for the start of the accumulation dates, the evaluation comparison cannot be carried out because the GGCMI only provides sowing and maturity dates.

The comparison with the data provided by Luo et al. (2020) indicates that, for UKESM1-0-LL, the mean biases for the heading dates are centred around 18.9 days (Figure B.4a), while maturity dates show a bimodality (centered around -30 and +30 days; Figure B.4c), likely due to the different performances of the model for winter and spring wheat.

In conclusion, the accumulation period from UKESM1-0-LL is estimated reasonably well at a global level (GGCMI comparison), but in the case of China (ChinaCropPhen1km comparison) the maturity is shifted either forward or backward, i.e., towards a warmer or colder season, potentially leading to a higher or lower O_3 dose uptake over this region.

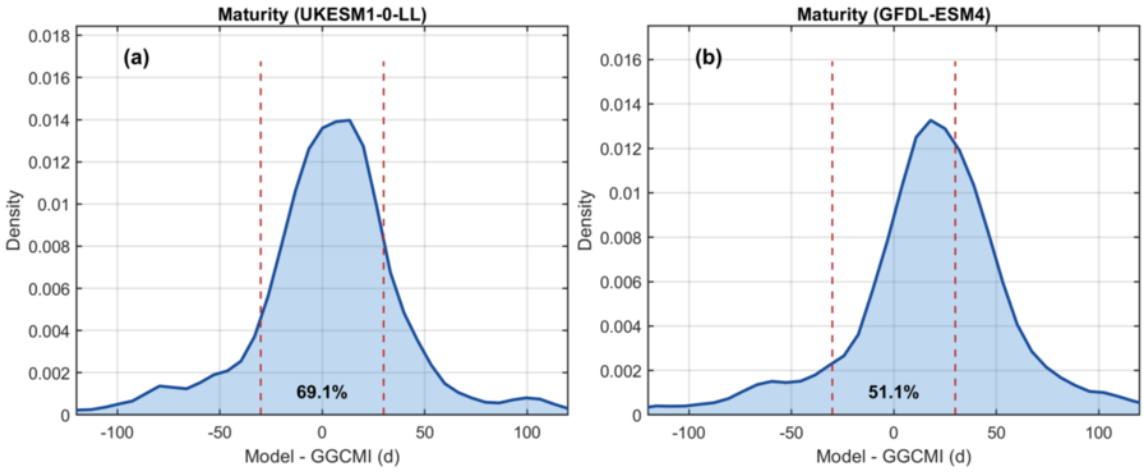

Figure B.3. Histogram (kernel density estimation) of the Mean Bias (Model – GGCMI) of the maturity dates across the globe as predicted by UKESM1-0-LL (a) and by GFDL-ESM4 (b).

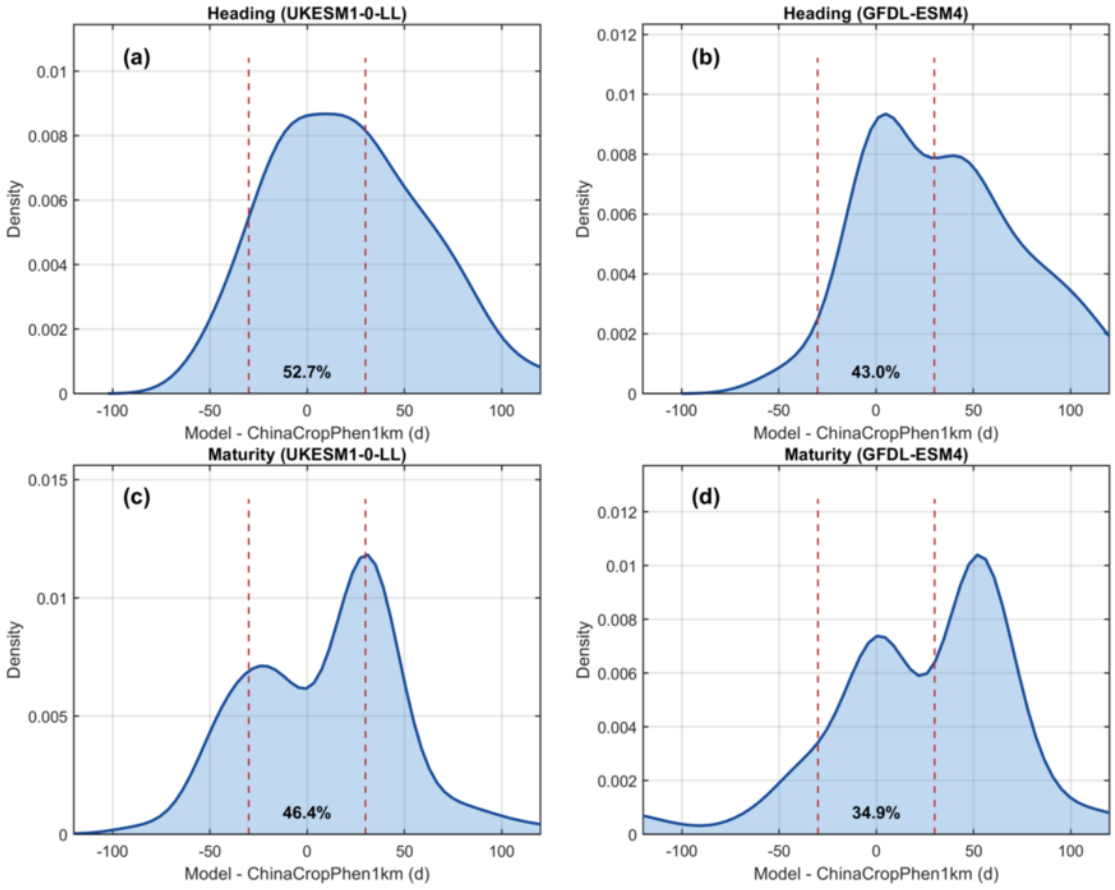

Figure B.4. Histogram (kernel density estimation) of the Mean Bias (modelled – ChinaCropPhen1km) for the heading (a,b) and maturity (c,d) dates across nodes for UKESM1-0-LL (a,c) and GFDL-ESM4 (b,d).

B.6 ANOVA

A two-way ANalysis Of VAriance (ANOVA; von Storch and Zwiers, 1999) is applied to the POD_6 values computed at the end of the century in order to assess the areas of the globe where the changes of POD_6 with respect to the baseline period are highly certain. We consider radiative forcing and control emission policies as the two factors, each one applied at two levels, i.e. low/high for radiative forcing (RF), and weak/strong for emission policy (EP). These levels are determined by the different SSPs, as described in Table B.4.

ANOVA is performed on the POD_6 output produced through the UKESM1-0-LL. First, the data in every node is tested for normality with the Shapiro–Wilk test in case the data is platykurtic, and with the Shapiro–Francia test if it is leptokurtic (Royston, 1993). In case the test fails, the data in that node is normalized through log-transformation. ANOVA is performed independently in every grid node of the map with $POD_6 > 0$ and a Bonferroni correction is applied to the p-values to account for multiple tests and for multiple locations

$$\#\text{tests} \times \#(\text{nodes with } POD_6 > 0) = \left(\frac{8 \cdot 7}{2}\right) \times 2751 = 77028. \tag{B.7}$$

Furthermore, this analysis allows to calculate the fraction of explained total variance by each factor, defined as R^2, according to the definition by von Storch and Zwiers (1999). The ANOVA analysis was performed with MATLAB.

TABLE B.4

CONFIGURATION FOR ANOVA BY SSPS, CLASSIFIED BY EMISSION CONTROL POLICIES (EP) AND RADIATIVE FORCING (RF).

	Emission control policies (EP)	
Radiative forcing (RF)	Strong	Weak
Low	SSP1-2.6	SSP3-7.0pdSST
High	SSP5-8.5	SSP3-7.0

APPENDIX C

APPENDIX OF "THE GROWING SEASONS OF GLOBAL FOREST ECOSYSTEMS FROM 1850 TO 2100 ESTIMATED WITH A PROBABILISTIC TEMPERATURE-BASED MODEL"

C.1 GS-P description

GS-P is a probabilistic, temperature-based model designed to estimate the SGS and EGS through a two-step procedure that combines machine-learning classification with inference based on probabilistic thresholds.

In the first step, GS-P estimates the daily likelihood that a given grid cell is in a GS or non-GS state based on the following temperature-based features: the 14-day moving average of daily temperature (T_{14d}), the associated regression slope (∇T_{14d}) and moving standard deviation (σ_{14d}), and the 60-day moving average (T_{60d}). This is achieved through a binary classification model calibrated using the XGBoost algorithm (Chen and Guestrin, 2016, see Table C.1 for hyperparameters). XGBoost constructs an ensemble of decision trees iteratively, where each successive tree is trained to reduce the residual error of the previous ensemble. For each day and grid cell, the model outputs a raw score representing the model's confidence in the GS state. This raw score is then transformed using a logistic function, producing a daily probability that indicates the likelihood of being in a GS state. The probabilistic output accounts for non-linear interactions among the input features (T_{14d}, ∇T_{14d}, σ_{14d}, T_{60d}), allowing the model to capture both absolute temperature thresholds and dynamic patterns in temperature changes.

In the second step, SGS and EGS are inferred from the daily GS probabilities by introducing two probability thresholds (p_{SGS} and p_{EGS}), which define the probability levels at which transitions between non-GS and GS are considered to occur. For each year, the model identifies the temporal window corresponding to that year and considers the probability curve for each node. The convexity of the probability curve at each node is assessed using smoothed daily probabilities (5-day moving average). A second-degree polynomial is fitted to the smoothed probability curve over the year, and

the coefficient of the quadratic term is used to classify the curve shape: a positive coefficient indicates a convex curve, whereas a negative coefficient indicates a concave curve. Convex and concave shapes are typical (but not exclusive) of Northern Hemisphere (NH) and Southern Hemisphere (SH) seasonal cycles, respectively. Using this information, candidate SGS and EGS days are constrained relative to the peak probability: in the NH, SGS occurs before the peak and EGS after it, while in the SH the ordering is reversed. The final SGS and EGS for each node and year are selected as the earliest and latest valid candidate days, ensuring that each year has a single, consistent start and end of the growing season, even in cases where multiple threshold crossings occur due to variability or noise in the probability signal.

TABLE C.1

HYPERPARAMETERS FOR THE XGBOOST ALGORITHM. THE `R` PACKAGE `XGBOOST` WAS USED (`HTTPS://CRAN.R-PROJECT.ORG/PACKAGE=XGBOOST`).

General parameters	
objective	binary:logistic
eval_metric	logloss
max_depth	5
tree_method	hist
nrounds	100

C.2 Parameter calibration details

The loss function for GS-Lin2 and GS-BC2 is based on the RMSE, which is defined as:

$$\mathrm{RMSE}(Y, \hat{Y}) = \sqrt{\frac{\sum_{i \in I} \left(Y_i - \hat{Y}_i\right)^2}{n}} \tag{C.1}$$

where $Y = (Y_i)_{i \in I}$ are the MODIS observations, $\hat{Y} = (\hat{Y}_i)_{i \in I}$ are the values predicted by the model, and $I = \{1, \ldots, n\}$ is the set of values for which the model actually predicts SGS and EGS dates. The RMSE is computed separately for SGS and EGS by comparing observed and predicted dates. For each model, the loss function is defined as the median of the two RMSEs, with a penalization to account for the number of times $\tilde{n}$ in which the model fails to produce a viable result:

$$\lambda(Y, \hat{Y}) = \left(1 + \frac{\tilde{n}}{N}\right)^2 \cdot \frac{\mathrm{RMSE}_{\mathrm{SGS}}(Y, \hat{Y}) + \mathrm{RMSE}_{\mathrm{EGS}}(Y, \hat{Y})}{2} \tag{C.2}$$

where $N = n + \tilde{n}$. When the GS model always succeeds in predicting SGS and EGS over a given dataset, $\tilde{n} = 0$ and $n = N$, and no penalization is applied. Conversely, the more frequently the model fails, the larger $\tilde{n}/N$ becomes, and therefore $\lambda(Y, \hat{Y})$ increases. To avoid parameter calibration over too few points, $\lambda(Y, \hat{Y})$ is set to 1000 d when $\tilde{n}/N > 0.2$.

The joint RMSE for SGS and EGS is required by the GS-Lin2 model, as this model enforces that SGS occurs either before or after EGS depending on the hemisphere. Therefore, at the global scale, SGS cannot be estimated independently of EGS, and vice versa. In contrast, GS-BC2 minimizes the RMSE separately for SGS and EGS, as the parameters $t_{1,\mathrm{SGS}}$ and $t_{1,\mathrm{EGS}}$ naturally enforce event separation. GS-Lat depends only on geographical coordinates and not on temperature; consequently, it always predicts SGS and EGS by design, and the penalization term is null. In this case, ordinary least squares is equivalent to minimizing the defined loss function.

For GS-P, probability thresholds are inferred separately for SGS and EGS at the grid-node level. For each grid cell, observed SGS and EGS dates derived from MODIS are matched to the corresponding daily GS probabilities produced by the classifier. These probabilities form node-level samples of transition probabilities $\{P_{i,t}\}_{t=1}^{n_i}$, where i indicates the grid node and n_i the number of observations at node i. Threshold inference is performed within each KG climate class using a hierarchical Bayesian Normal–Normal model with empirical shrinkage (Gelman et al., 2025). This model assumes that node-specific thresholds p_i (either $p_{i,\mathrm{SGS}}$ or $p_{i,\mathrm{EGS}}$) are drawn from a KG class-level distribution $\mathcal{N}(\mu, \tau^2)$, where μ is the class-level mean threshold and τ^2 is the between-node

variance. Observed node-level probabilities are modeled as $\mathcal{N}(\mu_i, \sigma^2)$, where μ_i is the within-node mean and σ^2 is the pooled within-node variance. The node-specific thresholds are obtained via shrinkage as a precision-weighted average of the node-level sample mean $\bar{P}_i$ (an estimator of μ_i) and the KG class-level mean:

$$p_i = w_i \, \bar{P}_i + (1 - w_i) \, \mu \tag{C.3}$$

where the weights w_i are defined as:

$$w_i = \frac{\tau^2}{\tau^2 + \sigma^2 / n_i} \tag{C.4}$$

Here, σ^2 is estimated from the pooled within-node variance and τ^2 using the method of moments. In practice, when within-node variance is high or the number of node-level observations is small, $w_i \to 0$ and consequently $p_i \to \mu$. Conversely, when within-node variance is small, $w_i \to 1$ and $p_i \to \bar{P}_i$. For readability, the node index i is omitted elsewhere in the text, and node-level thresholds $p_{i,\mathrm{SGS}}$ and $p_{i,\mathrm{EGS}}$ are referred to as p_{SGS} and p_{EGS}.

APPENDIX D

SUPPLEMENTARY FIGURES AND TABLES OF "THE GROWING SEASONS OF GLOBAL FOREST ECOSYSTEMS FROM 1850 TO 2100 ESTIMATED WITH A PROBABILISTIC TEMPERATURE-BASED MODEL"

TABLE D.1

CRITERIA TO DEFINE AREAS ACCORDING TO THE KÖPPEN–GEIGER (KG) CLASSIFICATION USING ONLY TEMPERATURE. T_{hot} AND T_{cold} REFER TO THE CLIMATOLOGICALLY WARMEST AND COLDEST MONTHS, RESPECTIVELY. T_{mon10} INDICATES THE NUMBER OF MONTHS WITH TEMPERATURE ABOVE 10 °C.

Main group	Subgroup	Criteria
C (temperate)		$0 < T_{\mathrm{cold}} < 18 \wedge T_{\mathrm{hot}} > 10$
	C*a (subtropical / hot-summer Mediterranean)	$T_{\mathrm{hot}} \geq 22$
	C*b (warm-summer Mediterranean / oceanic / dry-winter subtropical)	$\neg(\mathrm{C*a}) \wedge T_{\mathrm{mon10}} \geq 4$
	C*c (cold-summer Mediterranean / subpolar oceanic / dry-winter cold subtropical highland)	$\neg(\mathrm{C*a} \vee \mathrm{C*b}) \wedge 1 \leq T_{\mathrm{mon10}} \leq 4$
D (continental)		$T_{\mathrm{hot}} > 10 \wedge T_{\mathrm{cold}} \leq 0$
	D*a (hot summer)	$T_{\mathrm{hot}} \geq 22$
	D*b (warm summer)	$\neg(\mathrm{D*a}) \wedge T_{\mathrm{mon10}} \geq 4$
	D*c (subarctic)	$\neg(\mathrm{D*a} \vee \mathrm{D*b} \vee \mathrm{D*d})$
	D*d (subarctic with severe winter)	$\neg(\mathrm{D*a} \vee \mathrm{D*b}) \wedge T_{\mathrm{cold}} < -38$

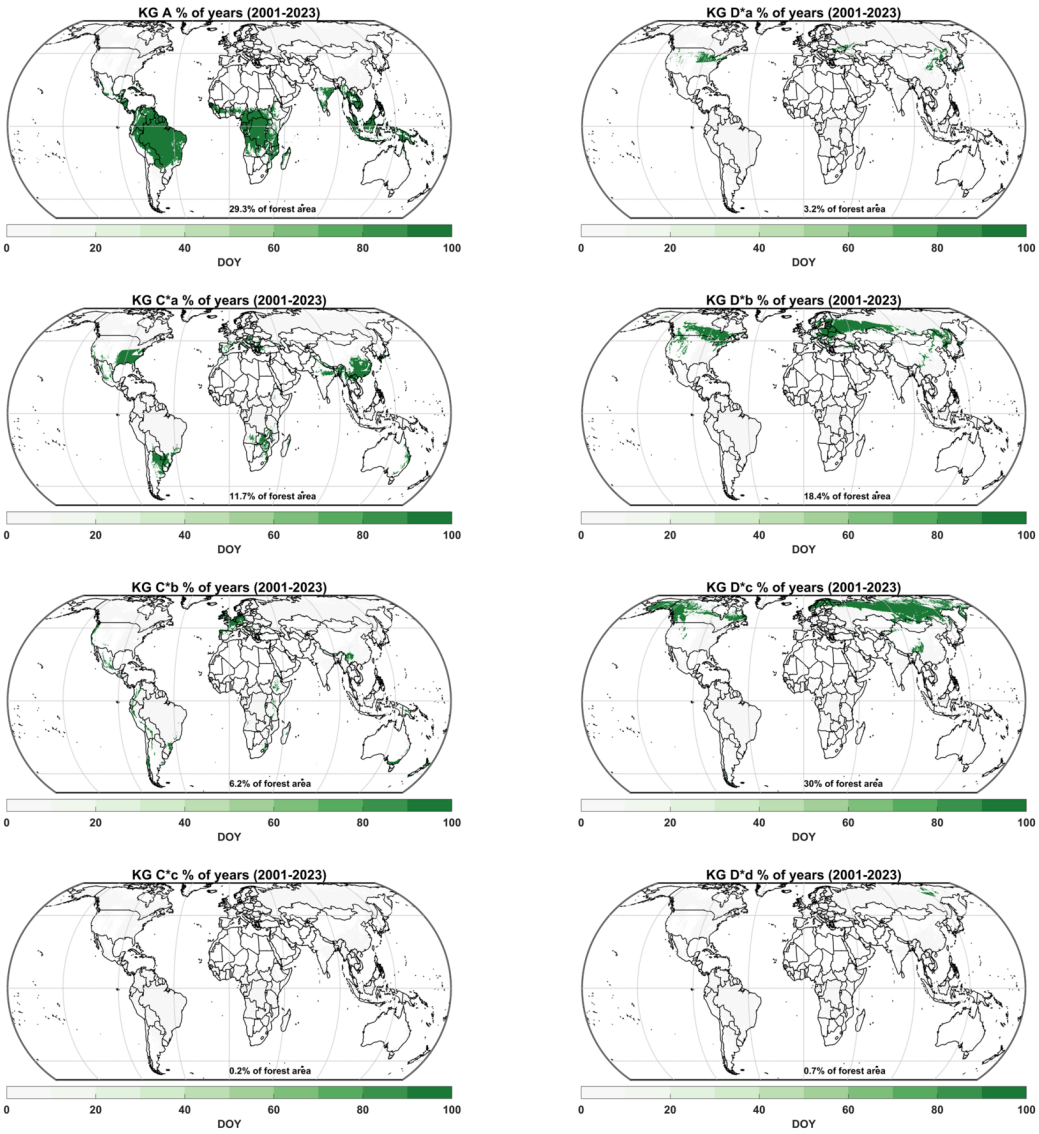

Figure D.1. Percentage of the years 2001–2023 falling within each KG classification derived from ERA5 temperatures. Note that climatological shifts can lead to transitions between KG classes.

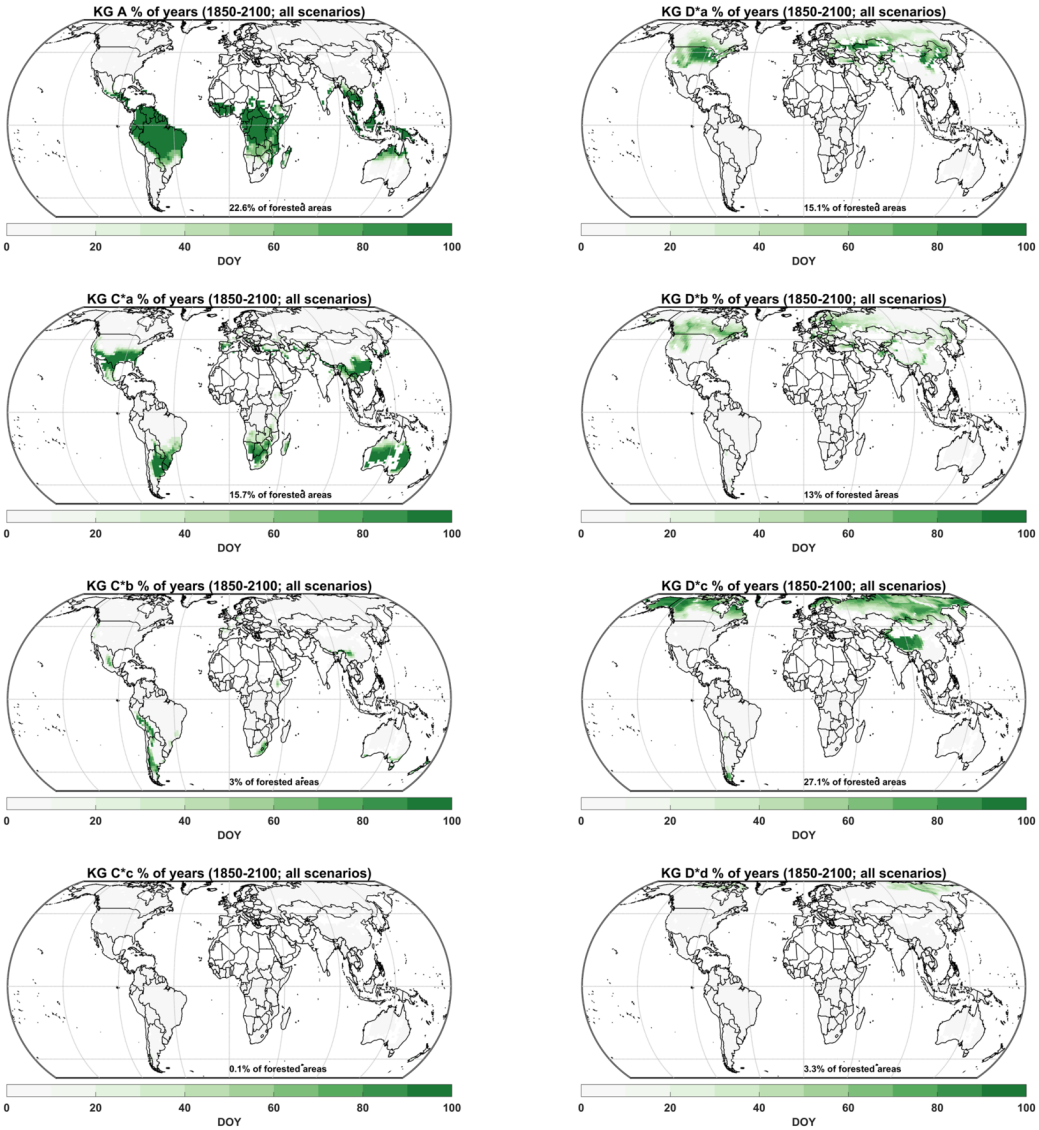

Figure D.2. Percentage of the years 1850-2100 (jointly historical, SSP1-2.6, SSP3-7.0, and SSP5-8.5 experiments) falling within each KG classification from the UKESM1 temperatures. Note that climatological shifts lead to transitions between KG classes.

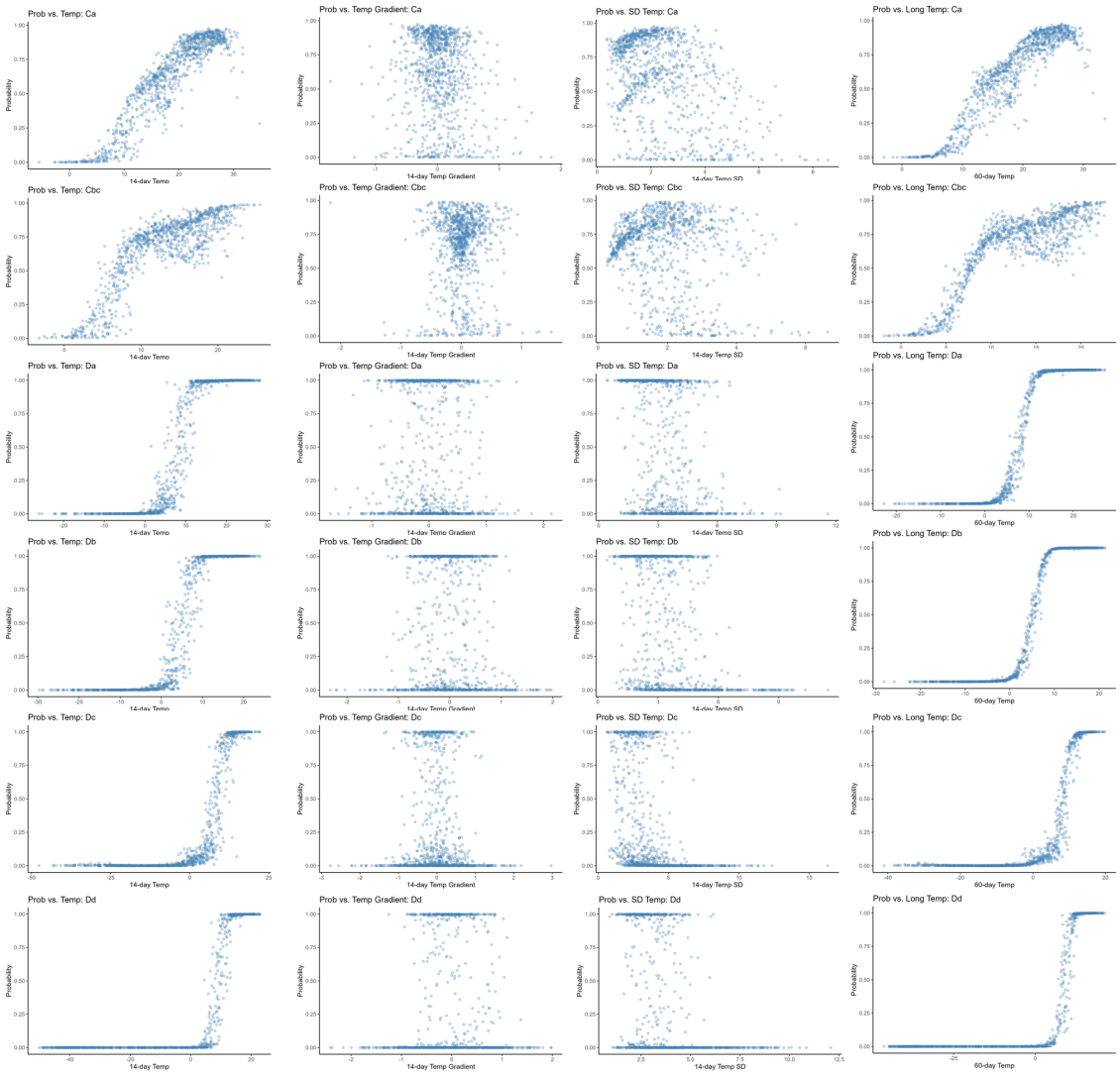

Figure D.3. Probabilities of the growing season (GS) predicted by the binary classifier over each KG class, as a function of input features: T_{14d} (first column), ∇T_{14d} (second column), σ_{14d} (third column), and T_{60d} (fourth column).

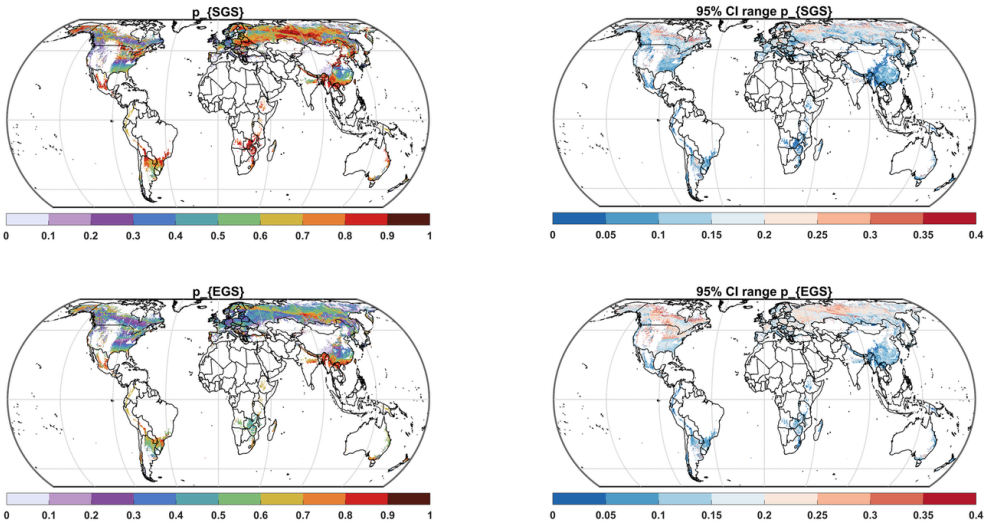

Figure D.4. Node-level probability thresholds for growing season (GS) transitions: p_{SGS} and p_{EGS}, together with the corresponding 95% confidence interval (CI) range.

TABLE D.2

95% CONFIDENCE INTERVALS (CIS) FOR GS-P AND GS-LAT PARAMETERS ACROSS DIFFERENT KG CLASSIFICATIONS. NH AND SH INDICATE NORTHERN AND SOUTHERN HEMISPHERE REGRESSION COEFFICIENTS FOR GS-LAT.

Parameter	C*a	C*b ∨ C*c	D*a	D*b	D*c	D*d
GS-P						
μ_{SGS}	[0.548,0.561]	[0.522,0.551]	[0.587,0.627]	[0.572,0.598]	[0.567,0.599]	[0.560,0.648]
τ^2_{SGS}	[0.055,0.059]	[0.053,0.059]	[0.048,0.055]	[0.051,0.058]	[0.058,0.065]	[0.042,0.056]
σ^2_{SGS}	[0.011,0.013]	[0.014,0.017]	[0.027,0.034]	[0.027,0.033]	[0.028,0.034]	[0.030,0.044]
μ_{EGS}	[0.491,0.517]	[0.534,0.576]	[0.338,0.409]	[0.375,0.434]	[0.456,0.527]	[0.392,0.509]
τ^2_{EGS}	[0.038,0.044]	[0.035,0.045]	[0.031,0.039]	[0.028,0.035]	[0.038,0.047]	[0.019,0.041]
σ^2_{EGS}	[0.014,0.018]	[0.017,0.024]	[0.039,0.055]	[0.041,0.051]	[0.035,0.049]	[0.036,0.059]
GS-Lat						
	NH			SH		
Parameter	CI			CI		
$\beta_{0,\text{SGS}}$	[19.19,19.63]			[296.67,299.11]		
$\beta_{1,\text{SGS}}$	[1.92,1.93]			[-1.41,-1.34]		
$\beta_{2,\text{SGS}}$	[10.00,10.14]			[-8.97,-7.94]		
$\beta_{0,\text{EGS}}$	[341.81,342.46]			[196.24,198.29]		
$\beta_{1,\text{EGS}}$	[-1.14,-1.13]			[-1.31,-1.25]		
$\beta_{2,\text{EGS}}$	[-10.05,-9.84]			[-6.29,-5.42]		

TABLE D.3

MB (MODEL – MODIS), MAE, AND PERCENTAGE OF FAILED INSTANCES IN PREDICTING SGS OVER EACH KG CLASS, CALCULATED OVER THE VALIDATION DATASET. METRICS ARE ADJUSTED USING THE PENALIZATION FACTOR.

SGS; Validation dataset size: 582,213							
Metric	Model	C*a	C*b ∨ C*c	D*a	D*b	D*c	Global
Failed pred (%)	GS-Lin2	2.01	31.78	0.00	0.22	0.45	3.64
	GS-BC2	0.00	0.13	0.00	0.00	1.22	0.49
	GS-P	0.54	2.49	0.00	0.03	0.09	0.37
	GS-Lat	0.00	0.00	0.00	0.00	0.00	0.00
MB (d)	GS-Lin2	23.5	78.7	8.7	12.8	2.0	12.9
	GS-BC2	1.4	-0.6	-0.4	2.5	-1.7	0.2
	GS-P	-15.4	-18.2	-1.4	-0.1	-1.3	-4.8
	GS-Lat	11.0	44.6	3.2	12.1	-11.6	5.1
MAE (d)	GS-Lin2	53.3	90.8	13.0	15.5	11.3	23.7
	GS-BC2	17.3	23.6	6.0	7.2	10.0	11.5
	GS-P	22.3	39.1	4.9	4.9	5.6	11.2
	GS-Lat	28.0	53.1	9.4	15.3	15.0	20.6
ρ	GS-Lin2	0.73	0.44	0.54	0.58	0.32	0.67
	GS-BC2	0.95	0.90	0.65	0.72	0.56	0.91
	GS-P	0.92	0.68	0.82	0.87	0.85	0.85
	GS-Lat	0.94	0.86	0.16	0.35	0.59	0.84

TABLE D.4

SAME AS TABLE D.3, BUT FOR EGS.

EGS; Validation dataset size: 581,901							
Metric	Model	C*a	C*b ∨ C*c	D*a	D*b	D*c	Global
Failed pred (%)	GS-Lin2	1.98	31.73	0.00	0.22	0.45	3.63
	GS-BC2	16.95	0.13	0.00	0.00	0.00	2.84
	GS-P	0.52	2.47	0.00	0.03	0.09	0.37
	GS-Lat	0.00	0.00	0.00	0.00	0.00	0.00
MB (d)	GS-Lin2	-7.1	-6.5	-1.9	2.9	6.3	2.1
	GS-BC2	13.9	0.1	0.2	-1.2	0.6	1.4
	GS-P	21.7	17.3	0.4	0.1	1.4	5.8
	GS-Lat	20.2	7.1	-18.0	-17.4	15.5	4.6
MAE (d)	GS-Lin2	49.9	41.3	12.8	11.6	13.4	20.7
	GS-BC2	33.6	22.2	6.6	7.6	7.7	12.1
	GS-P	32.0	35.9	7.6	7.3	6.8	13.8
	GS-Lat	43.8	48.2	18.3	17.9	17.9	25.2
ρ	GS-Lin2	0.55	0.47	0.38	0.58	0.49	0.63
	GS-BC2	0.62	0.88	0.53	0.70	0.60	0.82
	GS-P	0.70	0.70	0.59	0.76	0.79	0.75
	GS-Lat	0.64	0.71	0.39	0.41	0.37	0.65

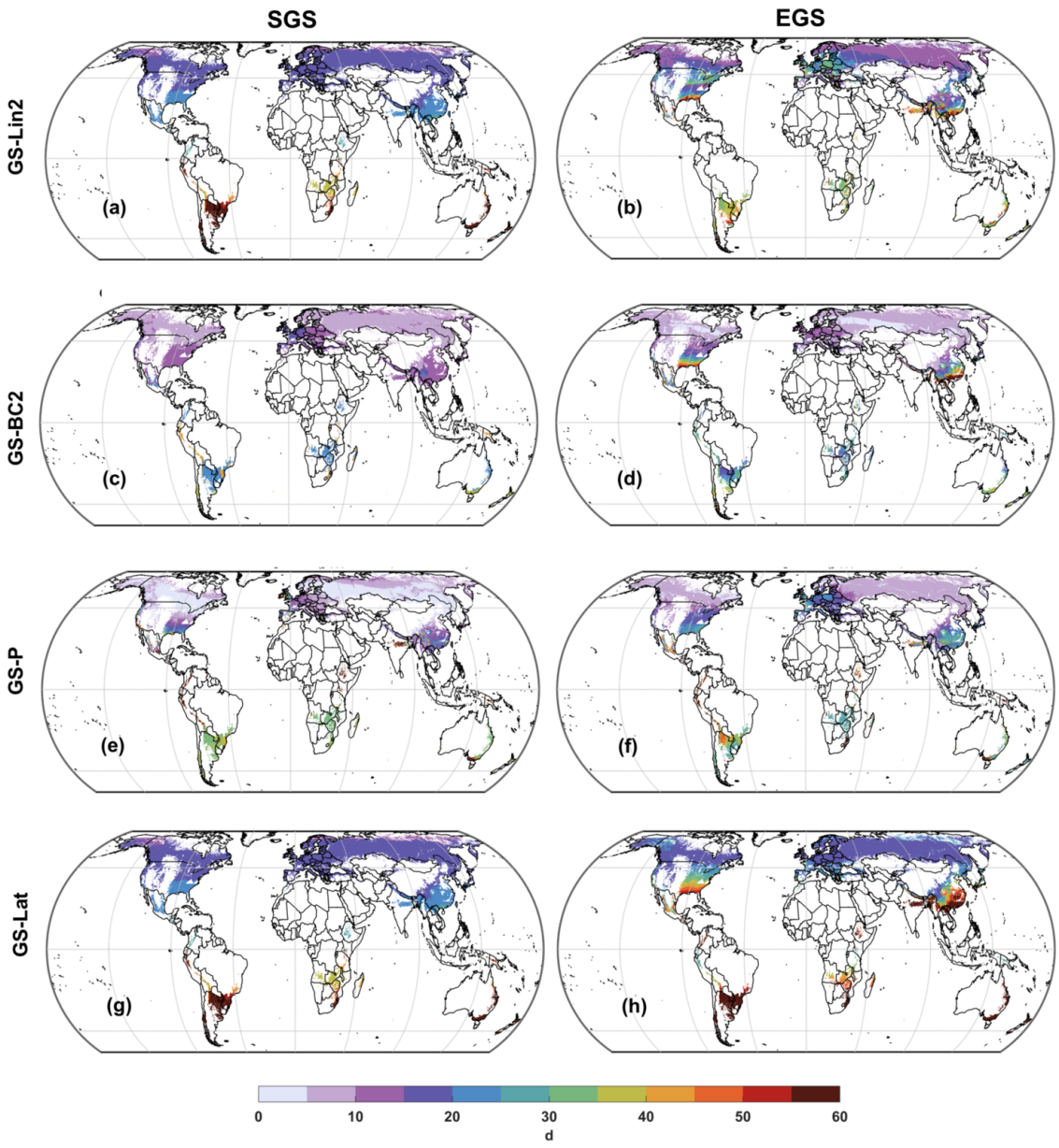

Figure D.5. Estimated error spread (95th percentile, p_{95}) for SGS (first column) and EGS (second column), for the different GS models, using 2001–2023 ERA5 temperatures.

TABLE D.5

MEAN SGS, EGS AND GS DURATION DURING THE PREINDUSTRIAL PERIOD (1850–1879) AND RELATIVE SHIFTS FOR DIFFERENT EXPERIMENTS.

		SGS				
Hemisphere	KG class	1850–1879	1985–2014	SSP1-2.6	SSP3-7.0	SSP5-8.5
NH	C*a	87.7	-2.0	-17.3	-33.2	-36.4
	C*b ∨ C*c	78.7	-3.1	2.4	-2.0	-8.3
	D*a	105.4	-0.9	-9.5	-20.4	-24.0
	D*b	115.5	-0.5	-5.2	-14.1	-17.5
	D*c	164.3	-0.9	-23.9	-35.7	-41.0
	D*d	182.0	-2.3	-20.3	-29.7	-37.9
SH	C*a	259.3	-6.7	-20.4	-33.8	-43.2
	C*b ∨ C*c	232.3	2.3	7.7	17.4	17.4
	D*a	–	–	–	–	–
	D*b	238.7	5.1	18.3	-8.8	-11.1
	D*c	251.6	-5.2	3.3	-11.9	-22.0
	D*d	–	–	–	–	–

TABLE D.6

SAME AS TABLE D.5, BUT FOR EGS

		EGS				
Hemisphere	KG class	1850–1879	1985–2014	SSP1-2.6	SSP3-7.0	SSP5-8.5
NH	C*a	307.0	3.4	18.7	29.2	28.6
	C*b ∨ C*c	315.8	1.6	-3.3	4.0	8.0
	D*a	299.7	1.9	10.9	21.1	24.2
	D*b	292.4	0.9	7.8	17.3	20.3
	D*c	248.0	0.5	24.6	38.5	43.6
	D*d	225.1	1.5	22.9	38.5	47.5
SH	C*a	152.7	6.5	12.8	16.6	10.7
	C*b ∨ C*c	153.1	0.4	4.0	7.0	5.8
	D*a	–	–	–	–	–
	D*b	133.0	0.3	-4.3	24.1	21.6
	D*c	128.6	5.1	-3.7	8.5	12.9
	D*d	–	–	–	–	–

TABLE D.7

SAME AS TABLE D.5, BUT FOR GS DURATION

		GS Duration				
Hemisphere	KG class	1850–1879	1985–2014	SSP1-2.6	SSP3-7.0	SSP5-8.5
NH	C*a	219.3	5.4	36.1	62.4	65.1
	C*b ∨ C*c	237.2	4.8	-5.7	6.0	16.3
	D*a	194.3	2.8	20.4	41.5	48.2
	D*b	176.8	1.4	12.9	31.4	37.8
	D*c	83.7	1.4	48.5	74.2	84.7
	D*d	43.0	3.8	43.2	68.3	85.4
SH	C*a	258.3	13.2	33.2	50.4	53.9
	C*b ∨ C*c	285.7	-1.9	-3.8	-10.4	-11.7
	D*a	–	–	–	–	–
	D*b	259.3	-4.8	-22.6	32.9	32.8
	D*c	242.0	10.2	-7.0	20.4	34.8
	D*d	–	–	–	–	–

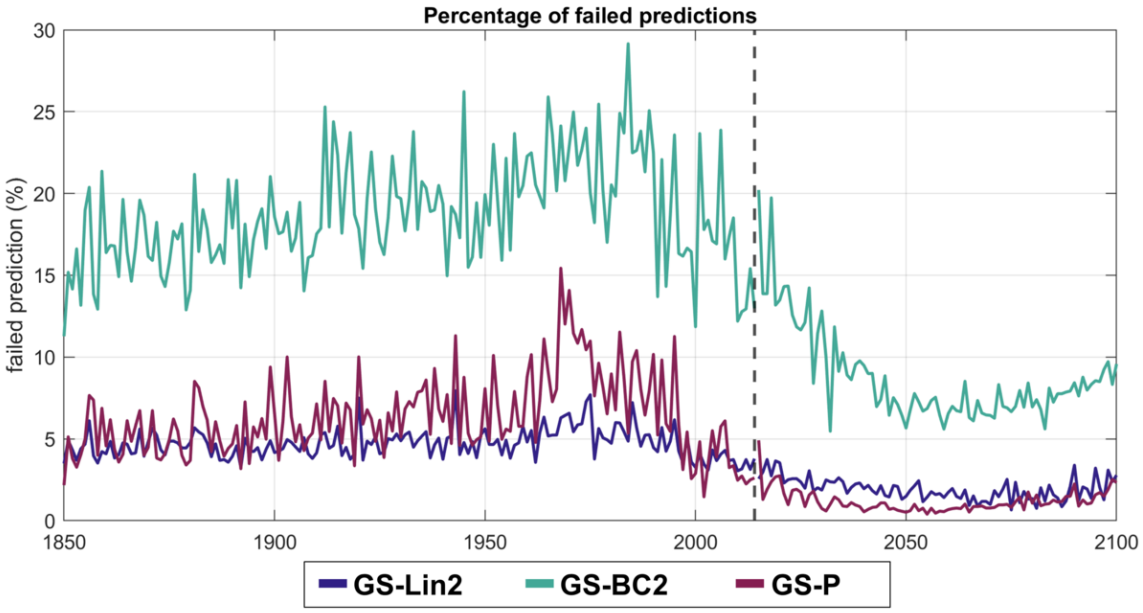

Figure D.6. Percentage of failed predictions for the three temperature-based GS models (GS-Lin2, GS-BC2, GS-P) using UKESM1-0-LL temperatures from the historical (1850–2014) and SSP5-8.5 (2015–2100) experiment. Vertical dashed line indicates the separation year between the two experiments. The peak in failed prediction percentage around 1970 corresponds to a small cooling of about 0.5°C in UKESM1-0-LL temperatures with respect to the previous years (data not shown).

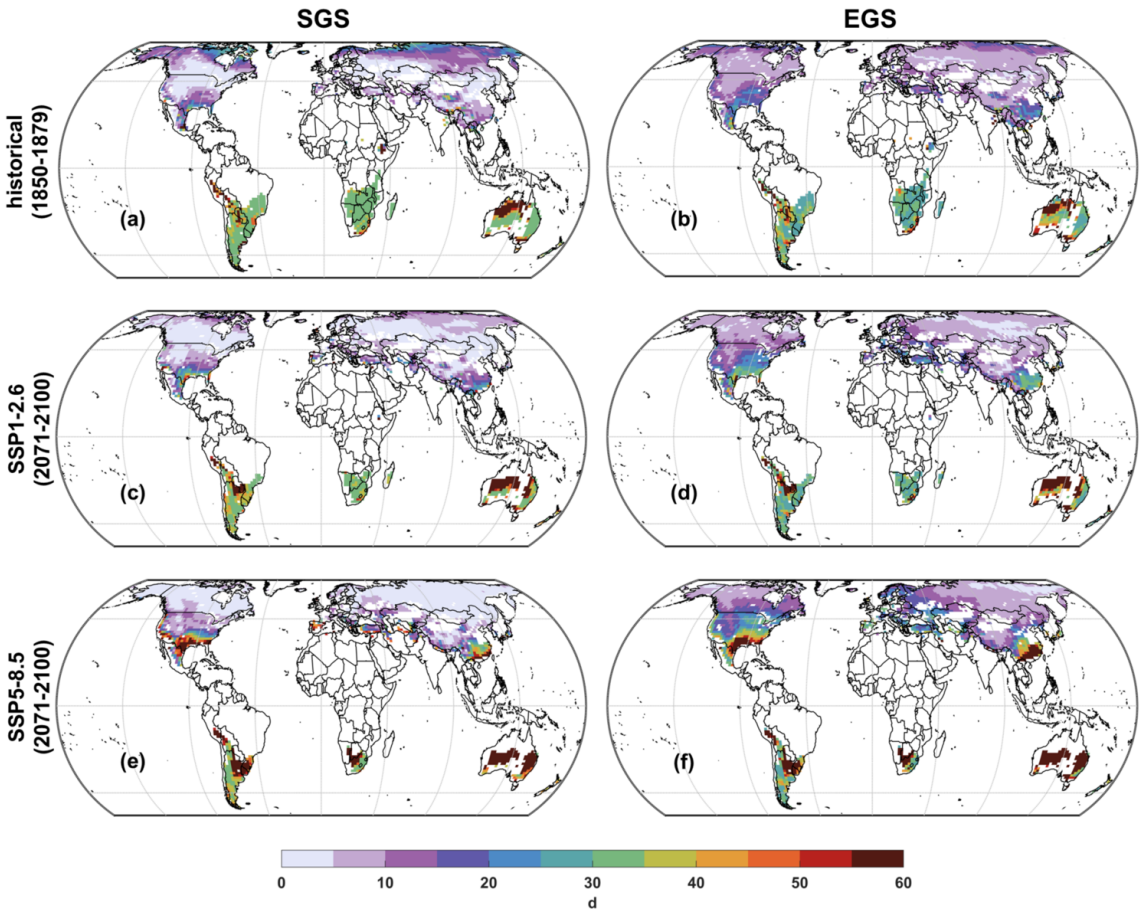

Figure D.7. Estimated error spread ($p_9 5$) for SGS (first column) and EGS (second column), for GS-P over UKESM1-0-LL temperatures, for the preindustrial period (historical, 1850-1880; a,b), and for the end-century period (SSP1-2.6, c,d; SSP5-8.5, e,f).

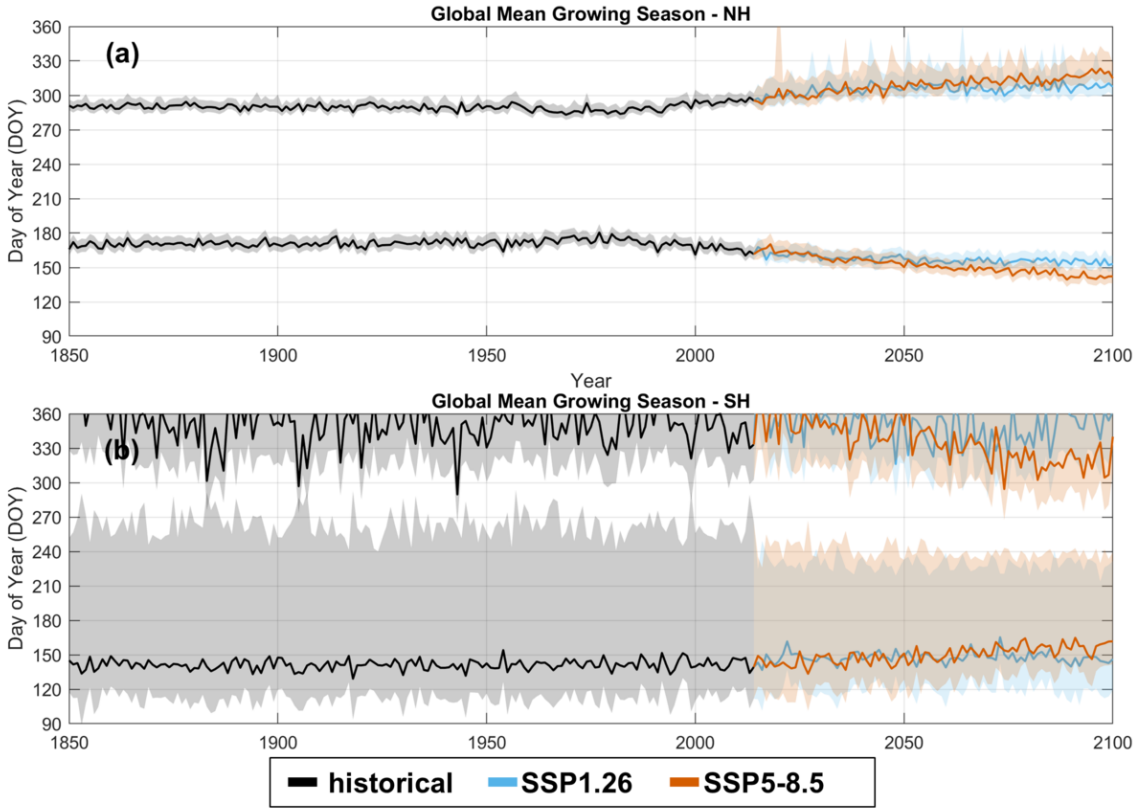

Figure D.8. Area-weighted yearly averages of SGS and EGS from 1850 to 2100 for the Northern Hemisphere (a) and Southern Hemisphere (b), as simulated by GS-Lin2 over UKESM1-0-LL temperatures. Only non-KG-transition and non-flipping nodes are considered. In the NH, the bottom lines refer to SGS, while the top lines refer to EGS; in the SH, the order is reversed. Shaded areas indicate the 95% confidence interval.

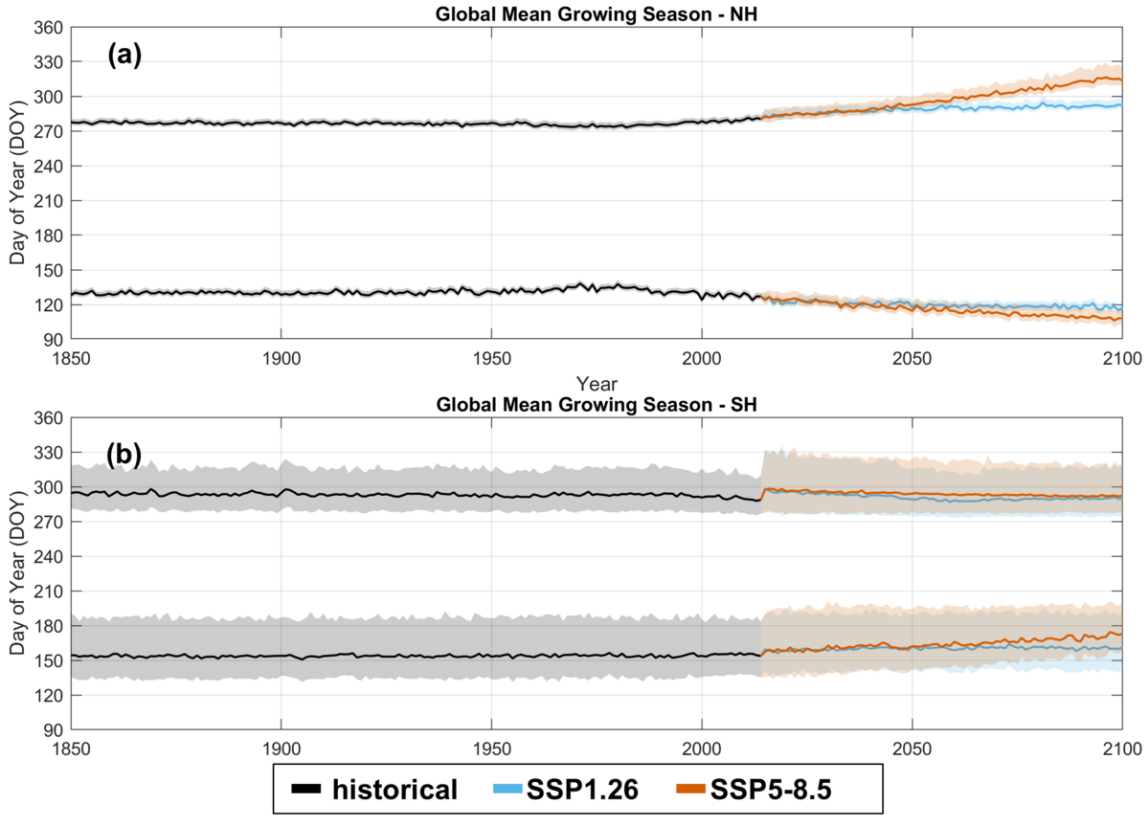

Figure D.9. Area-weighted yearly averages of SGS and EGS from 1850 to 2100 for the Northern Hemisphere (a) and Southern Hemisphere (b), as simulated by GS-BC2 over UKESM1-0-LL temperatures. Only non-KG-transition and non-flipping nodes are considered. In the NH, the bottom lines refer to SGS, while the top lines refer to EGS; in the SH, the order is reversed. Shaded areas indicate the 95% confidence interval.

APPENDIX E

ADDITIONAL METHODOLOGY FOR "GLOBAL FLUX-BASED ASSESSMENT OF OZONE RISK TO FOREST ECOSYSTEMS UNDER FUTURE CLIMATE CHANGE SCENARIOS"

To apply the dry deposition scheme for O_3 stomatal flux calculations, some transformation of the input variables and model parameters are required. The following sections describe calculations of roughness lenght, soil water content and soil water potential.

E.1 Calculations of the momentum roughness length of the reference surface

The roughness length for momentum of the reference surface ($z_{0,\mathrm{ref}}$) is calculated following the MOSES2.2/JULES documentation and Mason (1988):

$$z_{0,\mathrm{ref}} = l_b \exp\left\{ -\sqrt{\sum_j \frac{\nu_j}{\ln^2(l_b/z_{0j})}} \right\} \tag{E.1}$$

where l_b is the blending height (20 m in UKESM1-0-LL), ν_j are the fractional areas of each land-use type, and z_{0j} are the roughness lengths for each land-use type. More specifically, the aggregated roughness length for a tile is computed as:

$$z_0 = l_b \exp\left\{ -\sqrt{\sum_{j=1}^{5} \frac{\nu_j}{\ln^2(l_b/z_{0j})} + \frac{\nu_w - \nu_{\mathrm{ice}}}{\ln^2(l_b/z_{0w})} + \frac{\nu_{\mathrm{ice}}}{\ln^2(l_b/z_{0\mathrm{ice}})}} \right\} \tag{E.2}$$

This formula aggregates contributions from land not covered by snow, water bodies, and sea ice. For the land types, roughness lengths are calculated as $h_c/20$ for forests, and $h_c/10$ for crops and pastures, where h_c is the canopy height (m). After the aggregated roughness length is calculated, it is adjusted for snow mass in each tile:

$$z_{0,\mathrm{ref}} = \max\left(z_0 - 4 \cdot 10^{-4}\, S,\, 5 \cdot 10^{-4}\right) \tag{E.3}$$

TABLE E.1

ROUGHNESS LENGTH VALUES FOR EACH LAND COVER TYPE USED IN O_3 DRY DEPOSITION CALCULATIONS.

Symbol	Land cover	Value
z_{01}	Forest	$h/20$
z_{02}	Crops	$h/10$
z_{03}	Pasture	$h/10$
z_{04}	Urban	1.5
z_{05}	Bare soil	3×10^{-4}
z_{0w}	Water	3×10^{-4}
$z_{0\text{ice}}$	Ice	1×10^{-4}

E.1.1 Calculations of soil water content and soil water potential

Soil water content (SWC) and soil water potential (ψ) are variables required by the dry deposition model. As they are not provided directly by UKESM1-0-LL, we need a method to compute them from available quantities.

First, we convert available water content of soil quantities from UKESM1-0-LL ([kg m^{-2}]) to volumetric soil moisture ([m^3 H_2O m^{-3} soil]):

- The UKESM1-0-LL variable `mrsofc` (soil moisture content at field capacity) is converted to volumetric soil moisture content at field capacity (θ_{FC}):

$$\theta_{\text{FC,ESM}} = \frac{\text{mrsofc}}{1000}$$

- The variable `mrso` (mass content of water in soil) is converted to the volumetric soil moisture content (θ, frozen + liquid):

$$\theta = \frac{\text{mrso}}{1000 \cdot 3}$$

  where the number 3 accounts for the total depth of the soil layers (3 m).

- The volumetric soil moisture content referred to the assumed vegetation root depth (RD = 1 m) is converted from `mrsll` (liquid water content of soil layer). First, the volumetric soil water content for each layer i ($\theta_{\text{layer}}(i)$) is calculated as

$$\theta_{\text{layer}}(i) = \frac{\text{mrsll}(i)}{1000 \cdot (lb(i) - ub(i))}$$

  Then, the volumetric soil water content that is covered by a given root depth (θ_{RD}) is calculated as

$$\theta_{\text{RD}} = \frac{\sum_{i=1}^{4} w_i \, \theta_{\text{layer}}(i)}{\sum_{i=1}^{4} w_i}$$

where the weights w_i are proportional to layer thickness:

$$w_i = \min\left\{lb(i) - ub(i),\, \mathrm{RD} - ub(i)\right\},$$

with lb and ub representing the lower and upper bound depths of soil layer i.

To convert these quantities to soil water potential (ψ_m) and to soil water content (SWC), which are the variables employed within the Jarvis algorithm, we need to employ pedotransfer functions and the volumetric soil moisture content at wilting point (θ_{WP}), which are specific properties associated with the different soil types. Knowing θ_{FC}, and knowing that θ (frozen + liquid) cannot be smaller than the residual volumetric soil water content (θ_r), or greater than the volumetric soil water content at saturation (θ_s), we can infer the most similar soil type, according to Table E.2, and then compute the required values for the calculations of ψ_m and SWC by using the model of Van Genuchten (Van Genuchten, 1980). More specifically, the following procedure is employed:

1. Define soil types based on sand and clay percentages following Saxton and Rawls (2006) (first four columns of Table E.2).
2. For each soil type, calculate the residual soil moisture (θ_r), soil moisture at saturation (θ_s), and the Van Genuchten parameters α and n (Zhang and Schaap, 2017, see fifth to eighth columns of Table E.2).
3. Compute volumetric soil moisture at wilting point (θ_{WP}; ninth column) and at field capacity (θ_{FC}; last column) using the Van Genuchten equation:

$$\theta = \theta_r + (\theta_s - \theta_r)\left(1 + \alpha|\psi_m|^n\right)^{-m}, \quad m = 1 - \frac{1}{n} \tag{E.4}$$

   with ψ_m in cm (1 cm = 0.098 kPa).
4. Determine the soil type for each grid node:
   (a) Exclude soil types where $\theta < \theta_r$ or $\theta > \theta_s$.
   (b) From remaining types, choose the one with θ_{FC} closest to the ESM output $\theta_{\mathrm{FC,ESM}}$.
5. Based on the selected soil type, calculate SWC:

$$\mathrm{SWC} = 100 \cdot \max\left\{0, \min\left[1, \frac{\theta_{\mathrm{RD}} - \theta_{\mathrm{WP}}}{\theta_{\mathrm{FC}} - \theta_{\mathrm{WP}}}\right]\right\} \tag{E.5}$$

6. Invert the Van Genuchten (1980) equation to calculate ψ_m for the deposition model, converting from cm to MPa:

$$\psi_m = -\left[\frac{1}{\alpha}\left(\max\left\{0, \left(\max\{0, (\theta_{\mathrm{RD}} - \theta_r)/(\theta_s - \theta_r)\}\right)^{-1/m} - 1\right\}\right)\right]^{1/n} \cdot \frac{0.098}{1000} \tag{E.6}$$

   where the use of $\max\{0, \theta_{\mathrm{RD}} - \theta_r\}$ prevents $\theta_{\mathrm{RD}} - \theta_r$ to be negative, which can happen e.g., when a large portion of soil water is frozen, since θ_{RD} only accounts for the liquid fraction.

TABLE E.2

SOIL PROPERTIES BY SOIL TYPE AND PARAMETERIZATIONS FOR CALCULATING MATRIC POTENTIAL (ψ_m) FROM VOLUMETRIC SOIL WATER CONTENT. SAND (SA), LOAM (L), SILT (SI), CLAY (C). VALUES OF θ_r, θ_s, α, AND n ARE OBTAINED FROM ROSETTA (ZHANG & SCHAAP, 2017), WHILE θ_{WP} AND θ_{FC} ARE CALCULATED USING VAN GENUCHTEN (1980) AT $\psi_m = -1.5$ MPA AND $\psi_m = -0.033$ MPA, RESPECTIVELY.

Soil Type	Map ID	Sand (%)	Clay (%)	θ_r	θ_s	α	n	θ_{WP}	θ_{FC}
Sa	1	88	5	0.055	0.369	0.028	2.102	0.063	0.325
LSa	2	80	5	0.054	0.376	0.024	1.166	0.289	0.372
SaL	3	65	10	0.063	0.383	0.016	1.439	0.188	0.375
L	4	40	20	0.089	0.404	0.007	1.419	0.252	0.401
SiL	5	20	15	0.079	0.430	0.003	1.546	0.249	0.428
Si	6	10	5	0.063	0.451	0.004	1.650	0.193	0.447
SaCL	7	60	25	0.095	0.384	0.015	1.328	0.250	0.379
CL	8	30	35	0.114	0.429	0.007	1.343	0.308	0.426
SiCL	9	10	35	0.114	0.463	0.005	1.396	0.321	0.460
SaC	10	50	40	0.118	0.405	0.014	1.260	0.302	0.401
SiC	11	10	45	0.112	0.482	0.007	1.335	0.344	0.479
C	12	25	50	0.125	0.461	0.011	1.268	0.347	0.458

Citation: Saxton & Rawls (2006); Zhang & Schaap (2017); Van Genuchten (1980).

APPENDIX F

SUPPLEMENTARY FIGURES AND TABLES OF "GLOBAL FLUX-BASED ASSESSMENT OF OZONE RISK TO FOREST ECOSYSTEMS UNDER FUTURE CLIMATE CHANGE SCENARIOS"

TABLE F.1

KEY FEATURES OF UKESM1-0-LL: RESOLUTION, ATMOSPHERE AND CHEMISTRY MODULES, VARIANT , AND OUTPUT FREQUENCY

Property	**UKESM1-0-LL**
Horizontal resolution (lon × lat)	Land: 1.250° × 1.875° Ocean: 1° tripolar
Vertical atmosphere resolution	85 levels to ∼85 km
Mean lowest model level height (cell centre; m agl)	20
Atmosphere module	HadGEM3-GC3.1
Chemistry module	UKCA-StratTrop
Variant	r1i1p1f2
Output frequency	1 hour: ps, sfo3 3 hours: rlds, rsds, rsus, pr, tas, hfss 1 day: huss, rlus, sfcWind, mrsll Static: mrsofc
Documentation	Sellar et al. (2019)
Dataset citation	O'Connor (2020); Tang et al. (2019)

TABLE F.2

DOSE-RESPONSE RELATIONSHIPS (DRRS) USED TO ESTIMATE RELATIVE GROSS ANNUAL STEM VOLUME INCREMENT (RGAI) LOSSES (%) FROM POD_1 (MMOL M^{-2} PLA^{-1}). THE FACTOR 130/365 IS A CORRECTION APPLIED TO POD_1 (CALCULATED OVER THE WHOLE YEAR) TO ACCOUNT FOR THE SHORTER ACCUMULATION PERIOD USED IN THE CHEESMAN ET AL. EXPERIMENTS.

Species	**rGAI losses (DRR)**	**Reference**
Fagus sylvatica	$0.93 \cdot POD_1$	Karlsson et al. (2025)
Quercus robur	$0.57 \cdot POD_1$	Karlsson et al. (2025)
Picea abies	$0.57 \cdot POD_1$	Karlsson et al. (2025)
Inga edulis	$0.96 \cdot \left(\frac{130}{365} \cdot POD_1\right)$	Cheesman et al. (2024)

TABLE F.3

PARAMETERIZATIONS OF STOMATAL CONDUCTANCE USED IN THE STUDY FOR *PICEA ABIES*, *QUERCUS ROBUR/PETRAEA*, *FAGUS SYLVATICA*, AND *INGA EDULIS*. THE MEANING OF EACH PARAMETER IS DESCRIBED IN GUAITA ET AL. (2023). IN THE KÖPPEN–GEIGER (KG) CLIMATE CLASSIFICATION, ASTERISKS INDICATE THAT THE CORRESPONDING CLASSIFICATION LETTER IS OMITTED (E.G., D*B INCLUDES ALL PRECIPITATION SUBCLASSES).

Parameter / Unit	**Norway Spruce**	**Beech**	**Oak (Temperate)**	**Ingá-cipó**
Latin name	Picea abies	Fagus sylvatica	Quercus robur/petraea	Inga edulis
Associated KG climate	D ∗ b ∨ D ∗ c ∨ D ∗ d	C ∗ b ∨ C ∗ c	C ∗ ∗ ∨ D ∗ a	A
$g_{max,w}$ (mmol H_2O m^{-2} s^{-1})	-	-	-	-
$g_{max,O3}$ (mmol O_3 m^{-2} s^{-1})	125	155	255	279
fmin (adim)	0.1	0.13	0.06	0.19
lighta (adim)	0.006	0.006	0.003	0.01
Tmin (°C)	0	5	0	15
Topt (°C)	20	16	20	30
Tmax (°C)	200	33	35	45
VPDmax (kPa)	0.8	1.0	1.0	2.0
VPDmin (kPa)	2.8	3.1	3.25	3.8
SWCmax (%)	15	-	-	0
SWCmin (%)	1	-	-	0
SWPmax (MPa)	-	-0.05	-0.5	-
SWPmin (MPa)	-	-1.25	-1.2	-
fphen_a (adim)	0	0	0	1
fphen_b (adim)	1	1	1	1
fphen_c (adim)	1	1	1	1
fphen_d (adim)	1	1	1	1
fphen_e (adim)	0	0.4	0	1
fphen_1 (d)	20	20	20	0
fphen_2 (d)	200	200	200	200
fphen_3 (d)	200	200	200	200
fphen_4 (d)	30	20	30	0

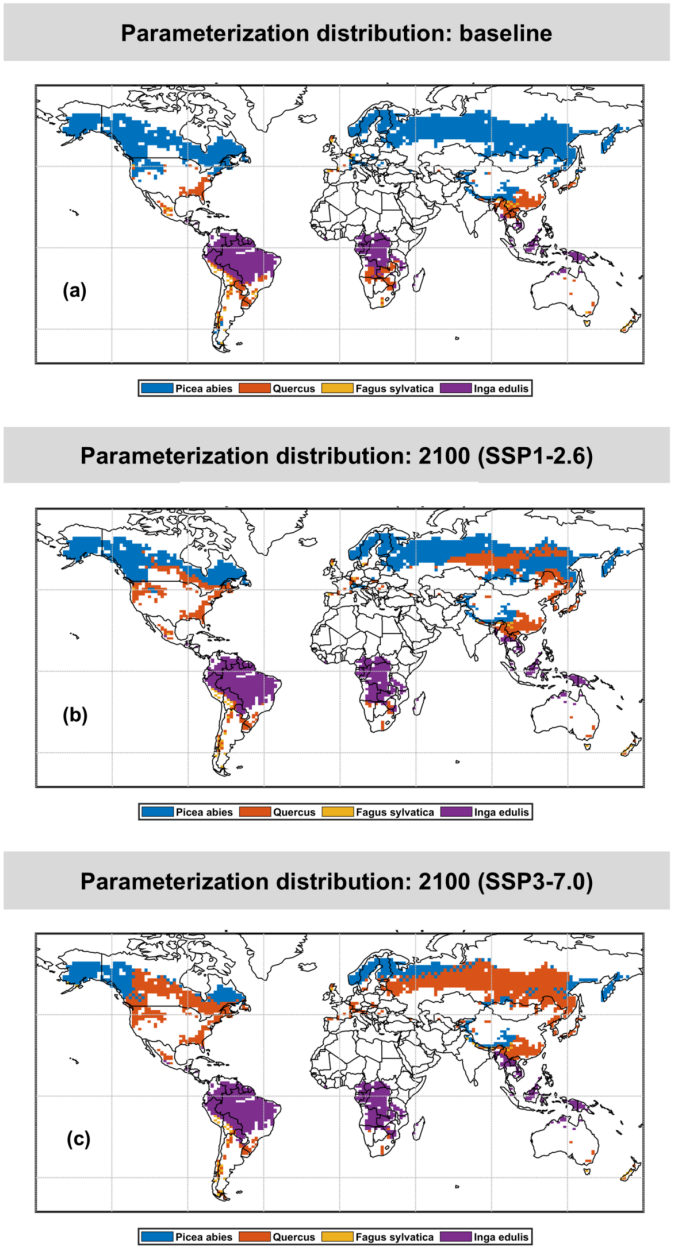

Figure F.1. Spatial distribution of the different parameterizations used in the study, during the baseline (a) and at 2100 under SSP1-2.6 (b) and SSP3-7.0 (c).

TABLE F.4

VALUES OF THE PARAMETERS OF f_{CO2} BY SPECIES. THE TERMS IN PARENTHESES REPRESENT THE 95% PREDICTION INTERVAL (PI) OF f_{CO2}, SHOWING THE LOWER AND UPPER BOUNDS OF THE FUNCTIONAL RESPONSE.

Species	a_{CO2}	$\mathbf{CO}_{2,\mathrm{ref}}$ **(ppm)**
Picea abies	−0.14[-0.31,0.04]	448.08[398.68,224.35]
Fagus sylvatica	−0.29[-0.39,-0.18]	371.72[366.13,375.67]
Quercus robur/petraea	−0.23[-0.37,-0.14]	357.13[357.53,368.6]
Tropical	−0.31[-0.42,-0.22]	342.43[329.25,366.39]

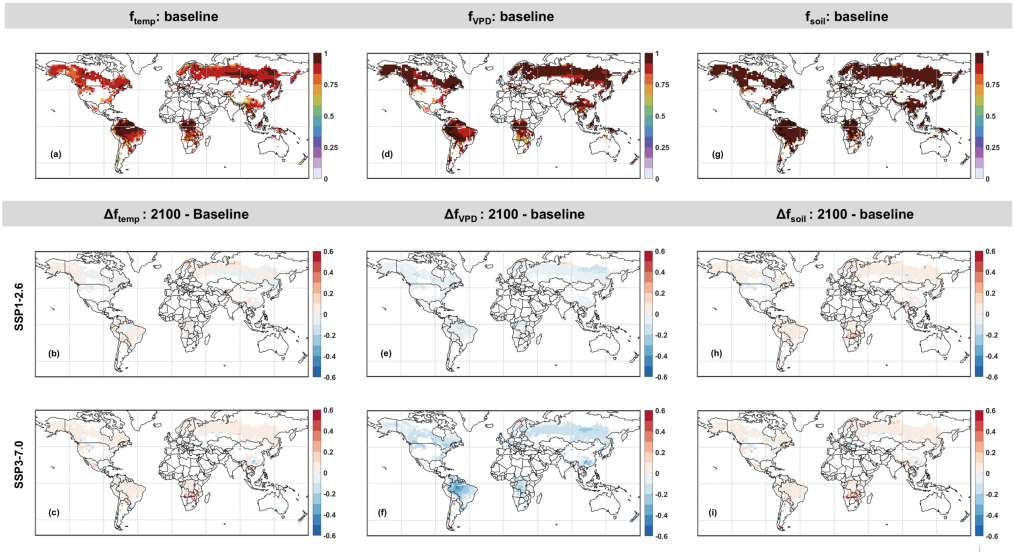

Figure F.2. Mean values of f_{temp} (a-c), f_{VPD} (d-f), and f_{soil} (g-i) over the baseline period (first row) and differences (Δ) at 2100 with respect to the baseline for SSP1-2.6 (second row) and SSP3-7.0 (third row).

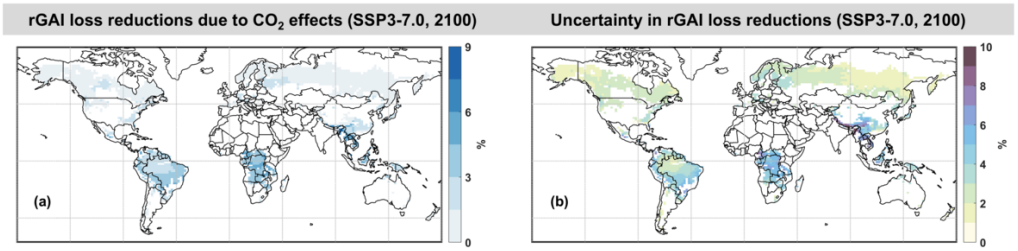

Figure F.3. Reductions in the relative rGAI losses in the MM+CO2 run (accounting for CO_2 effect on g_s) with respect to the MM run, under SSP3-7.0 at 2100 (a), and uncertainty range related to CO2 effect on g_s (b).

TABLE F.5

ANNUAL AVERAGE OF RELATIVE GROSS ANNUAL INCREMENT BY REGION, AT THE BASELINE, AND AT 2050 AND 2100 FOR SSP1-2.6 AND SSP3-7.0, WITH AND WITHOUT CO_2 EFFECTS.

Region	Baseline	2050				2100			
	Historical	SSP1-2.6		SSP3-7.0		SSP1-2.6		SSP3-7.0	
	MM	MM	MM+CO_2	MM	MM+CO_2 [low,up]	MM	MM+CO_2	MM	MM+CO_2 [low,up]
North America	4.5	3.3	3.1	5.2	4.7 [4.3,5.2]	7.7	7.1	5.7	3.9 [2.6,4.9]
Europe	6.1	5.1	4.9	7.7	7.2 [6.6,7.8]	3.7	3.5	7.7	5.7 [4.1,7.2]
South Asia	15.1	17	16.2	24.1	22.1 [20.7,23.4]	2.7	2.5	31.7	24.1 [19.8,28.1]
East Asia	13.2	11.1	10.5	16.5	15.1 [14,16]	4.6	4.4	14	10.6 [8.3,12.7]
South-East Asia	14.7	14.1	12.9	19.7	17.3 [16,18.4]	13.1	12.4	21.2	14.5 [11.6,17]
Sub-Saharan Africa	18.3	19.3	17.6	20	17.4 [16,18.5]	8.4	7.9	19.5	13 [10.2,15.4]
Central America	14.1	10.6	9.6	13.8	11.9 [10.9,12.7]	11.2	10.2	12.7	8.2 [6.3,9.9]
South America	14.3	11.8	10.7	15	13 [11.9,13.9]	7.4	6.7	13	8.4 [6.4,10.1]
Russia-Belarus-Ukraine	1.9	2.1	2	3.3	3.1 [2.8,3.5]	0	0	5.2	3.3 [2.2,4.3]

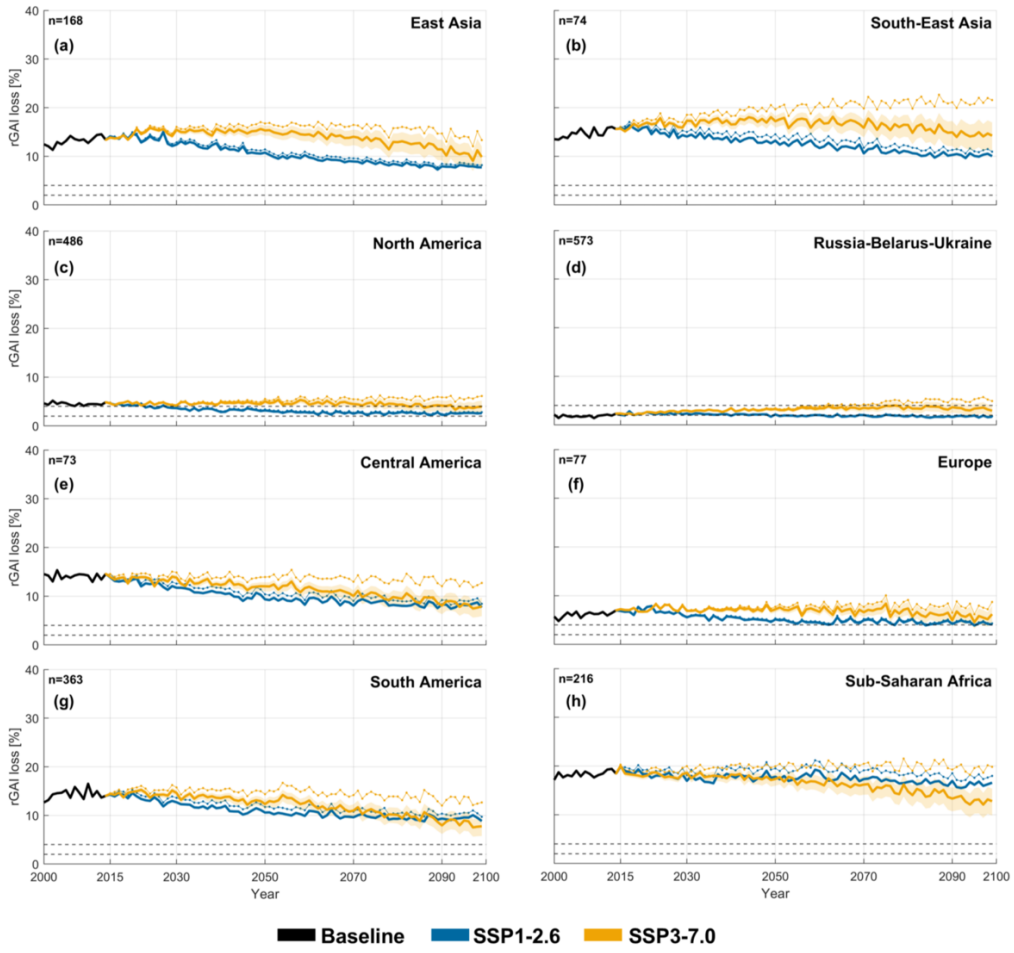

Figure F.4. Annual relative rGAI losses throughout the 21st century divided by region, for both the MM run (dotted lines) and the MM+CO2mid run (solid lines). The value (n) in the upper-left corner is the number of nodes in each area. Dashed horizontal line corresponds to the Critical Level for P. abies (2%) and for other species (4%).

BIBLIOGRAPHY

M. A. Adams, T. N. Buckley, and T. L. Turnbull. Diminishing CO2-driven gains in water-use efficiency of global forests. *Nat. Clim. Chang.*, 10(5):466–471, May 2020. ISSN 1758-678X, 1758-6798. doi: 10.1038/s41558-020-0747-7. URL https://www.nature.com/articles/s41558-020-0747-7.

M. Agrawal and S. Deepak. Physiological and biochemical responses of two cultivars of wheat to elevated levels of CO2 and SO2, singly and in combination. *Environmental Pollution*, 121 (2):189–197, Feb. 2003. ISSN 02697491. doi: 10.1016/S0269-7491(02)00222-1. URL https://linkinghub.elsevier.com/retrieve/pii/S0269749102002221.

E. A. Ainsworth and A. Rogers. The response of photosynthesis and stomatal conductance to rising [CO_2]: mechanisms and environmental interactions. *Plant Cell & Environment*, 30(3): 258–270, Mar. 2007. ISSN 0140-7791, 1365-3040. doi: 10.1111/j.1365-3040.2007.01641.x. URL https://onlinelibrary.wiley.com/doi/10.1111/j.1365-3040.2007.01641.x.

E. A. Ainsworth, C. R. Yendrek, S. Sitch, W. J. Collins, and L. D. Emberson. The Effects of Tropospheric Ozone on Net Primary Productivity and Implications for Climate Change. *Annu. Rev. Plant Biol.*, 63(1):637–661, June 2012. ISSN 1543-5008, 1545-2123. doi: 10.1146/annurev-arplant-042110-103829. URL https://www.annualreviews.org/doi/10.1146/annurev-arplant-042110-103829.

A. Anav, L. Menut, D. Khvorostyanov, and N. Viovy. Impact of tropospheric ozone on the Euro-Mediterranean vegetation. *Global Change Biology*, 17(7):2342–2359, July 2011. ISSN 13541013. doi: 10.1111/j.1365-2486.2010.02387.x. URL https://onlinelibrary.wiley.com/doi/10.1111/j.1365-2486.2010.02387.x.

A. Anav, A. De Marco, C. Proietti, A. Alessandri, A. Dell'Aquila, I. Cionni, P. Friedlingstein, D. Khvorostyanov, L. Menut, E. Paoletti, P. Sicard, S. Sitch, and M. Vitale. Comparing concentration-based (AOT40) and stomatal uptake (PODY) metrics for ozone risk assessment to European forests. *Global Change Biology*, 22(4):1608–1627, Apr. 2016. ISSN 1354-1013, 1365-2486. doi: 10.1111/gcb.13138. URL https://onlinelibrary.wiley.com/doi/10.1111/gcb.13138.

M. R. Ashmore. Assessing the future global impacts of ozone on vegetation. *Plant Cell & Environment*, 28(8):949–964, Aug. 2005. ISSN 0140-7791, 1365-3040. doi: 10.1111/j.1365-3040.2005.01341.x. URL https://onlinelibrary.wiley.com/doi/10.1111/j.1365-3040.2005.01341.x.

S. Avnery, D. L. Mauzerall, J. Liu, and L. W. Horowitz. Global crop yield reductions due to surface ozone exposure: 2. Year 2030 potential crop production losses and economic damage under two scenarios of O3 pollution. *Atmospheric Environment*, 45(13):2297–2309, Apr. 2011. ISSN 13522310. doi: 10.1016/j.atmosenv.2011.01.002. URL https://linkinghub.elsevier.com/retrieve/pii/S1352231011000070.

D. D. Baldocchi, B. B. Hicks, and P. Camara. A canopy stomatal resistance model for gaseous deposition to vegetated surfaces. *Atmospheric Environment (1967)*, 21(1):91–101, Jan. 1987.

ISSN 00046981. doi: 10.1016/0004-6981(87)90274-5. URL https://linkinghub.elsevier.com/retrieve/pii/0004698187902745.

J. T. Ball, I. E. Woodrow, and J. A. Berry. A Model Predicting Stomatal Conductance and its Contribution to the Control of Photosynthesis under Different Environmental Conditions. In J. Biggens, editor, *Progress in Photosynthesis Research*, volume 4, pages 221–224. Martinus Nijhoff Publishers, Netherlands, 1987. ISBN ISBN 90 247 3453 3. doi: 10.1007/978-94-017-0519-6_48. URL http://link.springer.com/10.1007/978-94-017-0519-6_48.

J. Barichivich, K. R. Briffa, R. B. Myneni, T. J. Osborn, T. M. Melvin, P. Ciais, S. Piao, and C. Tucker. Large-scale variations in the vegetation growing season and annual cycle of atmospheric CO_2 at high northern latitudes from 1950 to 2011. *Global Change Biology*, 19(10):3167–3183, Oct. 2013. ISSN 1354-1013, 1365-2486. doi: 10.1111/gcb.12283. URL https://onlinelibrary.wiley.com/doi/10.1111/gcb.12283.

A. Baronetti, J. C. González-Hidalgo, S. M. Vicente-Serrano, F. Acquaotta, and S. Fratianni. A weekly spatio-temporal distribution of drought events over the Po Plain (North Italy) in the last five decades. *Intl Journal of Climatology*, 40(10):4463–4476, Aug. 2020. ISSN 0899-8418, 1097-0088. doi: 10.1002/joc.6467. URL https://rmets.onlinelibrary.wiley.com/doi/10.1002/joc.6467.

B. Baruth, M. Van Den Berg, S. Niemeyer, B. Baruth, I. Biavetti, B. Bussay, A. Ceglar, G. De Sanctis, S. Garcia Condado, S. Karetsos, R. Lecerf, R. Lopez Lozano, L. Nisini Scacchiafichi, L. Panarello, L. Seguini, A. Toreti, M. Van Den Berg, and M. Van Der Velde. JRC MARS Bulletin Vol.24 No 9 - Crop monitoring in Europe, September 2016: EU-28 grain maize yields revised downwards. Scientific analysis or review LB-AW-16-009-EN-C (print),LB-AW-16-009-EN-N, Publications Office of the European Union, Luxembourg (Luxembourg), 2016.

J. Bender, U. Hertstein, and C. Black. Growth and yield responses of spring wheat to increasing carbon dioxide, ozone and physiological stresses: a statistical analysis of 'ESPACE-wheat' results. *European Journal of Agronomy*, 10(3-4):185–195, Apr. 1999. ISSN 11610301. doi: 10.1016/S1161-0301(99)00009-X. URL https://linkinghub.elsevier.com/retrieve/pii/S116103019900009X.

C. Berryman, D. Eamus, and G. Duff. Stomatal responses to a range of variables in two tropical tree species grown with CO_2 enrichment. *J Exp Bot*, 45(5):539–546, 1994. ISSN 0022-0957, 1460-2431. doi: 10.1093/jxb/45.5.539. URL https://academic.oup.com/jxb/article-lookup/doi/10.1093/jxb/45.5.539.

S. Biraud, M. Fischer, S. Chan, and M. Torn. FLUXNET2015 US-ARM ARM Southern Great Plains site- Lamont, 2016. URL https://www.osti.gov/servlets/purl/1440066/.

K. Blümel and F.-M. Chmielewski. Shortcomings of classical phenological forcing models and a way to overcome them. *Agricultural and Forest Meteorology*, 164:10–19, Oct. 2012. ISSN 01681923. doi: 10.1016/j.agrformet.2012.05.001. URL https://linkinghub.elsevier.com/retrieve/pii/S0168192312001700.

G. Bonan. *Climate Change and Terrestrial Ecosystem Modeling*. Cambridge University Press, 1 edition, Feb. 2019. ISBN 978-1-107-33921-7 978-1-107-04378-7 978-1-107-61907-4. doi: 10.1017/9781107339217. URL https://www.cambridge.org/core/product/identifier/9781107339217/type/book.

G. B. Bonan. Forests and Climate Change: Forcings, Feedbacks, and the Climate Benefits of Forests. *Science*, 320(5882):1444–1449, June 2008. ISSN 0036-8075, 1095-9203. doi: 10.1126/science.1155121. URL https://www.science.org/doi/10.1126/science.1155121.

G. B. Bonan. *Ecological climatology: concepts and applications*. Cambridge University Press, New York, NY, USA, third edition edition, 2016. ISBN 978-1-107-04377-0 978-1-107-61905-0.

D. Botti. A phytoclimatic map of Europe. *cybergeo*, Oct. 2018. ISSN 1278-3366. doi: 10.4000/cybergeo.29495. URL http://journals.openedition.org/cybergeo/29495.

K. A. Brauman, S. Siebert, and J. A. Foley. Improvements in crop water productivity increase water sustainability and food security—a global analysis. *Environ. Res. Lett.*, 8(2):024030, June 2013. ISSN 1748-9326. doi: 10.1088/1748-9326/8/2/024030. URL https://iopscience.iop.org/article/10.1088/1748-9326/8/2/024030.

M. Brice, K. Cazelles, P. Legendre, and M. Fortin. Disturbances amplify tree community responses to climate change in the temperate–boreal ecotone. *Global Ecol Biogeogr*, 28(11):1668–1681, Nov. 2019. ISSN 1466-822X, 1466-8238. doi: 10.1111/geb.12971. URL https://onlinelibrary.wiley.com/doi/10.1111/geb.12971.

M. Brice, S. Vissault, W. Vieira, D. Gravel, P. Legendre, and M. Fortin. Moderate disturbances accelerate forest transition dynamics under climate change in the temperate–boreal ecotone of eastern North America. *Global Change Biology*, 26(8):4418–4435, Aug. 2020. ISSN 1354-1013, 1365-2486. doi: 10.1111/gcb.15143. URL https://onlinelibrary.wiley.com/doi/10.1111/gcb.15143.

W. Brutsaert. *Evaporation into the Atmosphere*. Springer Netherlands, Dordrecht, 1982. ISBN 978-90-481-8365-4 978-94-017-1497-6. doi: 10.1007/978-94-017-1497-6. URL http://link.springer.com/10.1007/978-94-017-1497-6.

C. Buendía, A. Kleidon, and A. Porporato. The role of tectonic uplift, climate, and vegetation in the long-term terrestrial phosphorous cycle. *Biogeosciences*, 7(6):2025–2038, June 2010. ISSN 1726-4189. doi: 10.5194/bg-7-2025-2010. URL https://bg.copernicus.org/articles/7/2025/2010/.

J. A. Bunce. Stomatal conductance, photosynthesis and respiration of temperate deciduous tree seedlings grown outdoors at an elevated concentration of carbon dioxide. *Plant Cell & Environment*, 15(5):541–549, June 1992. ISSN 0140-7791, 1365-3040. doi: 10.1111/j.1365-3040.1992.tb01487.x. URL https://onlinelibrary.wiley.com/doi/10.1111/j.1365-3040.1992.tb01487.x.

G. S. Campbell and J. M. Norman. *An Introduction to Environmental Biophysics*. Springer New York, New York, NY, 1998. ISBN 978-0-387-94937-6 978-1-4612-1626-1. doi: 10.1007/978-1-4612-1626-1. URL http://link.springer.com/10.1007/978-1-4612-1626-1.

J. Cao, X. Yue, and M. Ma. Simulation of ozone–vegetation coupling and feedback in China using multiple ozone damage schemes. *Atmos. Chem. Phys.*, 24(7):3973–3987, Apr. 2024. ISSN 1680-7324. doi: 10.5194/acp-24-3973-2024. URL https://acp.copernicus.org/articles/24/3973/2024/.

L. E. Chambers, R. Altwegg, C. Barbraud, P. Barnard, L. J. Beaumont, R. J. M. Crawford, J. M. Durant, L. Hughes, M. R. Keatley, M. Low, P. C. Morellato, E. S. Poloczanska, V. Ruoppolo, R. E. T. Vanstreels, E. J. Woehler, and A. C. Wolfaardt. Phenological Changes in the Southern Hemisphere. *PLoS ONE*, 8(10):e75514, Oct. 2013. ISSN 1932-6203. doi: 10.1371/journal.pone.0075514. URL https://dx.plos.org/10.1371/journal.pone.0075514.

F. S. Chapin, P. A. Matson, and P. M. Vitousek. *Principles of Terrestrial Ecosystem Ecology*. Springer New York, New York, NY, 2011. ISBN 978-1-4419-9503-2 978-1-4419-9504-9. doi: 10.1007/978-1-4419-9504-9. URL http://link.springer.com/10.1007/978-1-4419-9504-9.

U. Charusombat, D. Niyogi, A. Kumar, X. Wang, F. Chen, A. Guenther, A. Turnipseed, and K. Alapaty. Evaluating a New Deposition Velocity Module in the Noah Land-Surface Model. *Boundary-Layer Meteorol*, 137(2):271–290, Nov. 2010. ISSN 0006-8314, 1573-1472. doi: 10.1007/s10546-010-9531-y. URL https://link.springer.com/10.1007/s10546-010-9531-y.

A. W. Cheesman, F. Brown, M. N. Farha, T. M. Rosan, G. A. Folberth, F. Hayes, B. B. Moura, E. Paoletti, Y. Hoshika, C. P. Osborne, L. A. Cernusak, R. V. Ribeiro, and S. Sitch. Impacts of ground-level ozone on sugarcane production. *Science of The Total Environment*, 904:166817, Dec. 2023. ISSN 00489697. doi: 10.1016/j.scitotenv.2023.166817. URL https://linkinghub.elsevier.com/retrieve/pii/S0048969723054426.

A. W. Cheesman, F. Brown, P. Artaxo, M. N. Farha, G. A. Folberth, F. J. Hayes, V. H. A. Heinrich, T. C. Hill, L. M. Mercado, R. J. Oliver, M. O' Sullivan, J. Uddling, L. A. Cernusak, and S. Sitch. Reduced productivity and carbon drawdown of tropical forests from ground-level ozone exposure. *Nat. Geosci.*, 17(10):1003–1007, Oct. 2024. ISSN 1752-0894, 1752-0908. doi: 10.1038/s41561-024-01530-1. URL https://www.nature.com/articles/s41561-024-01530-1.

T. Chen and C. Guestrin. XGBoost: A Scalable Tree Boosting System. In *Proceedings of the 22nd ACM SIGKDD International Conference on Knowledge Discovery and Data Mining*, pages 785–794, San Francisco California USA, Aug. 2016. ACM. ISBN 978-1-4503-4232-2. doi: 10.1145/2939672.2939785. URL https://dl.acm.org/doi/10.1145/2939672.2939785.

A. Chevalier, F. Gheusi, and R. Delmas. Influence of altitude on ozone levels and variability in the lower troposphere: a ground-based study for western Europe over the period 2001–2004. *Atmos. Chem. Phys.*, 2007.

D. D. Chiarelli, C. Passera, L. Rosa, K. F. Davis, P. D'Odorico, and M. C. Rulli. The green and blue crop water requirement WATNEEDS model and its global gridded outputs. *Sci Data*, 7(1):273, Aug. 2020. ISSN 2052-4463. doi: 10.1038/s41597-020-00612-0. URL https://www.nature.com/articles/s41597-020-00612-0.

F.-M. Chmielewski and T. Rötzer. Response of tree phenology to climate change across Europe. *Agricultural and Forest Meteorology*, 108(2):101–112, June 2001. ISSN 01681923. doi: 10.1016/S0168-1923(01)00233-7. URL https://linkinghub.elsevier.com/retrieve/pii/S0168192301002337.

K. Cho, S. Tiwari, S. B. Agrawal, N. L. Torres, M. Agrawal, A. Sarkar, J. Shibato, G. K. Agrawal, A. Kubo, and R. Rakwal. Tropospheric Ozone and Plants: Absorption, Responses, and Consequences. In D. M. Whitacre, editor, *Reviews of Environmental Contamination and Toxicology Volume 212*, volume 212, pages 61–111. Springer New York, New York, NY, 2011. ISBN 978-1-4419-8452-4 978-1-4419-8453-1. doi: 10.1007/978-1-4419-8453-1_3. URL http://link.springer.com/10.1007/978-1-4419-8453-1_3. Series Title: Reviews of Environmental Contamination and Toxicology.

I. Chuine, I. G. De Cortazar-Atauri, K. Kramer, and H. Hänninen. Plant Development Models. In M. D. Schwartz, editor, *Phenology: An Integrative Environmental Science*, pages 275–293. Springer Netherlands, Dordrecht, 2013. ISBN 978-94-007-6924-3 978-94-007-6925-0. doi: 10.1007/978-94-007-6925-0_15. URL https://link.springer.com/10.1007/978-94-007-6925-0_15.

C. Chuwah, T. Van Noije, D. P. Van Vuuren, E. Stehfest, and W. Hazeleger. Global impacts of surface ozone changes on crop yields and land use. *Atmospheric Environment*, 106:11–23, Apr. 2015. ISSN 13522310. doi: 10.1016/j.atmosenv.2015.01.062. URL https://linkinghub.elsevier.com/retrieve/pii/S1352231015000850.

M. Claverie, J. Ju, J. G. Masek, J. L. Dungan, E. F. Vermote, J.-C. Roger, S. V. Skakun, and C. Justice. The Harmonized Landsat and Sentinel-2 surface reflectance data set. *Remote Sensing of Environment*, 219:145–161, Dec. 2018. ISSN 00344257. doi: 10.1016/j.rse.2018.09.002. URL https://linkinghub.elsevier.com/retrieve/pii/S0034425718304139.

O. E. Clifton, D. Schwede, C. Hogrefe, J. O. Bash, S. Bland, P. Cheung, M. Coyle, L. Emberson, J. Flemming, E. Fredj, S. Galmarini, L. Ganzeveld, O. Gazetas, I. Goded, C. D. Holmes, L. Horváth, V. Huijnen, Q. Li, P. A. Makar, I. Mammarella, G. Manca, J. W. Munger, J. L. Pérez-Camanyo, J. Pleim, L. Ran, R. San Jose, S. J. Silva, R. Staebler, S. Sun, A. P. K. Tai, E. Tas, T. Vesala, T. Weidinger, Z. Wu, and L. Zhang. A single-point modeling approach for the intercomparison and evaluation of ozone dry deposition across chemical transport models (Activity 2 of AQMEII4), Mar. 2023. URL https://egusphere.copernicus.org/preprints/2023/egusphere-2023-465/.

W. J. Collins, J.-F. Lamarque, M. Schulz, O. Boucher, V. Eyring, M. I. Hegglin, A. Maycock, G. Myhre, M. Prather, D. Shindell, and S. J. Smith. AerChemMIP: quantifying the effects of chemistry and aerosols in CMIP6. *Geosci. Model Dev.*, 10(2):585–607, Feb. 2017. ISSN 1991-9603. doi: 10.5194/gmd-10-585-2017. URL https://gmd.copernicus.org/articles/10/585/2017/.

O. R. Cooper, D. D. Parrish, J. Ziemke, N. V. Balashov, M. Cupeiro, I. E. Galbally, S. Gilge, L. Horowitz, N. R. Jensen, J.-F. Lamarque, V. Naik, S. J. Oltmans, J. Schwab, D. T. Shindell, A. M. Thompson, V. Thouret, Y. Wang, and R. M. Zbinden. Global distribution and trends of tropospheric ozone: An observation-based review. *Elementa: Science of the Anthropocene*, 2: 000029, Jan. 2014. ISSN 2325-1026. doi: 10.12952/journal.elementa.000029. URL https://online.ucpress.edu/elementa/article/doi/10.12952/journal.elementa.000029/112944/Global-distribution-and-trends-of-tropospheric.

Copernicus Climate Change Service. Land cover classification gridded maps from 1992 to present derived from satellite observations, 2019. URL https://cds.climate.copernicus.eu/doi/10.24381/cds.006f2c9a.

M. Coyle, R. Smith, J. Stedman, K. Weston, and D. Fowler. Quantifying the spatial distribution of surface ozone concentration in the UK. *Atmospheric Environment*, 36(6):1013–1024, Feb. 2002. ISSN 13522310. doi: 10.1016/S1352-2310(01)00303-X. URL https://linkinghub.elsevier.com/retrieve/pii/S135223100100303X.

J. M. De Andrés, R. Borge, D. De La Paz, J. Lumbreras, and E. Rodríguez. Implementation of a module for risk of ozone impacts assessment to vegetation in the Integrated Assessment Modelling system for the Iberian Peninsula. Evaluation for wheat and Holm oak. *Environmental Pollution*, 165:25–37, June 2012. ISSN 02697491. doi: 10.1016/j.envpol.2012.01.048. URL https://linkinghub.elsevier.com/retrieve/pii/S0269749112000784.

A. De Ligne, T. Manise, C. Moureaux, M. Aubinet, and B. Heinesch. FLUXNET2015 BE-Lon Lonzee, 2016. URL https://www.osti.gov/servlets/purl/1440129/.

A. De Marco, P. Sicard, S. Fares, J.-P. Tuovinen, A. Anav, and E. Paoletti. Assessing the role of soil water limitation in determining the Phytotoxic Ozone Dose (PODY) thresholds. *Atmospheric Environment*, 147:88–97, Dec. 2016. ISSN 13522310. doi: 10.1016/j.atmosenv.2016.09.066. URL https://linkinghub.elsevier.com/retrieve/pii/S1352231016307853.

A. De Marco, A. Anav, P. Sicard, Z. Feng, and E. Paoletti. High spatial resolution ozone risk-assessment for Asian forests. *Environ. Res. Lett.*, 15(10):104095, Oct. 2020. ISSN 1748-9326. doi: 10.1088/1748-9326/abb501. URL https://iopscience.iop.org/article/10.1088/1748-9326/abb501.

A. De Marco, H. Garcia-Gomez, A. Collalti, Y. O. Khaniabadi, Z. Feng, C. Proietti, P. Sicard, M. Vitale, A. Anav, and E. Paoletti. Ozone modelling and mapping for risk assessment: An overview of different approaches for human and ecosystems health. *Environmental Research*, 211:113048, Aug. 2022. ISSN 00139351. doi: 10.1016/j.envres.2022.113048. URL https://linkinghub.elsevier.com/retrieve/pii/S0013935122003759.

A. Del Pozo, P. Pérez, R. Morcuende, A. Alonso, and R. Martínez-Carrasco. Acclimatory responses of stomatal conductance and photosynthesis to elevated CO2 and temperature in wheat crops grown at varying levels of N supply in a Mediterranean environment. *Plant Science*, 169(5): 908–916, Nov. 2005. ISSN 01689452. doi: 10.1016/j.plantsci.2005.06.009. URL https://linkinghub.elsevier.com/retrieve/pii/S0168945205002153.

D. Delahaye, S. Chaimatanan, and M. Mongeau. Simulated Annealing: From Basics to Applications. In M. Gendreau and J.-Y. Potvin, editors, *Handbook of Metaheuristics*, volume 272, pages 1–35. Springer International Publishing, Cham, 2019. ISBN 978-3-319-91085-7 978-3-319-91086-4. doi: 10.1007/978-3-319-91086-4_1. URL http://link.springer.com/10.1007/978-3-319-91086-4_1. Series Title: International Series in Operations Research & Management Science.

H. E. V. Donnou, A. B. Akpo, M. Ossohou, C. Delon, V. Yoboué, D. Laouali, M. Ouafo-Leumbe, P. G. Van Zyl, O. Ndiaye, E. Gardrat, M. Dias-Alves, and C. Galy-Lacaux. Measurement report: Long-term measurements of surface ozone and trends in semi-natural sub-Saharan African ecosystems. *Atmos. Chem. Phys.*, 24(23):13151–13182, Nov. 2024. ISSN 1680-7324. doi: 10.5194/acp-24-13151-2024. URL https://acp.copernicus.org/articles/24/13151/2024/.

J. Dumont, F. Spicher, P. Montpied, P. Dizengremel, Y. Jolivet, and D. Le Thiec. Effects of ozone on stomatal responses to environmental parameters (blue light, red light, CO2 and vapour pressure deficit) in three Populus deltoides × Populus nigra genotypes. *Environmental Pollution*, 173:85–96, Feb. 2013. ISSN 02697491. doi: 10.1016/j.envpol.2012.09.026. URL https://linkinghub.elsevier.com/retrieve/pii/S0269749112004368.

J. P. Dunne, L. W. Horowitz, A. J. Adcroft, P. Ginoux, I. M. Held, J. G. John, J. P. Krasting, S. Malyshev, V. Naik, F. Paulot, E. Shevliakova, C. A. Stock, N. Zadeh, V. Balaji, C. Blanton, K. A. Dunne, C. Dupuis, J. Durachta, R. Dussin, P. P. G. Gauthier, S. M. Griffies, H. Guo, R. W. Hallberg, M. Harrison, J. He, W. Hurlin, C. McHugh, R. Menzel, P. C. D. Milly, S. Nikonov, D. J. Paynter, J. Ploshay, A. Radhakrishnan, K. Rand, B. G. Reichl, T. Robinson, D. M. Schwarzkopf, L. T. Sentman, S. Underwood, H. Vahlenkamp, M. Winton, A. T. Wittenberg, B. Wyman, Y. Zeng, and M. Zhao. The GFDL Earth System Model Version 4.1 (GFDL-ESM 4.1): Overall Coupled Model Description and Simulation Characteristics. *J Adv Model Earth Syst*, 12(11): e2019MS002015, Nov. 2020. ISSN 1942-2466, 1942-2466. doi: 10.1029/2019MS002015. URL https://agupubs.onlinelibrary.wiley.com/doi/10.1029/2019MS002015.

Earth Resources Observation and Science (EROS) Center. USGS EROS archive digital elevation - global 30 arc-second elevation (GTOPO30). URL https://www.usgs.gov/centers/eros/science/usgs-eros-archive-digital-elevation-global-30-arc-second-elevation-gtopo30%2010.5066/F7DF6PQS.

EEA - European Environmental Agency. AirBase - the European Air Quality Database.

P. Egli, S. Maurer, M. S. Günthardt-Goerg, and C. Körner. Effects of elevated CO_2 and soil quality on leaf gas exchange and above-ground growth in beech–spruce model ecosystems. *New Phytologist*, 140(2):185–196, Oct. 1998. ISSN 0028-646X, 1469-8137. doi: 10.1046/j.1469-8137.1998.00276.x. URL https://nph.onlinelibrary.wiley.com/doi/10.1046/j.1469-8137.1998.00276.x.

L. Emberson. Effects of ozone on agriculture, forests and grasslands. *Phil. Trans. R. Soc. A.*, 378 (2183):20190327, Oct. 2020. ISSN 1364-503X, 1471-2962. doi: 10.1098/rsta.2019.0327. URL https://royalsocietypublishing.org/doi/10.1098/rsta.2019.0327.

L. D. Emberson, M. R. Ashmore, H. M. Cambridge, and D. Simpson. Modelling stomatal ozone flux across Europe. *Environmental Pollution*, 109:403–413, 2000a.

L. D. Emberson, D. Simpson, J.-P. Tuovinen, M. R. Ashmore, and H. M. Cambridge. Towards a model of ozone deposition and stomatal uptake over Europe. In *EMEP/MSC-W Note 6/2000*. DET NORSKE METEOROLOGISKE INSTITUTT, Oslo, Norway, 2000b.

L. D. Emberson, N. Kitwiroon, S. Beevers, P. Büker, and S. Cinderby. Scorched Earth: how will changes in the strength of the vegetation sink to ozone deposition affect human health and ecosystems? *Atmos. Chem. Phys.*, 13(14):6741–6755, July 2013. ISSN 1680-7324. doi: 10.5194/acp-13-6741-2013. URL https://acp.copernicus.org/articles/13/6741/2013/.

L. D. Emberson, H. Pleijel, E. A. Ainsworth, M. Van Den Berg, W. Ren, S. Osborne, G. Mills, D. Pandey, F. Dentener, P. Büker, F. Ewert, R. Koeble, and R. Van Dingenen. Ozone effects on crops and consideration in crop models. *European Journal of Agronomy*, 100:19–34, Oct. 2018. ISSN 11610301. doi: 10.1016/j.eja.2018.06.002. URL https://linkinghub.elsevier.com/retrieve/pii/S1161030118301606.

D. Epron, R. Liozon, and M. Mousseau. Effects of elevated CO2 concentration on leaf characteristics and photosynthetic capacity of beech (Fagus sylvatica) during the growing season. *Tree Physiology*, 16(4):425–432, Apr. 1996. ISSN 0829-318X, 1758-4469. doi: 10.1093/treephys/16.4.425. URL https://academic.oup.com/treephys/article-lookup/doi/10.1093/treephys/16.4.425.

European Environment Agency. *Air quality in Europe: 2020 report.* Publications Office, LU, 2020. doi: 10.2800/786656. URL https://data.europa.eu/doi/10.2800/786656.

European Parliament and Council of the European Union. Directive 2008/50/EC of the European Parliament and of the Council of 21 May 2008 on Ambient Air Quality and Cleaner Air for Europe. Technical Report L152, pp. 1–44, Brussels, Belgium, June 2008. URL https://eur-lex.europa.eu/eli/dir/2008/50/oj/eng?utm_source=chatgpt.com.

S. E. Everingham, R. A. J. Blick, M. E. B. Sabot, E. Slavich, and A. T. Moles. Southern hemisphere plants show more delays than advances in flowering phenology. *Journal of Ecology*, 111(2):380–390, Feb. 2023. ISSN 0022-0477, 1365-2745. doi: 10.1111/1365-2745.13828. URL https://besjournals.onlinelibrary.wiley.com/doi/10.1111/1365-2745.13828.

V. Eyring, S. Bony, G. A. Meehl, C. A. Senior, B. Stevens, R. J. Stouffer, and K. E. Taylor. Overview of the Coupled Model Intercomparison Project Phase 6 (CMIP6) experimental design and organization. *Geosci. Model Dev.*, 9(5):1937–1958, May 2016. ISSN 1991-9603. doi: 10.5194/gmd-9-1937-2016. URL https://gmd.copernicus.org/articles/9/1937/2016/.

X. Fan, Q. Duan, C. Shen, Y. Wu, and C. Xing. Global surface air temperatures in CMIP6: historical performance and future changes. *Environ. Res. Lett.*, 15(10):104056, Oct. 2020. ISSN 1748-9326. doi: 10.1088/1748-9326/abb051. URL https://iopscience.iop.org/article/10.1088/1748-9326/abb051.

Z. Fang, W. Zhang, M. Brandt, A. M. Abdi, and R. Fensholt. Globally Increasing Atmospheric Aridity Over the 21st Century. *Earth's Future*, 10(10):e2022EF003019, Oct. 2022. ISSN 2328-4277, 2328-4277. doi: 10.1029/2022EF003019. URL https://agupubs.onlinelibrary.wiley.com/doi/10.1029/2022EF003019.

G. D. Farquhar, S. Von Caemmerer, and J. A. Berry. A biochemical model of photosynthetic CO2 assimilation in leaves of C3 species. *Planta*, 149(1):78–90, June 1980. ISSN 0032-0935, 1432-2048. doi: 10.1007/BF00386231. URL http://link.springer.com/10.1007/BF00386231.

S. Fauset, L. Oliveira, M. S. Buckeridge, C. H. Foyer, D. Galbraith, R. Tiwari, and M. Gloor. Contrasting responses of stomatal conductance and photosynthetic capacity to warming and elevated CO2 in the tropical tree species Alchornea glandulosa under heatwave conditions. *Environmental and Experimental Botany*, 158:28–39, Feb. 2019. ISSN 00988472. doi: 10.1016/j.envexpbot.2018.10.030. URL https://linkinghub.elsevier.com/retrieve/pii/S0098847218311663.

K. J. Feeley, S. J. Davies, R. Perez, S. P. Hubbell, and R. B. Foster. Directional changes in the species composition of a tropical forest. *Ecology*, 92(4):871–882, Apr. 2011. ISSN 0012-9658. doi: 10.1890/10-0724.1. URL http://doi.wiley.com/10.1890/10-0724.1.

B. Felzer, D. Kicklighter, J. Melillo, C. Wang, Q. Zhuang, and R. Prinn. Effects of ozone on net primary production and carbon sequestration in the conterminous United States using a biogeochemistry model. *Tellus B: Chemical and Physical Meteorology*, 56(3):230, Jan. 2004. ISSN 1600-0889, 0280-6509. doi: 10.3402/tellusb.v56i3.16415. URL https://b.tellusjournals.se/article/10.3402/tellusb.v56i3.16415/.

B. Felzer, J. Reilly, J. Melillo, D. Kicklighter, M. Sarofim, C. Wang, R. Prinn, and Q. Zhuang. Future Effects of Ozone on Carbon Sequestration and Climate Change Policy Using a Global Biogeochemical Model. *Climatic Change*, 73(3):345–373, Dec. 2005. ISSN 0165-0009, 1573-1480. doi: 10.1007/s10584-005-6776-4. URL http://link.springer.com/10.1007/s10584-005-6776-4.

M. L. Fischer, D. P. Billesbach, J. A. Berry, W. J. Riley, and M. S. Torn. Spatiotemporal Variations in Growing Season Exchanges of CO2, H2O, and Sensible Heat in Agricultural Fields of the Southern Great Plains. *Earth Interactions*, 11(17):1–21, Oct. 2007. ISSN 1087-3562. doi: 10.1175/EI231.1. URL https://journals.ametsoc.org/doi/10.1175/EI231.1.

E. L. Fiscus, F. L. Booker, and K. O. Burkey. Crop responses to ozone: uptake, modes of action, carbon assimilation and partitioning. *Plant Cell & Environment*, 28(8):997–1011, Aug. 2005. ISSN 0140-7791, 1365-3040. doi: 10.1111/j.1365-3040.2005.01349.x. URL https://onlinelibrary.wiley.com/doi/10.1111/j.1365-3040.2005.01349.x.

D. Fowler, M. Coyle, U. Skiba, M. A. Sutton, J. N. Cape, S. Reis, L. J. Sheppard, A. Jenkins, B. Grizzetti, J. N. Galloway, P. Vitousek, A. Leach, A. F. Bouwman, K. Butterbach-Bahl, F. Dentener, D. Stevenson, M. Amann, and M. Voss. The global nitrogen cycle in the twenty-first century. *Phil. Trans. R. Soc. B*, 368(1621):20130164, July 2013. ISSN 0962-8436, 1471-2970. doi: 10.1098/rstb.2013.0164. URL https://royalsocietypublishing.org/doi/10.1098/rstb.2013.0164.

P. J. Franks, J. A. Berry, D. L. Lombardozzi, and G. B. Bonan. Stomatal Function across Temporal and Spatial Scales: Deep-Time Trends, Land-Atmosphere Coupling and Global Models. *Plant Physiol.*, 174(2):583–602, June 2017. ISSN 0032-0889, 1532-2548. doi: 10.1104/pp.17.00287. URL https://academic.oup.com/plphys/article/174/2/583-602/6117412.

M. Franz, R. Alonso, A. Arneth, P. Büker, S. Elvira, G. Gerosa, L. Emberson, Z. Feng, D. Le Thiec, R. Marzuoli, E. Oksanen, J. Uddling, M. Wilkinson, and S. Zaehle. Evaluation of simulated ozone effects in forest ecosystems against biomass damage estimates from fumigation experiments. *Biogeosciences*, 15(22):6941–6957, Nov. 2018. ISSN 1726-4189. doi: 10.5194/bg-15-6941-2018. URL https://bg.copernicus.org/articles/15/6941/2018/.

M. A. Friedl, D. Sulla-Menashe, B. Tan, A. Schneider, N. Ramankutty, A. Sibley, and X. Huang. MODIS Collection 5 global land cover: Algorithm refinements and characterization of new datasets. *Remote Sensing of Environment*, 114(1):168–182, Jan. 2010. ISSN 00344257. doi: 10.1016/j.rse.2009.08.016. URL https://linkinghub.elsevier.com/retrieve/pii/S0034425709002673.

J. Fuhrer, L. Skärby, and M. Ashmore. Critical levels for ozone effects on vegetation in Europe. *Environmental Pollution*, 97(1-2):91–106, 1997. ISSN 02697491. doi: 10.1016/S0269-7491(97)00067-5. URL https://linkinghub.elsevier.com/retrieve/pii/S0269749197000675.

J. Fuhrer, M. Val Martin, G. Mills, C. L. Heald, H. Harmens, F. Hayes, K. Sharps, J. Bender, and M. R. Ashmore. Current and future ozone risks to global terrestrial biodiversity and ecosystem processes. *Ecology and Evolution*, 6(24):8785–8799, Dec. 2016. ISSN 2045-7758, 2045-7758. doi: 10.1002/ece3.2568. URL https://onlinelibrary.wiley.com/doi/10.1002/ece3.2568.

S. Fujimori, T. Hasegawa, T. Masui, K. Takahashi, D. S. Herran, H. Dai, Y. Hijioka, and M. Kainuma. SSP3: AIM implementation of Shared Socioeconomic Pathways. *Global Environmental Change*, 42:268–283, Jan. 2017. ISSN 09593780. doi: 10.1016/j.gloenvcha.2016.06.009. URL https://linkinghub.elsevier.com/retrieve/pii/S0959378016300838.

R. García-Herrera, J. M. Garrido-Perez, D. Barriopedro, C. Ordóñez, S. M. Vicente-Serrano, R. Nieto, L. Gimeno, R. Sorí, and P. Yiou. The European 2016/17 Drought. *Journal of Climate*, 32 (11):3169–3187, June 2019. ISSN 0894-8755, 1520-0442. doi: 10.1175/JCLI-D-18-0331.1. URL https://journals.ametsoc.org/view/journals/clim/32/11/jcli-d-18-0331.1.xml.

V. S. F. Garnot, L. Spafford, J. Lever, C. Sigg, B. Pietragalla, Y. Vitasse, A. Gessler, and J. D. Wegner. Deep learning meets tree phenology modelling: PhenoFormer versus process-based models. *Methods Ecol Evol*, 16(7):1489–1506, July 2025. ISSN 2041-210X, 2041-210X. doi: 10.1111/2041-210X.70037. URL https://besjournals.onlinelibrary.wiley.com/doi/10.1111/2041-210X.70037.

C. Garosi, E. Paoletti, C. Pisuttu, L. Cotrozzi, E. Pellegrini, and Y. Hoshika. Ozone-induced 'sluggish' stomatal CO2 response depends on oxidative damage and pigment degradation in the Mediterranean shrub Viburnum lantana L. *Environmental and Experimental Botany*, 240:106273, Dec. 2025. ISSN 00988472. doi: 10.1016/j.envexpbot.2025.106273. URL https://linkinghub.elsevier.com/retrieve/pii/S009884722500190X.

A. Gaudel, O. R. Cooper, G. Ancellet, B. Barret, A. Boynard, J. P. Burrows, C. Clerbaux, P.-F. Coheur, J. Cuesta, E. Cuevas, S. Doniki, G. Dufour, F. Ebojie, G. Foret, O. Garcia, M. J. Granados-Muñoz, J. W. Hannigan, F. Hase, B. Hassler, G. Huang, D. Hurtmans, D. Jaffe, N. Jones, P. Kalabokas, B. Kerridge, S. Kulawik, B. Latter, T. Leblanc, E. Le Flochmoën, W. Lin, J. Liu, X. Liu, E. Mahieu, A. McClure-Begley, J. L. Neu, M. Osman, M. Palm, H. Petetin, I. Petropavlovskikh, R. Querel, N. Rahpoe, A. Rozanov, M. G. Schultz, J. Schwab, R. Siddans, D. Smale, M. Steinbacher, H. Tanimoto, D. W. Tarasick, V. Thouret, A. M. Thompson, T. Trickl, E. Weatherhead, C. Wespes, H. M. Worden, C. Vigouroux, X. Xu, G. Zeng, and J. Ziemke. Tropospheric Ozone Assessment Report: Present-day distribution and trends of tropospheric ozone relevant to climate and global atmospheric chemistry model evaluation. *Elementa: Science of the Anthropocene*, 6:39, Jan. 2018. ISSN 2325-1026. doi: 10.1525/elementa.291. URL https://online.ucpress.edu/elementa/article/doi/10.1525/elementa.291/112811/Tropospheric-Ozone-Assessment-Report-Present-day.

A. Gelman, J. B. Carlin, H. S. Stern, D. B. Dunson, A. Vehtari, and D. B. Rubin. Bayesian Data Analysis Third edition (with errors fixed as of 20 February 2025). 2025.

G. Gerosa, S. Cieslik, and A. Ballarin-Denti. Micrometeorological determination of time-integrated stomatal ozone fluxes over wheat: a case study in Northern Italy. *Atmospheric Environment*, 37 (6):777–788, Feb. 2003. ISSN 13522310. doi: 10.1016/S1352-2310(02)00927-5. URL https://linkinghub.elsevier.com/retrieve/pii/S1352231002009275.

G. Gerosa, R. Marzuoli, B. Monteleone, M. Chiesa, and A. Finco. Vertical Ozone Gradients above Forests. Comparison of Different Calculation Options with Direct Ozone Measurements above a Mature Forest and Consequences for Ozone Risk Assessment. *Forests*, 8(9):337, Sept. 2017. ISSN 1999-4907. doi: 10.3390/f8090337. URL https://www.mdpi.com/1999-4907/8/9/337.

M. M. Girona, H. Morin, S. Gauthier, and Y. Bergeron, editors. *Boreal Forests in the Face of Climate Change: Sustainable Management*, volume 74 of *Advances in Global Change Research*. Springer International Publishing, Cham, 2023. ISBN 978-3-031-15987-9 978-3-031-15988-6. doi: 10.1007/978-3-031-15988-6. URL https://link.springer.com/10.1007/978-3-031-15988-6.

I. González-Fernández, V. Bermejo, S. Elvira, D. De La Torre, A. González, L. Navarrete, J. Sanz, H. Calvete, H. García-Gómez, A. López, J. Serra, A. Lafarga, A. Armesto, A. Calvo, and R. Alonso. Modelling ozone stomatal flux of wheat under mediterranean conditions. *Atmospheric Environment*, 67:149–160, Mar. 2013. ISSN 13522310. doi: 10.1016/j.atmosenv.2012.10.043. URL https://linkinghub.elsevier.com/retrieve/pii/S1352231012010254.

P. Good, A. Sellar, Y. Tang, S. Rumbold, R. Ellis, D. Kelley, and T. Kuhlbrodt. MOHC UKESM1.0-LL model output prepared for CMIP6 ScenarioMIP ssp370, 2019a. URL http://cera-www.dkrz.de/WDCC/meta/CMIP6/CMIP6.ScenarioMIP.MOHC.UKESM1-0-LL.ssp370.

P. Good, A. Sellar, Y. Tang, S. Rumbold, R. Ellis, D. Kelley, and T. Kuhlbrodt. MOHC UKESM1.0-LL model output prepared for CMIP6 ScenarioMIP ssp585, 2019b. URL http://cera-www.dkrz.de/WDCC/meta/CMIP6/CMIP6.ScenarioMIP.MOHC.UKESM1-0-LL.ssp585.

J. Goodfellow, D. Eamus, and G. Duff. Diurnal and seasonal changes in the impact of CO2 enrichment on assimilation, stomatal conductance and growth in a long-term study of Mangifera indica in the wet-dry tropics of Australia. *Tree Physiology*, 17(5):291–299, May 1997. ISSN 0829-318X, 1758-4469. doi: 10.1093/treephys/17.5.291. URL https://academic.oup.com/treephys/article-lookup/doi/10.1093/treephys/17.5.291.

P. Goovaerts. *Geostatistics for natural resources evaluation*. Oxford university press, New York, 1997. ISBN 978-0-19-511538-3.

P. T. Griffiths, L. T. Murray, G. Zeng, A. T. Archibald, L. K. Emmons, I. Galbally, B. Hassler, L. W. Horowitz, J. Keeble, J. Liu, O. Moeini, V. Naik, F. M. O'Connor, Y. M. Shin, D. Tarasick, S. Tilmes, S. T. Turnock, O. Wild, P. J. Young, and P. Zanis. Tropospheric ozone in CMIP6 Simulations, Feb. 2020. URL https://acp.copernicus.org/preprints/acp-2019-1216/acp-2019-1216.pdf.

N. E. Grulke and R. L. Heath. Ozone effects on plants in natural ecosystems. *Plant Biol J*, 22(S1): 12–37, 2019. ISSN 1435-8603, 1438-8677. doi: 10.1111/plb.12971. URL https://onlinelibrary.wiley.com/doi/10.1111/plb.12971.

P. R. Guaita, R. Marzuoli, and G. A. Gerosa. A regional scale flux-based O3 risk assessment for winter wheat in northern Italy, and effects of different spatio-temporal resolutions. *Environmental Pollution*, 333:121860, Sept. 2023. ISSN 02697491. doi: 10.1016/j.envpol.2023.121860. URL https://linkinghub.elsevier.com/retrieve/pii/S026974912300862X.

P. R. Guaita, R. Marzuoli, L. Zhang, S. Turnock, G. Koren, O. Wild, P. Crippa, and G. Gerosa. Global Flux-Based Assessment Reveals Declining Ozone Risk for Wheat in Future Climate Change Scenarios. *Global Change Biology*, 31(12):e70643, Dec. 2025. ISSN 1354-1013, 1365-2486. doi: 10.1111/gcb.70643. URL https://onlinelibrary.wiley.com/doi/10.1111/gcb.70643.

W. Hagan Brown, E. Gloor, R. Fyfe, A. R. MacKenzie, N. J. Harper, P. Ganderton, K. Hart, G. Curioni, S. Quick, S. J. Davidson, E. Yetton, J. L. Diehl, and S. Fauset. Elevated CO_2 Increases the Canopy Temperature of Mature *Quercus robur* (Pedunculate Oak). *Global Change Biology*, 31(11):e70565, Nov. 2025. ISSN 1354-1013, 1365-2486. doi: 10.1111/gcb.70565. URL https://onlinelibrary.wiley.com/doi/10.1111/gcb.70565.

S. R. Hanna and J. C. Chang. Hybrid plume dispersion model (HPDM) improvements and testing at three field sites. *Atmospheric Environment. Part A. General Topics*, 27(9):1491–1508, June 1993. ISSN 09601686. doi: 10.1016/0960-1686(93)90135-L. URL https://linkinghub.elsevier.com/retrieve/pii/096016869390135L.

T. B. Hasper, M. E. Dusenge, F. Breuer, F. K. Uwizeye, G. Wallin, and J. Uddling. Stomatal CO2 responsiveness and photosynthetic capacity of tropical woody species in relation to taxonomy and functional traits. *Oecologia*, 184(1):43–57, May 2017. ISSN 0029-8549, 1432-1939. doi: 10.1007/s00442-017-3829-0. URL http://link.springer.com/10.1007/s00442-017-3829-0.

M. Haworth, D. Killi, A. Materassi, A. Raschi, and M. Centritto. Impaired Stomatal Control Is Associated with Reduced Photosynthetic Physiology in Crop Species Grown at Elevated [CO2]. *Front. Plant Sci.*, 7, Oct. 2016. ISSN 1664-462X. doi: 10.3389/fpls.2016.01568. URL http://journal.frontiersin.org/article/10.3389/fpls.2016.01568/full.

J. Heath. Stomata of trees growing in CO_2 -enriched air show reduced sensitivity to vapour pressure deficit and drought. *Plant Cell & Environment*, 21(11):1077–1088, Nov. 1998. ISSN 0140-7791, 1365-3040. doi: 10.1046/j.1365-3040.1998.00366.x. URL https://onlinelibrary.wiley.com/doi/10.1046/j.1365-3040.1998.00366.x.

J. Heath and G. Kerstiens. Effects of elevated CO_2 on leaf gas exchange in beech and oak at two levels of nutrient supply: consequences for sensitivity to drought in beech. *Plant Cell & Environment*, 20(1):57–67, Jan. 1997. ISSN 0140-7791, 1365-3040. doi: 10.1046/j.1365-3040.1997.d01-13.x. URL https://onlinelibrary.wiley.com/doi/10.1046/j.1365-3040.1997.d01-13.x.

W. W. Heck, O. C. Taylor, R. Adams, G. Bingham, J. Miller, E. Preston, and L. Weinstein. Assessment of Crop Loss from Ozone. *Journal of the Air Pollution Control Association*, 32(4):353–361, Apr. 1982. ISSN 0002-2470. doi: 10.1080/00022470.1982.10465408. URL http://www.tandfonline.com/doi/abs/10.1080/00022470.1982.10465408.

H. Hersbach, B. Bell, P. Berrisford, S. Hirahara, A. Horányi, J. Muñoz-Sabater, J. Nicolas, C. Peubey, R. Radu, D. Schepers, A. Simmons, C. Soci, S. Abdalla, X. Abellan, G. Balsamo, P. Bechtold, G. Biavati, J. Bidlot, M. Bonavita, G. De Chiara, P. Dahlgren, D. Dee, M. Diamantakis, R. Dragani, J. Flemming, R. Forbes, M. Fuentes, A. Geer, L. Haimberger, S. Healy, R. J. Hogan, E. Hólm, M. Janisková, S. Keeley, P. Laloyaux, P. Lopez, C. Lupu, G. Radnoti, P. De Rosnay, I. Rozum, F. Vamborg, S. Villaume, and J. Thépaut. The ERA5 global reanalysis. *Quart J Royal Meteoro Soc*, 146(730):1999–2049, July 2020. ISSN 0035-9009, 1477-870X. doi: 10.1002/qj.3803. URL https://rmets.onlinelibrary.wiley.com/doi/10.1002/qj.3803.

B. B. Hicks, D. D. Baldocchi, T. P. Meyers, R. P. Hosker, and D. R. Matt. A preliminary multiple resistance routine for deriving dry deposition velocities from measured quantities. *Water Air Soil Pollut*, 36(3-4):311–330, Sept. 1987. ISSN 0049-6979, 1573-2932. doi: 10.1007/BF00229675. URL http://link.springer.com/10.1007/BF00229675.

A. A. M. Holtslag and A. P. Van Ulden. A Simple Scheme for Daytime Estimates of the Surface Fluxes from Routine Weather Data. *J. Climate Appl. Meteor.*, 22(4):517–529, Apr. 1983. ISSN 0733-3021. doi: 10.1175/1520-0450(1983)022⟨0517:ASSFDE⟩2.0.CO;2. URL http://journals.ametsoc.org/doi/10.1175/1520-0450(1983)022<0517:ASSFDE>2.0.CO;2.

L. W. Horowitz, V. Naik, F. Paulot, P. A. Ginoux, J. P. Dunne, J. Mao, J. Schnell, X. Chen, J. He, J. G. John, M. Lin, P. Lin, S. Malyshev, D. Paynter, E. Shevliakova, and M. Zhao. The GFDL Global Atmospheric Chemistry-Climate Model AM4.1: Model Description and Simulation Characteristics. *J Adv Model Earth Syst*, 12(10):e2019MS002032, Oct. 2020. ISSN 1942-2466, 1942-2466. doi: 10.1029/2019MS002032. URL https://agupubs.onlinelibrary.wiley.com/doi/10.1029/2019MS002032.

Y. Hoshika, E. Paoletti, E. Agathokleous, T. Sugai, and T. Koike. Developing Ozone Risk Assessment for Larch Species. *Front. For. Glob. Change*, 3:45, May 2020. ISSN 2624-893X. doi: 10.3389/ffgc.2020.00045. URL https://www.frontiersin.org/article/10.3389/ffgc.2020.00045/full.

T. Hu, S. Liu, Y. Xu, Z. Feng, and V. Calatayud. Assessment of O3-induced yield and economic losses for wheat in the North China Plain from 2014 to 2017, China. *Environmental Pollution*, 258:113828, Mar. 2020. ISSN 02697491. doi: 10.1016/j.envpol.2019.113828. URL https://linkinghub.elsevier.com/retrieve/pii/S0269749119355915.

M. Huang, G. R. Carmichael, R. B. Pierce, D. S. Jo, R. J. Park, J. Flemming, L. K. Emmons, K. W. Bowman, D. K. Henze, Y. Davila, K. Sudo, J. E. Jonson, M. Tronstad Lund, G. Janssens-Maenhout, F. J. Dentener, T. J. Keating, H. Oetjen, and V. H. Payne. Impact of intercontinental pollution transport on North American ozone air pollution: an HTAP phase 2 multi-model study. *Atmos. Chem. Phys.*, 17(9):5721–5750, May 2017. ISSN 1680-7324. doi: 10.5194/acp-17-5721-2017. URL https://acp.copernicus.org/articles/17/5721/2017/.

K. Hufkens, D. Basler, T. Milliman, E. K. Melaas, and A. D. Richardson. An integrated phenology modelling framework in r. *Methods Ecol Evol*, 9(5):1276–1285, May 2018. ISSN 2041-210X, 2041-210X. doi: 10.1111/2041-210X.12970. URL https://besjournals.onlinelibrary.wiley.com/doi/10.1111/2041-210X.12970.

I. Hůnová, J. Horálek, M. Schreiberová, and M. Zapletal. Ambient Ozone Exposure in Czech Forests: A GIS-Based Approach to Spatial Distribution Assessment. *The Scientific World Journal*, 2012: 1–10, 2012. ISSN 1537-744X. doi: 10.1100/2012/123760. URL http://www.hindawi.com/journals/tswj/2012/123760/.

I. Hůnová, P. Kurfürst, and L. Baláková. Areas under high ozone and nitrogen loads are spatially disjunct in Czech forests. *Science of The Total Environment*, 656:567–575, Mar. 2019. ISSN 00489697. doi: 10.1016/j.scitotenv.2018.11.371. URL https://linkinghub.elsevier.com/retrieve/pii/S0048969718347272.

International Food Policy Research Institute (IFPRI). Global Spatially-Disaggregated Crop Production Statistics Data for 2020 Version 2.0, 2024. URL https://dataverse.harvard.edu/citation?persistentId=doi:10.7910/DVN/SWPENT.

i. n. d. S. ISTAT, 2023. URL http://dati.istat.it/Index.aspx?QueryId=33654.

C. P. Jacovides, F. S. Tymvios, D. N. Asimakopoulos, K. M. Theofilou, and S. Pashiardes. Global photosynthetically active radiation and its relationship with global solar radiation in the Eastern Mediterranean basin. *Theoretical and Applied Climatology*, 74(3-4):227–233, Mar. 2003. ISSN 0177-798X, 1434-4483. doi: 10.1007/s00704-002-0685-5. URL http://link.springer.com/10.1007/s00704-002-0685-5.

P. G. Jarvis. The interpretation of the variations in leaf water potential and stomatal conductance found in canopies in the field. *Phil. Trans. R. Soc. Lond. B*, 273(927):593–610, Feb. 1976. ISSN 0080-4622, 2054-0280. doi: 10.1098/rstb.1976.0035. URL https://royalsocietypublishing.org/doi/10.1098/rstb.1976.0035.

Y. Jolivet, M. Bagard, M. Cabané, M.-N. Vaultier, A. Gandin, D. Afif, P. Dizengremel, and D. Le Thiec. Deciphering the ozone-induced changes in cellular processes: a prerequisite for ozone risk assessment at the tree and forest levels. *Annals of Forest Science*, 73(4):923–943, Dec. 2016. ISSN 1286-4560, 1297-966X. doi: 10.1007/s13595-016-0580-3. URL https://annforsci.biomedcentral.com/articles/10.1007/s13595-016-0580-3.

J. Jägermeyr, C. Müller, S. Minoli, D. Ray, and S. Siebert. GGCMI Phase 3 crop calendar, July 2021. URL https://zenodo.org/record/5062513.

J. Jägermeyr, S. Rabin, J. Balkovic, T. Berton Ferreira, J. W. Elliott, B. Faye, C. Folberth, G. Hoogenboom, T. Iizumi, A. Jain, T. Kiyoshi, T.-S. Lin, W. Liu, O. Masashi, O. Mialyk, C. Müller, A. Smerald, T. Stella, C. Wang, H. Webber, H. Yang, Y. Yang, F. Zabel, and K. Frieler. ISIMIP3b Simulation Data from the Agriculture Sector, Apr. 2024. URL https://data.isimip.org/10.48364/ISIMIP.723340.2.

H. Kang, T. Zhu, Y. Zhang, X. Ke, W. Sun, Z. Hu, X. Zhu, H. Shen, Y. Huang, and Y. Tang. Elevated CO2 Enhances Dynamic Photosynthesis in Rice and Wheat. *Front. Plant Sci.*, 12: 727374, Oct. 2021. ISSN 1664-462X. doi: 10.3389/fpls.2021.727374. URL https://www.frontiersin.org/articles/10.3389/fpls.2021.727374/full.

P. Karlsson, S. Braun, M. Broadmeadow, S. Elvira, L. Emberson, B. Gimeno, D. Le Thiec, K. Novak, E. Oksanen, M. Schaub, J. Uddling, and M. Wilkinson. Risk assessments for forest trees: The performance of the ozone flux versus the AOT concepts. *Environmental Pollution*, 146(3):608–616, Apr. 2007. ISSN 02697491. doi: 10.1016/j.envpol.2006.06.012. URL https://linkinghub.elsevier.com/retrieve/pii/S0269749106003915.

P. E. Karlsson, P. Büker, S. Bland, D. Simpson, K. Sharps, F. Hayes, and L. Emberson. Ozone causes substantial reductions in the carbon sequestration of managed European forests, 2025. URL https://egusphere.copernicus.org/preprints/2024/egusphere-2024-3742/.

S. Kc and W. Lutz. The human core of the shared socioeconomic pathways: Population scenarios by age, sex and level of education for all countries to 2100. *Global Environmental Change*, 42: 181–192, Jan. 2017. ISSN 09593780. doi: 10.1016/j.gloenvcha.2014.06.004. URL https://linkinghub.elsevier.com/retrieve/pii/S0959378014001095.

S. G. Keel, S. Pepin, S. Leuzinger, and C. Körner. Stomatal conductance in mature deciduous forest trees exposed to elevated CO2. *Trees*, 21(2):151–159, Feb. 2007. ISSN 0931-1890, 1432-2285. doi: 10.1007/s00468-006-0106-y. URL http://link.springer.com/10.1007/s00468-006-0106-y.

E. Khurana and J. Singh. Response of five dry tropical tree seedlings to elevated CO2: Impact of seed size and successional status. *New Forests*, 27(2):139–157, Mar. 2004. ISSN 0169-4286, 1573-5095. doi: 10.1023/A:1025018108634. URL https://link.springer.com/10.1023/A:1025018108634.

T. Klein, M. K. Bader, S. Leuzinger, M. Mildner, P. Schleppi, R. T. Siegwolf, and C. Körner. Growth and carbon relations of mature *Picea abies* trees under 5 years of free-air CO_2 enrichment. *Journal of Ecology*, 104(6):1720–1733, Nov. 2016. ISSN 0022-0477, 1365-2745. doi: 10.1111/1365-2745.12621. URL https://besjournals.onlinelibrary.wiley.com/doi/10.1111/1365-2745.12621.

J. Klingberg, M. Engardt, J. Uddling, P. Karlsson, and H. Pleijel. Ozone risk for vegetation in the future climate of Europe based on stomatal ozone uptake calculations. *Tellus A: Dynamic Meteorology and Oceanography*, 63(1):174, Jan. 2011. ISSN 1600-0870. doi: 10.1111/j.1600-0870.2010.00465.x. URL https://a.tellusjournals.se/article/10.1111/j.1600-0870.2010.00465.x/.

J. Klingberg, M. Engardt, P. E. Karlsson, J. Langner, and H. Pleijel. Declining ozone exposure of European vegetation under climate change and reduced precursor emissions. *Biogeosciences*, 11(19):5269–5283, Oct. 2014. ISSN 1726-4189. doi: 10.5194/bg-11-5269-2014. URL https://bg.copernicus.org/articles/11/5269/2014/.

M. Košvancová, O. Urban, M. Šprtová, M. Hrstka, J. Kalina, I. Tomášková, V. Špunda, and M. Marek. Photosynthetic induction in broadleaved Fagus sylvatica and coniferous Picea abies cultivated under ambient and elevated CO2 concentrations. *Plant Science*, 177(2):123–130, Aug. 2009. ISSN 01689452. doi: 10.1016/j.plantsci.2009.04.005. URL https://linkinghub.elsevier.com/retrieve/pii/S0168945209001204.

J. P. Krasting, J. G. John, C. Blanton, C. McHugh, S. Nikonov, A. Radhakrishnan, K. Rand, N. T. Zadeh, V. Balaji, J. Durachta, C. Dupuis, R. Menzel, T. Robinson, S. Underwood, H. Vahlenkamp, K. A. Dunne, P. P. Gauthier, P. Ginoux, S. M. Griffies, R. Hallberg, M. Harrison, W. Hurlin, S. Malyshev, V. Naik, F. Paulot, D. J. Paynter, J. Ploshay, B. G. Reichl, D. M. Schwarzkopf, C. J. Seman, L. Silvers, B. Wyman, Y. Zeng, A. Adcroft, J. P. Dunne, R. Dussin, H. Guo, J. He, I. M. Held, L. W. Horowitz, P. Lin, P. Milly, E. Shevliakova, C. Stock, M. Winton, A. T. Wittenberg, Y. Xie, and M. Zhao. NOAA-GFDL GFDL-ESM4 model output prepared for CMIP6 CMIP historical, 2018. URL http://cera-www.dkrz.de/WDCC/meta/CMIP6/CMIP6.CMIP.NOAA-GFDL.GFDL-ESM4.historical.

E. Kriegler, N. Bauer, A. Popp, F. Humpenöder, M. Leimbach, J. Strefler, L. Baumstark, B. L. Bodirsky, J. Hilaire, D. Klein, I. Mouratiadou, I. Weindl, C. Bertram, J.-P. Dietrich, G. Luderer, M. Pehl, R. Pietzcker, F. Piontek, H. Lotze-Campen, A. Biewald, M. Bonsch, A. Giannousakis, U. Kreidenweis, C. Müller, S. Rolinski, A. Schultes, J. Schwanitz, M. Stevanovic, K. Calvin, J. Emmerling, S. Fujimori, and O. Edenhofer. Fossil-fueled development (SSP5): An energy and resource intensive scenario for the 21st century. *Global Environmental Change*, 42:297–315, Jan. 2017. ISSN 09593780. doi: 10.1016/j.gloenvcha.2016.05.015. URL https://linkinghub.elsevier.com/retrieve/pii/S0959378016300711.

R. K. Kunchala, B. B. Singh, R. K. Karumuri, R. Attada, V. Seelanki, and K. N. Kumar. Understanding the spatiotemporal variability and trends of surface ozone over India. *Environ Sci Pollut Res*, 29(4):6219–6236, Jan. 2022. ISSN 0944-1344, 1614-7499. doi: 10.1007/s11356-021-16011-w. URL https://link.springer.com/10.1007/s11356-021-16011-w.

C. Körner. Through enhanced tree dynamics carbon dioxide enrichment may cause tropical forests to lose carbon. *Phil. Trans. R. Soc. Lond. B*, 359(1443):493–498, Mar. 2004. ISSN 0962-8436, 1471-2970. doi: 10.1098/rstb.2003.1429. URL https://royalsocietypublishing.org/doi/10.1098/rstb.2003.1429.

C. Körner, P. Möhl, and E. Hiltbrunner. Four ways to define the growing season. *Ecology Letters*, 26(8):1277–1292, Aug. 2023. ISSN 1461-023X, 1461-0248. doi: 10.1111/ele.14260. URL https://onlinelibrary.wiley.com/doi/10.1111/ele.14260.

T. L. Laban, P. G. Van Zyl, J. P. Beukes, V. Vakkari, K. Jaars, N. Borduas-Dedekind, M. Josipovic, A. M. Thompson, M. Kulmala, and L. Laakso. Seasonal influences on surface ozone variability in continental South Africa and implications for air quality. *Atmos. Chem. Phys.*, 18(20):15491–15514, Oct. 2018. ISSN 1680-7324. doi: 10.5194/acp-18-15491-2018. URL https://acp.copernicus.org/articles/18/15491/2018/.

S. Leuzinger and M. K.-F. Bader. Experimental vs. modeled water use in mature Norway spruce (Picea abies) exposed to elevated CO2. *Front. Plant Sci.*, 3, 2012. ISSN 1664-462X. doi: 10.3389/fpls.2012.00229. URL http://journal.frontiersin.org/article/10.3389/fpls.2012.00229/abstract.

K. Li, R. Tan, W. Qiao, T. Lee, Y. Wang, D. Zhang, M. Tang, W. Zhao, Y. Gu, S. Fan, J. Zhang, X. Lyu, L. Xue, J. Xu, Z. Ma, M. T. Latif, T. Amnuaylojaroen, J. Gil, M.-H. Lee, J. Bak, J. Kim, H. Liao, Y. Kanaya, X. Lu, T. Nagashima, and J.-H. Koo. Surface and tropospheric ozone over East Asia and Southeast Asia from observations: distributions, trends, and variability, Jan. 2025a. URL https://egusphere.copernicus.org/preprints/2025/egusphere-2024-3756/.

S. Li, Y. Gao, J. Zhang, C. Hong, S. Zhang, D. Chen, O. Wild, Z. Feng, Y. Xu, X. Guo, W. Kou, F. Yan, M. Ma, X. Yao, H. Gao, and S. J. Davis. Mitigating climate change and ozone pollution will improve Chinese food security. *One Earth*, 8(2):101166, Feb. 2025b. ISSN 25903322. doi: 10.1016/j.oneear.2024.12.002. URL https://linkinghub.elsevier.com/retrieve/pii/S2590332224005967.

X. Li, S. Kang, J. Niu, Z. Huo, and J. Liu. Improving the representation of stomatal responses to CO2 within the Penman–Monteith model to better estimate evapotranspiration responses to climate change. *Journal of Hydrology*, 572:692–705, May 2019. ISSN 00221694. doi: 10.1016/j.jhydrol.2019.03.029. URL https://linkinghub.elsevier.com/retrieve/pii/S0022169419302264.

H. W. Linderholm, A. Walther, and D. Chen. Twentieth-century trends in the thermal growing season in the Greater Baltic Area. *Climatic Change*, 87(3-4):405–419, Apr. 2008. ISSN 0165-0009, 1573-1480. doi: 10.1007/s10584-007-9327-3. URL http://link.springer.com/10.1007/s10584-007-9327-3.

H. Liu, C. Lu, S. Wang, F. Ren, and H. Wang. Climate warming extends growing season but not reproductive phase of terrestrial plants. *Global Ecol. Biogeogr.*, 30(5):950–960, May 2021. ISSN 1466-822X, 1466-8238. doi: 10.1111/geb.13269. URL https://onlinelibrary.wiley.com/doi/10.1111/geb.13269.

X. Liu, B. Chu, R. Tang, Y. Liu, B. Qiu, M. Gao, X. Li, J. Xiao, H. Z. Sun, X. Huang, A. R. Desai, A. Ding, and H. Wang. Air quality improvements can strengthen China's food security. *Nat Food*, 5(2):158–170, Jan. 2024. ISSN 2662-1355. doi: 10.1038/s43016-023-00882-y. URL https://www.nature.com/articles/s43016-023-00882-y.

Y. Liu and T. Wang. Worsening urban ozone pollution in China from 2013 to 2017 – Part 1: The complex and varying roles of meteorology. *Atmos. Chem. Phys.*, 20(11):6305–6321, June 2020. ISSN 1680-7324. doi: 10.5194/acp-20-6305-2020. URL https://acp.copernicus.org/articles/20/6305/2020/.

A. Lohila, M. Aurela, J. Tuovinen, and T. Laurila. Annual CO_2 exchange of a peat field growing spring barley or perennial forage grass. *J. Geophys. Res.*, 109(D18):2004JD004715, Sept. 2004. ISSN 0148-0227. doi: 10.1029/2004JD004715. URL https://agupubs.onlinelibrary.wiley.com/doi/10.1029/2004JD004715.

A. Lohila, M. Aurela, J.-P. Tuovinen, J. Hatakka, and T. Laurila. FLUXNET2015 FI-Jok Jokioinen, 2016. URL https://www.osti.gov/servlets/purl/1440159/.

W. Loibl, W. Winiwarter, A. Kopsca, J. Zufger, and R. Baumann. Estimating the spatial distribution of ozone concentrations in complex terrain. *Atmospheric Environment*, 28(16):2557–2566, Sept. 1994. ISSN 13522310. doi: 10.1016/1352-2310(94)90430-8. URL https://linkinghub.elsevier.com/retrieve/pii/1352231094904308.

W. Loibl, H. R. Bolhàr-Nordenkampf, F. Herman, and S. Smidt. Modelling critical levels of ozone for the forested area of austria modifications of the aot40 concept. *Environ Sci & Pollut Res*, 11(3):171–180, May 2004. ISSN 0944-1344, 1614-7499. doi: 10.1007/BF02979672. URL http://link.springer.com/10.1007/BF02979672.

D. Lombardozzi, S. Levis, G. Bonan, P. G. Hess, and J. P. Sparks. The Influence of Chronic Ozone Exposure on Global Carbon and Water Cycles. *Journal of Climate*, 28(1):292–305, Jan. 2015. ISSN 0894-8755, 1520-0442. doi: 10.1175/JCLI-D-14-00223.1. URL http://journals.ametsoc.org/doi/10.1175/JCLI-D-14-00223.1.

LRTAP Convention. Chapter III: mapping critical level for vegetation. In *Modelling and Mapping Manual*. 2017. URL https://icpvegetation.ceh.ac.uk.

X. Lu, L. Zhang, X. Liu, M. Gao, Y. Zhao, and J. Shao. Lower tropospheric ozone over India and its linkage to the South Asian monsoon. *Atmos. Chem. Phys.*, 18(5):3101–3118, Mar. 2018. ISSN 1680-7324. doi: 10.5194/acp-18-3101-2018. URL https://acp.copernicus.org/articles/18/3101/2018/.

Y. Luo, Z. Zhang, Y. Chen, Z. Li, and F. Tao. ChinaCropPhen1km: a high-resolution crop phenological dataset for three staple crops in China during 2000–2015 based on leaf area index (LAI) products. *Earth Syst. Sci. Data*, 12(1):197–214, Jan. 2020. ISSN 1866-3516. doi: 10.5194/essd-12-197-2020. URL https://essd.copernicus.org/articles/12/197/2020/.

F. Lutz, T. Herzfeld, J. Heinke, S. Rolinski, S. Schaphoff, W. Von Bloh, J. J. Stoorvogel, and C. Müller. Simulating the effect of tillage practices with the global ecosystem model LPJmL (version 5.0-tillage). *Geosci. Model Dev.*, 12(6):2419–2440, June 2019. ISSN 1991-9603. doi: 10.5194/gmd-12-2419-2019. URL https://gmd.copernicus.org/articles/12/2419/2019/.

H. Mao, E. Felker-Quinn, B. Sive, L. Zhang, Z. Ye, and H. Fang. Examining indicators and methods for quantifying ozone exposure to vegetation. *Atmospheric Environment*, 316:120195, Jan. 2024. ISSN 13522310. doi: 10.1016/j.atmosenv.2023.120195. URL https://linkinghub.elsevier.com/retrieve/pii/S1352231023006210.

A. Marenco, H. Gouge, P. Nédélec, and J.-P. Pagés. Evidence of a long-term increase in tropospheric ozone from Pic du Midi data series: Consequences: Positive radiative forcing. *J. Geophys. Res.*, 99(D8):16617–16632, Aug. 1994. ISSN 0148-0227. doi: 10.1029/94JD00021. URL https://agupubs.onlinelibrary.wiley.com/doi/10.1029/94JD00021.

P. J. Mason. The formation of areally-averaged roughness lengths. *Quart J Royal Meteoro Soc*, 114(480):399–420, Jan. 1988. ISSN 0035-9009, 1477-870X. doi: 10.1002/qj.49711448007. URL https://rmets.onlinelibrary.wiley.com/doi/10.1002/qj.49711448007.

W. Massman. A review of the molecular diffusivities of H2O, CO2, CH4, CO, O3, SO2, NH3, N2O, NO, and NO2 in air, O2 and N2 near STP. *Atmospheric Environment*, 32(6):1111–1127, Mar. 1998. ISSN 13522310. doi: 10.1016/S1352-2310(97)00391-9. URL https://linkinghub.elsevier.com/retrieve/pii/S1352231097003919.

J. M. Mathias and R. B. Thomas. Global tree intrinsic water use efficiency is enhanced by increased atmospheric CO_2 and modulated by climate and plant functional types. *Proc. Natl. Acad. Sci. U.S.A.*, 118(7):e2014286118, Feb. 2021. ISSN 0027-8424, 1091-6490. doi: 10.1073/pnas.2014286118. URL https://pnas.org/doi/full/10.1073/pnas.2014286118.

R. Matyssek, G. Wieser, R. Ceulemans, H. Rennenberg, H. Pretzsch, K. Haberer, M. Löw, A. Nunn, H. Werner, P. Wipfler, W. Oßwald, P. Nikolova, D. Hanke, H. Kraigher, M. Tausz, G. Bahnweg, M. Kitao, J. Dieler, H. Sandermann, K. Herbinger, T. Grebenc, M. Blumenröther, G. Deckmyn, T. Grams, C. Heerdt, M. Leuchner, P. Fabian, and K.-H. Häberle. Enhanced ozone strongly reduces carbon sink strength of adult beech (Fagus sylvatica) – Resume from the free-air fumigation study at Kranzberg Forest. *Environmental Pollution*, 158(8):2527–2532, Aug. 2010. ISSN 02697491. doi: 10.1016/j.envpol.2010.05.009. URL https://linkinghub.elsevier.com/retrieve/pii/S0269749110001879.

B. E. Medlyn, C. V. M. Barton, M. S. J. Broadmeadow, R. Ceulemans, P. De Angelis, M. Forstreuter, M. Freeman, S. B. Jackson, S. Kellomäki, E. Laitat, A. Rey, P. Roberntz, B. D. Sigurdsson, J. Strassemeyer, K. Wang, P. S. Curtis, and P. G. Jarvis. Stomatal conductance of forest species after long-term exposure to elevated CO_2 concentration: a synthesis. *New Phytologist*, 149(2): 247–264, Feb. 2001. ISSN 0028-646X, 1469-8137. doi: 10.1046/j.1469-8137.2001.00028.x. URL https://nph.onlinelibrary.wiley.com/doi/10.1046/j.1469-8137.2001.00028.x.

M. Meier and C. Bigler. Process-oriented models of autumn leaf phenology: ways to sound calibration and implications of uncertain projections. *Geosci. Model Dev.*, 16(23):7171–7201, Dec. 2023. ISSN 1991-9603. doi: 10.5194/gmd-16-7171-2023. URL https://gmd.copernicus.org/articles/16/7171/2023/.

E. K. Melaas, M. A. Friedl, and Z. Zhu. Detecting interannual variation in deciduous broadleaf forest phenology using Landsat TM/ETM+ data. *Remote Sensing of Environment*, 132:176–185, May 2013. ISSN 00344257. doi: 10.1016/j.rse.2013.01.011. URL https://linkinghub.elsevier.com/retrieve/pii/S0034425713000230.

A. Menzel, T. H. Sparks, N. Estrella, E. Koch, A. Aasa, R. Ahas, K. Alm-Kübler, P. Bissolli, O. Braslavská, A. Briede, F. M. Chmielewski, Z. Crepinsek, Y. Curnel, A. Dahl, C. Defila, A. Donnelly, Y. Filella, K. Jatczak, F. Måge, A. Mestre, O. Nordli, J. Peñuelas, P. Pirinen, V. Remišová, H. Scheifinger, M. Striz, A. Susnik, A. J. H. Van Vliet, F. Wielgolaski, S. Zach, and A. Zust. European phenological response to climate change matches the warming pattern. *Global Change Biology*, 12(10):1969–1976, Oct. 2006. ISSN 1354-1013, 1365-2486. doi: 10.1111/j.1365-2486.2006.01193.x. URL https://onlinelibrary.wiley.com/doi/10.1111/j.1365-2486.2006.01193.x.

A. R. meteorologica regionale, 2022. URL https://www.arpalombardia.it/Pages/Meteorologia/Richiesta-dati-misurati.aspx#.

G. Mills, F. Hayes, D. Simpson, L. Emberson, D. Norris, H. Harmens, and P. Büker. Evidence of widespread effects of ozone on crops and (semi-)natural vegetation in Europe (1990-2006) in relation to AOT40- and flux-based risk maps: OZONE EFFECTS ON VEGETATION IN EUROPE. *Global Change Biology*, 17(1):592–613, Jan. 2011a. ISSN 13541013. doi: 10.1111/j.1365-2486.2010.02217.x. URL https://onlinelibrary.wiley.com/doi/10.1111/j.1365-2486.2010.02217.x.

G. Mills, H. Pleijel, S. Braun, P. Büker, V. Bermejo, E. Calvo, H. Danielsson, L. Emberson, I. G. Fernández, L. Grünhage, H. Harmens, F. Hayes, P.-E. Karlsson, and D. Simpson. New stomatal flux-based critical levels for ozone effects on vegetation. *Atmospheric Environment*, 45(28):5064–5068, Sept. 2011b. ISSN 13522310. doi: 10.1016/j.atmosenv.2011.06.009. URL https://linkinghub.elsevier.com/retrieve/pii/S1352231011006029.

G. Mills, K. Sharps, D. Simpson, H. Pleijel, M. Broberg, J. Uddling, F. Jaramillo, W. J. Davies, F. Dentener, M. Van Den Berg, M. Agrawal, S. Agrawal, E. A. Ainsworth, P. Büker, L. Emberson, Z. Feng, H. Harmens, F. Hayes, K. Kobayashi, E. Paoletti, and R. Van Dingenen. Ozone pollution will compromise efforts to increase global wheat production. *Global Change Biology*, 24(8):3560–3574, Aug. 2018. ISSN 1354-1013, 1365-2486. doi: 10.1111/gcb.14157. URL https://onlinelibrary.wiley.com/doi/10.1111/gcb.14157.

Y. Mintz and G. K. Walker. Global Fields of Soil Moisture and Land Surface Evapotranspiration Derived from Observed Precipitation and Surface Air Temperature. *J. Appl. Meteor.*, 32(8): 1305–1334, Aug. 1993. ISSN 0894-8763, 1520-0450. doi: 10.1175/1520-0450(1993)032⟨1305:GFOSMA⟩2.0.CO;2. URL http://journals.ametsoc.org/doi/10.1175/1520-0450(1993)032<1305:GFOSMA>2.0.CO;2.

D. G. Miralles, J. Vilà-Guerau De Arellano, T. R. McVicar, and M. D. Mahecha. Vegetation–climate feedbacks across scales. *Annals of the New York Academy of Sciences*, 1544(1):27–41, Feb. 2025. ISSN 0077-8923, 1749-6632. doi: 10.1111/nyas.15286. URL https://nyaspubs.onlinelibrary.wiley.com/doi/10.1111/nyas.15286.

D. Mo, E. Yan, H. Lin, H. Sun, J. Li, and G. Zhang. Development and validation of 2-band EVI with MODIS data in Southeast China. In *Proceedings of 2012 International Conference on Measurement, Information and Control*, pages 88–91, Harbin, China, May 2012. IEEE. ISBN 978-1-4577-1604-1 978-1-4577-1601-0 978-1-4577-1603-4. doi: 10.1109/MIC.2012.6273306. URL http://ieeexplore.ieee.org/document/6273306/.

Y. Mo, J. Zhang, H. Jiang, and Y. H. Fu. A comparative study of 17 phenological models to predict the start of the growing season. *Front. For. Glob. Change*, 5:1032066, Jan. 2023. ISSN 2624-893X. doi: 10.3389/ffgc.2022.1032066. URL https://www.frontiersin.org/articles/10.3389/ffgc.2022.1032066/full.

C. Monfreda, N. Ramankutty, and J. A. Foley. Farming the planet: 2. Geographic distribution of crop areas, yields, physiological types, and net primary production in the year 2000. *Global Biogeochemical Cycles*, 22(1):2007GB002947, Mar. 2008. ISSN 0886-6236, 1944-9224. doi: 10.1029/2007GB002947. URL https://agupubs.onlinelibrary.wiley.com/doi/10.1029/2007GB002947.

J. L. Monteith. Evaporation and environment. *Symp Soc Exp Biol*, 19:205–234, 1965. ISSN 0081-1386.

J. L. Monteith and M. H. Unsworth. *Principles of environmental physics: plants, animals, and the atmosphere*. Elsevier/Academic Press, Amsterdam Boston, 4th edition edition, 2013. ISBN 978-0-12-386910-4.

C. Moureaux, A. Debacq, B. Bodson, B. Heinesch, and M. Aubinet. Annual net ecosystem carbon exchange by a sugar beet crop. *Agricultural and Forest Meteorology*, 139(1-2):25–39, Sept. 2006. ISSN 01681923. doi: 10.1016/j.agrformet.2006.05.009. URL https://linkinghub.elsevier.com/retrieve/pii/S0168192306001493.

A. H. Murphy. Skill Scores Based on the Mean Square Error and Their Relationships to the Correlation Coefficient. *Mon. Wea. Rev.*, 116(12):2417–2424, Dec. 1988. ISSN 0027-0644, 1520-0493. doi: 10.1175/1520-0493(1988)116⟨2417:SSBOTM⟩2.0.CO;2. URL http://journals.ametsoc.org/doi/10.1175/1520-0493(1988)116<2417:SSBOTM>2.0.CO;2.

F. W. Murray. On the Computation of Saturation Vapor Pressure. *J. Appl. Meteor.*, 6(1):203–204, Feb. 1967. ISSN 0021-8952. doi: 10.1175/1520-0450(1967)006⟨0203:OTCOSV⟩2.0.CO;2. URL http://journals.ametsoc.org/doi/10.1175/1520-0450(1967)006<0203:OTCOSV>2.0.CO;2.

J. M. Norman. SIMULATION OF MICROCLIMATES. In *Biometeorology in Integrated Pest Management*, pages 65–99. Elsevier, 1982. ISBN 978-0-12-332850-2. doi: 10.1016/B978-0-12-332850-2.50009-8. URL https://linkinghub.elsevier.com/retrieve/pii/B9780123328502500098.

S. Nussbaum, J. Remund, B. Rihm, K. Mieglitz, J. Gurtz, and J. Fuhrer. High-resolution spatial analysis of stomatal ozone uptake in arable crops and pastures. *Environment International*, 29(2-3):385–392, June 2003. ISSN 01604120. doi: 10.1016/S0160-4120(02)00174-5. URL https://linkinghub.elsevier.com/retrieve/pii/S0160412002001745.

F. O'Connor. NERC UKESM1.0-LL model output prepared for CMIP6 AerChemMIP, 2020. URL http://cera-www.dkrz.de/WDCC/meta/CMIP6/CMIP6.AerChemMIP.NERC.UKESM1-0-LL.

F. Otu-Larbi, A. Conte, S. Fares, O. Wild, and K. Ashworth. Current and future impacts of drought and ozone stress on Northern Hemisphere forests. *Global Change Biology*, 26(11):6218–6234, Nov. 2020. ISSN 1354-1013, 1365-2486. doi: 10.1111/gcb.15339. URL https://onlinelibrary.wiley.com/doi/10.1111/gcb.15339.

Y. Pan, R. A. Birdsey, J. Fang, R. Houghton, P. E. Kauppi, W. A. Kurz, O. L. Phillips, A. Shvidenko, S. L. Lewis, J. G. Canadell, P. Ciais, R. B. Jackson, S. W. Pacala, A. D. McGuire, S. Piao, A. Rautiainen, S. Sitch, and D. Hayes. A Large and Persistent Carbon Sink in the World's Forests. *Science*, 333(6045):988–993, Aug. 2011. ISSN 0036-8075, 1095-9203. doi: 10.1126/science.1201609. URL https://www.science.org/doi/10.1126/science.1201609.

E. Paoletti and W. J. Manning. Toward a biologically significant and usable standard for ozone that will also protect plants. *Environmental Pollution*, 150(1):85–95, Nov. 2007. ISSN 02697491. doi: 10.1016/j.envpol.2007.06.037. URL https://linkinghub.elsevier.com/retrieve/pii/S0269749107003144.

E. Paoletti, A. Alivernini, A. Anav, O. Badea, E. Carrari, S. Chivulescu, A. Conte, M. Ciriani, L. Dalstein-Richier, A. De Marco, S. Fares, G. Fasano, A. Giovannelli, M. Lazzara, S. Leca, A. Materassi, V. Moretti, D. Pitar, I. Popa, F. Sabatini, L. Salvati, P. Sicard, T. Sorgi, and Y. Hoshika. Toward stomatal–flux based forest protection against ozone: The MOTTLES approach. *Science of The Total Environment*, 691:516–527, Nov. 2019. ISSN 00489697. doi: 10.1016/j.scitotenv.2019.06.525. URL https://linkinghub.elsevier.com/retrieve/pii/S0048969719331110.

T. Park, S. Ganguly, H. Tømmervik, E. S. Euskirchen, K.-A. Høgda, S. R. Karlsen, V. Brovkin, R. R. Nemani, and R. B. Myneni. Changes in growing season duration and productivity of northern vegetation inferred from long-term remote sensing data. *Environ. Res. Lett.*, 11(8):084001, Aug. 2016. ISSN 1748-9326. doi: 10.1088/1748-9326/11/8/084001. URL https://iopscience.iop.org/article/10.1088/1748-9326/11/8/084001.

D. D. Parrish, K. S. Law, J. Staehelin, R. Derwent, O. R. Cooper, H. Tanimoto, A. Volz-Thomas, S. Gilge, H.-E. Scheel, M. Steinbacher, and E. Chan. Long-term changes in lower tropospheric baseline ozone concentrations at northern mid-latitudes. *Atmos. Chem. Phys.*, 12(23):11485–11504, Dec. 2012. ISSN 1680-7324. doi: 10.5194/acp-12-11485-2012. URL https://acp.copernicus.org/articles/12/11485/2012/.

G. Pastorello, C. Trotta, E. Canfora, H. Chu, D. Christianson, Y.-W. Cheah, C. Poindexter, J. Chen, A. Elbashandy, M. Humphrey, P. Isaac, D. Polidori, M. Reichstein, A. Ribeca, C. Van Ingen, N. Vuichard, L. Zhang, B. Amiro, C. Ammann, M. A. Arain, J. Ardö, T. Arkebauer, S. K. Arndt, N. Arriga, M. Aubinet, M. Aurela, D. Baldocchi, A. Barr, E. Beamesderfer, L. B. Marchesini, O. Bergeron, J. Beringer, C. Bernhofer, D. Berveiller, D. Billesbach, T. A. Black, P. D. Blanken, G. Bohrer, J. Boike, P. V. Bolstad, D. Bonal, J.-M. Bonnefond, D. R. Bowling, R. Bracho, J. Brodeur, C. Brümmer, N. Buchmann, B. Burban, S. P. Burns, P. Buysse, P. Cale, M. Cavagna, P. Cellier, S. Chen, I. Chini, T. R. Christensen, J. Cleverly, A. Collalti, C. Consalvo, B. D. Cook, D. Cook, C. Coursolle, E. Cremonese, P. S. Curtis, E. D'Andrea, H. Da Rocha, X. Dai, K. J. Davis, B. D. Cinti, A. D. Grandcourt, A. D. Ligne, R. C. De Oliveira, N. Delpierre, A. R. Desai, C. M. Di Bella, P. D. Tommasi, H. Dolman, F. Domingo, G. Dong, S. Dore, P. Duce, E. Dufrêne, A. Dunn, J. Dušek, D. Eamus, U. Eichelmann, H. A. M. ElKhidir, W. Eugster, C. M. Ewenz, B. Ewers, D. Famulari, S. Fares, I. Feigenwinter, A. Feitz, R. Fensholt, G. Filippa, M. Fischer, J. Frank, M. Galvagno, M. Gharun, D. Gianelle, B. Gielen, B. Gioli, A. Gitelson, I. Goded, M. Goeckede, A. H. Goldstein, C. M. Gough, M. L. Goulden, A. Graf, A. Griebel, C. Gruening, T. Grünwald, A. Hammerle, S. Han, X. Han, B. U. Hansen, C. Hanson, J. Hatakka, Y. He, M. Hehn, B. Heinesch, N. Hinko-Najera, L. Hörtnagl, L. Hutley, A. Ibrom, H. Ikawa, M. Jackowicz-Korczynski, D. Janouš, W. Jans, R. Jassal, S. Jiang, T. Kato, M. Khomik, J. Klatt, A. Knohl, S. Knox, H. Kobayashi, G. Koerber, O. Kolle, Y. Kosugi, A. Kotani, A. Kowalski,

B. Kruijt, J. Kurbatova, W. L. Kutsch, H. Kwon, S. Launiainen, T. Laurila, B. Law, R. Leuning, Y. Li, M. Liddell, J.-M. Limousin, M. Lion, A. J. Liska, A. Lohila, A. López-Ballesteros, E. López-Blanco, B. Loubet, D. Loustau, A. Lucas-Moffat, J. Lüers, S. Ma, C. Macfarlane, V. Magliulo, R. Maier, I. Mammarella, G. Manca, B. Marcolla, H. A. Margolis, S. Marras, W. Massman, M. Mastepanov, R. Matamala, J. H. Matthes, F. Mazzenga, H. McCaughey, I. McHugh, A. M. S. McMillan, L. Merbold, W. Meyer, T. Meyers, S. D. Miller, S. Minerbi, U. Moderow, R. K. Monson, L. Montagnani, C. E. Moore, E. Moors, V. Moreaux, C. Moureaux, J. W. Munger, T. Nakai, J. Neirynck, Z. Nesic, G. Nicolini, A. Noormets, M. Northwood, M. Nosetto, Y. Nouvellon, K. Novick, W. Oechel, J. E. Olesen, J.-M. Ourcival, S. A. Papuga, F.-J. Parmentier, E. Paul-Limoges, M. Pavelka, M. Peichl, E. Pendall, R. P. Phillips, K. Pilegaard, N. Pirk, G. Posse, T. Powell, H. Prasse, S. M. Prober, S. Rambal, U. Rannik, N. Raz-Yaseef, C. Rebmann, D. Reed, V. R. D. Dios, N. Restrepo-Coupe, B. R. Reverter, M. Roland, S. Sabbatini, T. Sachs, S. R. Saleska, E. P. Sánchez-Cañete, Z. M. Sanchez-Mejia, H. P. Schmid, M. Schmidt, K. Schneider, F. Schrader, I. Schroder, R. L. Scott, P. Sedlák, P. Serrano-Ortíz, C. Shao, P. Shi, I. Shironya, L. Siebicke, L. Šigut, R. Silberstein, C. Sirca, D. Spano, R. Steinbrecher, R. M. Stevens, C. Sturtevant, A. Suyker, T. Tagesson, S. Takanashi, Y. Tang, N. Tapper, J. Thom, M. Tomassucci, J.-P. Tuovinen, S. Urbanski, R. Valentini, M. Van Der Molen, E. Van Gorsel, K. Van Huissteden, A. Varlagin, J. Verfaillie, T. Vesala, C. Vincke, D. Vitale, N. Vygodskaya, J. P. Walker, E. Walter-Shea, H. Wang, R. Weber, S. Westermann, C. Wille, S. Wofsy, G. Wohlfahrt, S. Wolf, W. Woodgate, Y. Li, R. Zampedri, J. Zhang, G. Zhou, D. Zona, D. Agarwal, S. Biraud, M. Torn, and D. Papale. The FLUXNET2015 dataset and the ONEFlux processing pipeline for eddy covariance data. *Sci Data*, 7(1):225, July 2020. ISSN 2052-4463. doi: 10.1038/s41597-020-0534-3. URL `https://www.nature.com/articles/s41597-020-0534-3`.

M. C. Peel, B. L. Finlayson, and T. A. McMahon. Updated world map of the K¨oppen-Geiger climate classification. *Hydrol. Earth Syst. Sci.*, 2007.

H. Pleijel, H. Danielsson, K. Vandermeiren, C. Blum, J. Colls, and K. Ojanperä. Stomatal conductance and ozone exposure in relation to potato tuber yield—results from the European CHIP programme. *European Journal of Agronomy*, 17(4):303–317, Nov. 2002. ISSN 11610301. doi: 10.1016/S1161-0301(02)00068-0. URL `https://linkinghub.elsevier.com/retrieve/pii/S1161030102000680`.

H. Pleijel, H. Danielsson, L. Emberson, M. Ashmore, and G. Mills. Ozone risk assessment for agricultural crops in Europe: Further development of stomatal flux and flux–response relationships for European wheat and potato. *Atmospheric Environment*, 41(14):3022–3040, May 2007. ISSN 13522310. doi: 10.1016/j.atmosenv.2006.12.002. URL `https://linkinghub.elsevier.com/retrieve/pii/S1352231006012271`.

H. Pleijel, M. C. Broberg, J. Uddling, and G. Mills. Current surface ozone concentrations significantly decrease wheat growth, yield and quality. *Science of The Total Environment*, 613-614:687–692, Feb. 2018. ISSN 00489697. doi: 10.1016/j.scitotenv.2017.09.111. URL `https://linkinghub.elsevier.com/retrieve/pii/S0048969717324531`.

H. Pleijel, H. Danielsson, and M. C. Broberg. Benefits of the Phytotoxic Ozone Dose (POD) index in dose-response functions for wheat yield loss. *Atmospheric Environment*, 268:118797, Jan. 2022. ISSN 13522310. doi: 10.1016/j.atmosenv.2021.118797. URL `https://linkinghub.elsevier.com/retrieve/pii/S1352231021006191`.

D. T. Price, R. Alfaro, K. Brown, M. Flannigan, R. Fleming, E. Hogg, M. Girardin, T. Lakusta, M. Johnston, D. McKenney, J. Pedlar, T. Stratton, R. Sturrock, I. Thompson, J. Trofymow, and L. Venier. Anticipating the consequences of climate change for Canada's boreal forest ecosystems. *Environ. Rev.*, 21(4):322–365, Dec. 2013. ISSN 1181-8700, 1208-6053. doi: 10.1139/er-2013-0042. URL `http://www.nrcresearchpress.com/doi/10.1139/er-2013-0042`.

C. Proietti, A. Anav, A. De Marco, P. Sicard, and M. Vitale. A multi-sites analysis on the ozone effects on Gross Primary Production of European forests. *Science of The Total Environment*, 556:1–11, June 2016. ISSN 00489697. doi: 10.1016/j.scitotenv.2016.02.187. URL https://linkinghub.elsevier.com/retrieve/pii/S0048969716303990.

C. Purcell, S. P. Batke, C. Yiotis, R. Caballero, W. K. Soh, M. Murray, and J. C. McElwain. Increasing stomatal conductance in response to rising atmospheric CO2. *Annals of Botany*, 121(6):1137–1149, May 2018. ISSN 0305-7364, 1095-8290. doi: 10.1093/aob/mcx208. URL https://academic.oup.com/aob/article/121/6/1137/4823760.

S. Qiao, S. P. Harrison, I. C. Prentice, and H. Wang. Optimality-based modelling of wheat sowing dates globally. *Agricultural Systems*, 206:103608, Mar. 2023. ISSN 0308521X. doi: 10.1016/j.agsy.2023.103608. URL https://linkinghub.elsevier.com/retrieve/pii/S0308521X23000136.

Y. Ramos, W. J. Requia, B. St-Onge, J.-P. Blanchet, Y. Kestens, and A. Smargiassi. Spatial modeling of daily concentrations of ground-level ozone in Montreal, Canada: A comparison of geostatistical approaches. *Environmental Research*, 166:487–496, Oct. 2018. ISSN 00139351. doi: 10.1016/j.envres.2018.06.036. URL https://linkinghub.elsevier.com/retrieve/pii/S0013935118303402.

A. Ramya, P. Dhevagi, R. Poornima, S. Avudainayagam, M. Watanabe, and E. Agathokleous. Effect of ozone stress on crop productivity: A threat to food security. *Environmental Research*, 236:116816, Nov. 2023. ISSN 00139351. doi: 10.1016/j.envres.2023.116816. URL https://linkinghub.elsevier.com/retrieve/pii/S0013935123016201.

N. Raz-Yaseef, D. P. Billesbach, M. L. Fischer, S. C. Biraud, S. A. Gunter, J. A. Bradford, and M. S. Torn. Vulnerability of crops and native grasses to summer drying in the U.S. Southern Great Plains. *Agriculture, Ecosystems & Environment*, 213:209–218, Dec. 2015. ISSN 01678809. doi: 10.1016/j.agee.2015.07.021. URL https://linkinghub.elsevier.com/retrieve/pii/S0167880915300359.

E. G. Reekie and F. A. Bazzaz. Competition and patterns of resource use among seedlings of five tropical trees grown at ambient and elevated CO2. *Oecologia*, 79(2):212–222, 1989. ISSN 0029-8549, 1432-1939. doi: 10.1007/BF00388481. URL http://link.springer.com/10.1007/BF00388481.

W. Ren, H. Tian, B. Tao, A. Chappelka, G. Sun, C. Lu, M. Liu, G. Chen, and X. Xu. Impacts of tropospheric ozone and climate change on net primary productivity and net carbon exchange of China's forest ecosystems: Climate and O_3 impacts on forest carbon. *Global Ecology and Biogeography*, 20(3):391–406, May 2011. ISSN 1466822X. doi: 10.1111/j.1466-8238.2010.00606.x. URL https://onlinelibrary.wiley.com/doi/10.1111/j.1466-8238.2010.00606.x.

K. Riahi, D. P. Van Vuuren, E. Kriegler, J. Edmonds, B. C. O'Neill, S. Fujimori, N. Bauer, K. Calvin, R. Dellink, O. Fricko, W. Lutz, A. Popp, J. C. Cuaresma, S. Kc, M. Leimbach, L. Jiang, T. Kram, S. Rao, J. Emmerling, K. Ebi, T. Hasegawa, P. Havlik, F. Humpenöder, L. A. Da Silva, S. Smith, E. Stehfest, V. Bosetti, J. Eom, D. Gernaat, T. Masui, J. Rogelj, J. Strefler, L. Drouet, V. Krey, G. Luderer, M. Harmsen, K. Takahashi, L. Baumstark, J. C. Doelman, M. Kainuma, Z. Klimont, G. Marangoni, H. Lotze-Campen, M. Obersteiner, A. Tabeau, and M. Tavoni. The Shared Socioeconomic Pathways and their energy, land use, and greenhouse gas emissions implications: An overview. *Global Environmental Change*, 42:153–168, Jan. 2017. ISSN 09593780. doi: 10.1016/j.gloenvcha.2016.05.009. URL https://linkinghub.elsevier.com/retrieve/pii/S0959378016300681.

A. D. Richardson, T. F. Keenan, M. Migliavacca, Y. Ryu, O. Sonnentag, and M. Toomey. Climate change, phenology, and phenological control of vegetation feedbacks to the climate system. *Agricultural and Forest Meteorology*, 169:156–173, Feb. 2013. ISSN 01681923. doi: 10.1016/j.agrformet.2012.09.012. URL https://linkinghub.elsevier.com/retrieve/pii/S0168192312002869.

P. Royston. A Toolkit for Testing for Non-Normality in Complete and Censored Samples. *The Statistician*, 42(1):37, 1993. ISSN 00390526. doi: 10.2307/2348109. URL https://www.jstor.org/stable/10.2307/2348109?origin=crossref.

J. Rydsaa, F. Stordal, G. Gerosa, A. Finco, and O. Hodnebrog. Evaluating stomatal ozone fluxes in WRF-Chem: Comparing ozone uptake in Mediterranean ecosystems. *Atmospheric Environment*, 143:237–248, Oct. 2016. ISSN 13522310. doi: 10.1016/j.atmosenv.2016.08.057. URL https://linkinghub.elsevier.com/retrieve/pii/S1352231016306501.

J. Sager, J. McFarlane, and T. Tibbits. Radiation. In *Plant growth chamber handbook*, volume 340, pages 1–29. Iowa State University: NorthCentral Regional Research Publication, 1997.

F. Savi, E. Nemitz, M. Coyle, M. Aitkenhead, K. Frumau, G. Gerosa, A. Finco, C. Gruening, I. Goded, B. Loubet, P. Stella, T. Ruuskanen, T. Weidinger, L. Horvath, T. Zenone, and S. Fares. Neural Network Analysis to Evaluate Ozone Damage to Vegetation Under Different Climatic Conditions. *Front. For. Glob. Change*, 3:42, Apr. 2020. ISSN 2624-893X. doi: 10.3389/ffgc.2020.00042. URL https://www.frontiersin.org/article/10.3389/ffgc.2020.00042/full.

K. E. Saxton and W. J. Rawls. Soil Water Characteristic Estimates by Texture and Organic Matter for Hydrologic Solutions. *Soil Science Soc of Amer J*, 70(5):1569–1578, Sept. 2006. ISSN 0361-5995, 1435-0661. doi: 10.2136/sssaj2005.0117. URL https://acsess.onlinelibrary.wiley.com/doi/10.2136/sssaj2005.0117.

B. Schauberger, S. Rolinski, S. Schaphoff, and C. Müller. Global historical soybean and wheat yield loss estimates from ozone pollution considering water and temperature as modifying effects. *Agricultural and Forest Meteorology*, 265:1–15, Feb. 2019. ISSN 01681923. doi: 10.1016/j.agrformet.2018.11.004. URL https://linkinghub.elsevier.com/retrieve/pii/S0168192318303502.

S. Schröder, M. G. Schultz, N. Selke, J. Sun, J. Ahring, A. Mozaffari, M. Romberg, E. Epp, M. Lensing, S. Apweiler, L. H. Leufen, C. Betancourt, B. Hagemeier, and S. Rajveer. TOAR Data Infrastructure, 2021. URL https://b2share.fz-juelich.de/records/4d9a287dec0b42f1aa6d244de8f19eb3.

S. Schucht, F. Tognet, and L. Létinois. Wheat yield loss in 2019 in Europe due to ozone exposure. Technical report, Eionet Report - ETC/ATNI, 2021.

R. J. Seguel, L. Castillo, C. Opazo, N. Y. Rojas, T. Nogueira, M. Cazorla, M. Gavidia-Calderón, L. Gallardo, R. Garreaud, T. Carrasco-Escaff, and Y. Elshorbany. Changes in South American surface ozone trends: exploring the influences of precursors and extreme events. *Atmos. Chem. Phys.*, 24(14):8225–8242, July 2024. ISSN 1680-7324. doi: 10.5194/acp-24-8225-2024. URL https://acp.copernicus.org/articles/24/8225/2024/.

R. Seidl and M. G. Turner. Post-disturbance reorganization of forest ecosystems in a changing world. *Proc. Natl. Acad. Sci. U.S.A.*, 119(28):e2202190119, July 2022. ISSN 0027-8424, 1091-6490. doi: 10.1073/pnas.2202190119. URL https://pnas.org/doi/full/10.1073/pnas.2202190119.

A. A. Sellar, C. G. Jones, J. P. Mulcahy, Y. Tang, A. Yool, A. Wiltshire, F. M. O'Connor, M. Stringer, R. Hill, J. Palmieri, S. Woodward, L. De Mora, T. Kuhlbrodt, S. T. Rumbold, D. I. Kelley, R. Ellis, C. E. Johnson, J. Walton, N. L. Abraham, M. B. Andrews, T. Andrews, A. T. Archibald, S. Berthou, E. Burke, E. Blockley, K. Carslaw, M. Dalvi, J. Edwards, G. A. Folberth, N. Gedney, P. T. Griffiths, A. B. Harper, M. A. Hendry, A. J. Hewitt, B. Johnson, A. Jones, C. D. Jones, J. Keeble, S. Liddicoat, O. Morgenstern, R. J. Parker, V. Predoi, E. Robertson, A. Siahaan, R. S. Smith, R. Swaminathan, M. T. Woodhouse, G. Zeng, and M. Zerroukat. UKESM1: Description and Evaluation of the U.K. Earth System Model. *J Adv Model Earth Syst*, 11(12):4513–4558, Dec. 2019. ISSN 1942-2466, 1942-2466. doi: 10.1029/2019MS001739. URL https://agupubs.onlinelibrary.wiley.com/doi/10.1029/2019MS001739.

P. J. Sellers, C. J. Tucker, G. J. Collatz, S. O. Los, C. O. Justice, D. A. Dazlich, and D. A. Randall. A Revised Land Surface Parameterization (SiB2) for Atmospheric GCMS. Part II: The Generation of Global Fields of Terrestrial Biophysical Parameters from Satellite Data. *J. Climate*, 9(4):706–737, Apr. 1996. ISSN 0894-8755, 1520-0442. doi: 10.1175/1520-0442(1996)009⟨0706:ARLSPF⟩2.0.CO;2. URL http://journals.ametsoc.org/doi/10.1175/1520-0442(1996)009<0706:ARLSPF>2.0.CO;2.

K. Sharps, M. Vieno, R. Beck, F. Hayes, and H. Harmens. Quantifying the impact of ozone on crops in Sub-Saharan Africa demonstrates regional and local hotspots of production loss. *Environ Sci Pollut Res*, 28(44):62338–62352, Nov. 2021. ISSN 0944-1344, 1614-7499. doi: 10.1007/s11356-021-14967-3. URL https://link.springer.com/10.1007/s11356-021-14967-3.

C. Sheih, M. Wesely, and C. Walcek. A dry deposition module for regional acid deposition. Technical report, 1986. URL https://api.semanticscholar.org/CorpusID:91342161.

D. Shepard. A two-dimensional interpolation function for irregularly-spaced data. In *Proceedings of the 1968 23rd ACM national conference on* -, pages 517–524, Not Known, 1968. ACM Press. doi: 10.1145/800186.810616. URL http://portal.acm.org/citation.cfm?doid=800186.810616.

Y. Shimizu, Y. Lu, M. Aono, and K. Omasa. A novel remote sensing-based method of ozone damage assessment effect on Net Primary Productivity of various vegetation types. *Atmospheric Environment*, 217:116947, Nov. 2019. ISSN 13522310. doi: 10.1016/j.atmosenv.2019.116947. URL https://linkinghub.elsevier.com/retrieve/pii/S1352231019305862.

P. Sicard, R. Serra, and P. Rossello. Spatiotemporal trends in ground-level ozone concentrations and metrics in France over the time period 1999–2012. *Environmental Research*, 149:122–144, Aug. 2016. ISSN 00139351. doi: 10.1016/j.envres.2016.05.014. URL https://linkinghub.elsevier.com/retrieve/pii/S0013935116301864.

P. Sicard, A. Anav, A. De Marco, and E. Paoletti. Projected global ground-level ozone impacts on vegetation under different emission and climate scenarios. *Atmos. Chem. Phys.*, 17(19):12177–12196, Oct. 2017. ISSN 1680-7324. doi: 10.5194/acp-17-12177-2017. URL https://acp.copernicus.org/articles/17/12177/2017/.

B. D. Sigurdsson, P. Roberntz, M. Freeman, M. Næss, H. Saxe, H. Thorgeirsson, and S. Linder. Impact studies on Nordic forests: effects of elevated CO_2 and fertilization on gas exchange. *Can. J. For. Res.*, 32(5):779–788, May 2002. ISSN 0045-5067, 1208-6037. doi: 10.1139/x01-114. URL http://www.nrcresearchpress.com/doi/10.1139/x01-114.

D. Simpson, M. Ashmore, L. Emberson, and J.-P. Tuovinen. A comparison of two different approaches for mapping potential ozone damage to vegetation. A model study. *Environmental Pollution*, 146(3):715–725, Apr. 2007. ISSN 02697491. doi: 10.1016/j.envpol.2006.04.013. URL https://linkinghub.elsevier.com/retrieve/pii/S0269749106002740.

D. Simpson, A. Benedictow, H. Berge, R. Bergström, L. D. Emberson, H. Fagerli, C. R. Flechard, G. D. Hayman, M. Gauss, J. E. Jonson, M. E. Jenkin, A. Nyíri, C. Richter, V. S. Semeena, S. Tsyro, J.-P. Tuovinen, A. Valdebenito, and P. Wind. The EMEP MSC-W chemical transport model – technical description. *Atmos. Chem. Phys.*, 12(16):7825–7865, Aug. 2012. ISSN 1680-7324. doi: 10.5194/acp-12-7825-2012. URL https://acp.copernicus.org/articles/12/7825/2012/.

S. Sitch, P. M. Cox, W. J. Collins, and C. Huntingford. Indirect radiative forcing of climate change through ozone effects on the land-carbon sink. *Nature*, 448(7155):791–794, Aug. 2007. ISSN 0028-0836, 1476-4687. doi: 10.1038/nature06059. URL https://www.nature.com/articles/nature06059.

J. Staehelin, J. Thudium, R. Buehler, A. Volz-Thomas, and W. Graber. Trends in surface ozone concentrations at Arosa (Switzerland). *Atmospheric Environment*, 28(1):75–87, Jan. 1994. ISSN 13522310. doi: 10.1016/1352-2310(94)90024-8. URL https://linkinghub.elsevier.com/retrieve/pii/1352231094900248.

M. Stemkovski, M. H. Cortez, J. R. Bernhardt, K. K. Bladen, J. B. Bradford, K. Clark-Wolf, M. E. K. Evans, L. C. Johnson, A. J. Lynch, M. A. Pastore, M. L. Pinsky, C. R. Rollinson, O. Selmoni, A. P. Walker, J. W. Williams, and P. B. Adler. Linking Community-Climate Disequilibrium to Ecosystem Function. *Ecology Letters*, 29(1):e70314, Jan. 2026. ISSN 1461-023X, 1461-0248. doi: 10.1111/ele.70314. URL https://onlinelibrary.wiley.com/doi/10.1111/ele.70314.

D. S. Stevenson, P. J. Young, V. Naik, J.-F. Lamarque, D. T. Shindell, A. Voulgarakis, R. B. Skeie, S. B. Dalsoren, G. Myhre, T. K. Berntsen, G. A. Folberth, S. T. Rumbold, W. J. Collins, I. A. MacKenzie, R. M. Doherty, G. Zeng, T. P. C. Van Noije, A. Strunk, D. Bergmann, P. Cameron-Smith, D. A. Plummer, S. A. Strode, L. Horowitz, Y. H. Lee, S. Szopa, K. Sudo, T. Nagashima, B. Josse, I. Cionni, M. Righi, V. Eyring, A. Conley, K. W. Bowman, O. Wild, and A. Archibald. Tropospheric ozone changes, radiative forcing and attribution to emissions in the Atmospheric Chemistry and Climate Model Intercomparison Project (ACCMIP). *Atmos. Chem. Phys.*, 13 (6):3063–3085, Mar. 2013. ISSN 1680-7324. doi: 10.5194/acp-13-3063-2013. URL https://acp.copernicus.org/articles/13/3063/2013/.

J. Stewart. Modelling surface conductance of pine forest. *Agricultural and Forest Meteorology*, 43 (1):19–35, June 1988. ISSN 01681923. doi: 10.1016/0168-1923(88)90003-2. URL https://linkinghub.elsevier.com/retrieve/pii/0168192388900032.

F. Stuart Chapin III, J. McFarland, A. David McGuire, E. S. Euskirchen, R. W. Ruess, and K. Kielland. The changing global carbon cycle: linking plant–soil carbon dynamics to global consequences. *Journal of Ecology*, 97(5):840–850, Sept. 2009. ISSN 0022-0477, 1365-2745. doi: 10.1111/j.1365-2745.2009.01529.x. URL https://besjournals.onlinelibrary.wiley.com/doi/10.1111/j.1365-2745.2009.01529.x.

Z. Sun, J. Zhao, H. Zhang, Y. Wang, L. Fan, Z. Zhang, X. Guo, Z. Ren, T. Xiong, W. Du, M. Wang, and M. Deng. Predicting the Start of the Growing Season in Boreal Forest Under High and Low Emission Scenarios. *Earth's Future*, 13(8):e2024EF005622, Aug. 2025. ISSN 2328-4277, 2328-4277. doi: 10.1029/2024EF005622. URL https://agupubs.onlinelibrary.wiley.com/doi/10.1029/2024EF005622.

A. P. K. Tai, M. Sadiq, J. Y. S. Pang, D. H. Y. Yung, and Z. Feng. Impacts of Surface Ozone Pollution on Global Crop Yields: Comparing Different Ozone Exposure Metrics and Incorporating Co-effects of CO2. *Front. Sustain. Food Syst.*, 5:534616, Mar. 2021. ISSN 2571-581X. doi: 10.3389/fsufs.2021.534616. URL https://www.frontiersin.org/articles/10.3389/fsufs.2021.534616/full.

H. Tang, J. Pang, G. Zhang, M. Takigawa, G. Liu, J. Zhu, and K. Kobayashi. Mapping ozone risks for rice in China for years 2000 and 2020 with flux-based and exposure-based doses. *Atmospheric Environment*, 86:74–83, Apr. 2014. ISSN 13522310. doi: 10.1016/j.atmosenv.2013.11.078. URL https://linkinghub.elsevier.com/retrieve/pii/S1352231013009497.

Y. Tang, S. Rumbold, R. Ellis, D. Kelley, J. Mulcahy, A. Sellar, J. Walton, and C. Jones. MOHC UKESM1.0-LL model output prepared for CMIP6 CMIP historical, 2019. URL http://cera-www.dkrz.de/WDCC/meta/CMIP6/CMIP6.CMIP.MOHC.UKESM1-0-LL.historical.

Z. Tuba, K. Szente, and J. Koch. Response of Photosynthesis, Stomatal Conductance, Water Use Efficiency and Production to Long-Term Elevated CO2 in Winter Wheat. *Journal of Plant Physiology*, 144(6):661–668, Nov. 1994. ISSN 01761617. doi: 10.1016/S0176-1617(11)80657-7. URL https://linkinghub.elsevier.com/retrieve/pii/S0176161711806577.

S. T. Turnock, R. J. Allen, M. Andrews, S. E. Bauer, M. Deushi, L. Emmons, P. Good, L. Horowitz, J. G. John, M. Michou, P. Nabat, V. Naik, D. Neubauer, F. M. O'Connor, D. Olivié, N. Oshima, M. Schulz, A. Sellar, S. Shim, T. Takemura, S. Tilmes, K. Tsigaridis, T. Wu, and J. Zhang. Historical and future changes in air pollutants from CMIP6 models. *Atmos. Chem. Phys.*, 20 (23):14547–14579, Nov. 2020. ISSN 1680-7324. doi: 10.5194/acp-20-14547-2020. URL https://acp.copernicus.org/articles/20/14547/2020/.

B. Tóth, M. Weynants, L. Pásztor, and T. Hengl. 3D soil hydraulic database of Europe at 250 m resolution. *Hydrological Processes*, 31(14):2662–2666, July 2017. ISSN 0885-6087, 1099-1085. doi: 10.1002/hyp.11203. URL https://onlinelibrary.wiley.com/doi/10.1002/hyp.11203.

J. Uddling and G. Wallin. Interacting effects of elevated CO2 and weather variability on photosynthesis of mature boreal Norway spruce agree with biochemical model predictions. *Tree Physiology*, 32(12):1509–1521, Dec. 2012. ISSN 0829-318X, 1758-4469. doi: 10.1093/treephys/tps086. URL https://academic.oup.com/treephys/article-lookup/doi/10.1093/treephys/tps086.

J. Uddling, H. Pleijel, and P. E. Karlsson. Measuring and modelling leaf diffusive conductance in juvenile silver birch, Betula pendula. *Trees*, 18(6):686–695, Nov. 2004. ISSN 0931-1890, 1432-2285. doi: 10.1007/s00468-004-0353-8. URL http://link.springer.com/10.1007/s00468-004-0353-8.

United Nations Department of Economic and Social Affairs, Population Division. World population prospects 2022: summary of results. Technical Report 3, UN DESA/POP/2022/TR/NO, 2022. OCLC: 1377293288.

O. Urban, K. Klem, P. Holišová, L. Šigut, M. Šprtová, P. Teslová-Navrátilová, M. Zitová, V. Špunda, M. V. Marek, and J. Grace. Impact of elevated CO2 concentration on dynamics of leaf photosynthesis in Fagus sylvatica is modulated by sky conditions. *Environmental Pollution*, 185:271–280, Feb. 2014. ISSN 02697491. doi: 10.1016/j.envpol.2013.11.009. URL https://linkinghub.elsevier.com/retrieve/pii/S0269749113005988.

O. Urban, M. Hrstka, P. Holub, B. Veselá, K. Večeřová, K. Novotná, J. Grace, and K. Klem. Interactive effects of ultraviolet radiation and elevated CO2 concentration on photosynthetic characteristics of European beech saplings during the vegetation season. *Plant Physiology and Biochemistry*, 134:20–30, Jan. 2019. ISSN 09819428. doi: 10.1016/j.plaphy.2018.08.026. URL https://linkinghub.elsevier.com/retrieve/pii/S0981942818303644.

U.S. Environmental Protection Agency. Final Decision to Retain the Ozone National Ambient Air Quality Standards. Technical Report 86 FR 87256, U.S. Environmental Protection Agency, 2020. URL https://www.epa.gov/ground-level-ozone-pollution/final-decision-retain-ozone-national-ambient-air-quality-standards.

R. J. Van Der A, B. Mijling, J. Ding, M. E. Koukouli, F. Liu, Q. Li, H. Mao, and N. Theys. Cleaning up the air: effectiveness of air quality policy for SO_2 and NO_x emissions in China. *Atmos. Chem. Phys.*, 17(3):1775–1789, Feb. 2017. ISSN 1680-7324. doi: 10.5194/acp-17-1775-2017. URL https://acp.copernicus.org/articles/17/1775/2017/.

R. Van Dingenen, F. J. Dentener, F. Raes, M. C. Krol, L. Emberson, and J. Cofala. The global impact of ozone on agricultural crop yields under current and future air quality legislation. *Atmospheric Environment*, 43(3):604–618, Jan. 2009. ISSN 13522310. doi: 10.1016/j.atmosenv.2008.10.033. URL https://linkinghub.elsevier.com/retrieve/pii/S1352231008009424.

M. T. Van Genuchten. A Closed-form Equation for Predicting the Hydraulic Conductivity of Unsaturated Soils. *Soil Science Soc of Amer J*, 44(5):892–898, Sept. 1980. ISSN 0361-5995, 1435-0661. doi: 10.2136/sssaj1980.03615995004400050002x. URL https://acsess.onlinelibrary.wiley.com/doi/10.2136/sssaj1980.03615995004400050002x.

D. P. Van Vuuren, E. Stehfest, D. E. Gernaat, J. C. Doelman, M. Van Den Berg, M. Harmsen, H. S. De Boer, L. F. Bouwman, V. Daioglou, O. Y. Edelenbosch, B. Girod, T. Kram, L. Lassaletta, P. L. Lucas, H. Van Meijl, C. Müller, B. J. Van Ruijven, S. Van Der Sluis, and A. Tabeau. Energy, land-use and greenhouse gas emissions trajectories under a green growth paradigm. *Global Environmental Change*, 42:237–250, Jan. 2017. ISSN 09593780. doi: 10.1016/j.gloenvcha.2016.05.008. URL https://linkinghub.elsevier.com/retrieve/pii/S095937801630067X.

A. Venkatram, P. Karamchandani, and P. Misra. Testing a comprehensive acid deposition model. *Atmospheric Environment (1967)*, 22(4):737–747, Jan. 1988. ISSN 00046981. doi: 10.1016/0004-6981(88)90011-X. URL https://linkinghub.elsevier.com/retrieve/pii/000469818890011X.

A. Venäläinen, I. Lehtonen, M. Laapas, K. Ruosteenoja, O. Tikkanen, H. Viiri, V. Ikonen, and H. Peltola. Climate change induces multiple risks to boreal forests and forestry in Finland: A literature review. *Global Change Biology*, 26(8):4178–4196, Aug. 2020. ISSN 1354-1013, 1365-2486. doi: 10.1111/gcb.15183. URL https://onlinelibrary.wiley.com/doi/10.1111/gcb.15183.

M. Vignudelli and P. Gizzi. Bollettino Fenologico. Technical report, 2017.

R. Vingarzan. A review of surface ozone background levels and trends. *Atmospheric Environment*, 38(21):3431–3442, July 2004. ISSN 13522310. doi: 10.1016/j.atmosenv.2004.03.030. URL https://linkinghub.elsevier.com/retrieve/pii/S1352231004002808.

W. Von Bloh, S. Schaphoff, C. Müller, S. Rolinski, K. Waha, and S. Zaehle. Implementing the nitrogen cycle into the dynamic global vegetation, hydrology, and crop growth model LPJmL (version 5.0). *Geosci. Model Dev.*, 11(7):2789–2812, July 2018. ISSN 1991-9603. doi: 10.5194/gmd-11-2789-2018. URL https://gmd.copernicus.org/articles/11/2789/2018/.

H. von Storch and F. Zwiers. Analysis of Variance. In *Statistical Analysis in Climate Research*, pages 171–192. Cambridge University Press, 1999.

C. J. Walcek, R. A. BROSr, and J. S. Chang. SO2, SULFATE AND HNOa DEPOSITION VELOCITIES COMPUTED USING REGIONAL LANDUSE AND METEOROLOGICAL DATA. 1986.

J. Walton, J. Mulcahy, Y. Tang, S. Rumbold, C. Hardacre, M. Stringer, R. Hill, T. Kuhlbrodt, and C. Jones. MOHC UKESM1.1-LL model output prepared for CMIP6 ScenarioMIP ssp126, 2022. URL http://cera-www.dkrz.de/WDCC/meta/CMIP6/CMIP6.ScenarioMIP.MOHC.UKESM1-1-LL.ssp126.

Q. Wang, M. Huang, S. Wang, B. Chen, Z. Liu, Z. Wang, C. Chen, H. Li, T. Zhu, D. Li, Y. Li, H. Lin, and L. Sun. Evaluation of the impacts of ozone on the vegetation productivity of woodland and grassland ecosystems in China. *Ecological Modelling*, 483:110426, Sept. 2023. ISSN 03043800. doi: 10.1016/j.ecolmodel.2023.110426. URL https://linkinghub.elsevier.com/retrieve/pii/S0304380023001576.

Y. Wang, O. Wild, K. Ashworth, X. Chen, Q. Wu, Y. Qi, and Z. Wang. Reductions in crop yields across China from elevated ozone. *Environmental Pollution*, 292:118218, Jan. 2022. ISSN 02697491. doi: 10.1016/j.envpol.2021.118218. URL https://linkinghub.elsevier.com/retrieve/pii/S0269749121018005.

T. Watanabe, T. Izumi, and H. Matsuyama. Accumulated phytotoxic ozone dose estimation for deciduous forest in Kanto, Japan in summer. *Atmospheric Environment*, 129:176–185, Mar. 2016. ISSN 13522310. doi: 10.1016/j.atmosenv.2016.01.016. URL https://linkinghub.elsevier.com/retrieve/pii/S1352231016300243.

A. Weiss and J. Norman. Partitioning solar radiation into direct and diffuse, visible and near-infrared components. *Agricultural and Forest Meteorology*, 34(2-3):205–213, Apr. 1985. ISSN 01681923. doi: 10.1016/0168-1923(85)90020-6. URL https://linkinghub.elsevier.com/retrieve/pii/0168192385900206.

M. L. Wesely. Parameterization of surface resistances to gaseous dry deposition in regional-scale numerical models. *Atmospheric Environment*, 23(6):1293–1304, 1989. doi: 10.1016/0004-6981(89)90153-4.

M. L. Wesely and B. M. Lesht. Comparison of RADM dry deposition algorithms with a site-specific method for inferring dry deposition. *Water Air Soil Pollut*, 44(3-4):273–293, Apr. 1989. ISSN 0049-6979, 1573-2932. doi: 10.1007/BF00279259. URL http://link.springer.com/10.1007/BF00279259.

S. Wilkinson, G. Mills, R. Illidge, and W. J. Davies. How is ozone pollution reducing our food supply? *Journal of Experimental Botany*, 63(2):527–536, Jan. 2012. ISSN 0022-0957, 1460-2431. doi: 10.1093/jxb/err317. URL https://academic.oup.com/jxb/article-lookup/doi/10.1093/jxb/err317.

J. R. Williams, C. A. Jones, J. R. Kiniry, and D. A. Spanel. The EPIC Crop Growth Model. *Transactions of the ASAE*, 32(2):0497–0511, 1989. ISSN 2151-0059. doi: 10.13031/2013.31032. URL http://elibrary.asabe.org/abstract.asp??JID=3&AID=31032&CID=t1989&v=32&i=2&T=1.

V. E. Wittig, E. A. Ainsworth, S. L. Naidu, D. F. Karnosky, and S. P. Long. Quantifying the impact of current and future tropospheric ozone on tree biomass, growth, physiology and biochemistry: a quantitative meta-analysis. *Global Change Biology*, 15(2):396–424, Feb. 2009. ISSN 1354-1013, 1365-2486. doi: 10.1111/j.1365-2486.2008.01774.x. URL https://onlinelibrary.wiley.com/doi/10.1111/j.1365-2486.2008.01774.x.

L. P. Wright, L. Zhang, I. Cheng, J. Aherne, and G. R. Wentworth. Impacts and Effects Indicators of Atmospheric Deposition of Major Pollutants to Various Ecosystems - A Review. *Aerosol Air Qual. Res.*, 18(8):1953–1992, 2018. ISSN 16808584, 20711409. doi: 10.4209/aaqr.2018.03.0107. URL https://aaqr.org/articles/aaqr-18-03-ir-0107.

H. Wu, L. Yu, X. Shen, F. Hua, Z. Zhao, Y. Li, and K. Ma. A systematic review of assessing climate change risks on species and ecosystems: bibliometric overview, concepts, approaches, and trends. *Glob. Sustain.*, 8:e5, 2025. ISSN 2059-4798. doi: 10.1017/sus.2025.8. URL https://www.cambridge.org/core/product/identifier/S2059479825000080/type/journal_article.

S. Yeşilköy, F. Bakanoğulları, L. Şaylan, B. Çaldağ, T. Aslan, and N. Akatas. VARIATION OF ALBEDO DURING THE GROWING PERIOD OF DIFFERENT WINTER WHEAT CULTIVARS. 2015.

X. Yin, D. Rupakheti, G. Zhang, J. Luo, S. Kang, B. De Foy, J. Yang, Z. Ji, Z. Cong, M. Rupakheti, P. Li, Y. Hu, and Q. Zhang. Surface ozone over the Tibetan Plateau controlled by stratospheric intrusion. *Atmos. Chem. Phys.*, 23(17):10137–10143, Sept. 2023. ISSN 1680-7324. doi: 10.5194/acp-23-10137-2023. URL https://acp.copernicus.org/articles/23/10137/2023/.

P. Zanis, D. Akritidis, S. Turnock, V. Naik, S. Szopa, A. K. Georgoulias, S. E. Bauer, M. Deushi, L. W. Horowitz, J. Keeble, P. Le Sager, F. M. O'Connor, N. Oshima, K. Tsigaridis, and T. Van Noije. Climate change penalty and benefit on surface ozone: a global perspective based on CMIP6 earth system models. *Environ. Res. Lett.*, 17(2):024014, Feb. 2022. ISSN 1748-9326. doi: 10.1088/1748-9326/ac4a34. URL https://iopscience.iop.org/article/10.1088/1748-9326/ac4a34.

M. D. Zelinka, T. A. Myers, D. T. McCoy, S. Po-Chedley, P. M. Caldwell, P. Ceppi, S. A. Klein, and K. E. Taylor. Causes of Higher Climate Sensitivity in CMIP6 Models. *Geophysical Research Letters*, 47(1):e2019GL085782, Jan. 2020. ISSN 0094-8276, 1944-8007. doi: 10.1029/2019GL085782. URL https://agupubs.onlinelibrary.wiley.com/doi/10.1029/2019GL085782.

J. Zhang, H. Tian, J. Yang, and S. Pan. Improving Representation of Crop Growth and Yield in the Dynamic Land Ecosystem Model and Its Application to China. *J Adv Model Earth Syst*, 10(7):1680–1707, July 2018. ISSN 1942-2466, 1942-2466. doi: 10.1029/2017MS001253. URL https://agupubs.onlinelibrary.wiley.com/doi/10.1029/2017MS001253.

L. Zhang, J. R. Brook, and R. Vet. A revised parameterization for gaseous dry deposition in air-quality models. *Atmos. Chem. Phys.*, 2003a.

X. Zhang, M. A. Friedl, C. B. Schaaf, A. H. Strahler, J. C. Hodges, F. Gao, B. C. Reed, and A. Huete. Monitoring vegetation phenology using MODIS. *Remote Sensing of Environment*, 84(3):471–475, Mar. 2003b. ISSN 00344257. doi: 10.1016/S0034-4257(02)00135-9. URL https://linkinghub.elsevier.com/retrieve/pii/S0034425702001359.

X. Zhang, M. A. Friedl, C. B. Schaaf, and A. H. Strahler. Climate controls on vegetation phenological patterns in northern mid- and high latitudes inferred from MODIS data. *Global Change Biology*, 10(7):1133–1145, July 2004. ISSN 1354-1013, 1365-2486. doi: 10.1111/j.1529-8817.2003.00784.x. URL https://onlinelibrary.wiley.com/doi/10.1111/j.1529-8817.2003.00784.x.

Y. Zhang and M. G. Schaap. Weighted recalibration of the Rosetta pedotransfer model with improved estimates of hydraulic parameter distributions and summary statistics (Rosetta3). *Journal of Hydrology*, 547:39–53, Apr. 2017. ISSN 00221694. doi: 10.1016/j.jhydrol.2017.01.004. URL https://linkinghub.elsevier.com/retrieve/pii/S0022169417300057.

L. Zheng, Y. Qi, Y. Wang, J. Peng, and Z. Qin. Calibration and validation of phenological models for Biome-BGCMuSo in the grasslands of Tibetan Plateau using remote sensing data. *Agricultural and Forest Meteorology*, 322:109001, July 2022. ISSN 01681923. doi: 10.1016/j.agrformet.2022.109001. URL https://linkinghub.elsevier.com/retrieve/pii/S0168192322001915.

X. Zhou, X. Yue, and C. Tian. Responses of Ecosystem Productivity to Anthropogenic Ozone and Aerosols at the 2060. *Earth's Future*, 12(1):e2023EF003781, Jan. 2024. ISSN 2328-4277, 2328-4277. doi: 10.1029/2023EF003781. URL https://agupubs.onlinelibrary.wiley.com/doi/10.1029/2023EF003781.